Biomimetic Actuation Systems for Morphing Lifting Surfaces

Benjamin John Stacey

Submitted to the University of Hertfordshire in partial fulfilment of the requirements of the degree of
Doctor of Philosophy

February 2025

Abstract

Morphing lifting surfaces are increasingly being integrated into aerospace systems, with uncrewed aerial vehicles (UAV), micro aerial vehicles (MAV), and the general uncrewed aerial systems (UAS) at the forefront of this development. Recent innovations in actuator technology, particularly biomimetic actuators, now exhibit actuation characteristics comparable to traditional electromechanical and hydraulic systems. This dissertation reviews bio-inspired muscle-like actuation systems with a focus on pneumatic artificial muscles (PAMs) and evaluates their suitability for morphing aerospace structures. Actuators are compared to avian muscles using measurable characteristics, and conclusions are drawn regarding their implementation in aerospace applications.

Following this avian-based comparison methodology, experimentation has been conducted into the kinematics avian employ in vivo and the flight dynamics they enable. Span morphing retraction and extension rates determined from in vivo flight data of the Common Buzzard (Buteo buteo) and Harris Hawk (Parabuteo unicinctus)

Presented is the preliminary design and development of a novel span-wise morphing concept that heavily implements biomimetic design. Specifically, the skeletal structure of avian is mimicked, incorporating humerus, ulna/radius, and carpometacarpus analogues to enable a versatile range of motion, facilitating multiple manoeuvrers and flight types. PAM actuators are employed as a mechanism for actuation, achieving a semi-span length change and variable sweep angles. Initial computational fluid dynamics (CFD) results are discussed in comparison with similar concepts in the field, and a rapid prototype is produced to confirm the viability of the concept.

The span-wise morphing wing is subsequently modelled and controlled using inverse kinematics, enabling simplified span-length positioning. The control system incorporates PAM force models to individually model the pneumatic system driving each joint. The mechanical system of each joint is used to produce a direct kinematic model for wing tip position, and the inverse determined for control. The validity of both the model and system is experimentally tested on a fixed semi-span prototype rig of the morphing concept. Feedback is introduced through embedded potentiometers in each joint to provide joint angle feedback, with system tuning presented for different dynamic responses.

The dynamic response of the morphing concept is evaluated via external photogrammetry and metrology techniques, analysing wing-tip displacement and actuation repeatability under static and simulated aerodynamic loading conditions. A dynamic case is also evaluated for the concept in relation to the proposed aircraft application, with the resulting dynamic response compared to the similarly observed response in avian species. This static and dynamic case is then tested

under aerodynamic loading via a programme of wind tunnel testing.

This evaluation establishes a framework for integrating biomimetic morphing wings into UAV applications, contributing to the advancement of morphing aerospace structures and providing a foundation for future adaptive wing technologies in UAV and MAV systems.

Acknowledgements

This PhD has been both rewarding and challenging. Over the time I have gained lots, learnt more about work and overcoming obstacles than I imagined, and reflected on myself which has profoundly influenced my life. However, I would be amiss if I didn't acknowledge the overwhelming support I have had throughout the years. To everybody, thank you.

My supervisor, Dr Peter Thomas. Your patience will not be forgotten. Thank you for the opportunity in awarding me the project and the continued support, encouragement, and yet further opportunities which you have continued to offer.

My secondary supervisors, Dr Rachel Cunliffe and Dr Andrew Lewis. Your support and feedback were always appreciated.

Kevin Gilmore, thank you for your technical support in almost every aspect of the concept prototype development.

Alex van der Gragt, thank you for producing the machined components for the pneumatic rig and concept.

The CODA falconry, thank you for supporting all our work with your amazing bird's

To my partner Bianca Baciu, my friends, and my family. Thank you for all your unwavering support. Without your emotional support I would not have come close to the submission of this dissertation.

Contents

1 Introduction **15**
- 1.1 Objective . . . 15
- 1.2 Contribution . . . 15
- 1.3 Background on Morphing Concepts . . . 17
- 1.4 Overview . . . 20

2 Literature Review of Biomimetic Morphing Actuation **22**
- 2.1 Actuators . . . 23
  - 2.1.1 Hydraulic and Pneumatic Artificial Muscle Actuators . . . 26
  - 2.1.2 Shape Memory Alloy Artificial Muscle Actuators . . . 32
  - 2.1.3 Piezoelectric Artificial Muscle Actuators . . . 36
- 2.2 Comparison with Avian muscle standards . . . 39

3 Avian Span-wise Kinematics **44**
- 3.1 Background on Avian Biology . . . 45
- 3.2 Background on avian measurement methodologies . . . 48
- 3.3 Kinematics Capture . . . 50
  - 3.3.1 Infrared . . . 50
- 3.4 Avian Marking . . . 52
- 3.5 Span-wise kinematics . . . 56
- 3.6 Avian Kinematics Conclusion . . . 70

4 Span-wise Morphing Concept Development **72**
- 4.1 Concept Development . . . 72
- 4.2 Preliminary Computational Fluid Dynamic Analysis . . . 76
- 4.3 Conclusion on the viability of the proposed concept . . . 80

5 Concept Modelling and Control **84**
- 5.1 Kinematic Modelling . . . 85
  - 5.1.1 Denavit-Hartenberg notation . . . 85
  - 5.1.2 Wingspan simulation . . . 86
  - 5.1.3 Wing Area simulation . . . 86
- 5.2 Pneumatic Artificial Muscle System Modelling . . . 90
  - 5.2.1 System Identification . . . 94
- 5.3 Control System . . . 107
  - 5.3.1 Biomimetic application . . . 109
  - 5.3.2 Control validation . . . 112
- 5.4 Wing Control Conclusion . . . 117

6 Wind Tunnel Experimentation **118**
6.1 Structural Testing . . . 118
6.1.1 Position Experimental Setup . . . 121
6.1.2 Concept Precision . . . 123
6.2 Wind Tunnel Methodology . . . 128
6.2.1 Concept Lifting Surface . . . 128
6.2.2 Wind Tunnel Setup . . . 132
6.3 Static Performance . . . 136
6.4 Quasi-static Performance . . . 139

7 Conclusion **142**
7.1 Continued work . . . 144

A Avian Motion Capture Tables **146**

B Avian Motion Capture Plots **185**

List of Figures

2.1 Left to right; the braided PAM in an unactuated state, actuated, and the PAMs cross section showing the flexible inner-tube. Also shown are the variables used to define the actuator, as well as in modelling. 27

2.2 A representation of each of the sleeve variations on PAM actuators, left to right; McKibben/Braided, Pleated, Netted, ROMAC, and Hyperboloid. 28

2.3 Pneumatic concepts; (a), PAM actuated servo analogue Vocke et al; (b), Pressure actuated morphing skin Chillara et al; (c), Braided PAM actuated trailing edge flap mechanism Woods et al; (d) Positively pressurised PAM failure due to over pressurisation Woods et al; (e), Thin McKibben actuator bunched to produce an artificial muscle demonstrating the flexibility of PAMs Kurumaya et al; (f), Linear VAMP vacuum artificial muscle Yang et al. PAM: pneumatic artificial muscle VAMP: vacuum-actuated muscle- inspired pneumatic structures 29

2.4 Temperature hysteresis for a general shape memory alloy, based on Antonucci and Martone. 32

2.5 Shape memory alloy concepts; (a), Coiled SMA driven camber morphing concept Ko et al; (b), Solid SMA strips actuating chevrons Hartl et al; (c), McKibben muscle with SMA line to produce bending Xiang et al; (d), crankshaft based SMA rotary actuator Hwang et al; (e) and (f), SMA based camber morphing system proposed by Barbarino et al. 34

2.6 Piezoelectric materials concepts; (a), variable camber wing employing embedded MFC bimorph actuators Bilgen et al; (b), MFCs implemented in a camber morphing concept presented by Paradies et al; (c) and (d), Two MFC actuators to produce a localised camber change for control purposes Bilgen et al; (e) and (f), A similar roll control concept presented by Barret et al. using post-buckled precompressed axial force piezoelectric actuators to replace more typically actuated ailerons. MFC: Macro fibre composite 41

2.7 Actuation stress and strain presented in a plot, approximate values taken from the literature cited. Stresses represent the peak actuation stress, while the strain is presented as a percentage of the original unloaded length. 42

2.8 Specific power, versus power density presented in an Ashby plot, values taken or derived from the literature cited. 42

2.9 Actuation strain, presented as a percentage of the un-actuated and unloaded length; against bandwidth, the maximum actuation frequency; values taken from the literature cited. 43

3.1 Graphic illustrating the skeletal structure of the bird wing. Obtained from the Natural History Museum at Tring, specimen NHMUK 1940.7.6.1. 45
3.2 Illustration of the twin parallels mechanism. 47
3.3 Airfoil sections for the proposed avian-based concept (top) and the bird wing section results obtained through photogrammetry by Carruthers et al (bottom). 49
3.4 IR Diagram 51
3.5 A photograph of the capture volume for a majority of captures obtained. Shown are the 10 cameras parallel and adjacent to the flight direction. The cameras positioned below the volume maintain a line of sight with markers during diving flight. 52
3.6 The secondary capture volume used to force specific flight behaviours 53
3.7 A general layout of the marker placement over the specimens. Note that these positions give an approximate position. Each species presented a different skeletal geometry, which defined the marker position. A total of twelve markers were used across the back of the specimen. 55
3.8 Left, female Common Buzzard *Buteo buteo*, approximately 1kg. Right, male Harris Hawk *Parabuteo unicinctus*, approximately 0.7kg. Shown are the markers; however, the outer wing markers are obscured and not visible in the images 56
3.9 A series of figures showing a representative take-off manoeuvrer included in the presented data set. This series presents the flight of specimen CB *buteo buteo* (Common Buzzard). Shown in each plot are the six markers comprising the wing and a single fore spine marker taken as a reference point for the body of the specimen. Axes are centred about this reference point and remain so regardless of translational movement within the independent capture area. 58
3.10 A series of figures presenting the same flight capture data as shown in figure 3.9. Depicted here each point has been rotated onto the span-chord or xy plane to remove flapping motion. This allows a view of planar span-wise extension and retraction of the wing. 62
3.11 Position based plots for specimen CB common buzzard (*buteo buteo*). Showing the wing extensions captured via IR motion capture. Left and right wings are shown with the left wing y coordinates shown as absolute values, red and blue, respectively. 64
3.12 Joint angle plots for specimen CB common buzzard (*buteo buteo*). Derived from wing markers captured via IR motion capture. Left and right wing joints are shown in red and blue respectively. (a) Represents the shoulder angle, (b) the elbow, and (c) the wrist. . . . 66

3.13 Joint angle plots for specimen CB common buzzard (*buteo buteo*). Derived from wing markers captured via IR motion capture. Left and right wing joints are shown in red and blue respectively. (a) Represents the shoulder angular velocity, (b) the elbow, and (c) the wrist. 68
3.14 Joint angle plots for specimen CB common buzzard (*buteo buteo*). Derived from wing markers captured via IR motion capture. Left and right wing joints are shown in red and blue respectively. (a) Represents the shoulder angular acceleration, (b) the elbow, and (c) the wrist. 69
3.15 Joint angles, for specimen CB common buzzard (*buteo buteo*), plotted against wing semi-span as a percentage of maximum span length. Overlaid are the range bars denoting the uncertainty in the angle at each span location. This range is driven by the individual motion captured flights plotted transparently. 70

4.1 Computer aided design rendering of the jointed structural members forming the mechanical system for span-wise retraction. Omitting the aerofoil skin trailing edge plates, electrical, and pneumatic systems. The positioning of the two pairs of pneumatic artificial muscles is shown, in both the wing mid-span and the fuselage. 73
4.2 Proposed concept aerofoil 74
4.3 Computer aided design drawing of the avian span-wise morphing concept. Extended (top) and full retracted (bottom) 75
4.4 The proposed aerofoil as panellised in XFoil, 200 panels were used in the viscus analysis. 77
4.5 Shown is a plane section of the volume mesh taken at approximately 50% of the semi-span. The first view shows the wake refinement and volume gradient producing a finer mesh closer to the wing surface. The secondary view gives a closer illustration of the prism mesh used to obtain a suitable mesh sizing to resolve the boundary layer. 78
4.6 The velocity vectors for the flow over the upper surface of the concept, showing the 'leaking' airflow. 78
4.7 XFoil plots for the avian-based proposed aerofoil and Clark-Y results produced by C. Lyon et al, used for comparison. Avian-based section, (a) and (c) plots showing the lift and drag coefficients, respectively. Clark-Y, (b) and (d) plots showing the lift and drag coefficients, respectively. 79
4.8 The concept section showing the proposed interfacing section aft of the leading edge D-spar, which will be investigated further in future research. 80
4.9 Lift coefficient change with angle of attack, results from the three-dimensional computational fluid dynamic analysis. Clark-Y results produced by C. Lyon et al. 81
4.10 Drag coefficient change with angle of attack, results from the three-dimensional computational fluid dynamic analysis. Clark-Y results produced by C. Lyon et al. 82

4.11 Lift coefficient change against drag coefficient, results from the three-dimensional computational fluid dynamic analysis. Clark-Y results produced by C. Lyon et al. 83

5.1 The span-wise motion for the *Milvus milvus* given previously obtained member lengths and an assumed 1:2:2 joint motion ratio. 86
5.2 An image of *Milvus milvus* specimen NHMUK unregistered, arranged in a fully extended position. Overlaid is the sectional modelling method proposed to be used to approximate the area of an avian wing. 88
5.3 The graphical output for the area avian model. Similarly showing the sectional method for approximating the wing area using a quadrilateral and triangle. 89
5.4 The graphical output of the area model. Comparatively showing the modelled area approximation over the range of shoulder joint angles. 89
5.5 Proposed PAM model overview, outlining the sequencing of the individual component equations. 91
5.6 Three-way pneumatic control valve, Festo^{TM} MPYE-5-1/8-HF-010-B. Shown in the three operational states, with the central actuated spool (normally enclosed) visible. 91
5.7 An image of the electro-pneumatic setup used for model validation and the process of frequency response system identification. Not shown is the computer providing the voltage input and recording the response. It should also be noted that this equipment rig has duplicated items for the two joint actuation of the full span-wise morphing concept. 95
5.8 A comparison between the single pneumatic artificial muscle (PAM) joint actuated at different operating supply pressures. Shown is the measured joint angle as a percentage of the maximum angular deflection measured. This is presented as a result of a sinusoidal voltage input of 0.1 rad/s. 97
5.9 A similar comparison to figure 5.8. Shown against the voltage input to the proportional control valve. Of note is the range away from the median voltage 5V with a shallow gradient. 97
5.10 A plot showing the Internal pneumatic artificial muscle (PAM) pressure during the actuation period described in figure 5.8. Significant to note is the cycle formed by the pressure in the individual PAM and the inconsistent nature. 98
5.11 The joint angle response to a sinusoidal voltage input at the following frequencies: (a) 0.1 rad/s, (b) 0.5 rad/s, (c) 1 rad/s, (d) 3 rad/s, (e) 5 rad/s, (f) 7 rad/s, (g) 10 rad/s, (h) 15 rad/s, (i) 25 rad/s, (j) 50 rad/s, and (k) 100 rad/s. A constant amplitude was input; however, the resulting data was detrended over the 5 seconds shown. 103

5.12 Presented are the models estimated from the PAM sinusoidal response from each of the following frequency ranges. (a) 0.1 rad/s to 1 rad/s, (b) 1 rad/s to 3 rad/s, (c) 3 rad/s to 5 rad/s, (d) 5 rad/s to 7 rad/s, and (e) 7 rad/s to 10 rad/s. Plotted at each frequency range is the output from each derived model against the following input frequency. (a) 0.5 rad/s, (b) 1 rad/s, (c) 3 rad/s, (d) 5 rad/s, and (e) 7 rad/s. . 106
5.13 Bode plot of the frequency response system identification. 106
5.14 A visual representation of the notation used to define the span-wise morphing concept for application of inverse kinematics. Each linking member is denoted a_n with n the end effector joint number. The coordinate systems used are also represented and similarly subscripted in relation to joint number. 107
5.15 (a) Avian motion capture data showing the chord-wise y positions of the wing tip as a percentage of the maximum y position. Against the x position of the wingtip, similarly as a percentage of the maximum value for span position. Also shown is the derived curve used to approximate the relationship between the two variables. (b) Presented as the angle of attack against the span-wise position x. Similarly shown is the curve used to define the angle of attack θ as a function of span. 110
5.16 A diagram detailing the mechanical layout for the control system testing. Shown are both pairs of pneumatic artificial muscles (PAMs). Each actively actuates their respective joints, with the outboard pair passively actuating the final wrist joint. Note this diagram does not represent scale. 112
5.17 An overview of the electro-pneumatic system for the span-wise morphing concept. Featuring the pneumatic system outlined in ISO 1219-1:2012 symbols, the electronic system overview, and the feedback system overview. 113
5.18 An image of the complete setup used to validate the control system in a passive environment. Labelled are the additional components which make up the three-jointed system as opposed to the single-jointed pneumatic artificial muscle control setup. Note that none of the aerodynamic surfaces of the span-wise morphing concept are present during these tests. 114
5.19 Presented are the outputs at each stage of the control system these form the input to the subsequent stage. (a) the system input; span position as a percent of maximum span, (b) the output of the dependent variables based on avian derived relationships, (c) inverse kinematic output joint angles, (d) resultant measured PAM pressures, (e) measured joint angles produced by the concept. 116

6.1 Span-wise morphing structure in a fully extended position and retracted overlaid. Each pneumatic artificial muscle (PAM) antagonistic pair is visible actuating each respective joint. 120

6.2 The stereo high-speed camera setup shown with the simulated morphing concept loading. These cameras were run at 500 Hz and configured here to track the wing tip position within a capture volume of 40 mm x 50 mm x 50 mm. Visible on the concept are contrasting white and black markers this contrast allowing increased accuracy in identifying the concept's position. 123
6.3 Left and right camera views as calibrated for the wing tip measurement volume. Each view depicts the wing tip in the non-inverted orientation, as taken unloaded, with the contrast markers in place. . . 124
6.4 The quasi-static system response at the approach to a steady state after a 1 rad/s sinusoidal span position input. Plotted against the extension cycle angle where the datum represents 1 rad from the input signal for maximum extension. Note only the final 10 mm of the motion is shown due to the limitations of the cameras used. . . . 126
6.5 Left and ring camera views as calibrated for the full concept measurement volume 400 mm x 300 mm. Also note the contrast markers in place on the members and on the joint axis'. 127
6.6 The span-wise morphing concept with a lifting surface leading edge attached. Also shown are two trailing edge carbon fibre plates or 'feathers'. Linking mechanisms, comprising one aluminium and two ABS members, for both the wrist joint and feather actuation can be seen. 130
6.7 The span-wise morphing concept with lifting surface assembled, including leading edge and carbon composite upper-surface and trailing edge. Presented in mid-actuation approximately 550mm semi-span. . 131
6.8 Prototype of the span-wise morphing concept as configured in the wind tunnel working section. Projected onto the image are the coordinate axis of the balance. Note that the wing is mounted vertically from the balance situated on the ceiling of the tunnel. 133
6.9 Wing area change as a function of variable wing span. Shown in blue is the area change given a 2:1 joint angle ratio as assumed in previous chapters. In orange, the area change derived from the avian motion is applied to the span-wise morphing concept. 135
6.10 Lift (a), drag (b), and pitching moment (c) force polars for the span-wise morphing concept at 350,000 Reynolds number. Plotted for each is the measured and corrected values for full extension, full retraction, and mid-extension held at 50% deformation. Plots (d), (e), and (f) present the equivalent coefficient. Also represented here are the points collected over 12 runs. 137
6.11 Lift and Drag force measured during cyclical extension and retraction of the concept at $350,000$ Reynolds number. Plots (a), (b), and (c) present the forces acting on the concept against cycle time. A representative sample of the 120 cycles is shown for clarity. Plots (d), (e), and (f) show the calculated average of these cycles against cycle time. Also shown is the standard deviation presented as bars at 1.5 s intervals. 140

B.1 Common Buzzard - specimen: CB, Trial 4, Capture session 3, Frame interval 0.05 seconds 186
B.2 Common Buzzard - specimen: CB, Trial 7, Capture session 3, Frame interval 0.05 seconds 187
B.3 Common Buzzard - specimen: CB, Trial 8, Capture session 3, Frame interval 0.05 seconds 188
B.4 Common Buzzard - specimen: CB, Trial 15, Capture session 3, Frame interval 0.04 seconds 189

List of Tables

1.1 An overview of the types of morphing lifting surfaces discussed. . . . 18

2.1 The values shown represent the modal average for the species muscles across the literature cited in section 2.1. The avian data is representative of the in vivo pectoralis muscle during straight and level flapping flight. 24
2.2 Table for the comparison of pneumatic artificial muscle properties'. Alongside pectoral muscle values for *Columba Liva* (Pigeon) and *Sturnus Vulgaris* (European Starling). Values for the avian represent in vivo straight and level flapping flight. While actuator values are representative of maximum bandwidth actuation, and the braided PAM given as a range based on multiple sources discussed in section 2.1.1. 31
2.3 Table for the comparison of the properties' exhibited by shape memory alloys. Alongside pectoral muscle values for *Columba Liva* (Pigeon) and *Sturnus Vulgaris* (European Starling). Values for the avian represent in vivo straight and level flapping flight. While actuator values are representative of maximum bandwidth values collated and derived from multiple sources discussed in section 2.1.2. Values denoted with a (–) represent values unobtainable through the literature reviewed. 35
2.4 Table for the comparison of piezoelectric actuators, alongside pectoral muscle values for *Columba Liva* (Pigeon) and *Sturnus Vulgaris* (European Starling). Values for the avian represent in vivo straight and level flapping flight. The piezoelectric actuator properties are largely derived from Huber et al, as they are representative of the actuators discussed. 38

3.1 *Milvus milvus* wing bone length dimensions, including measured specimen and researched data. Including averaged values for use in further calculations. One specimen had no specimen number available (NSNA) as it was new to the museum's collection. 46
3.2 The adhesive technical details, including loading forces and specific use cases. Holding forces stated by the manufacturer. These values for tensile and shear force were tested under the American ASTM D3330 and ASTM D1002 standards, respectively. 54

3.3 Reference details relating to the birds used throughout the capture sessions. An ID, related to each specimen's species, will be used to refer to each specimen in the text. Presented against these are the given names used by the falconers, which can be used to identify the specimens outside the context of this work. The mass given is the nominal flying weight found by the handlers as best suited for the individual bird. 55
3.4 shoulder, elbow, and wrist joint angles and angular rates for a typical flight of specimen CB common buzzard (*buteo buteo*). Averages are the mean average the median average for the joint angle is inconsistent due to extension variation so is not given. 61

5.1 Festo Pneumatic artificial muscle (PAM) Fluidic Muscle DMSP/MAS physical characteristics as used in validation of the proposed model and frequency response model development. 96
5.2 Values for the span-wise morphing concept proposed following the notation defined in figure 5.14. 107

6.1 Wing tip error observed in the unloaded concept across $n = 500$ cycles. Span-wise morphing concept was actuated as pressurised at 6 bar. Error referenced to an initial position 125
6.2 Wing tip error observed in the loaded concept across $n = 500$ cycles. Span-wise morphing concept was actuated as pressurised at 6 bar. Error referenced to an initial position 125

A.1 Common Buzzard - specimen: CB, Trial 2, Capture session 2, Frames: 1535-1625 147
A.2 Common Buzzard - specimen: CB, Trial 3, Capture session 2, Frames: 7288-7389 151
A.3 Common Buzzard - specimen: CB, Trial 4, Capture session 2, Frames: 1581-1688 156
A.4 Eurasian Eagle Owl - specimen: EEO, Trial 9, Capture session 3, Frames: 67-168 161
A.5 Harris Hawk - specimen: HH, Trial 11, Capture session 3, Frames: 951-1073 165
A.6 Common Buzzard - specimen: CB, Trial 8, Capture session 3, Frames: 1505-1555 170
A.7 Common Buzzard - specimen: CB, Trial 4, Capture session 3, Frames: 188-240 172
A.8 Common Buzzard - specimen: CB, Trial 7, Capture session 3, Frames: 780-866 174
A.9 Common Buzzard - specimen: CB, Trial 15, Capture session 3, Frames: 445-615 178

Chapter 1

Introduction

1.1 Objective

The landscape of aircraft design is undergoing a significant change driven by the demand for mission capability and the emergence of uncrewed aerial vehicles (UAVs), micro-aerial vehicles (MAVs), and uncrewed aerial systems (UAS). This has led to a high level in the conceptualisation of morphing aircraft diverging from traditional fixed-wing configurations. However, conventional actuators face challenges in meeting the demands of these structures, prompting an exploration into specialised mechanisms and materials.

A diversified mission capability has long been a requirement for aircraft in all applications. UAS are no exception, and the development landscape and removal of the constraints inherent in manned flight have resulted in a field where adaptive structures/systems are increasingly viable [1]. Hartl makes this case most persuasively and quantitatively, noting the downsides of an adaptive structure, for example, increased weight, complexity, and decreased reliability [2]. However, they highlight that in cases where the aircraft is intended for multiple roles, the specifications are likely to be mutually exclusive or otherwise conflict. Furthermore, a concept aimed at one of these roles is likely to perform poorly in the other role, regardless of any compromises; the same holds true vice versa for two roles. Whereas the adaptive aircraft can be developed to outperform these compromised designs in both roles simultaneously, despite the drawbacks of a morphing structure.

A biomimetic approach is proposed as the basis for an adaptive lifting surface which aligns with these criteria.

1.2 Contribution

This thesis examines the cross-disciplinary fields of biomimetics and engineering, focusing on the application of biomimetic design principles in actuator development across various engineering domains. Biomimetics, centred on emulating nature's solutions to human challenges, holds promise for augmenting efficiency and performance within engineering systems.

The literature is reviewed, primarily focusing on actuation systems under development or not yet applied in aerospace vehicle design. In looking for a standard with which to act as a benchmark for very different actuators and actuation systems. An avian musculature comparison methodology for these morphing aircraft actuators is

particularly relevant within the domain of MAVs. Drawing inspiration from biological musculature, it enables the engineering of actuators that are not only efficient but also responsive and adaptable to the dynamics of morphing aircraft. This novel methodology allows objective comparison of actuation systems that are otherwise disparate. It is further used to define an actuator for the concept presented in later chapters.

The following chapter continues this bio-inspired development principle. Birds or avian are noted to be the subject and source of much biomimicry. Significant and well-established literature was identified, and the order *Accipitriformes* within the family *Accipitridae* was taken forward. The skeletal dimensions for a number of species are presented as a case study for wing proportions and subsequent correlation with the primary flight mode exhibited by the avian.

A novel series of in vivo wing kinematic measurements is presented. Marker-based position capture is devised as a methodology for these kinematic measurements. New techniques are presented to encourage the avian's natural behaviour, while a less obtrusive marker system is proposed. Accuracy and precision of the markers' position are considered in relation to the target structure, and systematic errors are reduced via a new method. The flight motion is captured via this method simultaneously to the local wing kinematic motion, allowing comparisons to be made between changes in wing geometry and flight dynamics. However, the local relative motion of the wing and the underlying musculoskeletal structure is uniquely presented. The relation of joint angles, angular velocities, and angular accelerations are derived and consistency across flights is highlighted and proposed as the basis for a novel morphing lifting surface and its dynamic control.

Following this process of avian kinematic capture, the development of a morphing structure was undertaken, drawing inspiration from avian morphology. Computational fluid dynamics (CFD) analyses are conducted to evaluate the feasibility of these bio-mimetically inspired structures. Control system development is identified as key to the implementation of the concept, given the importance of precision and accuracy in actuation for realising dynamic morphing capabilities. Derived from avian wing biomechanics, the control system integrates pneumatic artificial muscles (PAMs), aiming to emulate specifically the span-wise motion exhibited by avian.

The concluding chapter outlines a programme of wind tunnel testing aimed at evaluating the aerodynamic performance of the concept. Alongside specific characterisation of the prototypes' aerodynamic behaviour, these experiments also looked to draw conclusions on the feasibility of the avian-based morphing approach. Static and dynamic results are presented, with the former compared to results gained via CFD. The dynamic position performance, looking at wing tip position repeatability and dynamic response, is gained through external position measurements under simulated loading.

The following can be considered an enumerated summary of the novel aspect presented.

1. A comparative method in quantifying existing actuation technology against a biological-based standard. Allowing conclusions as to the feasibility of application within biomimetic concepts to be drawn.

2. A novel application of kinematic position capture to *Accipitriformes* with techniques to promote unconstrained flight.

3. Derivation of a model representing the span-wise kinematics exhibited by *Accipitridae*

4. Development of a biomimetically derived span-wise morphing concept

5. Application of closed-loop control enabling position control of the wing tip via pneumatic artificial muscles validated through prototype testing.

6. Aerodynamic evaluation of the proposed concept for a UAV application.

1.3 Background on Morphing Concepts

The development of morphing aircraft concepts has increased significantly in the past decade, [3] due in part to the increasing requirement for efficiency and the advent of uncrewed aerial vehicles where the design is unrestrained from the ergonomic requirements of a pilot. Due to these factors, emerging concepts are increasingly deviating from the traditional fixed-wing, aft-tail configuration widely adopted throughout the industry. Alongside this development is the continued adoption of biomimetics within the industry [4], particularly in the field of morphing structures where bio-esque movement is required.

Morphing has been applied to most features of traditional aircraft and those specialist for specific applications often military. Popular and well-known examples include the droop nose of the Concord, enabling efficient supersonic flight and cockpit shielding. While in its lowered state, it provides an unobscured line of sight on landing approach. Despite these examples, there is a notable difference between the number of conceptual proposals for the morphing of the general aircraft structure and that of the wing. Although in some areas of development the difference between fuselage and wing has been reduced. Lifting bodies where multiple structures on the airframe are, not only optimised for aerodynamic efficiency, but are actively designed to produce lift. Even with the definitions of individual features making up aircraft becoming more of a spectrum. The wing is the most morphed aircraft structure by a notable margin. The wing structure for any particular aircraft is a compromise between efficiency in different flight conditions and mission requirements. Typical aircraft with a wing specific for an environment can be inefficient or unsuitable in situations outside the optimal operation range. Morphing wings are subsequently employed to allow an increased range of flight operations and optimisation in necessary situations, which is accomplished by assuming the most aerodynamically suitable structure. Increased control can be attained by applying morphing to control surfaces or by directly causing perturbations through manipulation of the wing structure. Morphing structures often produce greater perturbations than traditional control surfaces due to their increased size allowed by the adoption of abnormal internal structures.

Wing aerodynamic features allow the greatest influence over the suitability of an aerofoil for any particular role. These parameters can therefore be morphed to alter the overall wing role. Wing aspects that have been used as a morphing subject can be seen in the table 1.1, although many variations on these have been previously carried out.

Review papers have extensively covered the development and introduction of morphing concepts over the last few decades. Notable papers, including Barbarino

Table 1.1: An overview of the types of morphing lifting surfaces discussed.

Chordwise	Spanwise	Out of Plane
Camber	Wingspan	Twist
Thickness	Sweepangle	Dihedral
Chord length		

[5] and Sun [6], discuss the different morphing features in detail. However, arguably, the wing parameters with the most significant aerodynamic impact are wing area and span-length (by extension aspect ratio). These will therefore be the focus for this novel concept going forward, as opposed to the alternative morphing techniques also employed by avian.

Chordwise Morphing

Camber morphing is the alteration of the camber line of the aerofoil resulting a coefficient change in both lift and drag. This morphing therefore is used to alter the lift and drag produced by the morphed wing section, essentially acting as flaps and slats and thus often being used for the same purpose.

Camber morphing is the most common type of wing morphing which is a result of various factors. Foremost, camber changes produce the highest aerodynamic effect in relation to the size of the deformation and percentage of the structure morphed. These reduced deformation areas result in simpler mechanisms and control systems, and increased compatibility with existing systems in typical aircraft. In these concepts trailing edge actuation is commonly used to produce the camber change due to its high impact of the aerodynamic coefficients. Concepts such as the Fish bone active camber concept use a compliant wing structure along with motor-driven tendons causing deformation of the central spar under compression and subsequently a camber change. [7] Traditionally actuated designs such as the Fish Bac are mechanically complex, relying on structural components to limit the morphing resulting in excess stresses within the structure.

Development in piezoelectric materials over the past twenty years has resulted in their implementation into these concepts. Bimorph strips are used for simple unidirectional movement and manipulate a compliant aerofoil structure. These concepts provide a low-weight and mechanically simple alternative to traditional actuators [8] which is particularly evident in UAV applications. As a result, the following concepts are some of the most well-progressed 'smart' material based designs currently in development. A concept that exemplifies this trend was proposed by Roelof Vos et al [9] and the morphing is employed for roll control about the longitudinal axis of a small radio-controlled UAV. The piezoelectric strips used are both postbuckled and precompressed a design developed to have a stroke length four times greater than traditional bimorph strips. This allows an increase in morphing deformation and subsequently control authority, while maintaining a similarly sized and powered piezoelectric strip. The reduction in complexity and subsequently weight and component failure rates has resulted in the increased development of piezoelectric materials in morphing wing applications. However, the limitations inherent in the materials such as the 1-2cm actuation stroke lengths [10] will restrict piezoelectric bimorphs to small actuation stroke systems. Which will reduce their applicability

to systems with greater morphing areas required by Span-wise morphing structures.

Spanwise Morphing

Wingspan morphing, the changing of the wing's span length, primarily results in the alteration of the wing's lift, drag, aspect ratio, and loading. Consequently, it allows significantly more control over the wing than other morphing parameters. Span morphing tends to be structurally complex due to up to 60% of the wing being morphed [11]. The effect of span morphing on Lift and drag is a result of the change in area of the wing generally calculated by $L = \frac{1}{2}\rho V^2 C_l S$ for straight wing designs. Aspect ratio (AR) can similarly be expressed through it's equation. The roll control rates can be altered through the AR effect on the moments of inertia thus the controllability of the aircraft can be changed.

Concepts proposed for fixed-span morphing include R. Ajaj et al [12] a recent zigzag-based design. The wing utilises a traditional semi-monocoque inboard structural section, primarily transferring the load to the fuselage. The morphing section contains a pin joint mechanical structure allowing actuation through the use of lead screw electromechanical actuators. Mechanically operated morphing structures such as this tend to be heavier than the base aerofoil and alternative actuation techniques. This however is often offset and surpassed by the efficiency gained by the morphing. Another mechanically actuated span morphing design proposed by P. Santos et al [11], employs a rack and pinion mechanism. A telescopic wing design is adopted to allow a rigid skin to be used. The outboard section comprises 50% of the span, while an overlap of 8% provided sufficient stiffness. This rigid skin reduces aeroelastic effects that can be exhibited by flexible elastomeric-matrix composite skins commonly used in morphing concepts.

Telescoping structures, such as those described by J. Blondeau [13], which focus on changes in aspect ratio, can also employ hydraulic or, more commonly, pneumatic actuation. Telescopic pneumatic spars acting as cylinders produce the 114% increase in span-length, while also acting as the primary structural element supporting the wing loading. As a result, the weight of the combined actuator-structure assembly can be reduced compared to separated designs. Early telescopic systems tend to target large changes in area compared to newer flexible and compliant structures, Parancheerivilakkathil [14] adds to this work by demonstrating a practical design that avoids some of the common drawbacks seen in earlier concepts. Previous approaches often achieved significant changes in wingspan but introduced problems such as increased weight, mechanical complexity, or large increases in structural loads, while flexible designs faced challenges in maintaining a smooth, aerodynamically useful wing surface. The ASAPP wing presents a solution by limiting span extension to 25% and using a sliding spar, flexible skin, and added ribs to control unintended deformation, which is claimed to result in improved aerodynamic efficiency without the severe load penalties associated with designs that exhibit a high degree of morphing. This reinforces a trend in the spanwise morphing literature: moderate, controlled span changes can provide meaningful performance benefits for small UAVs while remaining resistant to perturbations and easier to implement.

The CGull UAV [15] builds on earlier bio-inspired concepts [16] that explored individual morphing modes—such as sweep, dihedral, feather spreading, and tail articulation—but often without fully integrating them into a complete aircraft. Previous seagull-inspired systems, including variable gull-wing platforms, independently

swept-wing drones, and feather-folding designs, demonstrated the aerodynamic value of avian-like shape change but were typically constrained by limited degrees of freedom or conventional tail layouts. CGull proposes to advance this by combining coupled two-degree-of-freedom wing sweep with a dual-axis morphing tail in a single composite airframe, allowing coordinated wing–tail shape changes that more closely reproduce the Great Black-Backed Gull's gliding adaptations. The literature highlights that few prior morphing UAVs achieved this level of integration or structural biomimicry, and CGull's successful actuation and flight tests therefore provide a noteworthy demonstration of multi-mode, bird-inspired morphing in a practical UAV platform. A precedent is therefore set that significant morphing or a high magnitude of lifting surface change can benefit UAVs in flight.

Pneumatics are being increasingly considered of applications in morphing concepts particularly micro UAVs. [12] Pneumatics in the field of aerospace, passed traditional cylinder based designs, are underdeveloped in comparison to piezoelectric and SMAs. Support systems for pneumatics tend to be heavy with increased power requirements, however this results in powerful actuators capable of producing stroke lengths significantly greater. One of the developing pneumatic variants is the 'Thin McKibben muscle' [17] being developed for robotic applications. The design consists of individual strands approximately 1.8mm comprised of a flexible inner tube encased in a strengthening fibre mesh latticed with a 18° braiding angle. Pressurising the inner tube results in a controlled radial expansion, producing the required length contraction actuation. In testing carried out [17], strands 300mm in length produced upwards of 22N of static contraction force at 0.55 MPa. The durability and fatigue effects of this pressure were not discussed and the effects of variable loading were also not explored. As a result, conclusions about the maximum failure pressure and safe operating pressure cannot be drawn.

While McKibben actuators rely on positive internal pressure to force useful actuation there are concepts that utilise a negative internal pressure. This causes a greater external force causing a collapse of the structure, which is exploited as the actuation movement. A primary example of this type of vacuum actuation is the vacuum-actuated muscle-inspired pneumatic structures (VAMPs) concept [18] Developed initially for applications in soft robotics similarly to other pneumatic actuators due to the exclusive use of compliant materials. VAMPs however are designed to collapse and strategically buckle to produce a controlled contraction force. The structure contains cambers that collapse reducing the volume of the actuator, and manipulation of the internal structure and the position of these cells could produce an anisotropic actuation specific to a application. A wide range of materials can be used as the actuator body EcoFlex a platinum catalysed silicone and Elastosil a stronger silicone variant, have both been used previously. Potentially any silicone/rubber material could be used provided it is sufficiently elastic. Silicone that could be used in an FDM manufacturing process could enable efficient prototyping of the structures.

1.4 Overview

Conventional actuation technologies impose limitations related to weight, complexity, and reliability, biomimetic strategies offer an alternative by drawing on nature's solutions to multifunctional movement. Within this context, a biologically grounded

framework for assessing adaptive structure actuators has been proposed, enabling objective comparison across disparate technologies. The adoption of avian muscles as a reference standard provides a means of identifying actuation principles that are both efficient and adaptable, forming a foundation for the development of a novel span-wise morphing concept inspired by bird wing mechanics.

Building on this work, this dissertation integrates biological observation, kinematic measurement, and engineering implementation to examine the feasibility of avian-based morphing strategies for UAV applications. A detailed investigation into the wing morphology and motion of selected species within the *Accipitriformes* provides empirical insight into span-wise kinematic behaviour, which is subsequently modelled and translated into an engineering context through the development of a pneumatically actuated morphing structure. The validation of this concept through CFD analysis, closed-loop control implementation, prototype development, and wind-tunnel evaluation establishes a coherent trajectory from biological inspiration to engineering realisation. The following literature review chapter situates this work within the wider field, examining existing morphing concepts, actuation technologies, and biomimetic methodologies that inform the research presented throughout the chapters.

Chapter 2

Literature Review of Biomimetic Morphing Actuation

Often cited as the driver of morphing structure development is the more widespread advent of uncrewed aerial vehicles (UAVs), in particular micro-aerial vehicles (MAVs), where the design is not constrained by the ergonomic requirements of a pilot. [3, 19, 20] As a result of these factors, emerging concepts are deviating progressively from the traditional fixed-wing and aft tail configuration widely adopted throughout the industry. The new concepts have subsequently outpaced traditional actuators such as hydraulic pistons and motors, as they cannot produce the unique actuation profiles that morphing structures demand. Moreover, the airframes designed to position and apply these traditional actuators are often unsuited for morphing elements due to their rigid assemblies. Thus, the adoption of specialised mechanisms and materials for advanced multi-purpose and atypical actuators is underway. This chapter examines the application of biomimetics, or bio-inspired design, in the development of new actuators across engineering fields.

Biomimicry can produce systems and processes with significantly increased efficiency and performance [4]. The progression of actuator technologies has been aided by the mimicking of biological muscle, particularly in robotics fields where human limb muscles are used as a comparison. However, for aerospace applications, different specifications are required, including a greater power-to-weight ratio and a decreased response time. It is therefore proposed that a better comparison for actuators suggested for morphing aircraft is avian muscle, especially in MAVs where the dimensions and forces are comparable to avian species. Thus, the characteristics of avian muscle will be presented and provide a benchmark for artificial actuators and their suitability in aerospace applications. Biomimetic and novel actuator technologies are presented and compared with avian muscle standards, allowing assumptions to be made about the effectiveness of each design aspect. Similarly, morphing concepts that currently employ traditional actuators are discussed regarding the adoption of the proposed developing actuators. Consideration is given to any significant improvements that can be achieved through biomimetics and the comparison with avian.

2.1 Actuators

Biological muscles provide the avian with the power and control required for flight. The muscular system associated with limb motion comprises skeletal muscle, a subtype of Striated muscle. This category of muscle commonly found in Avian, Mammalian, and Rodentia, is so called due to the striated microstructure from which it is formed. The attribute most of interest for defining artifical muscles is its unidirectional strain, varying across muscles but approximately 40% in human [21]. Skeletal muscle produces a useful force or actuation only as it contracts, hence it is unidirectional. Subsequently, skeletal muscular systems employ skeletal muscles in antagonistic pairs such as the muscles controlling the extension of a bird's forelimb, comprised of the humerus, ulna, and radius bones. This system also provides actuation for multiple joints for increased efficiency, as individual control is not required [22]. These factors that allow flight in avian are desirable in artificial aircraft, and are therefore suited for biomimetic design.

Definition of Artificial Muscle

Biologically inspired actuator concepts are actuators that could be categorised as having muscular attributes; these are often referred to as artificial muscle actuators. Artificial muscles are most commonly found in robotics, where robotic systems are based on biological systems, as well as in soft robotics, where artificial muscles constructed of soft materials produce safer robots for human interaction. Actuators are categorised as artificial muscles if they replicate the unidirectional actuation stroke of biological straited skeletal muscles mentioned previously, although often actuators comprised of soft or intelligent materials are also included. This type of actuation also typically reproduces other quantitative characteristics as explored in section 2.1.1.

Systems utilising these actuators also mimic biology through the use of antagonistic pairs which, along with the flexible nature of soft artificial muscles, can allow actuation profiles unachievable with traditional actuators. An example of this would be a curved profile that is required due to a low-volume working area with obstructions, common within an aerofoil structure. Biomimetic humanoid robotics is an application of this and research conducted by Kurumaya [23] shows artificial muscles in a situation where the number of traditional hydraulic cylinders required to perform a similar movement would make the system inefficient.

The complex multi-dimensional deformation of morphing airframes, particularly adaptive wings, lends itself to biologically inspired design. The overlap with soft robotics here is evident. Artificial muscles replicate the soft or deformable structure when not actuated making them very suitable for integration in adaptive structures that may deform around them making their compliant nature a requirement. The forces on typical adaptive structures, such as UAVs under the civil aviation authority's (CAA) 25 kg weight class, tend to be within the capabilities of these manufactured muscles. A significant number of current morphing concepts are bio-inspired [6]. This adoption, however, has been limited by structural constraints and the complexity of the actuation demanded by the biological systems. Thus, the implementation of artificial muscles could allow increased morphing capability across a lift-generating surface, resulting in better aircraft control and efficiency.

Avian Muscle Characteristics

Avian muscle characteristics are of interest in the application of these actuators in morphing airframe structures, particularly in UAVs and MAVs where the size of the aircraft is comparable with the bird species. The attributes of these muscles are a gauge for the suitability of the actuator concepts in airborne vehicles. In avian muscles, three predominant discrete measurements can be compared to artificial actuators: stress, muscle force per unit cross-sectional area, specific power, and power density, all of which have been studied [24, 25, 26]. The other characteristics of interest when comparing to artificial muscles are actuation range and fatigue limits; all of these are presented for several avian species in Table 2.1. Muscle characteristics vary substantially across species but also across the different muscles in the avian anatomy. Studies of avian striated muscles have primarily focused on the pectoral muscle (*pectoralis*) as it is the largest in most avian, this is because it drives the wing flapping motion, it therefore directly relates to the power of the bird's flight. The values used to represent avian muscles in table 2.1 are for the pectoral muscle. The two avian for which values were collated are *Columba Liva* (Pigeon) and *Sturnus Vulgaris* (European Starling). As these are both small and common birds they are the subject of more literature. Larger birds and birds of prey would provide a better comparison for MAVs which are approximately the same size and weight. However, these species are often endangered and more difficult to manage, and so the literature is limited.

Properties	Units	Pigeon	Starling
Sustainable Stress	kPa	54	34
Peak Stress	kPa	77	57
Actuation length	ΔL %	12 - 40	12 - 40
Specific Power	W.kg^{-1}	167	104
Power Density	W.cm^{-3}	0.17	0.11
Maximum Bandwidth	Hz	8-10	10-15

Table 2.1: The values shown represent the modal average for the species muscles across the literature cited in section 2.1. The avian data is representative of the in vivo pectoralis muscle during straight and level flapping flight.

Vertebrate straited muscle has an isometric stress that is commonly calculated at approximately 200 kPa [27]. Human muscle is calculated as having an average maximum sustainable stress of approximately 100 kPa [21], while values for the peak stress only sustainable for brief periods can be around three times this at 350 kPa [28].

In avian stress measurements are calculated from directly measured strain data, recorded from in-flight [29]. The research conducted in the field concludes few species of avian have an isometric stress above 150 kPa. Starlings (*Sturnus Vulgaris)* have a pectoralis with an isometric stress measured at 122 kPa [29], Biewener noted this was low compared to the previously mentioned 200 kPa average for straited muscle. However, Dial and Biewener conducted the experiment again on pigeons and concluded a peak stress of 77 kPa [30], also noticeably lower than the vertebrate

average.

Actuation length, presented here as a strain percentage is commonly between 20% - 50% in vertebrate straited muscle. Although strain varies significanly due to the similarly varied requirments demanded of the applications in avian and human muscle systems [28]. Actuation strain is also related to the work output of the muscle and therefore directly proportional to the power output. Thus, arguably the more significant characteristic to actuators particularly actuators with applications in aircraft, is the power per unit of mass, which deviates decidedly across order and to a lesser extent species. Related to this metric is power density, which isn't as widely researched in biological publications, but can, however, be determined using the raw values presented in most of the literature accessed.

Biological papers present different and developing methods for estimating and calculating the power output for a skeletal muscle in different flight conditions. Pennycuick [31] presents a method for estimating power density of the mitochondria present in the muscle cells. The method uses electron microscopy to determine the ratio of mitochondria to myofibrils allowing conclusions to be made regarding the specific power and power density. As with muscle stress Biewener et al. [29, 30, 24] presented an experimental method for determining the mass specific power for avian pectoral muscles. The in vivo force measurements alongside the actuation length were used to produce the work done by the pectoralis muscle and subsequently factoring in the wing beat frequency the power output was calculated. The latter method produces a specific power of 119 W/kg for pigeons and 104 W/kg for starlings, while the former method puts the pigeon at 167 W/kg. On review of the literature in the field, a range of 104 W/kg to 177 W/kg can be reliably inferred for small avian ranging in mass up to 1 kg [32, 33, 34]. Power density was calculated for the pigeon using the researched power and volume values, while the starling's was found by Biewener et al.. The values for both fall within 0.1-0.2 W/cm^3, which was found to be consistent with the other publications.

Strain rate is commonly used to represent the contraction rate in muscle and has been used to compare artificial muscle actuators as, similarly to the other presented characteristics, it allows dimensionless analysis. The strain rate in vertebrate striated skeletal muscle is broadly constant for the pectoral muscle data collected and the general human values also collated, at approximately 5 s^{-1}. Where avian muscles vary from general vertebrate characteristics is direct contraction time. Avian muscles due to their decreased size compared to other vertebrates, such as human, have significantly reduced fast muscle contraction times. Measured in the pectoral muscles in both avian species for the duration of the contraction, neglecting reaction times, the minimum contraction time was found to occur during flapping flight. The minimum contraction time for pigeons is around 0.07 s and the smaller starling approximately 0.04 s, where as for humans the minimum contraction time is approximately 0.11 s. As this is not a fair comparison due to the size difference, it will not be examined further, it is important to note that the reduced contraction time may be vital to allow stable flight.

Human Muscles

Human muscle values are used as a comparison and are an averaged or typical muscle value often used to represent vertebrate striated skeletal muscles [35, 36, 37]. There are similarities and differences apparent between avian and human muscles, which

is to be expected. Differences in specific power and power density are due to the avian requirement for minimising weight and a reduced size. This is consistent with other avian systems (such as the unique lightweight structure of bone), which also prioritise weight reduction. As for the lower stresses exhibited in avian a consensus has not been reached in the literature studied. It has been suggested that low stresses allow fewer muscle fibres to be active, and is thus a method for increased energy efficiency in straight and level flight [29]. It has also been shown that the supracoracoideus (the antagonistic muscle to the pectoralis in avian) operates at a higher stress around 85 – 125 kPa [25], suggesting varied loading on the muscles articulating the wing.

2.1.1 Hydraulic and Pneumatic Artificial Muscle Actuators

Hydraulic and pneumatic actuation systems are commonly used in aerospace applications, reliability and adaptability being among the many reasons for their ubiquity. Typically associated with the traditional bi-directional hydraulic cylinders employed in commercial aircraft, there are numerous variations which allow a wide range of applications. Development in the area of pneumatic and particularly hydraulic actuators is significant, allowing performance in many areas including achievable stresses to be unmatched by most other actuator types. Hydraulic actuators and the systems they require have inherent limitations the most apparent is the system's weight, which often restricts applications in lighter aircraft, UAVs and MAVs where lighter electromechanical actuators are used. Pneumatic systems are less often used in UAVs to reduce weight. However, development in pneumatics is being carried out in morphing UAV concepts due to other unique characteristics [38].

Pneumatically actuated morphing concepts can roughly be defined by two categories: skin morphing pneumatics, where a skin or structure is inflated or deflated, and actuated structure pneumatics, where more traditional control surfaces or similar morphing structures are actuated with a pneumatic-based actuator. The concepts fitting into former category [39, 40, 6, 41] employ pressurised skins or elements embedded within the skin to active actuation. A composite skin proposed by Chillara [41] consists of a fluid layer, comprised of a pneumatically pressurised chamber and walls which is sandwiched by a pre-stressed elastomeric matrix composite (EMC), providing a restoring force and a constraining layer. The validated analytical model presented shows a linear actuation with regards to the relatively low pressure (maximum 82.7 kPa) applied. While these skin actuators evidently produce significant deformation within their specific morphing structure, they are relatively unadaptable for alternative applications. Morphing concepts that utilise discrete actuators therefore allow adaptability and exhibit actuator-structure systems reflective of biological muscle systems.

Pneumatic artificial muscles (PAMs) are the most developed and applied biomimetic actuator in the field of morphing aircraft [42, 43]. Originally developed for use in prosthetics, and later developed in the field of soft robotics, PAMs are otherwise referred to as McKibben actuators after the development conducted by J. L. McKibben in the 1950s. Due to this development time across multiple disciplines different variations have been proposed, those shown in figure 2.2 contain differences in the manufacture processes, fatigue life, and actuation profile better suited for specific applications. [44] The majority of the structure and operation remain the same.

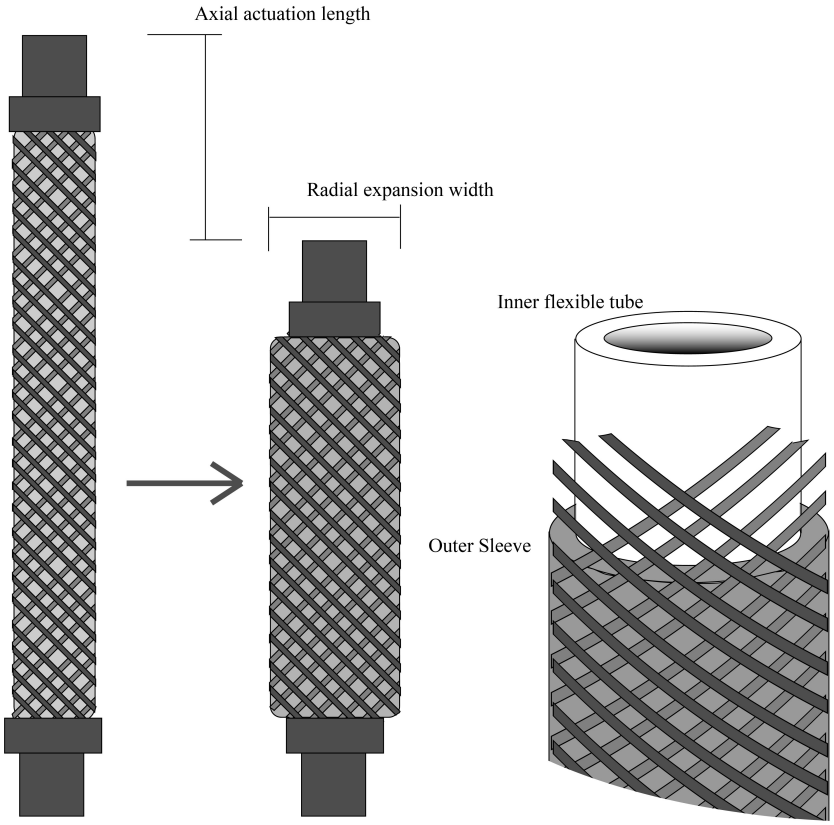


Figure 2.1: Left to right; the braided PAM in an unactuated state, actuated, and the PAMs cross section showing the flexible inner-tube. Also shown are the variables used to define the actuator, as well as in modelling.

PAMs replicate the contraction actuation exhibited in skeletal striated muscle. This produces actuation profiles that mimic human muscle for applications in robotics. The structure is formed of a flexible elastic polymer or rubber bladder contained by a braided, quilted, pleated or netted dry composite fibre sleeve. In the case of braided sleeves this is typically maypole braiding. In the form of a cylindrical shape PAMs actuate under positive internal pressure causing a radial expansion which is controlled by the sleeve placing it under tension, thus resulting in an axial contraction. This is depicted in figure 2.1 and is consistent across most variants.

Hydraulic variants of artificial muscles (hydraulic artificial muscles; HAMs or fluidic artificial muscles; FAMs) have been proposed [47], constructed using the same structure and actuated with the same technique. Operating pressures remain consistent to pneumatics along with the static actuation force, resulting in a similar performance [48]. This is due to the output being limited by the construction of the muscle rather than the fluid. There is a significant difference in stiffness between pneumatic and hydraulic muscles.[49] The muscle's effective stiffness is limited by the compressibility of the fluid within the bladder, which is an order of magnitude higher in the HAM as the fluid does not compress under load. It should also be noted that the inlet orifice of the muscle has an increased impact on stiffness in hydraulic muscles over pneumatic. In this case the HAM hydraulic fluid behaves

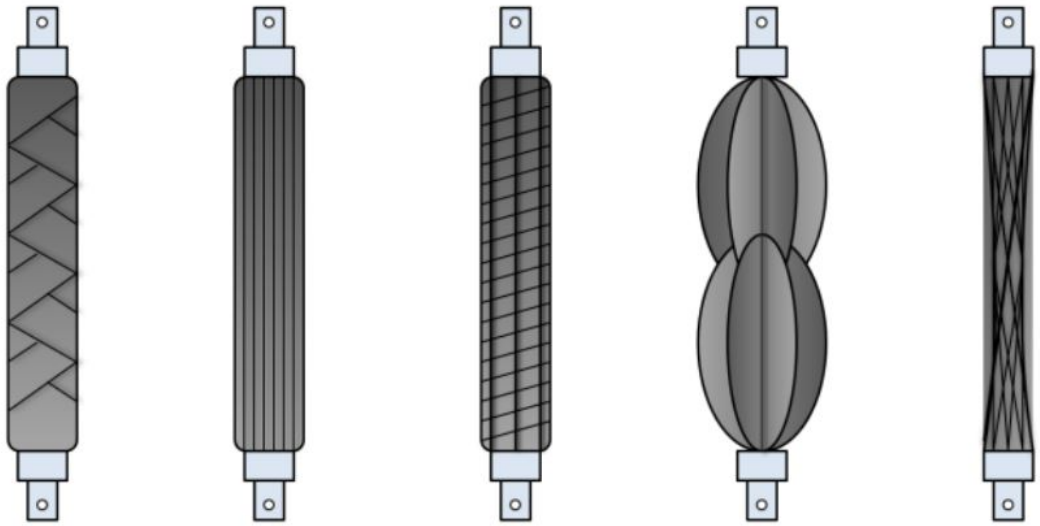
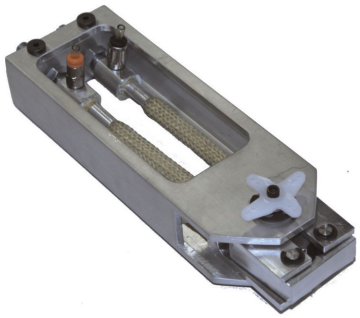


Figure 2.2: A representation of each of the sleeve variations on PAM actuators, left to right; McKibben/Braided, Pleated, Netted, ROMAC, and Hyperboloid [43].

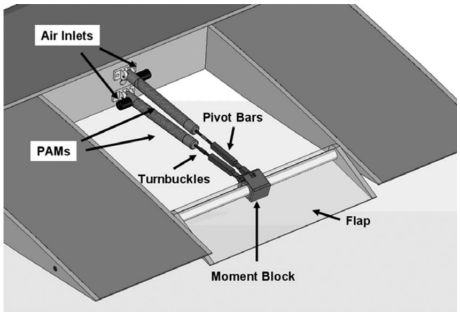
almost like a fixed-volume solid. The additional weight required support a hydraulic system has resulted in reduced interest in HAMs; as a result, this review will focus on the development of pneumatics. Future development and the implementation of artificial muscles into aircraft where hydraulic systems are already utilised may result in the eventual adoption of hydraulic over pneumatic muscles.

The outer composite sleeve is the component that differs the most between proposed variants. Perhaps the most common is the braided sleeve McKibben actuator, which is based on a maypole braid where during the filament winding process alternate strands are interwoven similar to the manufacturing process for composite cylindrical components [50]. Braided sleeves have the advantage of adjustable braiding angles which have been shown enable control over the actuator's properties [17]. The pleated sleeve design follows on from the development of the 'ROMAC' muscle. The latter employed a geometrically complex fabric sleeve with integrated wire netting [51]. This allows the actuator a strain of approximately 50%, while the pleated sleeve with a significantly less complex design produces a strain of 45% [52]. Pleated PAMs expand radially by the largest amount compared to the previously mentioned sleeve designs as shown in figure 2.2, this reduces power density and suitability for use in small aircraft. Alternative sleeve and bladder designs have been proposed [44] with the intention of reducing the operating pressure [53].

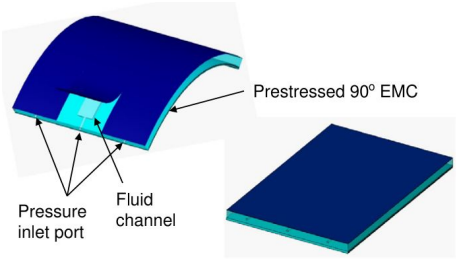
PAM actuators recently started being integrated into aerospace concepts, initially proposed to simply replace the actuators already employed due to the weight reduction they allow. More complex implementations are currently being explored to produce increased reliability and power efficiency. Woods et al. [46] proposed the actuation of a trailing edge flap using PAMs, a typical braided sleeve comprised of PET plastic filament was used along with a latex inner tube. This design was limited geometrically by the constraints of the aerofoil into which it was to be implemented, the total volume of the actuator was 10.1 cm^3. The peak force for the actuator was found to be 111 N at 620 kPa internal pressure, while at frequency of



(a)



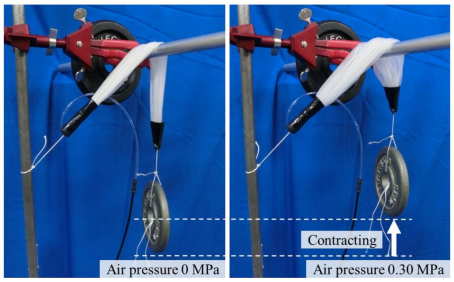
(c)



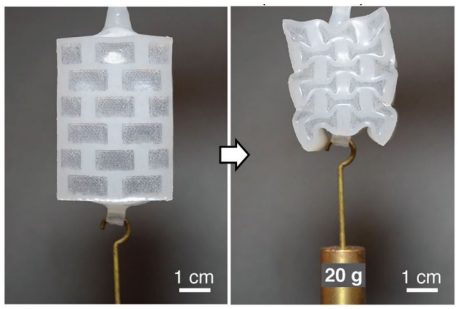
(b)



(d)



(e)



(f)

Figure 2.3: Pneumatic concepts; (a), PAM actuated servo analogue Vocke et al. [45]; (b), Pressure actuated morphing skin Chillara et al. [41]; (c), Braided PAM actuated trailing edge flap mechanism Woods et al. [46]; (d) Positively pressurised PAM failure due to over pressurisation Woods et al. [7]; (e), Thin McKibben actuator bunched to produce an artificial muscle demonstrating the flexibility of PAMs Kurumaya et al. [17]; (f), Linear VAMP vacuum artificial muscle Yang et al. [18].

25 Hz a force of 90 N was determined. These values are typical for PAMs of this size as corroborated by [54, 55]. The other characteristics determined from Woods et al. [56] following wind tunnel testing of the concept, have been collated in Table 2.2. The frequency of around 60-100 Hz quoted for these actuators is sufficient to replicate the wing beat frequency of common avian at 8-9 Hz [30]. Whereas the muscles responsible for smaller wing surface deflections can range 50-500 Hz [57], not currently replicable with PAMs of this size. Woods et al. concluded that a pneumatic compressor system with a higher flow rate would allow an increased frequency. Although given typical traditional pneumatic cylinders peak at approximately 300 Hz [58] it is unlikely this will improve rates to equal biological muscle.

Development has been undertaken to reduce the volume of braided artificial muscles to allow integration into MAVs and miniature robotics. Vocke et al. [45] reduced the volume of a braided actuator with the integration of a Kevlar braided sleeve and a braiding angle of 69^o. The resultant actuator could produce a force of approximately 300 N at the same pressure of 620 kPa as other PAM actuators. Vocke et al. proposed a mechanism consisting of an antagonistic pair of miniature PAMs, to produce electromechanical servo style actuation with double the specific torque (shown in figure 2.3). A developing Mckibben variant with reduced volume is the 'Thin Mckibben muscle' [17] being developed for robotic applications. The design reduces the thickness of each individual strand to approximately 1.8 mm, a significant reduction from the 10 - 40 mm designs typical for PAMs [50]. As with most other McKibben actuators the thin muscle utilises a flexible inner tube encased in a strengthening fibre mesh, however the smaller size results in unique characteristics. In testing carried out [17] strands 300 mm in length produced upwards of 22 N static contraction force, while under 0.55 MPa. As with all PAMs the effectiveness of these thin muscles is predominantly dependent on inner tube hardness, number of covering fibre strands and their braiding angle. The testing done indicates an optimum fibre number of 32 at an angle of 19^o, paired with a silicon inner tube. These Thin McKibben strands have been shown to mimic different types of muscle systems. Combining the individual strands in different muscular arrangements the resulting 'Multifilament muscle' [23] can act similarly to the mimicked biological muscle. The durability and fatigue effects of applied pressure were not discussed and the effects of variable loading were also not explored. As a result, a conclusion about the maximum failure pressure and safe operating pressure cannot be made.

Failure of a positive pressure PAM is often catastrophic, due to the high pressure required for their operation. This is coupled with low fatigue life of <18000 cycles (at 90 kPa, <5000 at 360 kPa at a frequency of 1 Hz) [59], resulting from crack formation and propagation in the materials of the inner tube and wear of the tube against contacting hard components [60]. These characteristics are unacceptable for aerospace applications and as such fatigue life has been addressed in the literature. Woods et al. [61] concluded applying a swaged thin walled tube around the endcap assembly would reduce abrasion and sleeve separation by clamping the sleeve directly to the end cap allowing tension forces to be transferred without being applied to the latex inner tube. The aforementioned techniques resulted in a fatigue life extension to 120 x10^6 cycles at a pressure in the same order as previous literature but with a higher frequency of 30 Hz, resulting in higher temperatures generated which was commented on as possibly having a detrimental effect on the fatigue life [7].

Properties	Pigeon	Starling	Braided PAM	Pleated PAM	Thin Mckibben	VAMPs
Peak Stress (kPa)	77	57	9500	7000	4000	100
Actuation length ΔL (%)	12 - 40	12 - 40	<40	40	20	30
Specific Power ($W.kg^{-1}$)	167	104	500 - 2000	1200	3000	18.5
Power Density ($W.cm^{-3}$)	0.17	0.11	30 - 4000	15	1.5	0.01
Maximum Bandwidth (Hz)	8 - 10	10 - 15	30 - 100	15	-	1 - 10

Table 2.2: Table for the comparison of pneumatic artificial muscle properties'. Alongside pectoral muscle values for *Columba Liva* (Pigeon) and *Sturnus Vulgaris* (European Starling). Values for the avian represent in vivo straight and level flapping flight. While actuator values are representative of maximum bandwidth actuation, and the braided PAM given as a range based on multiple sources discussed in section 2.1.1.

While PAMs and its variants rely on positive internal pressure to force useful actuation there are concepts that utilise a negative internal pressure. This causes a greater external force causing a collapse of the structure, which is exploited as the actuation movement. This actuation technique is underdeveloped in comparison to traditional PAMs, the most recent development being the vacuum-actuated muscle inspired pneumatic structure (VAMPs) concept [62]. Developed initially for applications in soft robotics similarly to other pneumatic actuators due to the exclusive use of compliant materials. VAMPs however are designed to collapse and strategically buckle to produce a controlled contraction force. As displayed in figure 2.3 the structure contains chambers that collapse reducing the volume of the actuator, and manipulation of the internal structure and the position of these cells produce an isotropic or anisotropic actuation depending on the specific application. Linear unidirectional VAMPsare most comparable to vertebrate striated muscle and are comprised on the least complex structure compared to twisting and, bending variations [63]. A wide range of materials have been used as the actuator body: EcoFlex, a platinum catalysed silicone; and Elastosil, a stronger silicone variant have both have been used previously by Yang [18]. Potentially any silicone/rubber material could be used provided it is sufficiently elastic, although 3D printable silicone could allow the efficient prototyping of the structures. The fatigue life has yet to be determined in literature; although, given the elastomer construction a life approximately 100,000-1,000,000 cycles can be expected [64]. Yang presents a comparison of an Elastosil linear VAMP to vertebrate muscle, with a human bicep VAMP actuator. Actuation frequency was not accounted for and it is assumed that all the values were collected at quasi-static conditions, these are shown in Table 2.2 for comparison with avian muscle.

Despite all the actuators collated in Table 2.2 employing similar or identical principles to induce actuation significant differences can be seen. Peak stresses exceed the maximum avian require for flight. Similarly, specific power required from avian muscles is surmounted by the above atmospheric pressure PAMs. In comparison with traditional hydraulic cylinders with strains up to 100%, pneumatic artificial muscles achieve a maximum of approximately 40%. Avians however, require only 12% - 40% for flight, suggesting all the concepts discussed would be suitable if consideration is given to the mechanics of the actuated structure.

2.1.2 Shape Memory Alloy Artificial Muscle Actuators

Shape memory alloys (SMAs) or Shape memory materials (SMMs due to the developments in shape memory polymers) are referred to as 'smart materials' due to a controllable deformation under temperature variations. This has been exploited in aerospace fields to produce components with reduced complexity over temperature sensing electronic systems. The first application of SMAs in aerospace was in hydraulic tube couplings [65]. Expanded using this deformation the alloy was fitted and allowed to cool to ambient temperatures, where its contraction produced a reliable, simple, and strong joint. The complexities of pump systems have also been reduced with the application of SMA impellers and nozzles. The component reacts to the temperature of the fluid and affects the flow rate as required, reducing the required electronic systems [66]. Alongside these applications shape memory materials have been developed into actuators to provide useful actuation in traditional and morphing structures. The unidirectional actuation force most SMMs exhibit is comparable to that of biological muscle. Similarly to muscle, SMM concepts employ antagonistic pairs to produce bi-directional actuation.

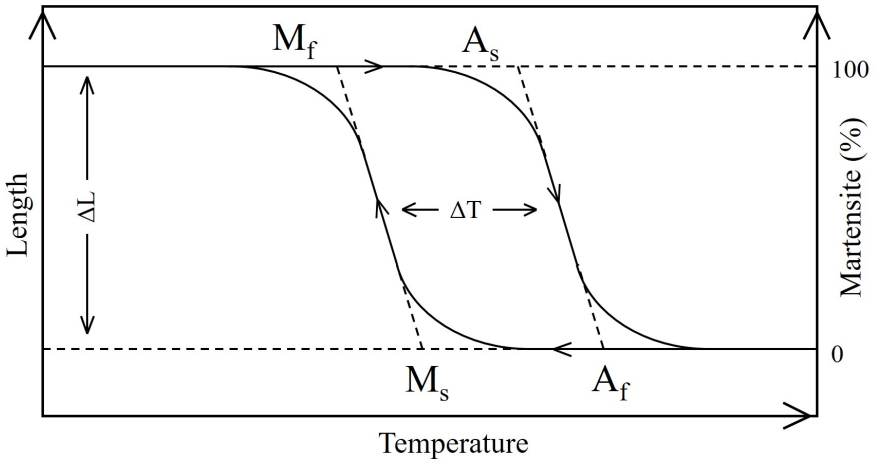


Figure 2.4: Temperature hysteresis for a general shape memory alloy, based on Antonucci and Martone [67].

Shape memory alloys (SMAs) are metals that exhibit a reversible martensitic transformation, resulting in a microstructure phase change and in turn an actuation stroke. Widely accepted to have been introduced in 1963 by Buehler [68] during heat shield research with the discovery of NiTi, a nickel-titanium alloy that demonstrates the shape memory effect. The shape memory effect is the cause of the transformation in SMAs and occurs when a deformed alloy in its low temperature martensitic phase is heated. This causes it to revert to its body centred cubic microstructure austenite phase, resulting in it reforming into its original shape. This can be summarised by plotting, in figure 2.4, the thermal hysteresis, material temperature against length (in the case of an SMA wire).

The heating (A_s to A_f) produces the useful contraction force, which is determined by the microstructure of the alloy. This heating in the case of most actuator concepts produced using joule heating, exploiting the internal resistance of the SMA material. The alloy then cools to return to the un-actuated state, this process oc-

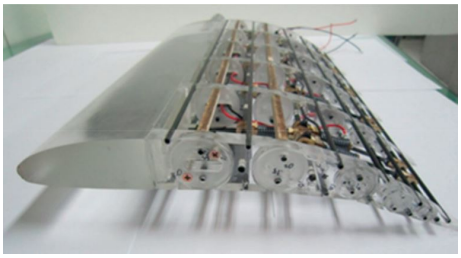
curs over a maximum of 8% strain (occurring in NiTi) before elastic deformation occurs. As the stresses produced by the actuator are predominantly dependent on the alloy composition; alloys have been produced with specific characteristics including stresses as well as the activation temperatures, and strains. Table 2.3 depicts the common commercial SMAs' material properties, however the application of the alloy's in an actuation system has an equal impact on the performance.

SMA based actuators are based on an alloy in wire or solid form. Examples are shown in figure 2.5 (a) and (b) respectively. Wire SMA actuators tend to require a more significant mechanism to facilitate the actuation over solid SMAs but benefit from the increased surface area during cooling.

While SMAs are the most extensively used in biomedical applications [74], it is in prosthetic and robotic applications where the most wire actuator development occurred [75, 76], with recent developments in hand actuation, given the limitations of an actuation strain of <8% [77, 78, 79, 80]. Coiling an SMA wire is the primary method for significantly increasing the actuation length [81]. Coiling exploits the shear stress in the wire resulting in a significant reduction in actuation stress, this relationship has been defined using multiple methods [82] Mechanical systems have also been developed for SMA wires and springs, to produce a useful actuation. Structures such as [83, 84] reduce complexity and increase actuation strain by actuating a lever or pulley system. Similarly, SMA springs have been employed in human joint biomimetic hinged systems [85] for robotic applications requiring multiple degrees of freedom. Although SMAs share inherent similarities with muscle concepts have been proposed to mimic muscle further by embedding SMA springs in a silicon matrix alongside a steel spring to provide a restoring force [86] allowing compressive and twisting actuations.

Novel concepts integrating SMA and PAMS have also been proposed to provide multiple actuation types from the same system. Xiang [71] proposed a 'SMA-Fishing-line-McKibben bending actuator' which utilises a >40% strain McKibben actuator for compressive actuation and axis-offset parallel NiTi wires interwoven with fishing-line [87] for bending actuation. The case study presented for the novel actuator was a three fingered gripper for robotic applications, providing a lifting weight of 650 g, and was considered successful although precise control was cited as an issue for the system as a result of the actuator. Possible aerospace applications for the SMA-Fishing-line-McKibben bending actuator were not considered in the literature, however the double actuation could be applied to a trailing edge flap. The bending actuation provides camber morphing while the PAM alters the flap extension and as a result the wing area. Braided PAM actuators have also been implemented with a shape memory polymer (SMP) embedded within the sleeve, enabling the actuated PAM to retain its actuated position without the need for constant control [88]. The SMP also significantly increases the stiffness of the actuator without the requirement for an antagonistic pair, reducing the weight of the system.

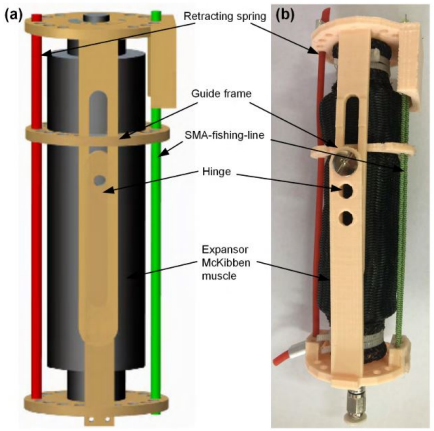
SMA wires have also been manipulated with mechanical systems to produce rotary actuation [89]. While not biomimetic the mechanisms, and the SMA they are based on, are worth mentioning due to the varied applications of rotary power in aircraft. SMA wires fixed to a rigid body while coiled around and then affixed to a solid axle form the bases of most SMA rotary actuators [90, 91, 92]. Output torque is up to 2500 Nmm [89], competitive with high torque electromechanical servos while weighing significantly less [93]. These actuators are however limited in output stroke



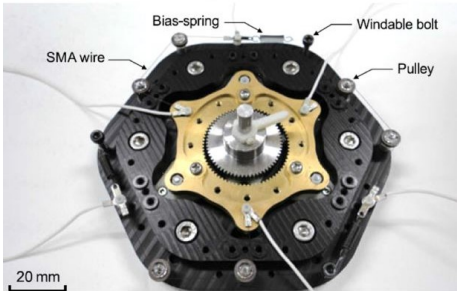
(a)



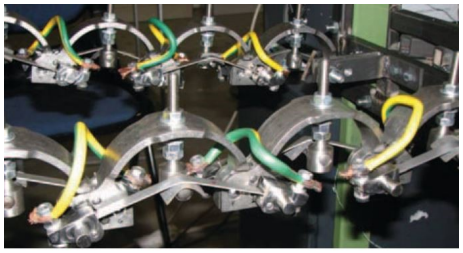
(b)



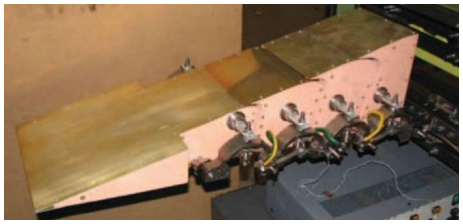
(c)



(d)



(e)



(f)

Figure 2.5: Shape memory alloy concepts; (a), Coiled SMA driven camber morphing concept Ko et al. [69]; (b), Solid SMA strips actuating chevrons Hartl et al. [70]; (c), McKibben muscle with SMA line to produce bending Xiang et al. [71]; (d), crankshaft based SMA rotary actuator Hwang et al. [72]; (e) and (f), SMA based camber morphing system proposed by Barbarino et al. [73].

SMA: Shape memory alloy

Table 2.3: Table for the comparison of the properties' exhibited by shape memory alloys. Alongside pectoral muscle values for *Columba Liva* (Pigeon) and *Sturnus Vulgaris* (European Starling). Values for the avian represent in vivo straight and level flapping flight. While actuator values are representative of maximum bandwidth values collated and derived from multiple sources discussed in section 2.1.2. Values denoted with a (–) represent values unobtainable through the literature reviewed.

Properties	Pigeon	Starling	Nickel titanium (NiTi)	Ni60Ti	NiTiCu
Peak Stress (kPa)	77	57	100,000 - 700,000	150,000	155,000
Actuation length ΔL (%)	12 - 40	12 - 40	<8	1.6	3
Specific Power ($W.kg^{-1}$)	167	104	100 - 20,000	-	-
Power Density ($W.cm^{-3}$)	0.17	0.11	0.7 - 100	-	-
Maximum Bandwidth (Hz)	8-10	10-15	0.01 - 10	<1	<0.02

and cannot achieve continuous rotation. Continuous rotation SMA rotary actuators typically resemble a piston crankshaft system [72] with the increased complexity and the resulting reduction in reliability being the drawback. In the literature collated, it was found that rotary SMA actuators have not been implemented in aerospace concepts, except for use as simple rotary release latches in satellite spacecraft [70]. It is therefore proposed that rotary SMA actuators could be implemented into systems in place of electromechanical servo motors, with the benefit of reduced weight, reduced mechanical complexity, and increased output torque. The fish bone active camber morphing wing concept [94] currently utilises a 'high torque' servo motor to produce camber deformations via a pulley system, this is an example of a morphing concept that could benefit from rotary SMAs.

Solid SMAs involve more complex geometries and tend also to form a structural element within the actuated structure, although SMA strips are also commonly used to actuate thin skin structures [70]. Torque tubes are a single solid SMA component that have been employed in aerofoils to produce twist, particularly in rotary blades [95]. Jardine et al.. [96] produced a 5^o span-wise twisting wing actuated using torque tubes, which was developed as part of a 'SMART' wing project [97]. The notable use of solid SMA strips was in Calkins et al.[6]. variable-geometry chevrons on a GE-115B turbofan engine, with the aim of reducing noise by more effectively mixing different air streams. An alloy was developed for the actuator Ni60Ti to produce a more stable mechanical response, as demanded by this aerospace application. A reduction in maximum strain to 1.6% was also exhibited, while a maximum load force was quoted at 300N [98, 99].

There have been reviews conducted into the applications of SMAs in morphing concepts by Barbarino et al. [100]. and their impact on the field of morphing aircraft [6]. While these reveal the applications of both wire and solid SMA actuators SMA wires act more comparably to muscle and are therefore more greatly explored in this review. Barbarino et al. proposed an SMA based camber morphing system [101, 102], an actuation rib consisting of elastic hinges and SMA wires shown in figure 2.5. Later revisions of the concept employed SMA ribbons [73] and although no reason can be found in the literature reviewed, it was suggested the width the ribbon provides allows an increased area to affix the SMA to the controlled structure. The revised concept combines the elastic hinge and SMA elements into a single titanium rib structure, which also provides a pre-strain of 3% allowing increased

fatigue stability. The SMA material used (with a maximum recoverable strain of 3%) was a commercial Ni-Ti-Cu alloy with a high stress, the mechanism shown in figure 2.5 provides the restoring elastic force and a mechanism to convert the 3% strain into a 5^o rotation. The concept was proven to provide a 114 mm trailing edge deflection, although consideration regarding the poor performance due to fatigue from high stresses [73].

Despite the mechanical complexities that can arise in the implementation of SMAs in morphing aerofoils SMAs exhibit a fundamental flaw for actuator applications. As discussed previously this disadvantage is the actuation reaction time which directly affects bandwidth and subsequent power output. The joule heating method of control through electrical current as mentioned previously has power limitations, the contraction time is dependent on the thickness of the wire and the voltage and amplitude of the current passing through it [103]. The contraction time is therefore controllable and can be minimised or optimised for aerospace applications, provided the support systems can provide the required amperage. The limitation here would therefore be the power consumption and weight of the electrical system.

The SMA's cooling time, required for the material to return fully to its martensite state, is however not dependent on variables controllable with simple systems. The cooling of the material is dependent on the thermal convection and radiation (and to a lesser extent conduction through mounting points), thus the cooling is dependent on material surface area and, in the case of a SMA wire its thickness. Solid SMA structures such as the mentioned torque rod have increased cooling times due to this effect. Solutions to this limitation have been proposed. The common concepts include forced air cooling, heat sinks and water cooling through immersion [104, 105, 106]. Experiments to test the effectiveness of these concepts found water emersion to be the most effective, reducing actuation times by upwards of a factor of ten [107]. Heat sinks also yield noticeable results although not as extensive as water cooling. These concepts for improved cooling times however are largely impractical for aerospace situations. This is due to their development being in the field of robotics. Water immersion is impractical due to its weight, particularly in small UAV applications. Air cooling involves the use of the airflow past the aircraft to provide improved cooling over static air, it is proposed as the most efficient method of cooling SMAs in MAV although increased drag is a possible side-effect. This redirection of air flow coupled with heat sinks could potentially reduce the reaction time of the SMA further making it comparable with other actuators considered.

Shape memory materials produce the highest actuation stress of the actuation concepts collated allowing scalable applications in aerospace and morphing aircraft design. The reduced actuation strain in comparison to avian muscle shown in Table 2.3 can be compensated with the application of mechanical techniques and in the case of SMAs alloy manipulation. The limiting factor for the application of SMMs in morphing concepts is bandwidth or actuation frequency, which is without active cooling less than 1 Hz. Thus, current implementations are primarily limited to static morphing such as the low bandwidth actuation of flap systems and high lift devices.

2.1.3 Piezoelectric Artificial Muscle Actuators

Piezoelectric-based actuators are the most dissimilar actuator type to biological muscle to be discussed; due to the properties in piezoelectric ceramics such as <1%

strains and $> 10^6$ Hz bandwidths [93], in comparison to the avian muscles discussed. Piezoelectric ceramics can be stacked to produce linear articulation, similar to biological muscle as well as bending and twisting when arranged in strips or embedded in a matrix to produce piezoelectric composites. Piezoelectric composites referred to as active fibre composites (AFC) or macro fibre composites (MFC) typically incorporate piezoelectric fibres and a polymer matrix to produce an increased strain.

Piezoelectric actuators, ceramic piezoelectric strips, stacks and MFCs achieve an actuation stroke by employing the inverse piezoelectric effect. This effect is caused by a crystal lattice of anions and cations (negative and positive respectively) responding to an applied electric field by repelling in opposite directions and the resulting lattice deformation is the source of the actuation [112]. While the properties of the piezoelectric material itself can vary depending on the crystal structure, mechanisms to augment the characteristics have a greater effect similar to SMAs.

Piezoelectric actuators have been widely considered for aerospace applications including traditional control surfaces and incorporation into morphing systems [3]. The appeal, especially in UAV and MAVs, is as with the other smart materials discussed; the replacement of complex and significantly heavier mechanical motors. The most common application in morphing aircraft concepts is perhaps the positioning of the actuator chord-wise along the upper or lower surface of the wing in order to control camber or a control surface such as an aileron. Piezoelectric strips with a bending actuation provide a bi-directional deformation. These piezoelectric bimorph strips can be comprised of both basic ceramic and MFCs are often incorporated into the skin, reducing the weight further and reducing the requirement for an elastomeric skin [113]. Prominent examples of this concept include [114, 110, 115, 116, 109], using MFCs Bilgen et al.. induced a lift coefficient increase of 1.46 in a simple aerofoil in wind tunnel conditions. The same MFC actuators implemented for control purposes in a UAV test aircraft, could effectively deform to produce roll control [110]. The MFC strips approximately 8% the area of the wing positioned approximately 80% of the semi-span, produced a 6.5% change in camber resulting in a roll rate of 0.93 rad.s^{-1}. The increased bandwidth inherent in piezoelectric actuators enabled a response rate not achievable in actuators based on mechanical systems [93]. Bilgen and Friswell [108] proposed a camber morphing concept employing two pairs of MFC actuators arranged to produce a bimorph, one placed on the upper and lower aerofoil surfaces. The increased actuation variations shown in figure 2.6 allow an increased range of coefficient values to be achieved, while the added MFC layer enabling the bimorph increases the structural stiffness allowing higher aerodynamic loading to be sustained without aerodynamic authority degradation.

Camber alterations in morphing aircraft can also be achieved by using a compressive piezoelectric actuator. Similar in positioning and dimensions to bimorph strips and similar MFCs these actuators however produce a bending through compression induced buckling [111]. Vos [9] and Barrett et al. [117] based a camber morphing concept on this post-buckled precompressed (PBP) actuator principal. A UAV was proposed to implement the PBP actuators in place of ailerons, with the aim to increase positional accuracy as well as reducing the complexity and weight as achieved in other biomimetic actuator concepts The PBP actuators positioned on the un-actuated chord line in place of rib in the trailing 55% of the chord, could defect the trailing edge 15^o effecting an increase in roll authority.

Table 2.4: Table for the comparison of piezoelectric actuators, alongside pectoral muscle values for *Columba Liva* (Pigeon) and *Sturnus Vulgaris* (European Starling). Values for the avian represent in vivo straight and level flapping flight. The piezoelectric actuator properties are largely derived from Huber et al. [93], as they are representative of the actuators discussed.

Properties	Pigeon	Starling	Ceramic	Macro Fibre Composites	Polymer (PVDF)
Peak Stress (kPa)	77	57	1000 - 3000	4000 - 9000	1000 - 3000
Actuation length ΔL (%)	12 - 40	12 - 40	0.0005 - 0.003	0.005 - 0.02	0.02 - 0.1
Specific Power ($W.kg^{-1}$)	167	104	20,000 - 400,000	10,000 - 70,000	200,000
Power Density ($W.cm^{-3}$)	0.17	0.11	100 - 1000	10 - 500	300
Maximum Bandwidth (Hz)	8-10	10-15	3×10^7	2×10^7	1×10^7

Applications with reduced chord lengths such as rotary blades in rotary aircraft, fans and propellers, have implemented piezoelectric and MFC bimorphs and strips to affect camber change for performance gains [118]. Note that applications in turbines and compressors tend to employ shape memory materials to take advantage of the temperature-based actuation. Implemented as a trailing edge flap actuator in the main rotary blades of a light utility helicopter the smart material-actuated rotor technology (SMART) blade was found to reduce noise, vibrations and increased component life [119]. The SMART system used a piezoelectric 'stack' actuator as opposed to a bending composite for its temperature actuation profile, while its actuation strain was amplified though a two stage mechanism [120]. Linear piezoelectric actuators are formed of a stack of alternating piezoelectric material 'wafers' and electrodes. The piezoelectric 'wafers' are in parallel electrically and on application of an electric charge the 'wafers' uniformly deform to produce a stack extension [121]. Linear stack actuators, to the extent of the literature reviewed have not been implemented in a fixed-wing morphing concept due to $<10^{-5}$ typical actuation strains [122]. Although it is reported that the DARPA smart wing 2 program considered their use before low actuation strains forced a redesign without piezoelectric stacks [20].

Further to the ceramic and composite piezoelectric actuators explored the piezoelectric effect is also observed with in specific polymers such as stretched and polarised polyvinylidene fluoride (PVDF) [123]. These polymers exhibit increased actuation strains and similar or increased performances in most other measurable characteristics [124].

Piezoelectric actuators are one of the limited emerging technologies to be flight tested (in the case of rotary blade camber) morphing an aerofoil. Increased bandwidth over other concepts and smart materials makes it particularly applicable in >400 rpm environments posed by rotary aircraft. Table 2.4 shows these values compared with those of the avian presented, where the bandwidth in orders of magnitude greater. Similarly, peak actuation stress is comparable and higher than avian muscle, indicating suitability. In comparison to avian actuation strains however, it can be seen the PZT actuators presented are unsuitable for larger deformation morphing. This is considered the reason span-wise, sweep and large out-of-plane morphing has infrequently been attempted utilising piezoelectric materials.

2.2 Comparison with Avian muscle standards

Development of biomimetic or indeed any actuator system is ongoing, this review is therefore limited to the actuators; that exhibit biological traits, as defined, while also being currently applicable to scalable aerospace applications, including UAVs. Mention should be made to shape memory polymers which, when applied to current morphing concepts tends to be utilised as an active or flexible skin actuated be another means [6]. Similarly, electro-active polymers and magnetically active materials can be un-scalable or do not represent sufficient biomimetic qualities.

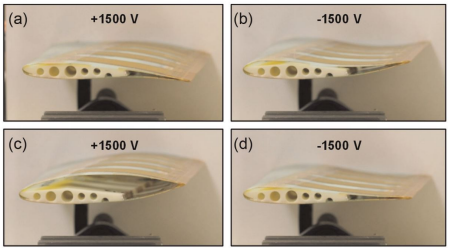
Ashby [125] presented a method for displaying material characteristics as an area plot, allowing comparison of materials. This method has been used by Ashby for the analysis of actuators, as similar characteristics are inherent and comparable. Figure 2.7 collates the actuation stresses and strain for the actuators presented as biomimetic muscle actuators. Biological muscles and the subset of avian muscle is being proposed as a benchmark for artificial muscles proposed for applications in UAVs and MAVs, as weight and size are similar. As such actuators which overlap or exceed the avian muscle are considered feasible for small uncrewed aircraft. Power output with regards to weight and volume are sort after for systems where both are restricted; the internal structure of an aerofoil is the key example of this regarding morphing lifting surfaces, particularly as this is often an area alternative aircraft systems require. Figure 2.8 allows a correlation to be observed regarding specific power and power density, which is to be expected [93]. Biological muscle and similar concepts with low actuation stresses, such as the thin McKibben PAM concept and the VAMP pneumatic concept (which is not included for visual clarity) exhibit poor power attributes in comparison to piezoelectric which despite low strains represent increased power performance in regards to weight and volume. Piezoelectric material actuators and similarly SMA based actuators are subsequently suggested to be suited to MAV applications where power-to-weight and power density are significantly influential design factors, while decreased strain and actuation bandwidth (respectively) pose unsubstantial shortcomings. Bandwidth otherwise referred to as actuation frequency defines the maximum sustainable actuation cycles per second (Hz). Proportional to actuation power the bandwidth for the avian muscles presented ranges from 10 – 15 Hz. Any biomimetic actuator with applications in aircraft and dynamic systems should exceed this benchmark. Figure 2.9 presents bandwidth against strain, and while dimensionless this produces the strain rate. Piezoelectric are an edge case due to orders of magnitude higher frequencies', while biological muscles have a range of actuation strains across different muscle applications and types. Although not presented it should be noted hydraulic and pneumatic cylinders traditional in aviation; have strains across a similar range to biological muscle [93], due to the benefit of increased applications and development. Pneumatic artificial muscles, given similar development could possibly match the actuations strains set by biological muscle.

Piezoelectric material actuators, while possessing high specific power, power densities and frequencies allowing for possibly improved actuation responsiveness and resultantly contributing to increased stability and control characteristics, all present a low linear actuation strain. In comparison to the avian standards presented, and with applications limited to bending actuation and low strain actuation such as MAVs and morphing rotary blades, it is assumed that these would be unsuited

to fixed-wing morphing concepts actuated linearly. Shape memory materials in contrast are suited to fixed-wing morphing, despite 8% typical actuation strains. Mechanisms development and material research will continue to improve the actuation capabilities of these actuators, towards comparable values to the muscles of avian. The bandwidth of SMAs poses a drawback, and significant development needs to be invested before deployment in a dynamic system such as a biomimetic wingbeat morphing concept or any aircraft control surface morphing. Pneumatic artificial muscles consistently overlap and outperform biological muscles. As a result they are presently the most suited to morphing applications and similarities to conventional actuation systems will allow integration into aerospace systems without as significant a development. PAMs, similarly to the artificial muscles collated, present amongst other characteristics, reduced weight, decreased hardware complexity and increased suitability for morphing applications through structural integration and multiple role actuators.

Artificial muscle actuators, not limited to the ones presented, outperform biological muscles in most parameters applicable to aerospace morphing systems, in some cases by orders of magnitude. It is therefore important to note that although the artificial and biological muscles have been presented here for comparison and the purpose of assumptions on the suitability in morphing aircraft, the actuation system as a whole is not comparable. The biological systems that produce energy in the avian muscle system have benefited from years of evolution to produce an unmatched efficiency. The values collated are therefore not inclusive of the systems supporting the artificial actuators themselves, including power generation and control systems. It would be ideal to suggest for future work that a review or experimentation be conducted into the characteristics of the actuator and the support systems. It is unfortunate, however, that literature presenting novel or even developed actuation concepts rarely includes the supporting information required for such a review.

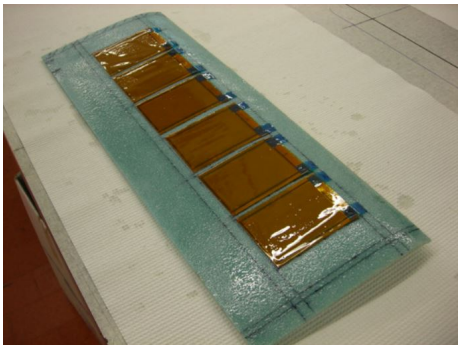
Presented in this chapter are the quantitative muscle characteristics of commonly studied avian species: actuation stress, strain, mass-specific power, volume-specific power, and actuation frequency referred to as bandwidth. It is proposed that the avian values for pectoral muscle provide a suitable benchmark for the artificial muscle actuators being proposed and implemented in the present biomimetic aircraft morphing concepts. As such, comparable values for the characteristics collated for the avian were also taken and derived from literature sources, while also presenting and discussing the morphing concepts utilising the actuators or that could benefit from the integration of biomimetic muscle-like actuators. Pneumatic artificial muscles (PAMs) were found most suitable (currently) for linear actuation applications in morphing concepts such as uncrewed aerial vehicles (UAVs) where suitable actuation strain is required. Whereas it is suggested that piezoelectric materials and shape memory alloys would suit micro air vehicles (MAVs) where specific power attributes are more preferable.



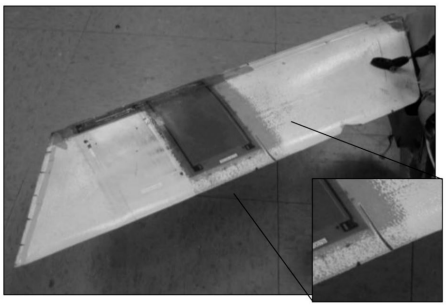
(a)



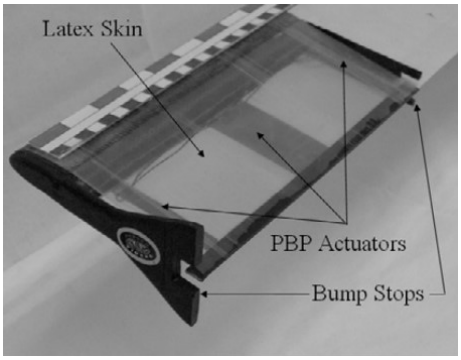
(c)



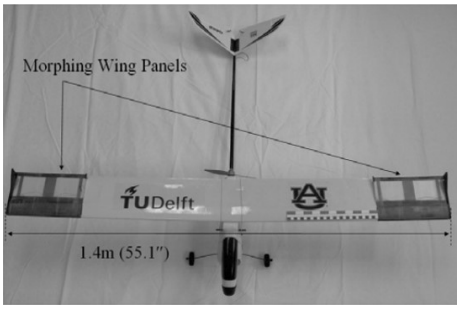
(b)



(d)



(e)



(f)

Figure 2.6: Piezoelectric materials concepts; (a), variable camber wing employing embedded MFC bimorph actuators Bilgen et al. [108]; (b), MFCs implemented in a camber morphing concept presented by Paradies et al. [109]; (c) and (d), Two MFC actuators to produce a localised camber change for control purposes Bilgen et al. [110]; (e) and (f), A similar roll control concept presented by Barret et al. using post-buckled precompressed axial force piezoelectric actuators to replace more typically actuated ailerons [111].

MFC: Macro fibre composite

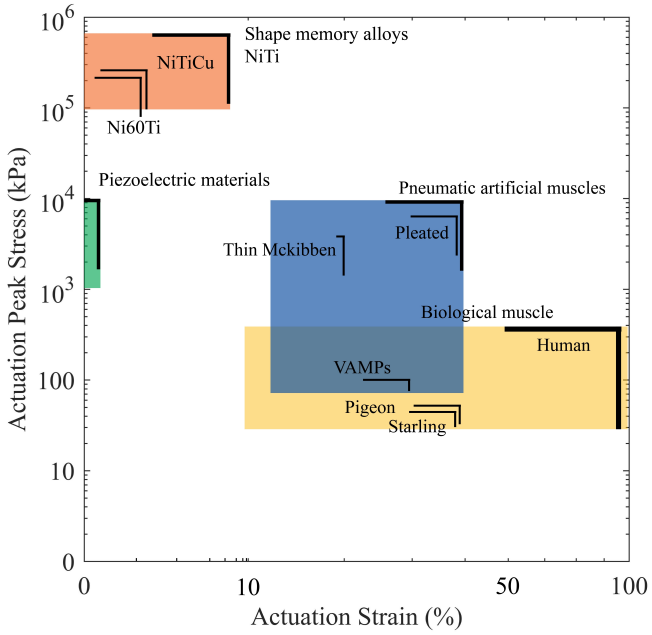


Figure 2.7: Actuation stress and strain presented in a plot, approximate values taken from the literature cited. Stresses represent the peak actuation stress, while the strain is presented as a percentage of the original unloaded length.

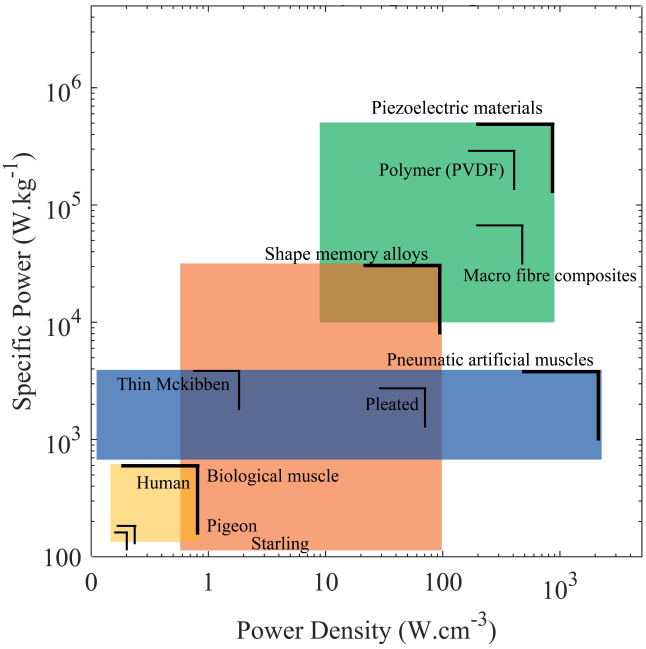


Figure 2.8: Specific power, versus power density presented in an Ashby plot, values taken or derived from the literature cited.

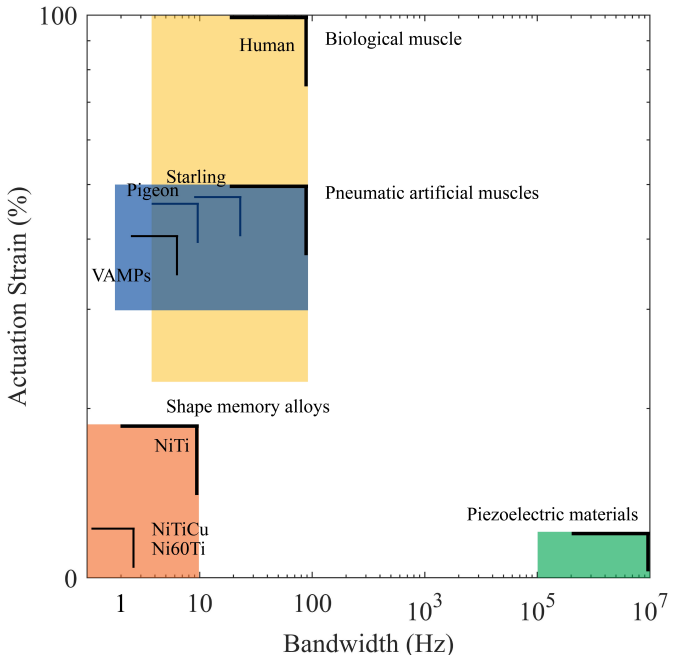


Figure 2.9: Actuation strain, presented as a percentage of the unactuated and unloaded length; against bandwidth, the maximum actuation frequency; values taken from the literature cited.

Chapter 3

Avian Span-wise Kinematics

The dynamics of avian flight have been of interest to researchers and engineers since the first concepts of human flight. The study of their dynamics, however, has presented a problem: what methodology should be used for measurement? Static analysis removes a dimension of the problem as the specimen can be positioned and measurements taken using developed reliable techniques. Dynamic measurements are more complex and will be discussed in general in the context of the literature currently available in the field. The overarching problem, however, can be summarised thusly. Once you position, move or otherwise prepare an individual bird for measurement, the natural flight behaviour has been altered. The result is a distorted or incorrect representation of avian flight dynamics. The primary consequence of this is that in order not impede the dynamic behaviour of the bird in flight (or in vivo), the method by which the results are measured must be either similarly dynamic or completely detached from the bird itself. The implications of these areas of research are numerous in the related fields of Biomimetic design and engineering. The applicability of some mechanisms present in avian has proven the viability of bio-copy and bio-inspired methods for engineers. The methodology used to derive any inspired or copied concept can broadly be summarised into two categories, separated by approach precedence. The two priorities can be summed up as either biologically driven or problem-driven. The former being where a study into a biological system is simply conducted irrespective of any specific human application. After analysing the results, a conclusion may be drawn regarding their applicability to any given engineering area. This is opposed to a problem-driven methodology whereby a specific issue within a field, such as wing morphing, is taken and an experimental process is undertaken, specifically, to provide insight and alternative concepts.
In the following section the latter approach is employed with the aim of producing a biometrically derived span-wise morphing concept. This follows the research conducted in chapter 2 as to the advantages of highly span-wise morphing lifting surfaces. It was found during the conducting of this literature review that a few sources have produced the kinematics required for a full analysis of the features of these birds worth replicating. Two methods for conducting the avian kinematics required are presented after the feasibility of others is assessed. Discussed are the accuracy, repeatability and viability for further application of both methods. Further, the kinematics themselves are presented and discussed in the context of applications in a morphing concept.

3.1 Background on Avian Biology

Span and area morphing in the proposed design were achieved through the mimicking of the bird wing. Avian exhibit a wing surface area change of 100% [126] and as discussed in chapter 3, deploy this in multiple instances including enable high roll rate manoeuvrers and significant centre of gravity (CG) changes, both longitudinally and laterally [127]. While the muscles and systems inherent in birds are complex, the skeletal structure is consistent across most species and orders. The work completed by Pennycuick cited in this work is considered an authoritative source in avian biomimetic engineering. The work conducted in avian flight modelling formed the basis of the literature on which this section is based. [128]

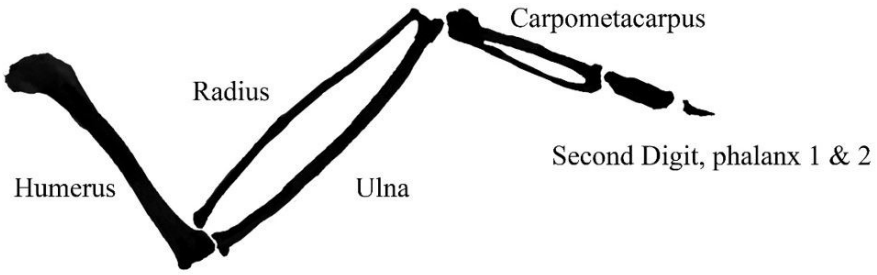


Figure 3.1: Graphic illustrating the skeletal structure of the bird wing. Obtained from the Natural History Museum at Tring, specimen NHMUK 1940.7.6.1.

Avian wing skeletons comprise *humerus, radius/ulna, Carpometacarpus,* and *digit phalanxes.* These shown in figure 3.1, can be modelled as three discrete structural members as the digits and *Carpometacarpus* move a negligible amount in relation to each other. However, this negligible angular change is transferred into the feathers embedded into these bones, the locations and type are species dependent, and it has been widely shown that these primary feathers impact the flow about the wing significantly [129] [130]. The bones themselves have been extensively dissected in the relevant fields of biological science. Key points to the span-wise motion or structure include the relation to primary lift surfaces, including the primary feathers, the mechanisms by which they actuate, and their internal and external physical structure. A typical skeletal model as derived from the examination of a Red Kite (*Milvus Milvus*) specimen is shown in figure 3.1 alongside a plot showing the typical range of motion.

Bone Structure

The internal bone structure itself is perhaps most well known to be 'hollow'. This is a simplification, but ongoing research is being conducted into the evolution of the complex structure specifically developed for mass-specific yield strength.

Comparing the three major wing bones was also intended to allow insight into the span-wise mechanisms of the avian wing. Arguably, the most noticeable among them is length. A primary study of specimens available at the Natural History Museum at Tring was conducted with the aim of collecting section lengths. Parallel to this, literature was collated with the same aim. Table 3.1 tabulates the results for the Red Kite (*Milvus Milvus*) chosen for its close relation to the birds studied in chapter 3, being of the same order *Accipitriformes* and family *Accipitridae*.

Table 3.1: *Milvus milvus* wing bone length dimensions, including measured specimen and researched data. Including averaged values for use in further calculations. One specimen had no specimen number available (NSNA) as it was new to the museum's collection.

Bone Name	NHMUK 1940.7.6.1 (mm)	NSNA (mm)	Otto, 1981 (mm)	$\bar{x}$ (mm)
Humerus	123.86	124.29	124.6	124.25
Ulna	142.5	142.77	142.45	142.57
Radius	134.66	134.37	135.1	134.71
Carpometacarpus	72.69	72.21	72.55	72.48
Second digit Phalanx 1	31.37	30.64	N/A	31.01
Second digit Phalanx 2	22.86	23.92	N/A	23.39

Whilst in isolation we can gain little from these values the relation between the sections themselves can be taken forward. Sullivan et al [131] concludes there is an upper limit for the scale of avian wings, in particular the humerus. However, perhaps of note in a discussion surrounding the skeletal structure and its impact on flight modes, is the implication that the bone dimensions and material directly impacts the feather structure to a micro-structure; impacting the compliant nature of the aerodynamic surface.

The nature of the span-wise retraction is largely impacted by the ratios in length between these bones, The primary literary source [132] for these bone lengths also explores other species with different flight modes. A conclusion can be drawn from the correlation between the length ratio and the major flight mode exhibited by the species. As discussed in [133] as the ratio tends towards one the species demonstrates a predominant low velocity soaring flight with long distance endurance being the primary flight mode. An example of the typical species would be those examined by Mitchell [134] or presented by Viscor [135]. In the former, it was also noted that there was a difference in effective bone density between species depending on their primary flight mode. Whereas it is more typical to find high-manoeuvrability predator species, such as the swift or falcon family, with larger ratios. This is perhaps unsurprising, as a similar correlation has already been shown between flight mode and wing aspect ratio [128]. An argument could therefore be made that the bone structure, dependent physically on the whole wing aspect ratio, is reflecting this relationship between AR and flight mode. As correlation well known in the human-designed aircraft in the industry.

Wing actuation

The actuation of the avian wing is highly complex and better explained by other sources. What follows here is a summary and more technical exploration of a feature significantly applicable to span-wise morphing of the wing.

A feature of avian wings known as the twin parallels or drawing parallels mechanism is of particular interest to the study of avian span-wise morphing. Inherent in all avian Vazq [22] summarises the mechanisms employed to extend the carpometacarpus about its joint. Physiologically, the mechanism consists of the two bones, the *ulna* and *radius*, the forearm muscles, and the passive muscle and tendon/ligaments. In this biological mechanism the rotation about the joints and the sliding of the radius along the ulna is regulated by ligament passive activity surrounding the joints. This, in conjunction with the particular geometry of each bone's point of interference with the other bones, allows an automatic synchronisation of the effective elbow and wrist joints. Mechanically, this system acts as two parallel rods, connected via two linkages to form an arrangement resembling a rhombus. Assuming one fixed member, this arrangement allows a torque to be transferred across the length of the members. This is shown in figure 3.2 where this figure also illustrates the mechanism's analogy in the skeletal structure of the avian.

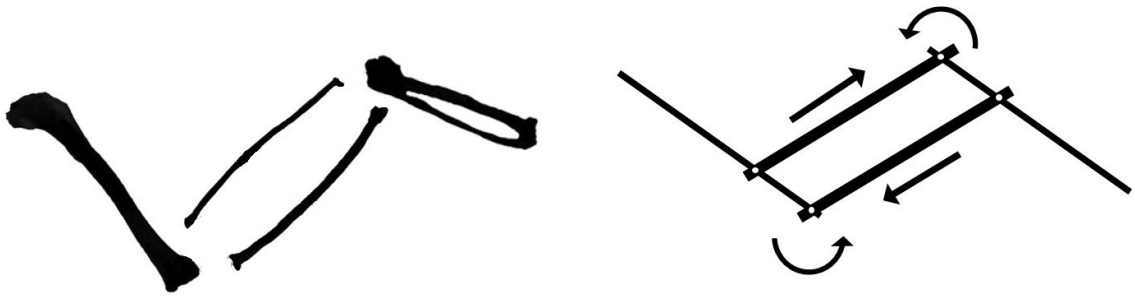


Figure 3.2: Illustration of the twin parallels mechanism.

It has been proposed that the presence of this mechanism aids in the reduction of energy expenditure by reducing muscular fatigue [136]. It has further been discuss that the linkage between the two joint is a factor in achieving the circular motion of the wing beat. Mimicking this mechanism in a two-dimensional form would reduce the number or complexity of any actuation systems required to actuate the span-wise morphing structure fully. It is therefore proposed that a morphing wing utilising this principle would provide significant benefits in producing a span-wise perturbation comparable to that of the avian.

Feathers

It is largely understood that the first successful attempts at heavier-than-air powered flight were based on significant aspects of avian research. Slightly eclipsed by the failed attempts based on flapping flight. The adoption of thin plate early aerofoil concepts into fixed-wings resulted in the advance of aerofoil understanding. Early work on camber and twisting has been discussed as the first instances of morphing in aircraft. It can be argued that avian-inspired design impacted the early design of aerofoils significantly. Recent literature has used advances in technologies, such as those discussed in chapter 3, to derive the form of the avian wing more precisely. Species exhibit significantly different profiles, and it has been found that many employ span-wise section changes similar to those of aircraft. Carruthers et al [137], conducted photogrammetry on an in-flight Steppe Eagle *Aquila nipalensis* . This

method allowed for a point cloud to be obtained for each wing. The aerofoil sections produced for three span positions suggested a highly cambered section with a thin 'plate' trailing edge, as shown in figure 3.3. Carruthers et al. conclude, after basic viscous panel method iteration, that its performance could be compared to the common aerofoils such as the Clark Y aerofoil. Liu [138] acquired a similar form of results for avian species, including: Gull, Merganser, Teal, and Owl; the exact species is not given. A non-contact laser-scanning method using a mechanical positioning arm was used in this case. The advantage is an increase in accuracy and repeatability on different specimens while limiting other factors. Whilst consideration has to be given to the deceased and out-of-flight errors that could be present in the results. A similar comparison was made regarding the likeness of the obtained thickness distribution and planform to aerofoils applied in current aircraft. It was found that both the gull and merganser exhibited wings comparable to high-lift, low Reynolds number aerofoils. The Teal a more symmetrical variation. Whilst the Owl was found to have a low thickness, 0.3-1.0 chord, with a significantly skewed distribution towards the leading edge.

The structure of the wing itself has been a focus for opportunities in biomimicry. The feathers themselves contain unique properties. Structurally and materially, avian feathers are designed for flight. The micro-structure is significant in maintaining a connected lifting surface through barbed and grooved connecting features. While this has formed the basis of research into application for this structure [131], it is not yet developed to the point of application into a morphing concept. The material properties of feathers, examined by McKittrick et al [139], also have implications in the areas of morphing skins. As discussed in chapter 2, this is a particular area where it has been conceded that more development is required. A more holistic approach to feather mimicry includes the structure and arrangement of each individual feather. A recent study into the attachment of flight feathers [140] concluded that the musculoskeletal linkages contained an increased amount of smooth muscle. Smooth muscle, fundamentally different to skeletal muscle used to actuate limbs, is associated with a lack of control via the somatic nervous system. It is noted for contracting to signals from the autonomous nervous system, suggesting a passive control. A skin concept that could be derived from this is an advancement on the common overlapping plate compromise. A number of concepts compromise on the issue of a non-conforming surface skin by introducing a limited number of simply overlapping lifting surfaces. It is therefore proposed that a biomimetic solution to this is the incorporation of a greater number of passively morphing feather substitutes. Similarly to the avian, these would be passively actuated with the wing mechanism and collate during retraction to form a reduced wingspan.

3.2 Background on avian measurement methodologies

A distinction should be made between two general categories of avian measurement. Static and dynamic. The former concerns the dissection of specimens and the generation of static 3D scans. Whilst dynamic primarily looks at locomotion or flight. This is not to say that either cannot provide insights into the other; a recent example is Durston's work on the inertial properties of avian [141]. Specimens of barn owls

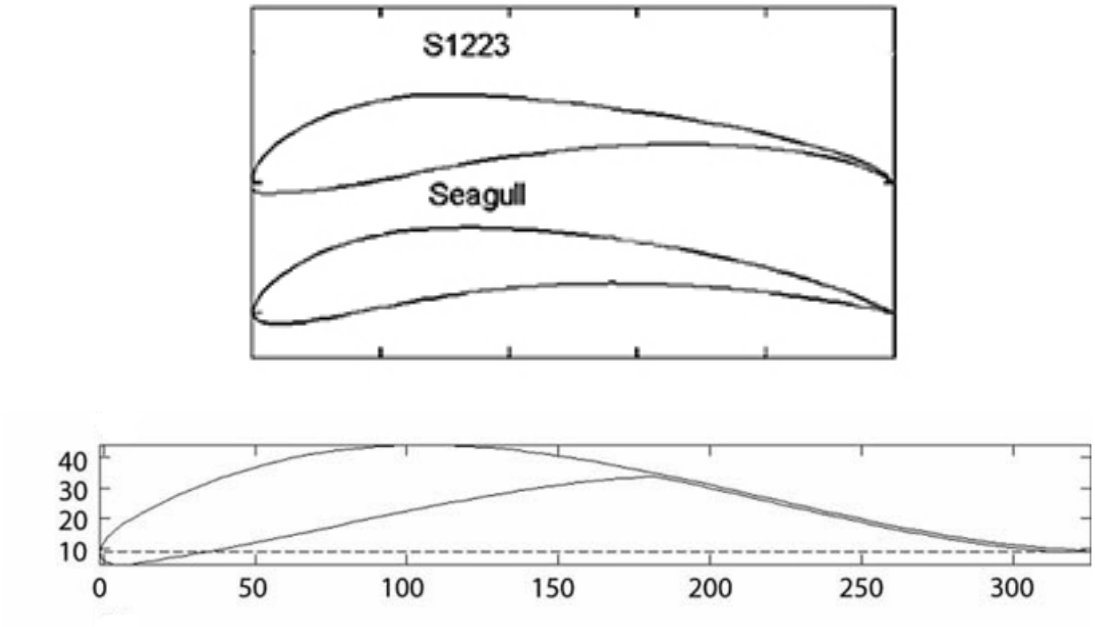


Figure 3.3: Aerofoil sections for the proposed avian-based concept (top) and the bird wing section results obtained through photogrammetry by Carruthers et al [137] (bottom).

(*Tyto alba*) and peregrine falcons (*falco peregrinus*), amongst others, were examined to determine estimates for centre of mass and mass moment of inertia. A wholly static process of measurements for properties pertaining to dynamic characteristics exhibited in avian flight. Static measurements of interest were covered in section 3.1

Primarily, research has focused on aerodynamics independent of control and stability as these aerodynamic forces more directly affect efficiency. Pennycuick [142], along with others [25], have presented research into the characteristics of avian muscle to compare to the power output of birds [24]. However, similarly to aerodynamic analysis, the methods avian employ for control have also been measured and modelled. Taylor et al [143], have conducted position tracking experimentation on in-flight birds using photogrammetry and inertial measurement units (IMUs). Photogrammetry is the process of capturing multiple images of a subject from offset angles to produce a point cloud of a subject using inherent features of that same subject. While IMUs provide comparatively accurate and reliable data compared to photogrammetry, the placement has the potential to disrupt normal flight behaviour. These methods both provide the angular positions, velocities, and accelerations necessary to begin to produce a model. Shepherd et al [144] used the measurements to produce rigid-body, linear state-space models using Observer/Kalman Filter identification. These models used input states from the tail of the avian and were limited by the values an IMU can produce; assumptions were therefore made to allow for this incomplete data. Consequently, the longitudinal axis was limited to 3 states. The method of measurement proposed for this program is a 'motion capture' system commonly used to capture the kinematics of animals and humans. Kinematic capture allows full position tracking of points on an avian in flight; thus, with correct marker placement, full longitudinal and lateral modes can potentially be assessed.

3.3 Kinematics Capture

Infrared capture and visible light capture, while similar in working principle, pose different challenges in the method of capture. Any system has compromises, and the predominant one in the case of Avian kinematic capture is the camera specifications. The recognition of expense as a fundamental variable in the selection of a methodology is explored in chapter 3.2. Equal is its effect on the specific camera's specifications and the restrictions, therefore, placed on the capture process.

3.3.1 Infrared

Infrared 'motion capture' systems, as discussed in the literature, pose different technical challenges when in use to capture subjects. Specific to avian capture however, is the capture location. Later sections of this chapter will discuss the procedures enacted to produce natural flight. However, the limitation for the IR system used is that it cannot distinguish between different sources of infrared light. Thus, cannot be used in partial or direct sunlight, this eliminates more natural outdoor flight locations. Methods for avoiding this issue included capturing in the hours of darkness. This however, was not carried out as several of the birds, while capable of nocturnal flight, do not perform their most natural flight during this time. Similarly, the bird handlers do not routinely fly the birds during this time and an acclimatisation period would be required. An interior location was chosen and a number of steps taken to promote normal flight conditions. The most effective of which was the use of industrial fans to provide air flow, including an upward flow to enable gliding flight. The capture area defined in both figures 3.6 and 3.4 are defined by the IR camera setup. This is due to the basis of IR system requiring a greater number of cameras, resulting in the capture area being the larger volumetrically. Consisting of 10-12 cameras, depending on location, the IR system used provided a total coverable area shown in figure 3.4. As discussed, this is defined by the resolution of the cameras used and the precision required in the spatial measurements. The cameras used were Raptor-E Digital Cameras, running at 1.31 megapixels or 1280x1024 per frame. These, however, are not relatable to the resolutions of visible-light cameras. The system captured at 200fps the limit of the data acquisition software used, Cortex produced by the Motion Analysis Corporation. Individual cameras were positioned accordingly so as to provide consistent coverage of the volume. Mentioned previously, the post-processing requires each tracked point be visible to a minimum of three cameras in each frame. Depicted in figure 3.4, the intended flight paths of the birds, during manoeuvres of interest, allowed an estimation of the optimal camera positions. Cameras (a) – (d) are positioned to provide an overview and the lens focused on the predicted flight plane. At a height of approximately 2.5m each are angled 10 degrees downward to enable increased coverage of rear and upper body positioned markers. The vertical coverage range was particularly important in these four cameras as low gliding manoeuvres were otherwise lost due to incomplete marker tracking. As such (a) – (d) included in their FOV any point greater than 20cm above the ground and upwards of 4m for the ceiling of the capture volume. (e) - (h) were positioned laterally to the origin of the volume and the flight path. (e) and (g) forming opposing corners of this inner square are offset outward from the origin to allow greater capture range at the expense of losing detail in the opposite

side of the capture volume. These four cameras were positioned with intent of continuing a clear line of sight to markers possibly obscured to other cameras during the turning manoeuvres. As the wing deforms to initiate the turn, the tail, which is also involved in controlling each turn, and the body obscure the back-positioned points. The final two cameras, (i) and (j), were positioned due to a specific problem occurring during our flights. The birds were predominantly launched from a raised handler or perch, except for the diving-based manoeuvres. This encouraged gliding flight to a lower landing perch, resulting in minimal flapping when not required and allowing small perturbations to remain unobscured by the greater motion induced by flapping. As a result, the first 30% of the flight path featured a moderate 5-25 degree pitch downward to accelerate before flapping or gliding. During this, the leading edge markers shown and described in figure 3.8 and section 3.4 respectively, would be obstructed from the cameras in place at the rear of the capture volume. Cameras (i) and (j) were positioned to mitigate this possibility by being positioned lower and facing the flight line.

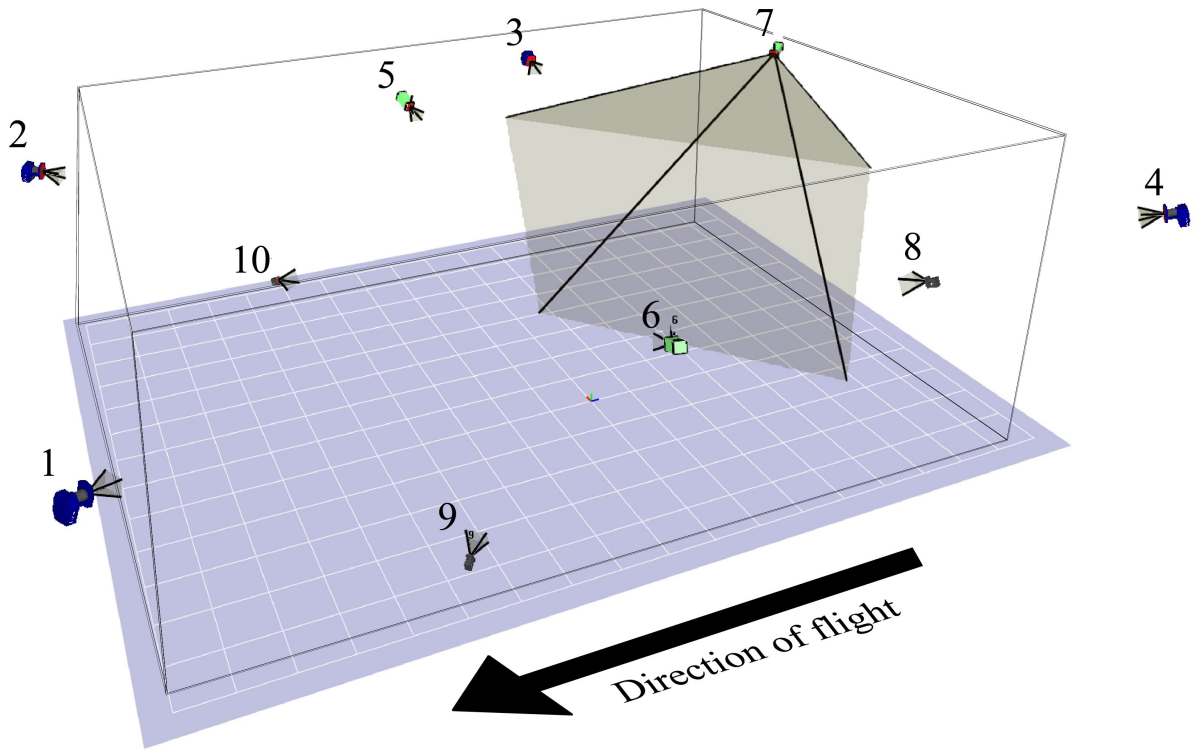


Figure 3.4: IR Diagram

The dimensions of the capture volume were measured both by the IR system and physically in each location. It should be noticed, as explained in section 3.2, that there is a capture quality drop-off towards the edges of these areas. The volume defined, therefore, is the maximum before significant marker dropout. This was defined as ¡50% of markers visible, while defining marker obstruction as 10 frames without a locatable three-axis point. This put the final volume at approximately 7.6m in the direction of flight, 4m perpendicular to the flight line, and a height of

3.5m. A detailed view of the flight volume can be seen in figure 3.5. This image also shows one of the landing perches, a bench, at the far side of the setup.



Figure 3.5: A photograph of the capture volume for a majority of captures obtained. Shown are the 10 cameras parallel and adjacent to the flight direction. The cameras positioned below the volume maintain a line of sight with markers during diving flight.

3.4 Avian Marking

Physical marking of avian for measurement and data capture is the basis of all IMU and migration tracking experiments. The specific practice of adhering inferred reflective material to subjects to be tracked in motion is also common in the field of human locomotion. It has been further applied to large mammals [145] [146], as discussed in 3.2. There have also been significant efforts toward marker-less 3D kinematics via traditional image recording with the obvious benefits of allowing 'wild' kinematic capture. [147] However, from the literature there appears to be a stagnation in the use for avian research.

The primary concern was for the animal's welfare. Predator birds are sensitive to changes in the environment, handling, human presence, and their physical state. As such all necessary procedures were put in place to ensure the physical and social wellbeing of the animals involved. A declaration can be found within this document in regards to this issue.

Reduction in the impact on the birds was the primary methodological concern. As highlighted in previous sections, 3.2, the disadvantage of some methodologies is the impact on natural flight and the subsequent compromise on the results acquired. The physical markers for IR motion capture systems are variable in size and a number of steps were taken with the aim of reducing the impact on flight. As shown in figure 3.8, the markers were removed from a rubber base typically used to provide a greater surface area when adhered to skin. This reduced the weight and size by a



Figure 3.6: The secondary capture volume used to force specific flight behaviours

factor of five. The compromise of this was a reduced contact area with the birds. It was, however, concluded that the impact of this on the stability of the marker, with regards to its relative position to the surface of the marked body, was negligible. The marker body comprised a 10mm diameter spherical rubber ball, coated in a retro-reflective tape with the microscopic glass lens specific to infrared radiation. Each marker weighs less than 2g comparable with the most basic electronic measurement unit discussed in 3.2.

Traditional adhesion methods for IR systems include skin-safe cyanoacrylates. These provide a stable adhesion to skin. While markers attached to fabrics worn are often permanently bonded using high-strength methods. The issue of affixing markers to avian wings and body posed a significant challenge. A specification of four criteria was developed to determine the viability of adhesive substances. Temporary, should not require excessive force to place or to remove. Non-disruptive, leaving no residue, oils or other irritants. Cause no lasting disruption to any feather coating such as dust or oil. Provide a stable connection to the surface both feather and down, able to withstand all flight regimes.

These criteria were found to be sufficient for the motion capture method. It was found that an extruded hot melt pressure sensitive adhesive met these criteria. In the form of a 9mm diameter disc of 0.5mm thickness. These 'tack' dots are most commonly used for postal stationery applications where a temporary bond between paper items is required. A comparison of available industrial solutions was conducted, and a range of tack dots was selected for different marker placement

positions and feather surfaces. The selected adhesives' properties can be seen in table 3.2, all sourced from accompanying product documents [148, 149, 150]. The diameter dimension was selected to suit the marker spherical diameter best. The thickness the lowest commercially available to provide a more accurate representation of the bird surface. It is also worth noting that these adhesive dots contain no transferable oils and have full material certification [151, 152].

Table 3.2: The adhesive technical details, including loading forces and specific use cases. Holding forces stated by the manufacturer [148, 149, 150]. These values for tensile and shear force were tested under the American ASTM D3330 and ASTM D1002 standards, respectively.

Manufacture stated tack strength	Tensile holding force/N	Shear holding force/N	Applied Species	Applied location
Low	0.44	1.8	Barn Owl (*Tyto alba*)	Spine, Elbow, where down is present.
High	4.0	5.8	Eurasian Eagle Owl (*Bubo bubo*), Common Buzzard (*Buteo buteo*)	Tail, Spine
Super High	17.3	45.8	Harris Hawk (*Parabuteo unicinctus*), Red-Tailed Buzzard (*Buteo jamaicensis*)	Wrist, Primary feathers

The layout of markers across the subjects is equally critical to the visibility of the markers. However, the driving factor from a positioning point of view is the positions to be tracked. Literature focuses on the wings of the avian and given the application discussed previously this was the focus. Three markers were positioned on each semi-span at the elbow the joint of the *humerus* and *ulna* and *radius*, wrist between the *ulna radius* and the *carpometacarpus*, and at the wing tip on the leading primary feather. An array of three markers placed along the spine allows the shoulder position to be measured relative to these markers. A shoulder marker proved impractical as it was frequently in the field of vision of the bird. Whilst the birds captured could not feel the weight of the placed markers on sight, most species would attempt to 'clean' or remove as they might natural debris. It was also found that shoulder-mounted markers were frequently obscured by the head and upper body in flight, and as such, capture data was often incomplete. This arrangement of three wing and three body markers allowed full kinematic capture of the three joint wing mechanism. It was decided in order to improve the recognisability of the birds once captured and also to distinguish direction of flight in static images, tail markers would be added. Three markers, two on the outer tail feathers, one on the centre were placed on each bird. This tail capture also has the added benefit of making for a more complete comparison with literature sources that have also tracked tail position.

These layout decisions are summarised in figure 3.7, on a typical avian body. While the accompanying figure 3.8 shows the markers in situ on the Common Buzzard (*Buteo buteo*) used in some captures. The applied species and location sections of table 3.2 highlight some of the issues still apparent in marker-based motion cap-

ture. It was found that the surface oils of the birds of the family *Accipitridae* were repellent to the lower adhesive force dots. This included the Common buzzard, Harris Hawk, and Red-tailed Buzzard, details regarding the birds captured are presented in table 3.3.

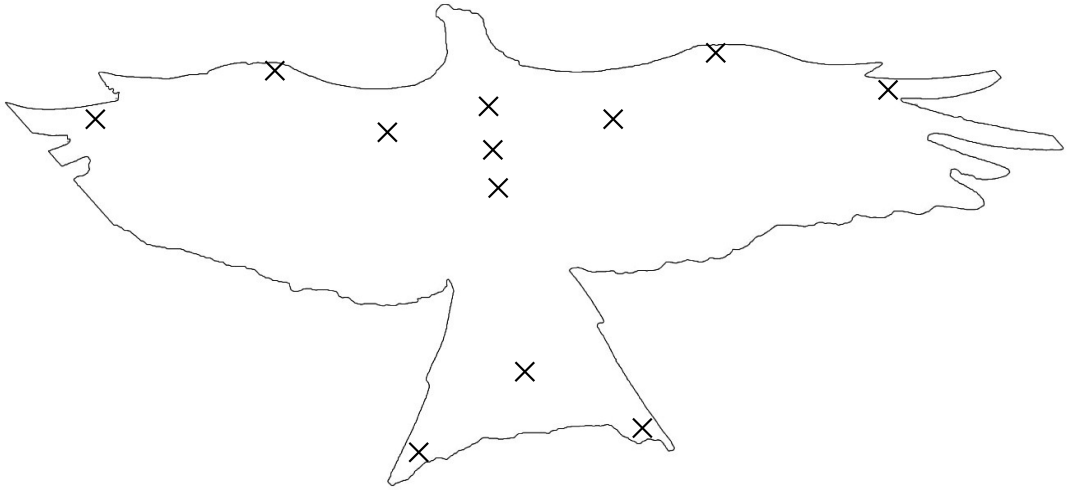


Figure 3.7: A general layout of the marker placement over the specimens. Note that these positions give an approximate position. Each species presented a different skeletal geometry, which defined the marker position. A total of twelve markers were used across the back of the specimen.

Table 3.3: Reference details relating to the birds used throughout the capture sessions. An ID, related to each specimen's species, will be used to refer to each specimen in the text. Presented against these are the given names used by the falconers, which can be used to identify the specimens outside the context of this work. The mass given is the nominal flying weight found by the handlers as best suited for the individual bird.

Specimen ID	Given Name	Species	Gender	Mass (kg)	Approx Wing-span (mm)
BO	'Dusk'	Barn Owl (*Tyto alba*)	M	0.43	810
HH 1	'Griffin'	Harris Hawk (*Parabuteo unicinctus*)	M	0.68	1000
EEO	'Logan'	Eurasian Eagle Owl (*Bubo bubo*)	M	1.814	1600
RTB	'Fortune'	Red-Tailed Buzzard (*Buteo jamaicensis*)	F	0.935	1400
HH 2	'Rico'	Harris Hawk (*Parabuteo unicinctus*)	M	0.66	1100
CB	'Kami'	Common Buzzard (*Buteo buteo*)	F	0.9	1400

The birds selected for capture in these flights were done so based on number of used flight modes. The objective was to capture the most varied range of manoeuvres and flight methods possible. To allow greater comparison between the methods. Similarly, the kinematic motion of each individual species could be compared. This



Figure 3.8: Left, female Common Buzzard *Buteo buteo*, approximately 1kg. Right, male Harris Hawk *Parabuteo unicinctus*, approximately 0.7kg. Shown are the markers; however, the outer wing markers are obscured and not visible in the images

would allow conclusions to be made regarding the kinematic motion and species-specific physical traits. The family *Accipitridae* was chosen as a focus due to hunting and scavenging behaviour resulting in loiter, soar, gliding and diving flight modes being exhibited. This is also true of the order, of which this family is a subset, *Accipitriformes*. This order noticeably excludes falcons themselves. It was deemed to impractical to expect falcons to achieve any substantial flight in an enclosed space.

Supplementing these birds was the inclusion of several birds of the order *strigiformes*. Owls were recommended for these captures, as they are often more comfortable flying in still air. This would allow them to achieve a more natural flight. Additionally, the Barn Owl (*Tyto alba*) with the least mass would also be most likely to exhibit an entirely gliding flight which would remove flapping as a variable in any flights where it would not be beneficial from a capture quality perspective. Unfortunately, the relative size of the Barn Owl in comparison with the markers, resulted in behaviour which impacted the quality of the capture results.

3.5 Span-wise kinematics

To determine an appropriate method of control for any avian derived morphing concept the kinematics associated with the full extension and retraction of the avian in flight must first be identified. The current assumption, and one employed in later chapters, is that of equivalent angular rotation of the shoulder and elbow, with the wrist exhibiting twice this motion. However, it is clear that this assumption will not be suitable for the control of any proposed span-wise morphing concepts.

Full extension and retraction is found in a number of flight modes, perhaps most interestingly in diving flight. However, despite examples in literature detailing this flight mode the setup is unsuitable for IR based motion capture. Thus, the flight mode identified for the capture of this behaviour was take-off and perch landing.

Figure 3.9 exemplifies the typical perch take-off to straight and level flapping flight. The coordinate points are centred on the fore spine marker. This proved a

reliable method for producing body-orientated motion such as in the case of span position. Data capture starts approximately 20-100 frames after motion commences due to markers obscured in the folded wing position. The extension motion initially starts with little flapping motion. Observe only small variations in the z axis between 3.9a, b and c. This period accounts for 50% of the extension by maximum span length. The extension, however, extends into the first flapping motion. This is notable as the overlapping motion could impact the efficiency of the latter motion with respect to power generation. However, the downstroke of the wing, which occurs in 3.9f, appears unaffected a the angle made between the humerus and radius-ulna are within the typical range for mid-flight flapping. The final figure 3.9g depicts the wing at full extension during this manoeuvre, notice the wing is not perpendicular to the axis. This occurs before the wing passes the axis and continues the flapping motion. This period is also approximately the moment the avian lifted off from the perch. There is no reliable method for determining this 'take-off' point at which the avian is fully supported only by its own flapping wings. This is due to no marking being present on the claws or perch itself. It was also noted that any attempt to gain this information from a separate video running parallel to the motion capture would result in a timing error, rendering the method unsuitable. Some motion capture systems support trigger inputs, which could indicate take-off via weight sensors or similar. However, it was determined that this was not critical to the analysis of span-wise wing motion.

It is interesting to note the differences in symmetry between the two semi-spans. In this flight, typical of the flights analysed for extension and retraction, the avian was encouraged to conduct a straight flight. The start and end perches were aligned with no obstacles. This was indented to reduce asymmetry between the wings. It is clear, however, that some small error is still present. In this particular flight by specimen CB a 0.61% different in maximum span is exhibited between each wing at the instance shown in figure 3.9g. Whereas, the maximum asymmetry in wing extension is observed at 24% during 3.9b. It is consistently found that maximum asymmetry between semi-spans occurs during transition between downward flapping motion and upward. Given maximum span-wise extension occurs at the opposite phase to this in the flapping cycle, the effect of this error can be considered minimal.

While the flapping motion present in these flights is of particular interest with regards to the power requirement for take-off, stability at low speeds, and in initiating the next phase of flight. Flapping motion obscures the span-wise motion of the extension with which it overlaps.The major motion visible in the flights shown is flapping with a significant part being in the z-axis the out-of-plane axis to the span and chord of the wing. Ornithopters are a large part of the field of avian biomimicry and as discussed have historically seen the most concepts presented. However, looking at span-wise motion out-of-plane motion can be removed.

Attention was given to encouraging the motion capture specimens to require minimum flapping to sustain flight; discussed in 3.3.1. However, a post-process method was applied to enable a greater capture sample set and include flights with flapping. It is proposed that the ideal case for removing z-axis motion would be to rotate each marker point onto the span-chord plane about the true skeletal pivot. As a majority of the x-axis rotation occurs about the shoulder this would be the pivot. It was noted, however, that the compound rotation of the shoulder and elbow resulted in x-axis rotation in the wrist. These resultant rotations are negligible in

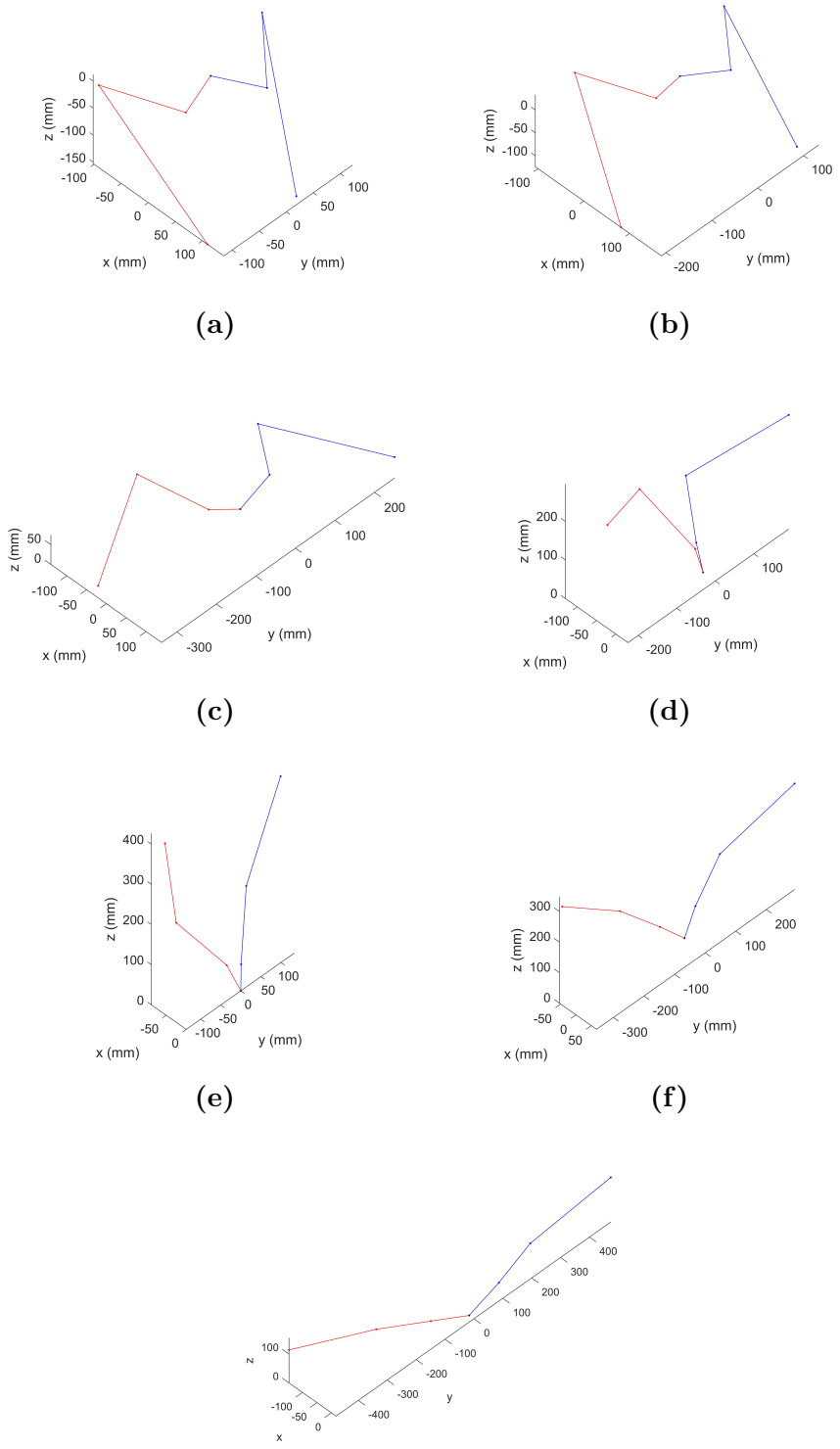


Figure 3.9: A series of figures showing a representative take-off manoeuvrer included in the presented data set. This series presents the flight of specimen CB *buteo buteo* (Common Buzzard). Shown in each plot are the six markers comprising the wing and a single fore spine marker taken as a reference point for the body of the specimen. Axes are centred about this reference point and remain so regardless of translational movement within the independent capture area.

contributing to the overall flapping rotation in the case of straight and level take-off. While the shoulder would present the ideal axis of rotation to bring the marker points to the required plane, there was no marker placed on the avian during the captures. An offset approximation was therefore used and the points rotated about the x-axis. A rotation matrix (3.1) was derived from the polar angle of the primary wing marker to the plane.

$$\mathbf{d} = \begin{bmatrix} 0 \\ d \\ 0 \end{bmatrix}, \quad R_x(\theta) = \begin{bmatrix} 1 & 0 & 0 \\ 0 & \cos\theta & -\sin\theta \\ 0 & \sin\theta & \cos\theta \end{bmatrix}.$$

Where $\mathbf{d}$ represents the shoulder joint offset from the origin along the y-axis of magnitude d. Whilst θ denotes the aforementioned polar angle of the primary wing marker.

$$R_x(\theta)\,\mathbf{d} = \begin{bmatrix} 1 & 0 & 0 \\ 0 & \cos\theta & -\sin\theta \\ 0 & \sin\theta & \cos\theta \end{bmatrix} \begin{bmatrix} 0 \\ d \\ 0 \end{bmatrix} = \begin{bmatrix} 0 \\ d\cos\theta \\ d\sin\theta \end{bmatrix}.$$

$$\mathbf{T} \;=\; \mathbf{d} - R_x(\theta)\,\mathbf{d} = \begin{bmatrix} 0 \\ d \\ 0 \end{bmatrix} - \begin{bmatrix} 0 \\ d\cos\theta \\ d\sin\theta \end{bmatrix} = \begin{bmatrix} 0 \\ d(1-\cos\theta) \\ -d\sin\theta \end{bmatrix}.$$

$$R_d(\theta) = \mathbf{T}(\mathbf{d}) R_x(\theta) \mathbf{T}(-\mathbf{d})$$

$$R_d(\theta) = \begin{bmatrix} 1 & 0 & 0 & 0 \\ 0 & \cos\theta & -\sin\theta & d - d\cos\theta \\ 0 & \sin\theta & \cos\theta & -d\sin\theta \\ 0 & 0 & 0 & 1 \end{bmatrix} \tag{3.1}$$

This was applied to each of the points in each wing. The remaining z values for the elbow and wrist were removed by projection of the points to the plane. This method was determined to best represent the bone dimensional member lengths as opposed to individually rotating each point about its own polar angle.

It is perhaps more apparent in the 2D representation of the data, shown in figure 3.10, that the asymmetry in the avian kinematics. Particularly, the longitudinal motion. This presents further evidence that the primary wing motion plays a significant role in longitudinal stability, as has been proposed in the literature. Figure 3.10 depicts the same frames as in figure 3.9. An average of 10 frames separates each plot at 0.05 seconds between frames and a negligible exposure time, specimen CB achieves full extension in 0.255 seconds. These figures show the longitudinal and lateral axes noted x and y, respectively. In 3.10a an initial rotation of the avian can be observed about the z axis. During motion capture the take-off perch was aligned with the system global coordinate axes. However, it is clear that despite this the specimen presented with an offset angle. While this is resolved in this flight by 3.9d it is clear a method to remove z-axis offsets is required. Although not shown in this section, as previously mentioned three spinal points were taken to give an understanding of body orientation. This was used to rotate coordinate axes about the z-axis, aligning the xz plane with a vector formed by two spine points. Only two

spine points were used as this allowed use of capture data with up to one missing spine point. It is also clear the extent of the span-wise extension exhibited by these avian. In this example flight, which best matches a flight averaged from the full sample, the primary feather marker was observed with a span-wise change (Δ) of 345mm averaged between the two wings. This represents a change of 75% in the span of the bird including body thickness.

These insights into the span behaviour can also be supplemented with the characterisation of each joint. Observation of the skeletal system of the avian has provided a mostly reliable understanding as to the angular range of each wing joint. However, these can only be looked at in isolation or when connected via ligament. The ratio of movement, angular velocity, and angular acceleration can only be estimated. Joints were defined as the angle formed by the two adjacent vectors. The elbow joint angle defined between the vector shoulder-elbow and elbow-wrist. Likewise the wrist joint between vectors elbow-wrist and wrist-primary. As the spine is aligned with the axes the shoulder angle was defined with the vector shoulder-elbow and the x-axis. These values could be defined for each 0.005 second interval. Thus, differentiated with respect to time allowed the first and second derivative, angular velocity ω and angular acceleration α, to be found for the duration of the extension. Table 3.4 outlines the components of extension in relation to each of the three major wing joints. Extrapolating from the minimum and maximum joint angles the change in angle Δ can be found, for the shoulder $\Delta\theta_S = 79.59^o$, elbow $\Delta\theta_E = 103.79^o$, and wrist $\Delta\theta_W = 142.08^o$. As perhaps expected the change in joint angle reflects what was previously estimated. The shoulder approaching a 90^o change in angle with the elbow and wrist approximately double. First, it is evident that all three angles fall short of the maximum kinematic angles of the simulated case. This can be primarily attributed to the offset each bone member must be allowed for proximate systems such as feathers and down, as well as the actuation mechanism itself. This can be quantified as 11.57% and 23.07% for the shoulder and wrist respectively. This indicated that there is more need for system proximity clearance at the wrist which is counter-intuitive when considering the number of body systems proximate to the joint. Observation of the un-rotated capture data indicates this is more accurately due to the compliant behaviour of the avian's body and an out-of-plane motion exhibited by the elbow. It is the elbow, however, that deviates the most from the ideal joint simulation. The general assumption was that the elbow would follow the wrist in being double the shoulder. This also follows the idea that the elbow and wrist joints are linked rigidly by a skeletal mechanism. It is clear that in this flight case the elbow joint does not follow the ideal parallel axis theorem described. The elbow's change in angle Δ looks more similar to the should joints behaviour for this avian. This discrepancy lends itself more towards the more recent literature in the field of avian biology. The idea is that the joints are not rigid and therefore cannot be related by a constant or linear relationship. This is developed further in comparison with the other species captured and in application within the span-wise morphing structure control system section 5.3.

The angular velocities ω presented for each joint in table 3.4 reflect the wing extension constraints. The minimum velocity values represent the slowest velocity measured between two captured frames and are all within a margin of error as this capture data does not include any periods without avian motion. The wrist exhibits the greatest rotational velocity as it traverses the greatest angle in the same amount

of time. Comparing the shoulder and wrist the shoulder presents a $\Delta\theta$ that is 54% of the wrist while the maximum velocity is 51%. This is close and suggests that this reasoning holds true. However, it is noticeable that this relationship does not hold for the elbow. Particularly when considering the average velocities where both the elbow and wrist show far higher velocities; 25% and 16% for the elbow and wrist respectively. It is more pertinent to represent this data graphically to understand this higher exhibited velocity. Similarly, to take away any meaningful conclusions this should be considered with the context of all the motion captured flights for specimen CB.

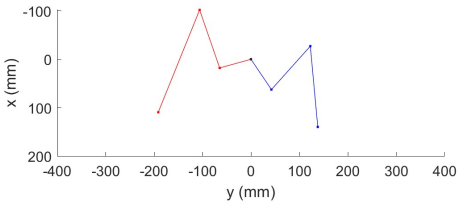
Table 3.4: shoulder, elbow, and wrist joint angles and angular rates for a typical flight of specimen CB common buzzard (*buteo buteo*). Averages are the mean average the median average for the joint angle is inconsistent due to extension variation so is not given.

	Joint angle θ $(^o)$	Angular Velocity ω $(^o/s)$	Angular Acceleration α $(^o/s^2)$
Shoulder			
Min	34.08	7.12	-900.07
Avg	-	167.17	1.58
Max	113.67	807.23	364.14
Elbow			
Min	75.92	5.79	-1124.7
Avg	-	340.65	-10.87
Max	179.71	1137.9	846.13
Wrist			
Min	36.87	6.41	-982.8
Avg	-	501.53	-3.68
Max	178.95	1670.2	596.8

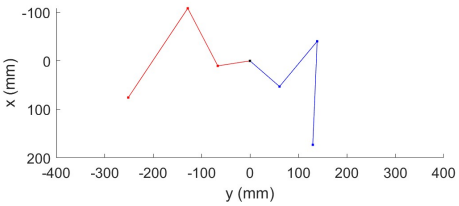
Aligning the independently captured data in time with variable and inconsistent motion will introduce error regardless of the method. Thus, this should be quantified and the impact on conclusions understood. A generally accepted method for this within the field of animal locomotion capture is physical trigger points. An argument could be made that a solution is a take-off pressure pad triggered when the weight on the perch is removed. However, this motion is independent of span-wise retraction of the wing and therefore unsuitable. Three points within the span-wise extension present themselves as a discrete time about which to sync the independent flights. The first at zero extension is the instant the motion starts. However, as previously discussed the marker points about this time are largely obscured by the wing's folds. The maximum extension was also disregarded as it was noted that a number of flights did not achieve this during the initial extension, rather reaching maximum span at some later point. Each flight was therefore aligned against each other flight using the extension mid-point or 50% of the maximum span observed for the species. This proved reliable and later observations showed key points within the span motion aligned in their time domain.

Position data was tabulated for each flight and specimen. Largely this format allowed manipulation of marker points not any meaningful analysis. The tables for each flight included in this chapter are collated in appendix A.

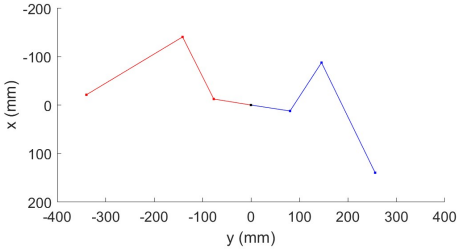
Subsequently, the position of each marker, most notably the primary marker for each wing, provided the highest level of insight into the motion. Figure 3.11 outlines



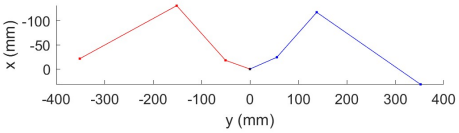
(a)



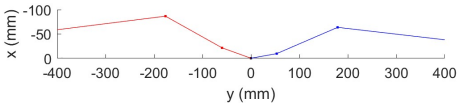
(b)



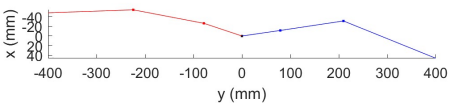
(c)



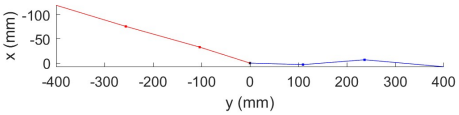
(d)



(e)



(f)



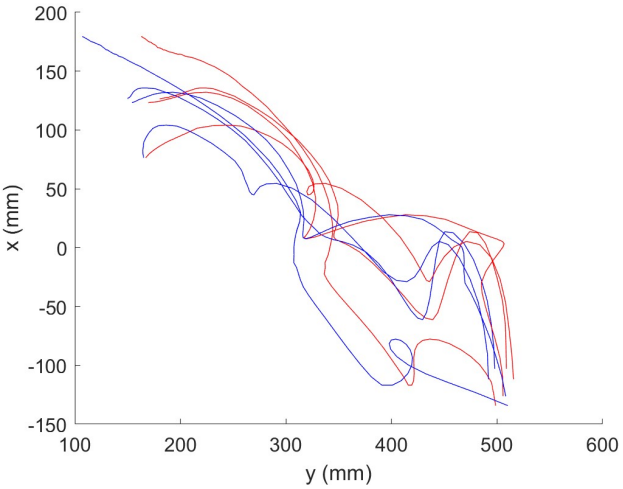
(g)

Figure 3.10: A series of figures presenting the same flight capture data as shown in figure 3.9. Depicted here each point has been rotated onto the span-chord or xy plane to remove flapping motion. This allows a view of planar span-wise extension and retraction of the wing.

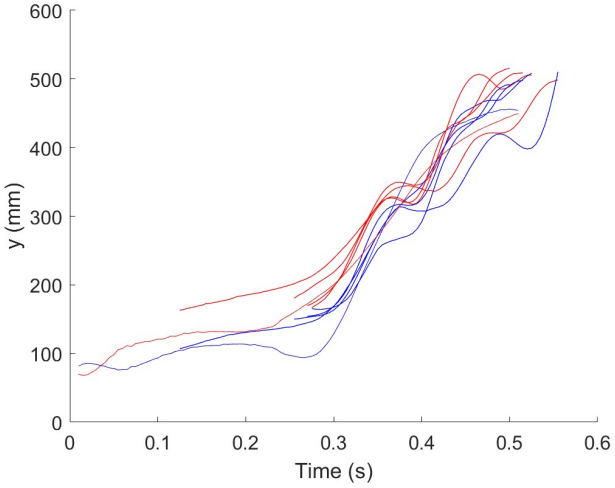
two plots pertaining to the motion of the primary feather marker. Note, left and right wing markers are shown in red and blue respectively. Axis convention used resulted in the left markers being represented by a negative span or y axis value. The absolute y value is plotted for comparison. While it was expected the left semi-spn and right would follow more or less identical motion several differences were observed. These are most apparent in 3.11a. In each paired set of left and right markers the left exhibits a forward, positive x axis, offset over the right. This is consistent across the span motion and the extension time in 3.11b. As any yaw angle offset has been removed from these data set and the offset occurring in multiple fights regardless. It can reliably be considered that this offset is present in the specimen CB.

Over the span motion a defined gradient can be found relating y and x axis motion in the primary marker. This gradient is particularly consistent during the first $150mm$ to $200mm$ of span travel. At approximately $325mm$ in extension the first flight constant deviation from this liner gradient can be seen. Consisting of a $30mm$ to $50mm$ negative x axis perturbation which is then corrected within $50mm$ of span motion. This phenomenon is discussed in further context with the joint angles. What might be considered the least conforming fight in this set is shown as a set of markers with a steeper negative gradient past $300mm$ span to $500mm$. This set is also notable for the reverse y motion in the right wing. This lends itself to the idea that the left wing leads the right for a stability purpose. The reverse motion occurs at the only location where the right wing leads the left. At this point some instability is noted by the specimen and a correction made in the form of right wing retraction. It should be observed that this action represents 0.05 seconds in time and as such is likely to be impulsive. Another consistent feature of each wing extension is a second but more significant forward perturbation. Exhibited in each fight, this occurs within the final $50mm$ or 12% of the span extension. It consists of a forward motion approximately $75mm$, however, in erroneous captured sets this tends to be reduced to $30mm$. That this motion is present despite holistic flight instability leads to the conclusion that this is not an active behaviour. Rather that this action is mechanical in the biological mechanisms comprising the wing structure and actuation system.

Overall the relation between the x and y position of the primary feathers is not unexpected. A gradient and a linear approximation can be used to accurately represent the overall motion. This aligns with the approximation used thus far for looking at joint motion. However, isolating span motion with respect to time shows the inherent non-linearity of the mechanism. Depicted in figure 3.11b two regimes of motion can be highlighted. A low velocity region followed by a region of significantly higher velocity. Interesting to note that the low velocity region is evidently variable in duration. Each flight is synchronised about the midpoint of extension and it is clear during a small number of flights the specimen commenced motion earlier in time to maintain this low velocity period for between 0.1 seconds and 0.3 seconds. This is increased over the 0.05 seconds which represents the median average. As there is no consistency or relation between the varied lengths of time the extension was delayed it is considered that this is hesitancy in the specimen. Given the time variation is below 0.5 seconds it was proposed that this could not be the specimen's active response to external factors. The alternative is that the extension was to be conducted at a decreased pace resulting from external factors. However, the second high velocity region in the extension motion contained no similar reduction



(a) Coordinate position of the primary feather markers over the length of the wing extension. x-axis represented the avian longitudinal axis and y-axis the span-wise axis



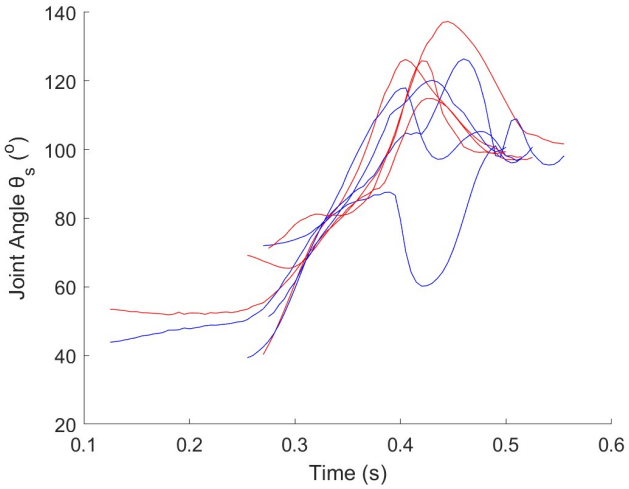
(b) Primary feather marker's span-wise y coordinate plotted against time taken for wing extension.

Figure 3.11: Position based plots for specimen CB common buzzard (*buteo buteo*). Showing the wing extensions captured via IR motion capture. Left and right wings are shown with the left wing y coordinates shown as absolute values, red and blue, respectively.

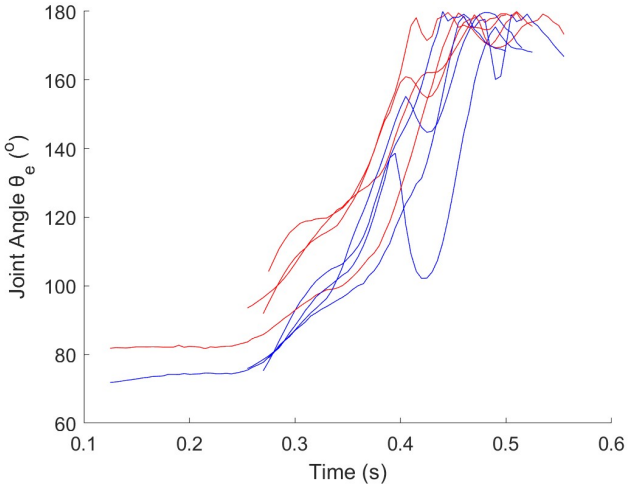
in velocity. This second velocity region, typically the final half of the extension time, is consistent across all flights. Consisting of a gradient of this represents a point average translational velocity of 2000 mm/s or 2 m/s. However, the average misrepresents the dynamics of the motion. The perturbations identified in the xy plots can also be seen here with the first identified at approximately 0.35 seconds into the extension. It is during these deviations from the linear motion that the peaks in velocity can be identified. Peak y translational velocity was found to be 3 m/s during the first perturbation. This significant increase identifies it as a largely span-wise deviation from the linear motion. Whereas the second deviation from this norm represents a greater deflection in the longitudinal direction.

A better understanding as to the source of this span-wise and longitudinal erroneous motion can be seen when considering the components of the primary feather motion. This can essentially be resolved as an inverse kinematics problem. So consideration of the individual joint motion is key. Particular note should be given to the derivations of these joints' rotary motion. Figure 3.12 presents the joint angles for each joint over the time taken for each extension. These are plotted against the same time duration as in 3.11 allowing the time range for each perturbation to be identified. In these figures both the left and right instances of each joint are presented however they have not been presented as the absolute of the value as the angles from each joint are taken about the same datum.

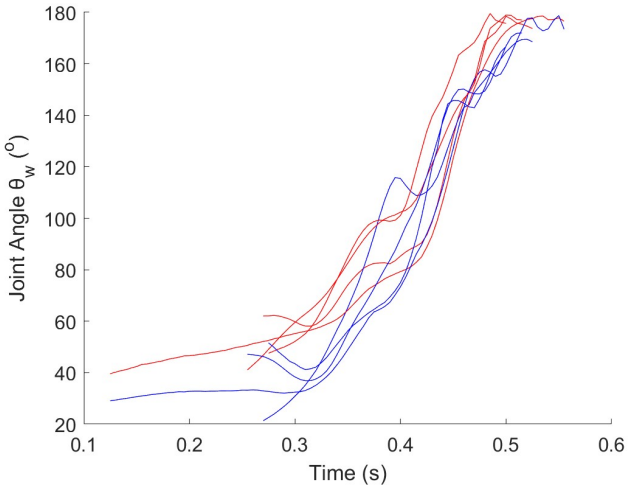
The first deviation, which presents in the span-wise direction, is observed at approximately 0.375 seconds into the extension as presented in 3.11 and 3.12. The corresponding motion predominantly occurs in the elbow joint 3.12b. Manifested as a stationary point followed by a period of high negative gradient reverse angular motion. Notable is the reverse motion, this is not present in all flights. However, the maximum stationary point can be found in some form on each flight. Pre-emptive to this elbow phenomenon is a similar action in the wrist. Not as pronounced, the wrist sees only a significantly reduced gradient and no stationary point. In the corresponding elbow and wrist angular velocity plots, 3.13b and 3.13c respectively, the reduction in velocity is visible for both. The elbow exhibits negative velocity across all but a small number of flights. Including what can represent the peak reverse velocity as shown where a flight included $2500^o/s$ or $415rpm$ of retracting rotary motion. The elbow's deceleration is more varied that that of the wrist so any average would be considered inaccurate. While the wrist shows a two distinct velocity stationary point representing a maximum and minimum change in acceleration. These are separated by an average of $800^o/s$ of deceleration. In general the acceleration data derived from the motion capture is too variable between flights to obtain meaningful comparison. However, figure 3.14c shows clear points for the maximum and minimum acceleration in the wrist at around 0.32 seconds and 0.36 seconds. This all indicates a consistent behaviour within the span-wise extension of the avian. Perhaps the more notable indication towards the nature of this behaviour is in the joint angle figures for the elbow and wrist 3.12b and 3.12c. The reduction in gradient or maximum stationary points are variable in joint angle. This deviation from the linear motion is not consistently occurring at one joint angle. Instead the behaviour is fixed at a time interval. The deviation is therefore initiated as a result of some independent external parameter such as the shoulder joint angle or overall span extension. No evidence of any interaction can be observed in this format of captured data linking this motion to the shoulder. It is also noted that any shoulder



(a)



(b)



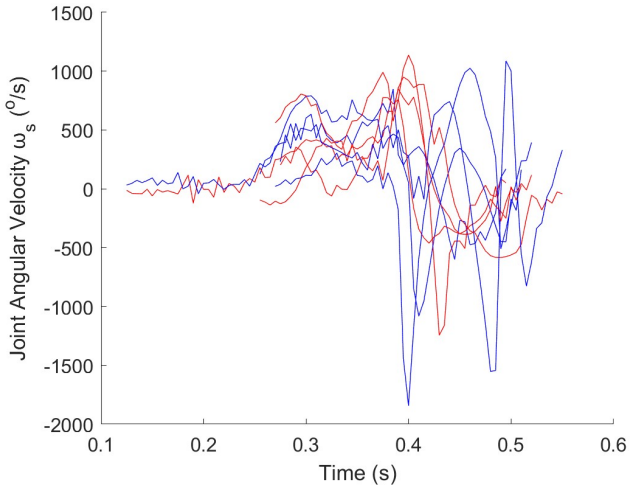
(c)

Figure 3.12: Joint angle plots for specimen CB common buzzard (*buteo buteo*). Derived from wing markers captured via IR motion capture. Left and right wing joints are shown in red and blue respectively. (a) Represents the shoulder angle, (b) the elbow, and (c) the wrist.

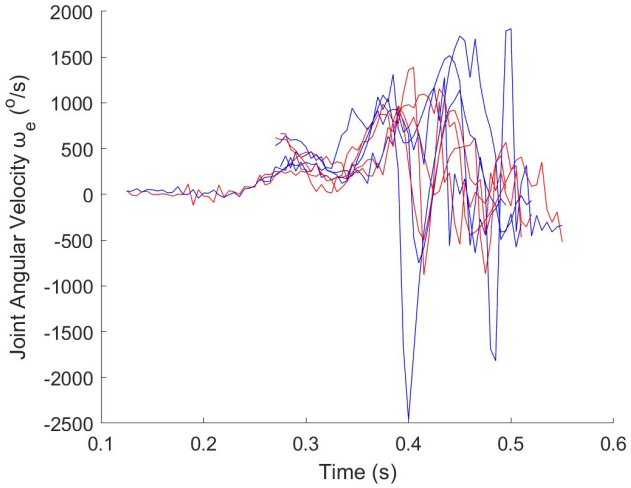
angle change would directly affect the span regardless. Thus, the span position is taken forward for investigation in any engineering application.

The second deviation, occurring in the longitudinal direction, is observed in the final 0.2 seconds of the extension as presented in 3.11 and 3.12. In particular, the nature of this is evident in 3.12a. A significant overshoot occurs in the angle position of the shoulder joint. Typical of an under-damped system and perhaps the most pronounced in the shoulder due to the inertia of the structure under motion. The average overshoot $\delta\theta_s = 22^o$ which represents $\delta\theta_s = 23.2\%$ over the steady state. Notable in this response is the overshoot compared to the settling time. Most flights do not consist of a second oscillation and, including the small number of flights which do, the settling time is noticeably short. Settling time is found to be between 25% and 40% of the rise time. The magnitude of this overshoot allows a reduced rise time. Further analysis may look at the damping coefficient of the joint system. Only modelling of the system and consideration of alternative damping could prove the efficiency of this compromise between overshoot and rise time, as the first joint in the wing structure, the shoulder, affects motion relative to its angle to the body. As a result, once approaching 90^o from the body the predominant effect of motion is on the longitudinal position of the primary feather. This is what is seen in figure 3.11a. The overshoot in shoulder joint angle therefore has a mechanically decreased effect on span-wise motion. In terms of span motion this allows for a decreased rise time and a resultant decreased span extension time. While any negative effects of the angular overshoot are only experienced in the longitudinal motion. As evidenced the kinematics of this system are optimised for reduced time to full extension while performing the take-off phase of flight.

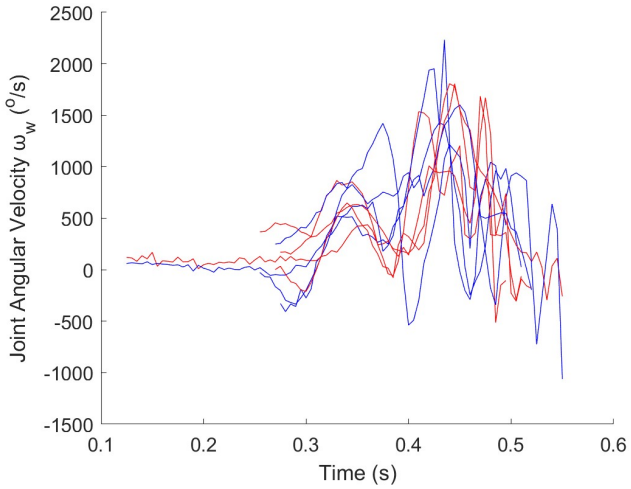
Joint angle relation is perhaps the most fundamental method for the mimicking of this system. Of interest is both the relation of the joints to the semi-span of the wing and to the connecting joints. Semi-span is variable across flights and is dependent of factors such as flight intension or mission, and external conditions. In relating the joints a non-dimensional variable is needed. The % span is therefore used. The target span length can be derived from the joints as the inverse is also true the relation between the two can be used as the kinematic basis of any biomimetic system based on these avian. However, it is necessary to define an average or a representative curve to collate the individual flights. This should also account for variations in the duration of each extension. It was found that for each joint a second or third order polynomial could represent the joint angle data. However, due the range of angles seen at each span length the third order solutions were not considered representative of all flight behaviours observed. It was also proposed that while a single curve was suitable for presenting the joint angle consideration of the errors accumulated was also required. When considering the span-wise data the most significant error arises from the marker axis projection process utilised during the removal of flapping motion. Given that the markers were only projected from a maximum of $54mm$ from the axis and the angle of the wing at these points consisted of a maximum of 9^o. A deviation of $\pm 8.55mm$ can be taken as the error that could result from this process. Representing 1.7% of the total wing span. The method used to account for this discrepancy was to instead base the error on the range of values across the flights. Any accumulative error would then fall within this error range. Figure 3.15 presents both the polynomial curve and error bars for this data set. As can be seen in comparison between the error bars and curve the fit



(a)

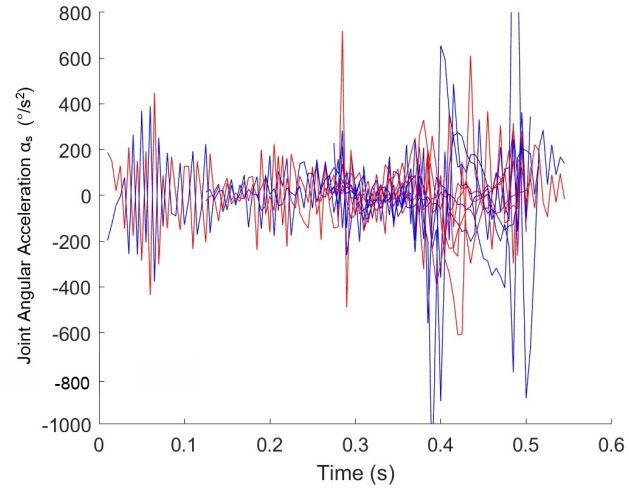


(b)

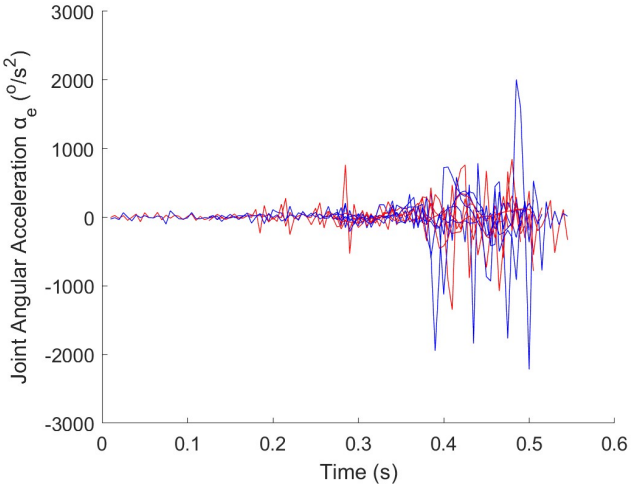


(c)

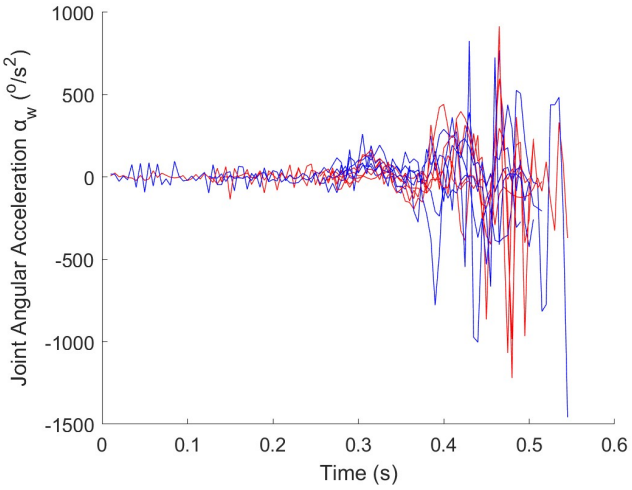
Figure 3.13: Joint angle plots for specimen CB common buzzard (*buteo buteo*). Derived from wing markers captured via IR motion capture. Left and right wing joints are shown in red and blue respectively. (a) Represents the shoulder angular velocity, (b) the elbow, and (c) the wrist.



(a)



(b)



(c)

Figure 3.14: Joint angle plots for specimen CB common buzzard (*buteo buteo*). Derived from wing markers captured via IR motion capture. Left and right wing joints are shown in red and blue respectively. (a) Represents the shoulder angular acceleration, (b) the elbow, and (c) the wrist.

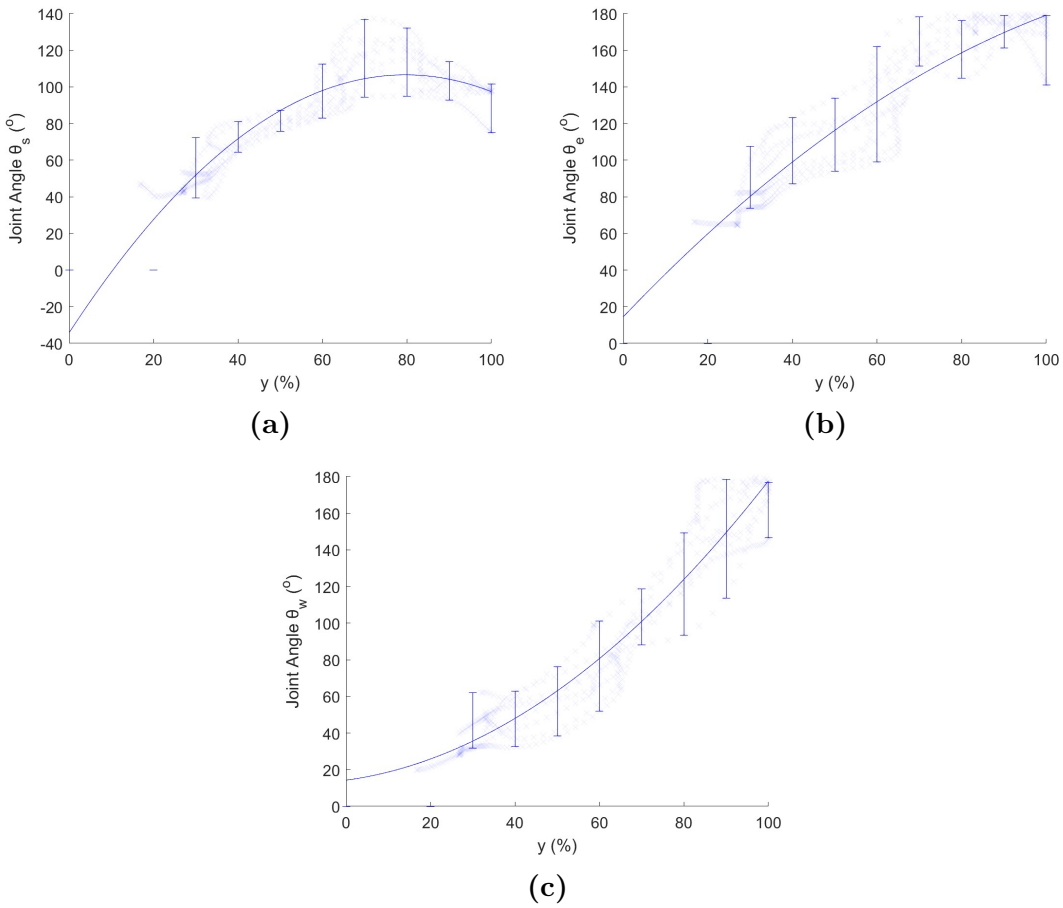


Figure 3.15: Joint angles, for specimen CB common buzzard (*buteo buteo*), plotted against wing semi-span as a percentage of maximum span length. Overlaid are the range bars denoting the uncertainty in the angle at each span location. This range is driven by the individual motion captured flights plotted transparently.

is largely representative. each joint curve falls within the uncertainty range defined by the bars with the exception of the elbow. This aligns with the first perturbation mentioned. However, this does not translate into the wrist joint as might have been expected. Similarly, the bar shown at 60% on 3.15b represented the greatest uncertainty resultant from the same source. Another abnormally large uncertainty can be seen at 70% in 3.15a. The cause is perhaps more apparent as this results from the second-order polynomial failing to accurately represent the overshoot exhibited in the shoulder motion.

3.6 Avian Kinematics Conclusion

Presented in this chapter was an experimental approach to collecting results pertaining to the in vivo kinematic motion of avian. A novel approach to physical marker placement was presented and evaluated. Upon which a series of infrared motion capture experiments were carried out. The flights largely consisted of specimens of the order *Accipitriformes*, specifically the family *Accipitridae* with some including owls of the order *Strigiformes*. Flight manoeuvres of interest were straight and level

flight with and without flapping, turning flight, and perching. Another area of kinematic motion explored for application into morphing aircraft structures was wing extension from a retracted state. This, in particular, was explored for applications as it is related directly to pertinent literature in the area of avian skeletal motion. However, it provides a novel insight into the dynamics of the systems previously studied statically.

While the motion capture technology is widely used in both industrial applications and in the study of biological systems, the application in avian has been seldom satisfactory. Ground-based locomotion has been employed with physical markers; however, flight has previously been limited. This has led to significant innovation in non-contact or marker-less capture processes. These are considered in the context of a full infrared system. During which it was found that when physical errors are mitigated, infrared presents significantly increased spatial resolution with similarly reduced positional marker error. Marker placement represented the largest potential for physical errors. These include incorrect or inconsistent marker position relative to target biological features, dynamic instability of the markers relative to the body, and marker obstruction. A methodology utilising a standard infrared capture marker technology of spherical rubber coated in retro-reflective tape proved effective. This was augmented using low-tack or non-permanent rubberised adhesive to provide a temporary bond onto the avian. Varying the strength of the adhesive, which is industrially most commonly used in temporary, stationary adhesion, ensured a consistent and stable marker placement regardless of location on the avian or feather coating.

Capture data collected of wing extensions was focused on the span-wise motion of the semi-span. This presents the most applications in biomimetic morphing structures. Resultantly, flapping motion was mitigated and then removed through manipulation of the flight via setup of the specimen and post-prepossessing, respectively. This was considered effective, and errors were quantified in the analysis of the effect on span-wise motion. The extension motion was found to be consistent between flights, while the avian presented a range of flight missions during testing. Despite the varying motivations for each flight, some features of the extension remained unchanged. Similarly, the differences in aspects of the expansion that changed were quantified and, where possible, related to other aspects of the motion. Arguably, the feature of most interest is the identification of features similar in presentation to control theory. Motion was observed in the shoulder joint angle which conformed to the behaviour of an under-damped system. It was noted that this allows a decreased rise time, the time taken for the joint to reach the desired angle. Presenting evidence that the extension option is optimised for rapid reaction. While the negative impacts of the overshooting which results from this are mitigated through the mechanics of the system.

Chapter 4

Span-wise Morphing Concept Development

Morphing structures are continually being proposed, each with unique characteristics and specifications. Progress is therefore producing systems that can be realistically produced as full-scale aircraft. However, the methods and designs that are currently being proposed as concepts for small-scale tests can deviate more significantly from conventional fixed-wing and aft-tail aircraft. This chapter sets out to propose a morphing aircraft, which demonstrates significantly increased adaptability through the use of a highly variable structure. This highly span-wise morphing concept was conceived to replicate the lateral motion of bird wings in flight. The application of the previously derived kinematics onto this structure will allow a conclusion to be proposed as to the effectiveness of avian style morphing on a human-designed aircraft. The subsequently proposed span-morphing concept is then compared to existing morphing aircraft and more traditional aerofoil sections. These comparisons are based on computational fluid dynamics (CFD) results, obtained through two independent methods. Firstly, a two-dimensional panel method is used to determine the viability of using a biologically derived aerofoil section. Secondly, a conventional CFD meshed analysis based on the numerical analysis of the Navier-Stokes equations to ascertain the viability of the unique structure before further physical testing is conducted.

4.1 Concept Development

The avian span-wise morphing concept consists of three structural members of lengths determined from review of the ratio average for bird of the *accipitriform* order. Allowing for a semi-span to be set according to external factors, such as mission-specific size restrictions, while still retaining the large range of morphing demonstrated by avian. The concept presented has a semi-span of 900 mm, with a *humerus* analogue of length 240 mm, *radius/ulna* of 270 mm, and *Carpometacarpus* of 390 mm. These segment the wing structure into three discrete sections: inboard, analogous to the upper arm, a mid-section for the forearm, and an outboard resembling the wrist/hand of the avian. The connecting joints themselves are simple radial bearing joints. The joint design is comprised of two needle roller bearings per joint, the backlash and motion due to the fit of these joints is measured in chapter 6. The joints allow only one degree of freedom (DoF) about the vertical axis. The



Figure 4.1: Computer aided design rendering of the jointed structural members forming the mechanical system for span-wise retraction. Omitting the aerofoil skin trailing edge plates, electrical, and pneumatic systems. The positioning of the two pairs of pneumatic artificial muscles is shown, in both the wing mid-span and the fuselage.

target for available motion in the wing-arm was 3 DoF, allowing full motion and position control. Defined using Gruebler's equation (4.1) for both a 2-jointed and 3-jointed arm, the DoF is 3. It is common for concepts to omit this last linkage for this reason. However, the additional extension directly resulting in a greater semi-span necessitates its inclusion.

$$DOF = 3(n-1) - 2L - H \tag{4.1}$$

Where n is the number of members in the system, L is the number of lower pairs (joints with one degree of freedom), and H represents the number of higher pairs (joints with two or more degrees of freedom). Actuation was obtained through the use of Pneumatic artificial muscles (PAMs) found via review in chapter 3 to be the most reliable muscle analogous actuation. The application of PAMs also has advantages specific to the three-jointed structure. The implication is that the PAM muscles can be located inside the structure of the wing itself due to the low mass of the pneumatic muscle body itself placing little additional loading on the structure. Holding force is a secondary advantage alongside low mass, as the internal volume of the aerofoil section is limited. This resulted in large disadvantageous moments against the muscles that are accounted for through the over-specified force of the PAMs. Similarly, to the force, actuation frequency was a consideration in the selection of pneumatic muscles, particularly over shape memory alloys.

Two antagonistic pairs of PAMs provide actuation for the system. The individual PAM, which each acts as a muscle substitute, contracts, producing a moment about the associated joint. Thus, the pair provides both a clockwise and counterclockwise actuation. Mechanical mechanisms developed for transferring work from PAMs have been extensively developed in the robotics field. This, as discussed, is due to their

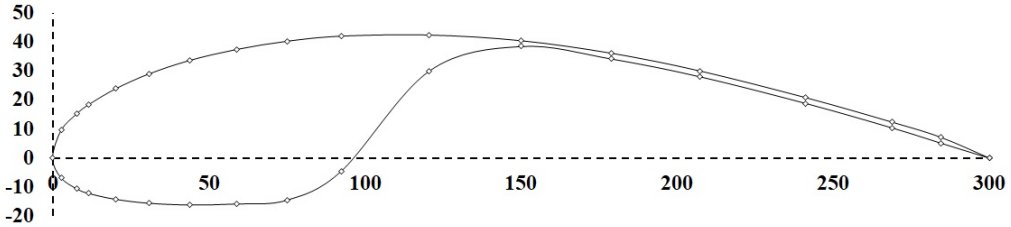


Figure 4.2: Proposed concept aerofoil

application in 'soft' robotics. There have been a number works applying these to actuation in aircraft. Woods et al [153] introduced a concept for control surface defection using a similar pair arrangement. This concept is explored further in section 5.2 as it has implications on the control of the actuators and subsequently the wing. The two pairs correspond to the shoulder joint and elbow joint equivalent, with the latter also actuating the wrist, by means of the 'twin parallels' mechanism. The use of this mechanism, as shown in figure 3.2, was a development aimed at reducing complexity in the actuation system. Obvious advantages include the reduction in the number of actuation muscle pairs required allowing a full three jointed actuation with a third reduction in actuators. Significantly, this eliminates the need for any systems pneumatic or electromechanical in the two outboard sections of the wing. Thus, reducing wing loading results in reduced wing mass due to structural redundancies. The reduced mechanical complexity enables a low internal volume wing section to be employed which more closely matches traditional aerofoil sections or the sections derived from avian.

The aerofoil section used replicated the characteristics of the *accipitriform* avian [137], and as such was based on the Wortmann series, specifically the FX 60-126. Exhibiting both high lift at low flow velocities and an increased stall angle of attack. Alterations were made to the thickness of the leading edge to allow for the incorporation of the elbow PAM actuators and additional mechanisms for skin actuation and sensor integration. The application of the FX 60-126 profile in this leading edge of the section allowed for this increased thickness. Aft of a third chord the section follows the flat plate principle from Carruthers with the upper surface geometry of the FX section. Thus, the concept aerofoil section has a final; 15% thickness and 4% camber. As a result of these modifications it was decided that further panel method-based aerodynamic evaluation was required alongside the CFD for validation purposes. Figure 4.2 shows the aerofoil section produced as the aerofoil section implemented.

To implement the aerofoil section onto the structural members the leading edge was isolated from the plate trailing edge. This allowed it to be rigid, akin to more conventional wings and more effective under aerodynamic load. Three of these D-spars correspond to each of the structural members. Pre-stressed flexible inserts consisting of a silicone sheet derivative were proposed to be used between the spars to ensure a consistent surface while actuated.

The trailing edge of a bird wing is formed on primary and secondary feathers which are directly rooted in the bone structure. These overlap during retraction due to the compliance of the individual feathers. This was essentially mimicked to produce the same effect but using 13 rigid curved plates which is shown in figure 4.3. The secondary feather analogue plates remain parallel to the body of the

aircraft, allowing the trailing edge plates to stack out-of-plane. This parallelism is maintained by the twin parallels mechanism as the plates are pin jointed to the leading structural member but only fixed laterally on the second member, resulting in the plate maintaining the desired angle.

The primary feather analogues, of which there are 3, are fixed to the outboard structural member and do not retain parallelism. This is due to the increased mechanical complexity of their actuation. Resultantly, the distribution of the plate is notably sparser than the inboard sections because of the interaction with these sections during retraction. This spacing was deemed acceptable compared with Hawk and Kite wings, which share similar characteristics. These plates were also given closer inspection during the CFD analysis.

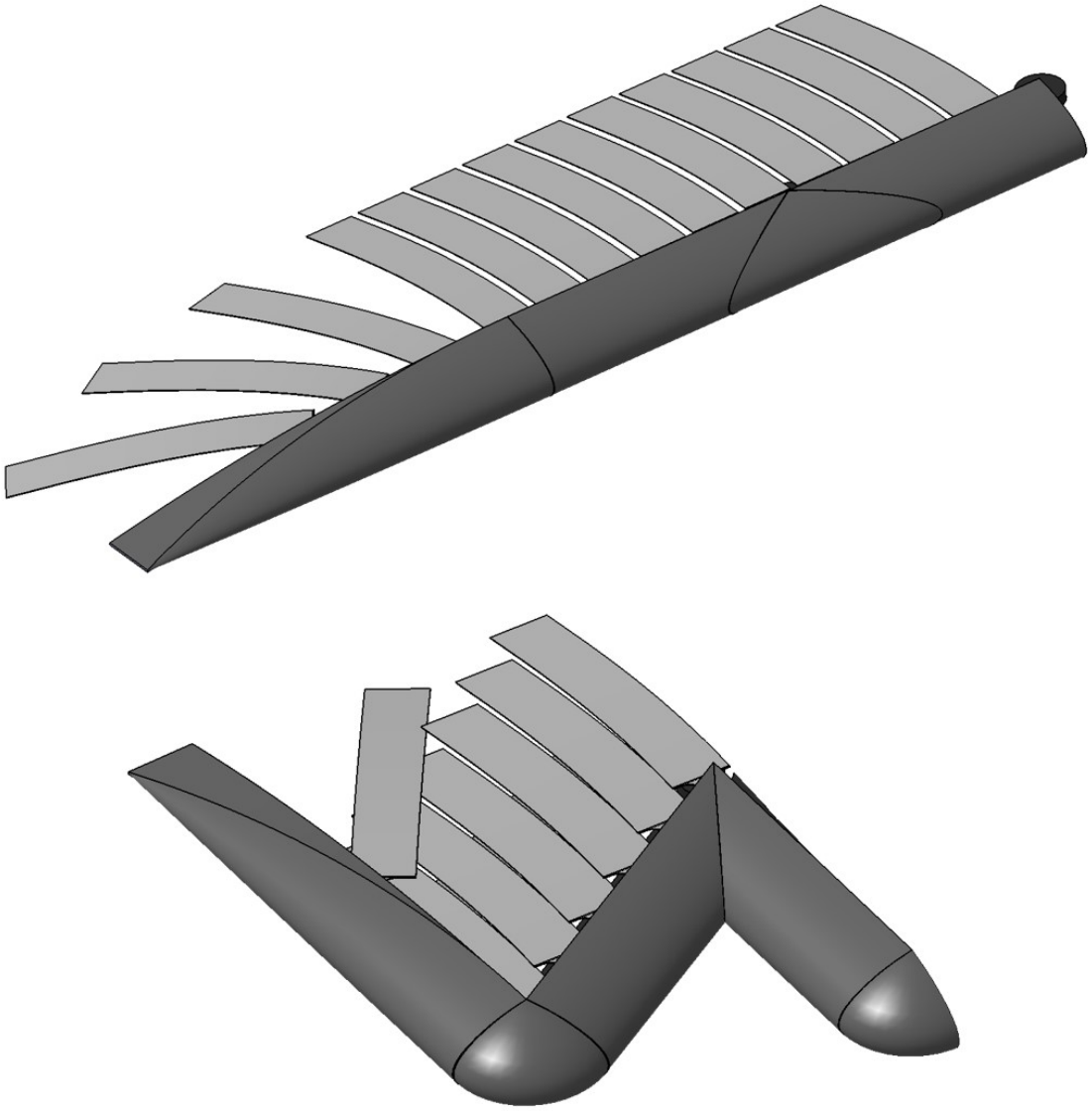


Figure 4.3: Computer aided design drawing of the avian span-wise morphing concept. Extended (top) and full retracted (bottom)

The in-board section of the wing intentionally retracts into the body of the

aircraft, with the aim of reducing the complexity. This also allows the section to morph 90° in relation to the aircraft body. On the other hand, the elbow analogue joint has a maximum rotation of 110°, which is limited by the strain of the actuators, as this is directly related to the volume of the PAMs that are required to be internally housed in the leading edge D-spar. Similarly, with the aim of reducing complexity, the lower surface of the wing where the leading edge connects to the trailing edge plates was left exposed. While this is expected to produce increased parasitic drag, the reduction in weight and points of failure are set to offset this increase.

4.2 Preliminary Computational Fluid Dynamic Analysis

XFoil was used to enable a comparison between the derived aerofoil section and the original bird wing that is represented by the Clark-Y section, which was found to be similar in thickness and camber. Initially a bird aerofoil was considered. Avian aerofoils are typically thin [137], around 5% to 12% of the chord, this was not feasible as commercially available PAMs could not be found in these thicknesses. The proposed aerofoil was panellised $n = 200$ which resulted in a maximum panel angle of 4.6°, see figure 4.4. A viscous flow setup with 4-5 Reynolds number values in the range of 5×10^5-1×10^6 were used to represent best the slow flight that would be typical of a small aircraft using this wing. Angles of attack (alpha) were increased until stalling occurred, and lift and drag coefficient values were recorded for each angle.

A three-dimensional CFD simulation was also conducted with the view of verifying the Xfoil results, and more realistically modelling the drag coefficients for the wing by modelling the span-wise changes in geometry necessitated by the actuation mechanism. This was also used as an opportunity to explore the need for a flexible lower surface connecting the leading edge and trailing plates.

A steady flow was employed as is typical, and the values for the different span-wise extensions were obtained individually. This also allowed for the assumption that the flexible interfaces between the sections were rigid. Deformation of these flexible materials is expected; however, it was concluded that the aerodynamic impact at this initial stage would be negligible. Star CCM+ was used for all three-dimensional CFD simulations. The model used for the CFD consisted of only the aerodynamic surfaces; the internal muscle actuator mechanism was omitted from the model. The omission of the internal mechanic reduced the mesh size and complexity, leading to increased mesh quality characteristics and subsequently a more reliable convergence.

The mesh consisted predominantly of a polyhedral volume mesh with a resolution down to 1mm maximum surface size. A wake refinement was also used to ensure sufficient definition of turbulent flow, this is shown in figure 4.5. Boundary layer meshing was done using a prism layer allowing for a finer mesh. The prism layer used a target cell size of 0.1mm. In order to ascertain if the proposed mesh would produce a reliably and accurately converging set of residuals, mesh quality characteristic values were defined; these characteristics included face validity, skewness angle, and cell volume change. Literature in the field has defined guidelines for acceptable values of mesh quality [154, 155], all of which were met for each simulation. While most of these values are provided by the CFD package and are unrelatable, all fall

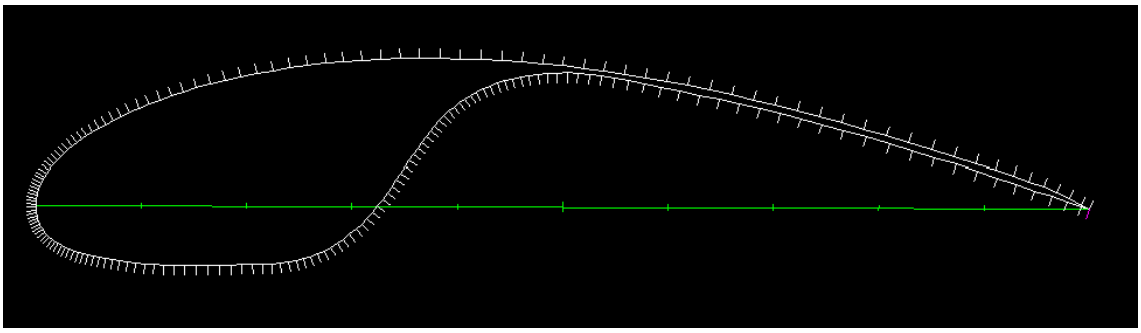


Figure 4.4: The proposed aerofoil as panellised in XFoil, 200 **panels were used in the viscus analysis.**

in the 99th percentile for validity, and the maximum observed cell volume change was 0.5, where 1 is no change and less than 0.01 is unacceptable. Skewness was measured non-orthogonality and determined to be on average 5° with a maximum of 82.1°, with a generally accepted limit of approximately 85°.

A k-epsilon turbulence model was used with low y+ values at a Reynolds number of 1×10^6 to reduce the possibility of low Reynolds number inaccuracy. Convergence was achieved with steady residuals for each angle of attack within 2000 iterations. Similarly, to the Xfoil plots, the values for a Clark-Y aerofoil have been plotted alongside the CFD coefficients for comparison. These have been plotted in figures 8, 9, and 10. Two extension configurations were modelled, fully extended and fully retracted. Although the retracted results were not completely comparable (due to significantly different geometries) with the base aerofoil, the results aim to show the difference in lift generation.

As expected, the Xfoil results show similar coefficient values. This is due to the assumptions and the similarities between the aerofoils. These are shown in figure 4.7. The increased lift produced across all angles of attack can be explained as a result of the greater camber of the proposed section. Similar lift curve slope gradients is further evidence that these differences can be attributed to camber. Similarities in the drag plots are due to the simplification of the geometries. However, the Clark-Y does produce lower drag at angles of attack lower than five, suggesting the complex geometry of the lower surface has a greater impact at lower dynamic pressures.

The proposed bird wing-influenced aerofoil also exhibits stall at a higher angle of attack than that of the Clark-Y. This can again be attributed to the increased camber. However, this is significant, as birds have been shown to perform and use manoeuvres at high angles of attack [137], often to exploit the increased drag inherent at such angles for manoeuvres such as perching.

Figure 4.9, shows the lift coefficient for the full wing semi-span. While the results for the retracted configuration are low, this is expected. The extended wing, however, is also similar to the Xfoil values but with stall occurring past 16^o. This increase in critical stall angle is due to an unforeseen effect of the lower surface remaining uncovered. Airflow was observed 'leaking' through to the lower pressure above the upper surface, with the consequence of encouraging laminar flow over the wing. Thus, effectively mimicking a leading-edge slat at high angles of attack, this flow is shown in figure 4.6. Figure 4.10, illustrates the significant difference between the full analysis and the Xfoil results, as well as the Clark-Y results gathered from literature. At low angles of attack, the drag coefficient for the extended wing is only

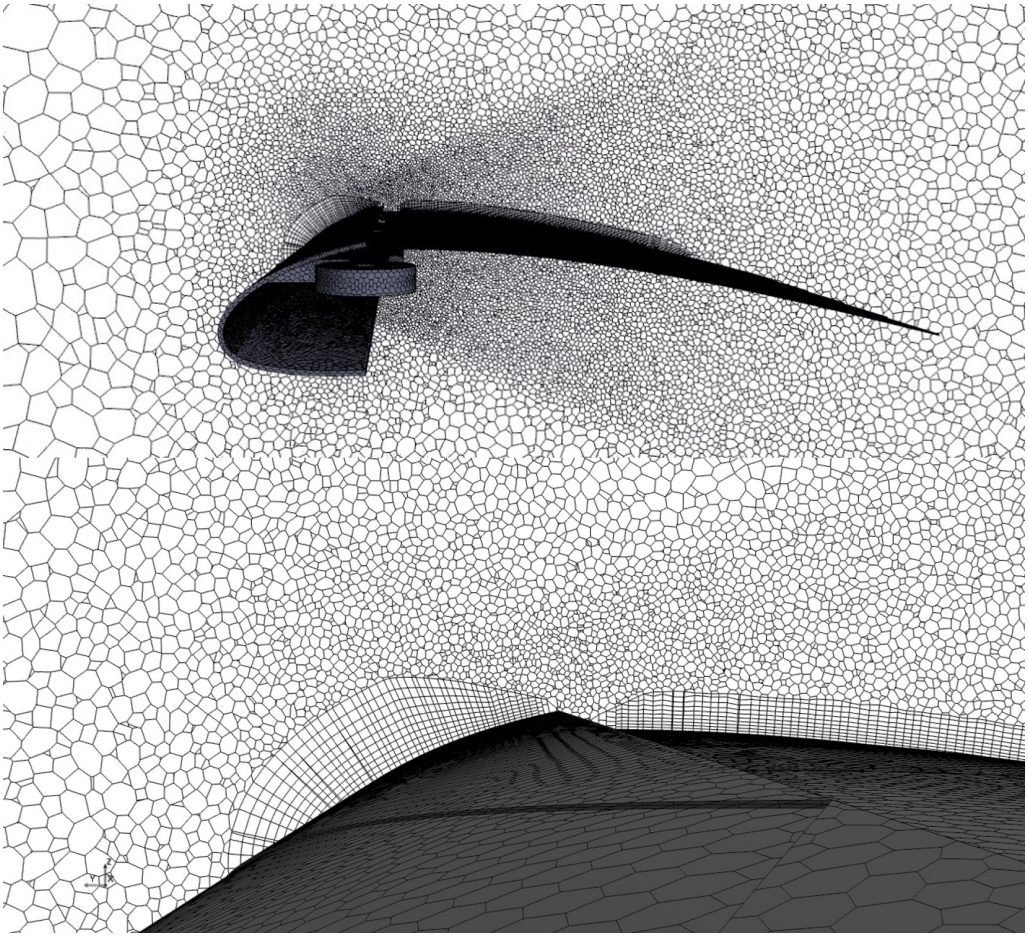


Figure 4.5: Shown is a plane section of the volume mesh taken at approximately 50% of the semi-span. The first view shows the wake refinement and volume gradient producing a finer mesh closer to the wing surface. The secondary view gives a closer illustration of the prism mesh used to obtain a suitable mesh sizing to resolve the boundary layer.

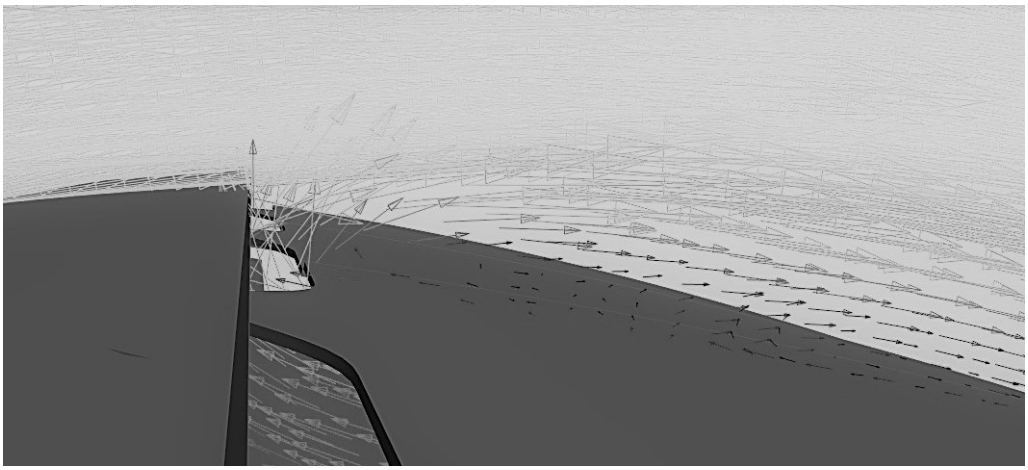


Figure 4.6: The velocity vectors for the flow over the upper surface of the concept, showing the 'leaking' airflow.

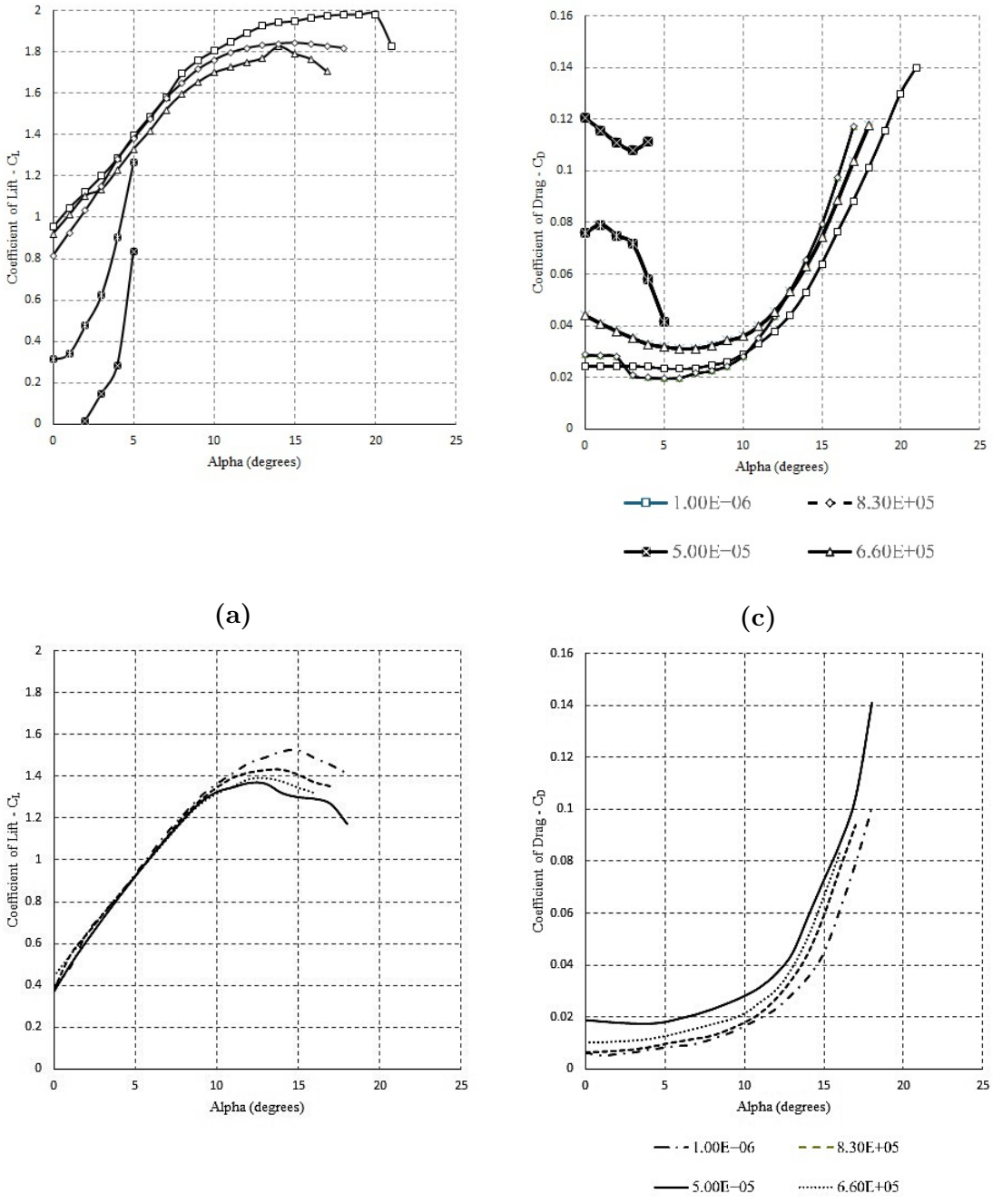


Figure 4.7: XFoil plots for the avian-based proposed aerofoil and Clark-Y results produced by C. Lyon et al [156], used for comparison. Avian-based section, (a) and (c) plots showing the lift and drag coefficients, respectively. Clark-Y, (b) and (d) plots showing the lift and drag coefficients, respectively.

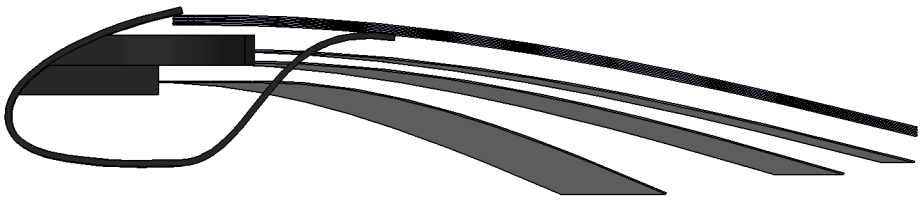


Figure 4.8: The concept section showing the proposed interfacing section aft of the leading edge D-spar, which will be investigated further in future research.

slightly increased from the base aerofoil, which, with the complex geometry, was expected. The divergence at increased angles of attack, however, suggests a lower surface interface between the leading edge and the plates is required. This is despite the extra complexity, with the weight and number of failure points increasing.

Modelling of a flexible interfacing member between the lower edge of the D-spar and the upper surface plates has been carried out. As shown in figure 4.8 the component mimics the profile of the avian wing more closely and better matches the preliminary Xfoil aerofoil shape. The complexity arises from the requirement for the member to move similarly to the leading edge, without impeding the retraction of the structural members or the upper surface plates. These will form the basis of the work going forward. Further to this, before the verification of the concept and preliminary results through wind tunnel modelling, an unsteady analysis of the actuation between the extended and retracted states could be carried out. The production of the prototype will lead to the integration of a control system utilising significant wing area morphing. Parallel work looking at the kinematics of bird manoeuvres will be employed to provide a basis for this control system. Wind tunnel studies into the aerodynamic effects of the manoeuvres and parameters such as roll rate and centre of gravity changes will inform the limits of this concept in uncrewed aerial vehicle applications.

4.3 Conclusion on the viability of the proposed concept

An avian span-wise morphing concept was presented, which can morph from its extended 900 mm semi-span to a retracted 225 mm. The 75% reduction in semi-span length results in an aspect ratio change of 1.45 (2.45 extended to 1 retracted), while inciting a planform area reduction of approximately 85%. Initial CFD results were introduced and presented in comparison with a Clark-Y aerofoil representative of the avian section on which the concept is based. These results suggest that the aerofoil design produces increased lift coefficient performance. However, slight modifications are required to reduce the drag before a prototype is presented for further wind tunnel verification.

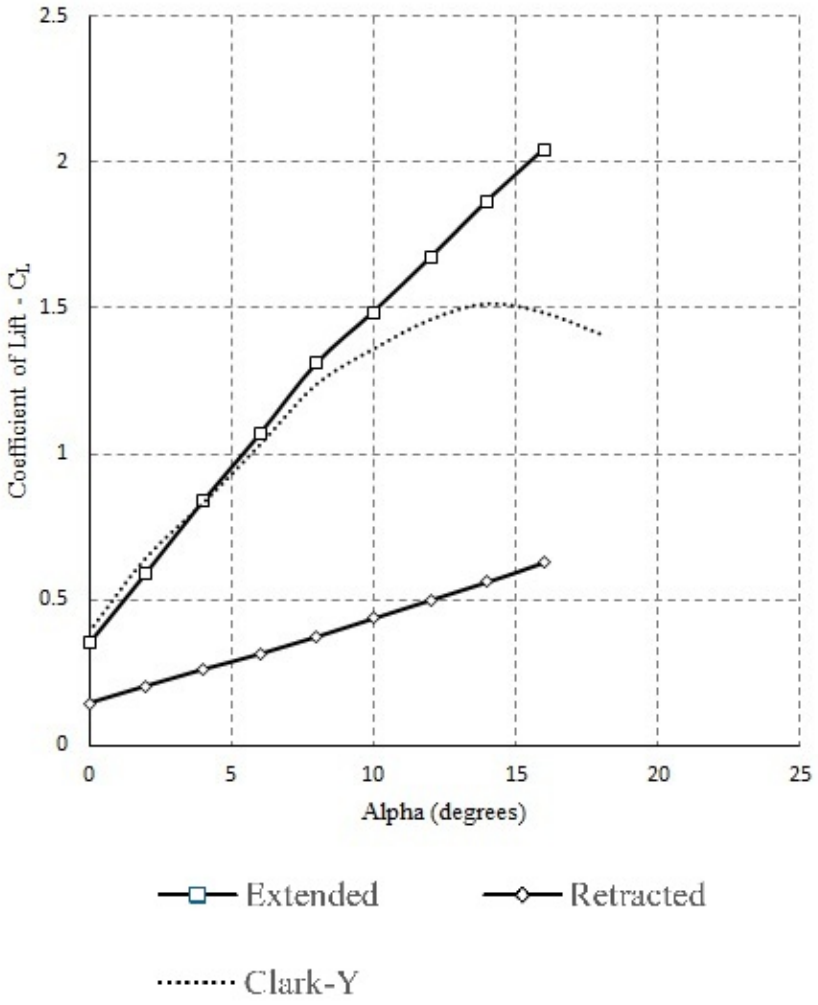


Figure 4.9: Lift coefficient change with angle of attack, results from the three-dimensional computational fluid dynamic analysis. Clark-Y results produced by C. Lyon et al [156].

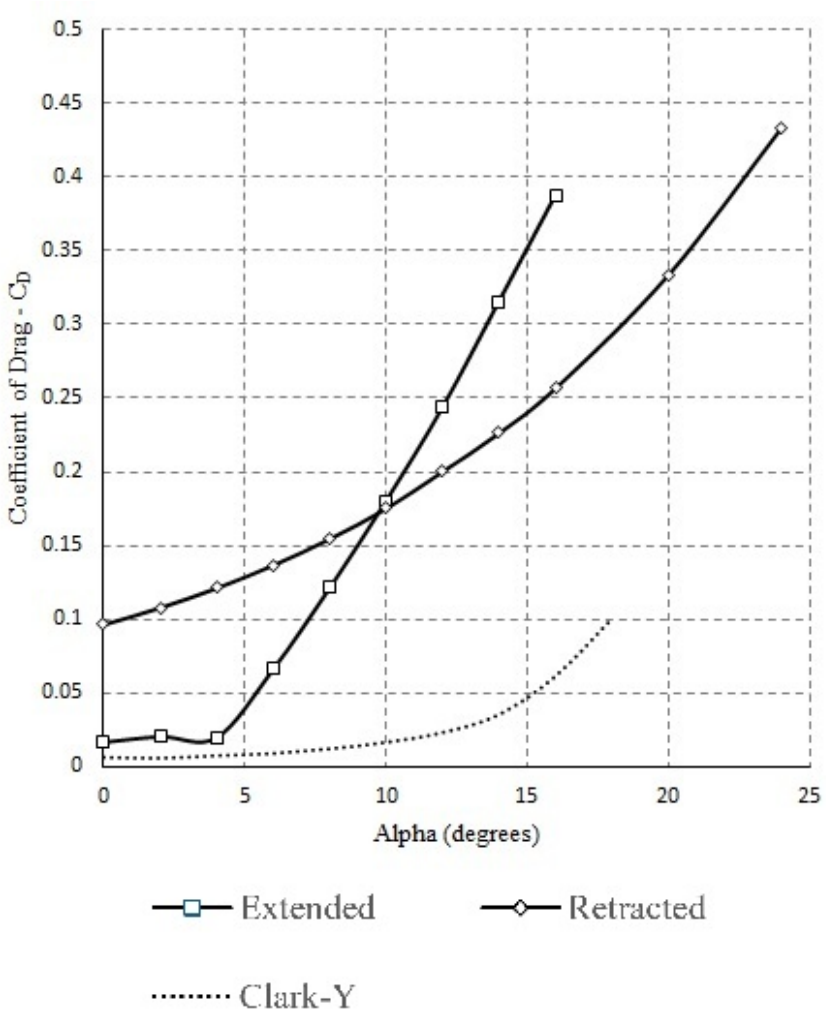


Figure 4.10: Drag coefficient change with angle of attack, results from the three-dimensional computational fluid dynamic analysis. Clark-Y results produced by C. Lyon et al [156].

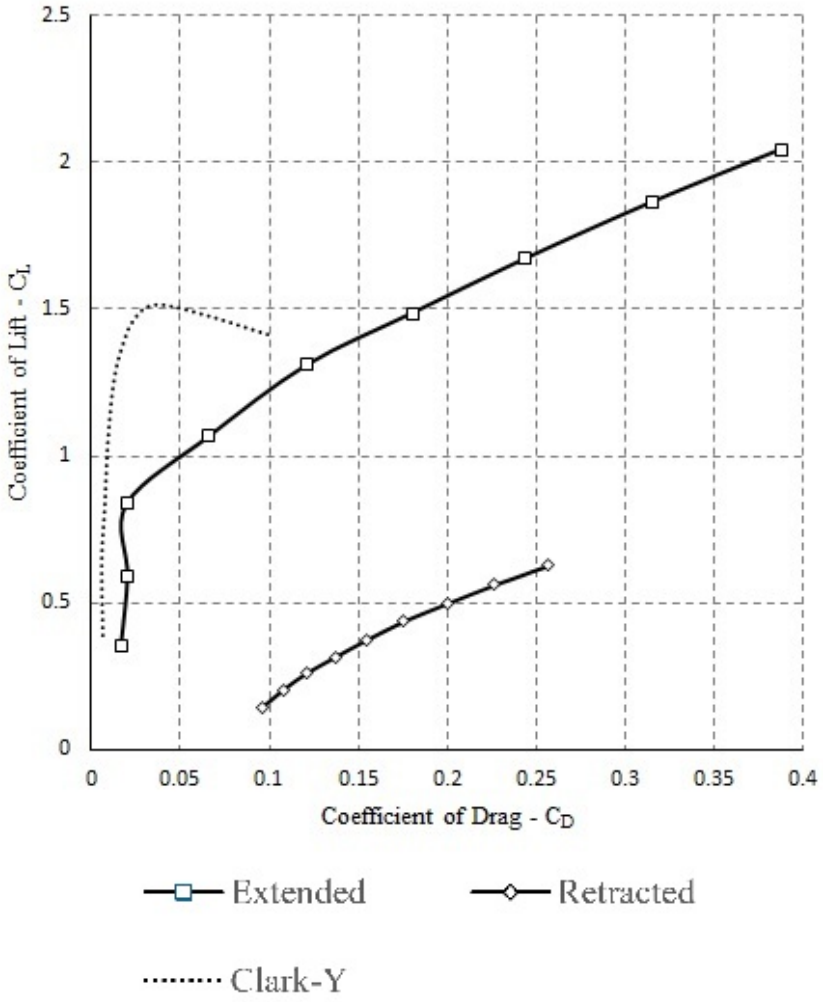


Figure 4.11: Lift coefficient change against drag coefficient, results from the three-dimensional computational fluid dynamic analysis. Clark-Y results produced by C. Lyon et al [156].

Chapter 5

Concept Modelling and Control

The development of a control system is a vital part of a dynamic concept's development. A method for control is particularly important in the presentation of a morphing aerodynamic structure as the actuation of the system is the primary method of introducing the morph. The benefit of the morph directly relying on the accuracy and precision of the actuation. The method for achieving this control is the development of a model and applying a form of control using different methods until the desired characteristics are reached. Presented in this chapter is this process in the context of a highly morphing structure a span-wise morphing concept developed to take advantage of the up to 100% morphing of avian wings. The concept utilises highly nonlinear pneumatic artificial muscles (PAMs) arranged in two dependent pairs of antagonistic muscles, allowing actuation of three revolute joints. These joints form the kinematic structure of the wing, and an inverse kinematic model of this mechanical system is presented in series with an actuator model. Derived from previous works this model produces a wing tip position with 2 DOF, then related to wingspan and sweep angle. The control system is then derived using conventional methods. However, the desired dynamic system characteristics are determined through the observations of avian wings. In vivo kinematic data was captured from birds in flight using infrared motion capture tracking markers positioned on the avian body and wings. This data is then analysed to produce the dynamic response of the bird wing during different types of extension. Finally, in this chapter, the PAM system is matched to reproduce the characteristics of the avian studied.

In order to develop a biomimetic avian wing skeleton, a suitable model to explore the dynamics of such a system should be produced. Thus, a kinematic-based model relating skeletal and wing parameters was developed to demonstrate the extension and retraction of an avian wing.

The avian extension model is built to produce a generic avian profile, with simplifying assumptions to this effect. Specific avian characteristics can be implemented with no significant code changes; this is verified with a test avian *milvus milvus*(Red Kite). *Milvus milvus* was chosen for exhibiting both efficient gliding flight and high manoeuvrability, particularly in diving manoeuvres, it is also common in the area and so easily observable. Avian wing skeletal structure is relatively consistent between species, consisting of an *Humerus, Ulna* and *radius* pair and *Carpometacarpus* as shown in figure 3.1. Bone dimension change between species can be input into the model, *Milvus milvus* dimensions are shown in table 3.1. These are the mean

average of measured results of the Natural History Museum's specimen 1940.7.6.1 and research data. [132]

2D kinematics were sufficient to model the span-wise and chord-wise positions of the semi-span extension. A method applied in robotic control systems, particularly robotic arm applications, was appropriated due to its simplicity and comparability to the avian wing system to be modelled. The Denavit-Hartenberg [157] method of notation uses matrix algebraic operations to produce an overall position coordinate for an end point of a robotic arm. Joints in the system each define a coordinate axis relating to the previous. This analytical tool formed the basis of direct kinematics the procedure of calculating a position using known joint angles.

5.1 Kinematic Modelling

This section is divided into two subsections: the kinematic modelling and the dynamic. Although the latter is very much dependent on the former, each is better presented independently. Regarding the kinematics, significant mention of the physical structure and its biomimetic inspirations has been made in previous sections and will be reiterated somewhat here in the control system context. The initial static modelling through common methods in robotics systems is presented before their implications on the control of the system are addressed. The biomimetic solution is then explored, and its impact on the system behaviour is assessed.

5.1.1 Denavit-Hartenberg notation

The Denavit-Hartenberg notation defines the four parameters; $a_i, d_i, \alpha_i, \theta_i$ governing joints in a system fixed at one end. D-H parameters populate a transformation matrix derived from equation 5.1 for links *i to i-1.* The parameters relate to the skeletal structure as shown in figure 3.1, while specific *Milvus milvus* values are shown in table 3.1. The derived transformation matrix 5.2 shows link offset d_i and link twist α_i values which can be dropped out to increase simplicity as they are not needed to model the system effectively. General avian characteristics can be input to the model and each demonstration *Milvus milvus* parameter was input at this point. The joint angles input θ_i are calculated through simple assumptions made about the wing's movements. It is assumed the shoulder joint θ_1 rotates 90° from flush with the body to fully extended; this assumption is based on observations of gliding birds with a greater aspect ratio. The elbow θ_2 and wrist θ_3 joints are then related to θ_1 by -2θ and θ respectively, these relationships are based on observations and research into the variable wing span of gliding birds [127].

$$A_i = R_{z,\theta_i}\ Trans_{z,d_i}\ Trans_{x,a_i}\ R_{x,\alpha_i} \tag{5.1}$$

$$^{i-1}_{i}T = \begin{bmatrix} c\theta_i & -s\theta_i\ c\alpha_i & s\theta_i\ s\alpha_1 & a_i\ c\theta_1 \\ s\theta_i & c\theta_i\ c\alpha_i & -c\theta_i\ s\alpha_i & a_i\ s\theta_i \\ 0 & s\alpha_i & c\alpha_i & d_i \\ 0 & 0 & 0 & 1 \end{bmatrix} \tag{5.2}$$

The transformation matrices are, in turn, multiplied to produce a matrix for each joint within a common coordinate axis. Where the end position is defined by a matrix which is the product of each link transformation matrix in turn:

$$^{shoulder}_{wrist}T = T_{shoulder}.T_{elbow}.T_{wrist} \tag{5.3}$$

Values $a_{1,4}$ and $a_{2,4}$ within each joint matrix are the common coordinate positions for that joint, x, y, respectively. Thus figure 5.1 shows the resulting plot of each joint and link at $\theta = \pi/4$, within a range $0 \leq \theta \geq \pi/2$.

5.1.2 Wingspan simulation

In order to produce a model with semi-span as the input the model required inverting. However due to the trigonometric ratios used within the transformation matrices simple rearrangement is not possible. Another mathematical process used for similar situations in robotics is inverse kinematics; this could be used to resolve this issue. Advancements in computational approaches have also been implemented in the field of inverse kinematics, including fuzzy logic and neural networks [158]. However, simply plotting the semi-span against shoulder angle produced a curve and piecewise polynomial or 'spline' interpolation proved computationally more efficient and produced adequate accuracy ± 1 mm. This plotting section can be recalculated for every iteration to allow different avian species to be modelled. As a result, the model input is the span-wise skeletal end position within a range 0 mm$\leq x \leq$ 391 mm for *Milvus milvus* assuming the common avian joint angle relationships. The resulting model range can be seen in figure 5.1.

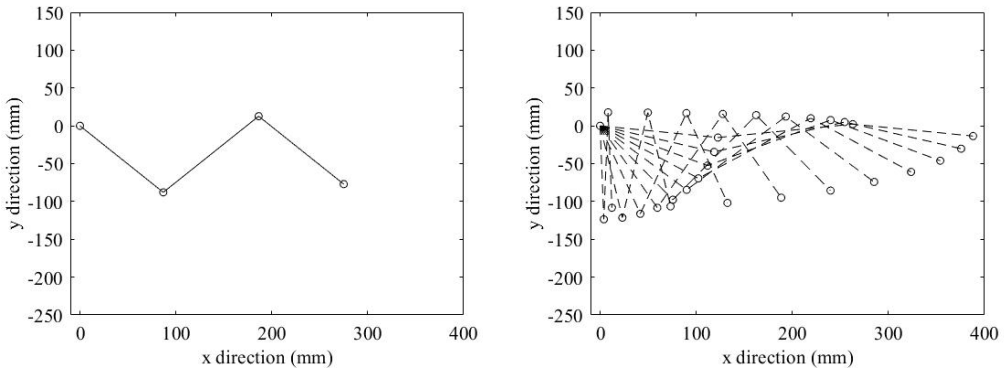


Figure 5.1: The span-wise motion for the *Milvus milvus* given previously obtained member lengths and an assumed 1:2:2 joint motion ratio.

5.1.3 Wing Area simulation

Development of the area input model followed a similar pattern to the span-wise simulation. Similarly based on the Denavit-Hartenberg notation, it relates the area of the semi-span to the shoulder joint angle. Observations were made of avian wing composition and dynamics, specifically *Milvus milvus, Apus apus* (Swift), and *Diomedeidae* (Albatross). This was done to examine wings designed for each common type of flight, gliding, bounding, diving, and flapping. The conclusion drawn

from these observations and from research into similar areas [128], is that the common bird semi-span wing can be modelled using a quadrilateral and a triangle. Shown in figure 5.2 is a mature *Milvus milvus* overlaid with the proposed modelling technique. The two areas correspond to the Primary and secondary feather areas inherent on avian wings. The quadrilateral can be assumed due to the span-wise movement during wing retraction. The shoulder and wrist joints act as forward corners with perpendicular feathers completing the shape.

The vertices which define the two polygons are defined by the DH transformation matrices. Simplified in this two-dimensional instance to those shown in equations, 5.4, 5.5, and 5.6.

$$\mathbf{S} = \begin{bmatrix} c\theta_s & -s\theta_s & 0 & a_1\ c\theta_s \\ s\theta_s & c\theta_s & 0 & a_1\ s\theta_s \\ 0 & 0 & 1 & 0 \\ 0 & 0 & 0 & 1 \end{bmatrix} \tag{5.4}$$

$$\mathbf{E} = \begin{bmatrix} c\theta_e & -s\theta_e & 0 & a_2\ c\theta_e \\ s\theta_e & c\theta_e & 0 & a_2\ s\theta_e \\ 0 & 0 & 1 & 0 \\ 0 & 0 & 0 & 1 \end{bmatrix} \tag{5.5}$$

$$\mathbf{W} = \begin{bmatrix} c\theta_w & -s\theta_w & 0 & a_3\ c\theta_w \\ s\theta_w & c\theta_w & 0 & a_3\ s\theta_w \\ 0 & 0 & 1 & 0 \\ 0 & 0 & 0 & 1 \end{bmatrix} \tag{5.6}$$

The area can be taken as that between these points where the shoulder and wrist locations define the quadrilateral and wrist and wing tip. The feather length is used here to define the points aft od the leading edge or skeletal structure. This is denoted **L** in the area equation presented in 5.7. The length **L** here is itself a coordinate vector representing the length of the feathers in the negative y axis in the case of the wrist point and parallel to the member a_3.

$$Area = |\mathbf{S} \times \mathbf{E}.L| + \frac{1}{2}|(\mathbf{E} - \mathbf{E}.\mathbf{L}) \times (\mathbf{E} - \mathbf{W}.\mathbf{L})| \tag{5.7}$$

As the wing retracts and extends, the quadrilateral compresses and expands respectively in the span-wise direction, while also inversely expanding and contracting in the chord-wise direction. This correlates to the secondary feathers, whereas the triangle closely maps the extension of the primary feathers as they pivot around the wrist joint. This pivot point can be assumed as the primary feathers are anchored into the length of both digits and thus move dependently. The resulting simulated area in figure 5.3 can be directly compared to the images collected of avian to show that the simplifying assumptions produce similar wing geometry.

As with the span-wise model for the area to be made the input it needed to be related to the shoulder angle, applying sine and cosine rules. However, it is not possible due to highly acute angles occurring at minimum span positions, while the rules are subject to the fundamental trigonometric limits.

Alternatively, the small-angle approximation commonly used in similar situations could be employed to produce sufficiently accurate geometric values. However, similarly to the span-wise model, linear interpolation using polynomial sections

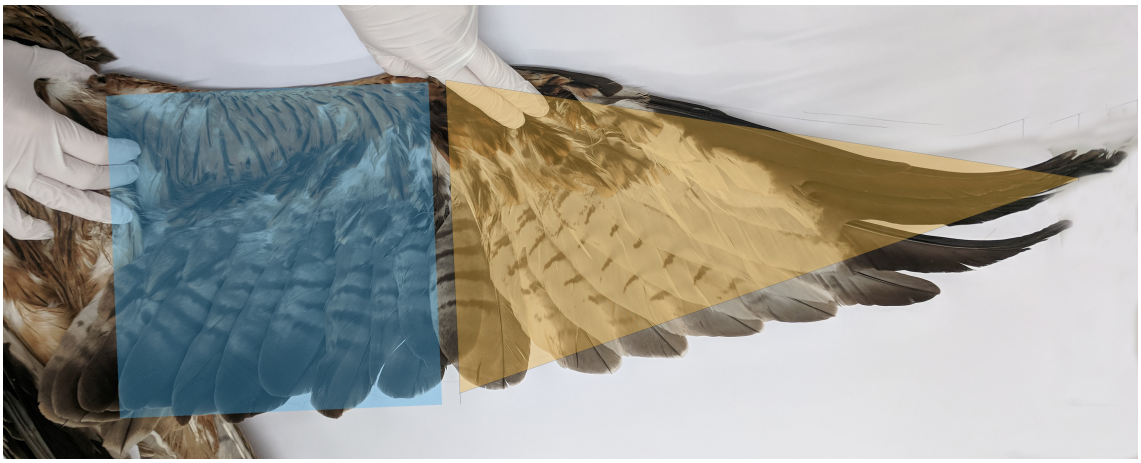


Figure 5.2: An image of *Milvus milvus* specimen NHMUK unregistered, arranged in a fully extended position. Overlaid is the sectional modelling method proposed to be used to approximate the area of an avian wing.

proved equally accurate while allowing quicker development due to the model's transferability between species. Figure 5.4 shows how the *Milvus milvus* skeletal structure changes as a result of the area input within a range $10,000\ \text{mm}^2 \leq \text{area} \leq 100,000\ \text{mm}^2$, while conforming to the assumed joint ratios.

While suitable for concept development the model could have further applications as the basis of a control system for prototypes with further development. Advanced applications would require increased accuracy and validation, which is regarded in section 3.5. The implementation of an inverse kinematic based relation would be recommended within the wingspan model. Whilst a small-angle approximation or similar method of relating area to the shoulder angle would also be recommended.

Validation for the model would also be necessary before use in any major applications, such as a control system. As mentioned previously in section 5.1 this was carried out through application to a specific avian *Milvus milvus.* The simulation's results would then be compared to literature data collected about the bird. While this was possible for traditional values such as bone length and wing span, unorthodox values like skeletal span, area, and joint angles were unavailable. Primary research was therefore conducted with the Natural History Museum at Tring upon their avian collection.

The direct kinematics and subsequent modelling detail the system mathematically and allow several conclusions to be drawn regarding a system for the control of the morphing wing. The direct kinematics exemplifies the range of morphing this concept can achieve. The notation and methodology commonly employed in robotics is highly applicable in this case due to the similarities between the jointed member system utilised. The notation shows a significant simplification can be made to the system due to two basic principles. Firstly, the exclusion of any 2 DOF joints in the concept and subsequently the model results in the elimination of any z terms in the DH matrices. A solution for the inverse kinematics can therefore be substantially less computationally intensive. The secondary characteristic to reduce the kinematic equations arises from the parallels mechanism. The dependency of the wrist analogous joint on the elbow results in equal joint angle terms. Resulting in the direct case one fewer input variable, but more significantly in the inverse case,

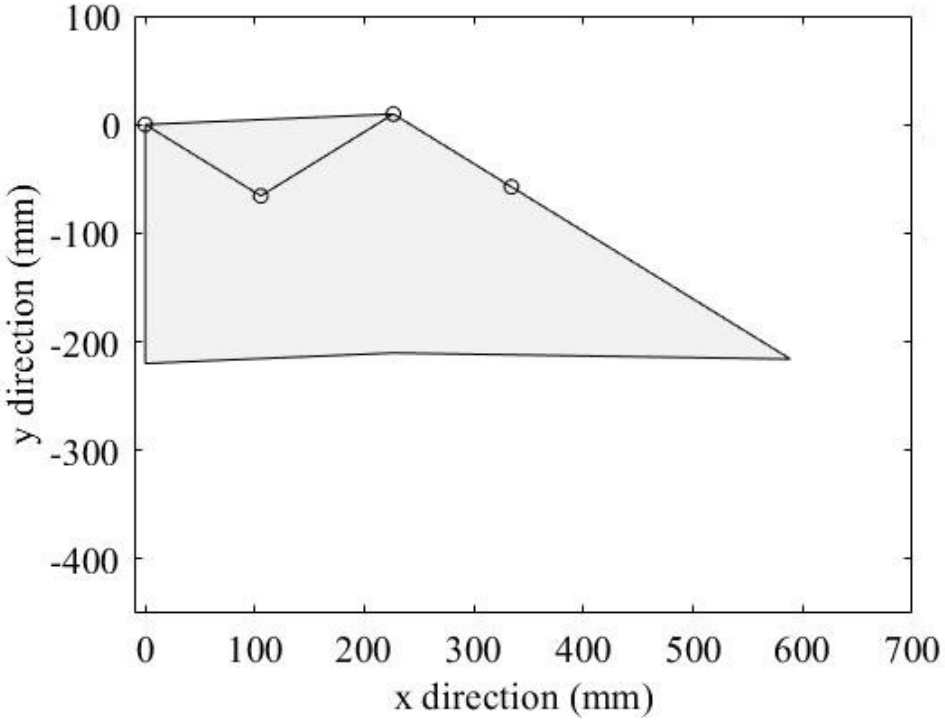


Figure 5.3: The graphical output for the area avian model. Similarly showing the sectional method for approximating the wing area using a quadrilateral and triangle.

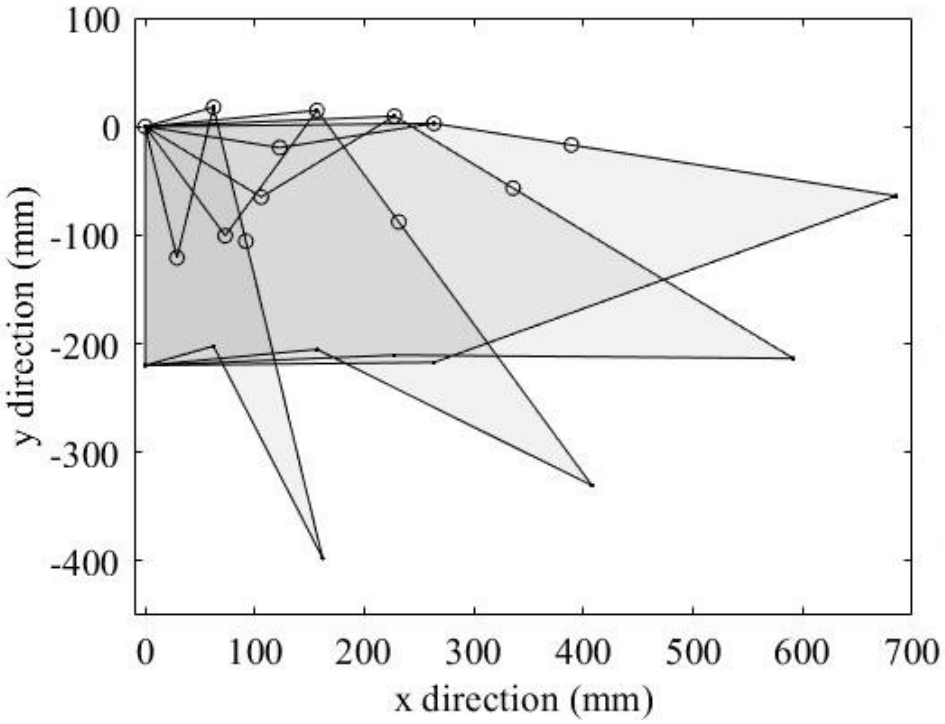


Figure 5.4: The graphical output of the area model. Comparatively showing the modelled area approximation over the range of shoulder joint angles.

one fewer required output variable.

The additional modelling of the wingspans based of several avian is a concept that was taken forward in the inverse kinematics. However, the process of inverting the DH notation was deemed unfeasible due to the simplifications mentioned rendering the process overly complicated and superfluous. Similarly, the modelling of wing area was not carried forward. While the process itself was insightful in the relationships between span length and area in avian of this order, further implementation would not be appropriate. The individual case such as full extension area the presented area methodology gives an acceptably accurate estimation of the semi-area of the avian and the concept. It is clear that the modelling methodology breaks down due to the complexities arising from the compliant and interlocking nature of the feathers and the leading edge muscular geometry. In particular, at full retraction, the compliance of the avian wing, so vital to effective morphing, becomes significant to the point that it would need to be accounted. In light of this, and the additional considerations that would be required for adaptation to the morphing concept. Any benefits of this addition to the effective control of the morphing concept system would be negligible.

5.2 Pneumatic Artificial Muscle System Modelling

Pneumatic artificial muscles are highly nonlinear resulting in difficulties in their modelling. However, the advantage of PAMs in other aspects such as low system complexity and low weight at the point of use has driven research into effective modelling and control. The pneumatic artificial muscles referred to in this study are commonly denoted as 'McKibben' muscles, and consist of an elastomeric bladder sheathed inside a braided fibre cylindrical sleeve affixed at both ends. The complexity in modelling PAMs both statically and dynamically derives from the interaction between the bladder and sleeve and the internal friction produced in the braid. These stresses alongside the elasticity of the bladder are non-negligible and as such, few comparisons can be drawn between PAMs and traditional rod actuators. The conclusion of a review into methodologies of PAM modelling is that there is currently no definitive consensus on an appropriate approach to modelling of PAMs and that an ideal model may not be achievable [159]. The current state of PAM modelling, therefore, is one of iteration and refinement. The common elements for a dynamic system are detailed in figure 5.5. The sections of the system to be modelled are divided into three parts for modelling. A pneumatic system consisting of the control valve, the PAM characterisation equations themselves, and the mechanical system consisting of the morphing wing structure.

The characterisation of the pneumatics is generally based on pressure and volume change models for traditional rigid-rod cylinders and on orifice-valve models used to represent control valves. The control valve selected for the morphing concept is the Festo^{TM} MPYE-5-1/8-HF-010-B three-state proportional control valve. Selected for several characteristics which suit the whole system. This valve also has a significant amount of literature, both from the manufacturer and due to other studies in the control of PAMs [160]. This valve is, however, limited to the states depicted in figure 5.6. The nature of the spool dictating the flow, also depicted in figure 5.6, results in operationally restrictive depressurisation. Essentially, meaning both, each of the PAMs pressurised and each PAM de-pressurised, are states that

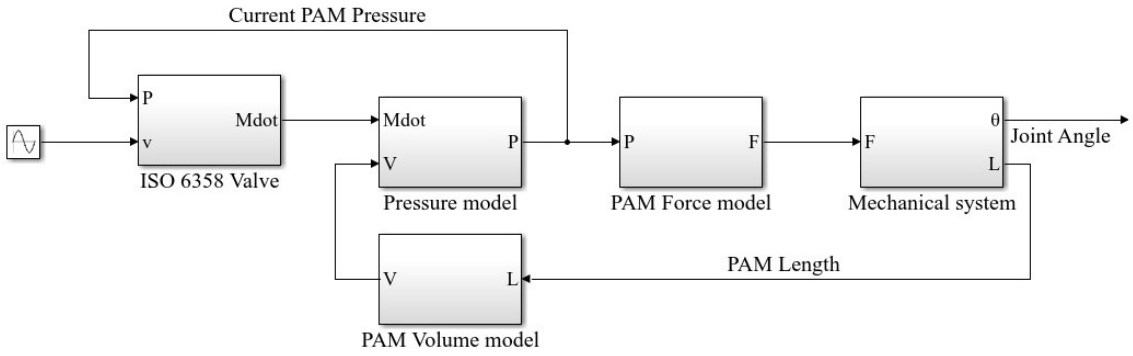


Figure 5.5: Proposed PAM model overview, outlining the sequencing of the individual component equations.

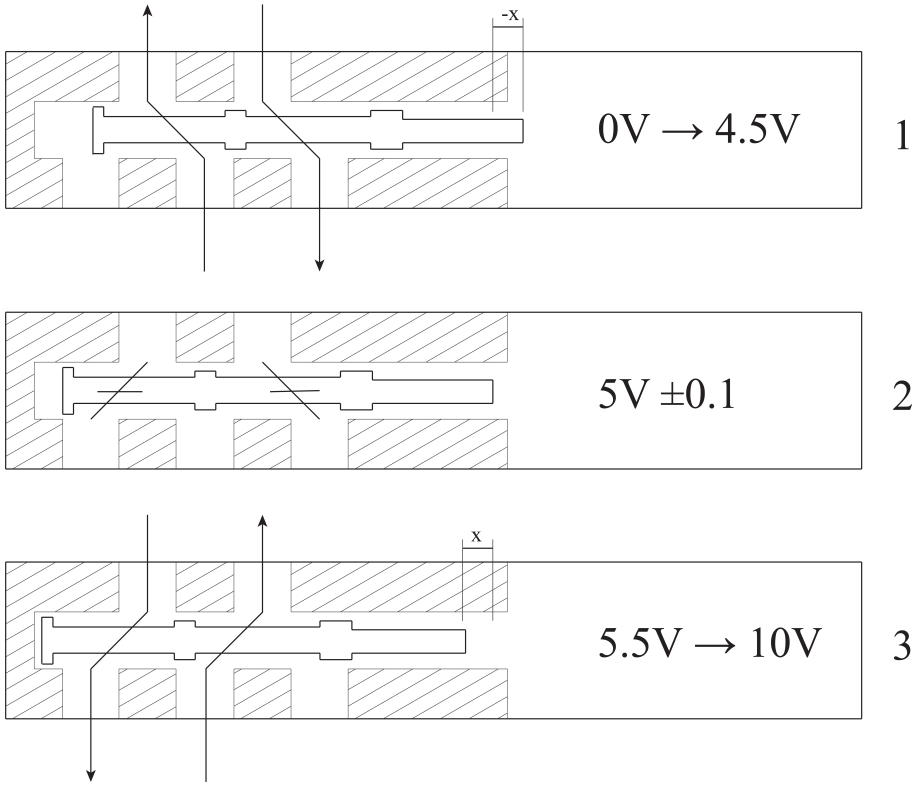


Figure 5.6: Three-way pneumatic control valve, Festo™ MPYE-5-1/8-HF-010-B. Shown in the three operational states, with the central actuated spool (normally enclosed) visible.

cannot be physically achieved. Others [161], have proposed implementing separate proportional valves. However, this solution is presented in applications where weight and system complexity, and by extension failure modes, are not as significant in the design as in the development of aircraft. It has been shown that the standard ISO 6358 mass flow model effectively reproduces that behaviour of the Festo™ MPYE valve [162]. These relate the gauge pressure of the pneumatic source and the proportionally controlled valve cross-sectional area. To the mass flow rate into and exiting each muscle. Outlined in 5.8 where, C, the sonic conductance of the valve and $p_{critical}$, the critical pressure ratio are derived from or supplied by, the manufacturers literature, respectively. However, to reduce computation it has been shown

effective to discount the laminar case. Due to the operating conditions, laminar flow is seldom present. The reduced form 5.9 was implemented in the system, assuming no temperature change across the valve. In the case of the sonic conductance the reverse was employed. The method chosen for deriving sonic conductance allowed for correlation between the spool displacement from a central position, state 2 in figure 5.6. This is preferable to other methods used for this control valve, as the displacement can be inferred from the input control voltage. This is opposed to obtaining this relationship through the study of the MPYE valve literature provided by the manufacturer. The advantage is to reduce any error occurred from this process, however, as stated before this results in a small computational cost. Here, the input control voltage between 0 – 10V proportionally outputs a spool displacement and orifice cross sectional area. This area can be used in the modified valve model, along with spool displacement, which determines the flow direction, to output the mass flow rate.

$$\dot{m} = \begin{cases} C\rho_0 \left(\frac{P_{out}-P_{in}}{1-p_{laminar}}\right)\sqrt{\frac{T_0}{T_{in}}}\left[1-\left(\frac{p_{ratio}-p_{critical}}{1-p_{critical}}\right)^2\right]^m \\ C\rho_0 P_{in}\sqrt{\frac{T_0}{T_{in}}}\left[1-\left(\frac{p_{ratio}-p_{critical}}{1-p_{critical}}\right)^2\right]^m \\ C\rho_0 P_{in}\sqrt{\frac{T_0}{T_{in}}} \end{cases} \tag{5.8}$$

$$\dot{m} = \begin{cases} C_1 C_d A \frac{P_{in}}{\sqrt{T}} & \frac{P_{out}}{P_{in}} \leq p_{critical}(ChockedFlow) \\ \\ C_2 C_d A \frac{P_{in}}{\sqrt{T}}\left(\frac{P_{out}}{P_{in}}\right)^{\frac{1}{k}} C & \frac{P_{out}}{P_{in}} > p_{critical}(SubsonicFlow) \end{cases} \tag{5.9}$$

$$With \qquad C = \sqrt{\left[1-\frac{P_{out}}{P_{in}}^{(k-1)/k}\right]}$$

$$and \qquad C_1 = \sqrt{\frac{k}{R}\left[\frac{2}{k+1}\right]^{\frac{k+1}{k-1}}} \qquad C_2 = \sqrt{\frac{2}{R}\left[\frac{k}{k-1}\right]}$$

Literary sources where similar models have been presented often include a tubing pressure loss model. Placed directly after the valve, these account for the losses in the connecting tubing between the PAMs and valve. This has not been included in this work, as in the application for small uncrewed aerial vehicles, which may employ this morphing concept. The likely maximum length of these connections therefore is below the threshold where these losses can be considered negligible. A pressure model for a cylinder of changing volume is common in actuated system characterisation due to its applicability to fixed-rod cylinders. As such the equation 5.10 is as presented in previous works [163]. Where the terms α_{in}, α_{out}, and α_{vol}, are used in place of the heat transfer coefficient k. These terms can be estimated also shown by Richer and Hurmuzlu [163], allowing the exact coefficient to be excluded.

$$\dot{P} = \frac{RT}{V}(\alpha_{in}\dot{m}_{in} - \alpha_{out}\dot{m}_{out}) - \alpha_{vol}P\frac{\dot{V}}{V} \tag{5.10}$$

The variable V and $\dot{V}$ denoting the volume for the individual PAM are necessary for the pressure derivation. As both are highly dependent on the current length of

the PAM and, subsequently, its output force. The current volume is calculated from the current length, as shown in figure 5.5. Equation (5.11) shows the static volume at rest. The internal bladder thickness volume is subtracted from the total PAM volume. Using the length L the cylindrical volume is produced. Total volume of the PAM is dependent on the PAM length via the kinematics of the sleeve and the individual fibres from which it is comprised. Woods [7] proposed a method for defining this relationship, which is employed in 5.12.

$$V_{fluid} = V_{totalvolume} - \pi[r_0^2 - (r_0 - t_{b0})^2]L_0 \tag{5.11}$$

$$V_{totalvolume} = \frac{B^2 - L^2}{4\pi^2 N^2} \tag{5.12}$$

Where, B, is the individual fiber length in the helical sleeve and N, is the number of turns that fiber makes in the length of the PAM. As the rate of change in the volume is also required (5.11) is differentiated with respect to time to produce (5.13) and simplified resulting in (5.14). This method is typical in PAM characteristic determination [160]. However, as previous authors have noted it assumes a cylindrical internal PAM geometry. Any observation of these artificial muscles in use makes it clear this is not the case. The crimping at each end of the sleeve, allowing attachment to connecting hardware, results in a convex rounding end.

$$\dot{V}_{fluid} = \frac{dL}{dt}\frac{d}{dL}\left[\frac{B^2 L - L^3}{4\pi N^2} - \pi[r_0^2 - (r_0 - t_{b0})^2]L_0\right] \tag{5.13}$$

$$\dot{V}_{fluid} = \dot{L}\left[\frac{B^2 - 3L^2}{4\pi N^2}\right] \tag{5.14}$$

The principal method for determining the muscle forces for each PAM is a quasistatic energy balancing method proposed and significantly developed in the literature. The overall force comprising of the sum of individually determined factors laid out in a PAM force equation:

$$F_{PAM} = F_G + F_C - F_B - F_S \tag{5.15}$$

A Gaylord force model, the most commonly employed, was derived by Gaylord [164] alongside the pioneering of the muscles themselves. Developed from this initial kinematic equation Schulte [165], later Tondu and Lopez [166] and Kang et al [167], the form shown in (5.16). In terms of Length, L, PAM diameter, D, and sleeve braid angle, α.

$$F_G = P\frac{D_0^2\pi}{4}\left[\frac{3\left(1 - \frac{L_0 - L}{L_0}^2\right)}{tan^2\alpha} - \frac{1}{sin^2\alpha}\right] \tag{5.16}$$

The three following force terms were largely collated in the series of work by Woods et al [160]. These proved effective in accurately simulating the internal forces and the subsequent effect on the overall contraction force of the PAM. Explained fully in other works, the bladder elasticity term FR_B (5.17) a model of material hyperelasticity, negatively effects the output force. The included terms, $V_{bladder}$ & V_{sleeve}, representing the volume of the PAM bladder and sleeve respectively, were calculated using the same method as previously stated in 5.11.

$$F_B = V_{bladder}\left[2C_{10}\left[\lambda_1\frac{d\lambda_1}{dL}+\lambda_2\frac{d\lambda_2}{dL}+\lambda_3\frac{d\lambda_3}{dL}\right]\right.$$
$$+2C_{01}\left[\lambda_1(\lambda_2^2+\lambda_3^2)\frac{d\lambda_1}{dL}+\lambda_2(\lambda_1^2+\lambda_3^2)\frac{d\lambda_2}{dL}\right.$$
$$\left.\left.+\lambda_3(\lambda_1^2+\lambda_2^2)\frac{d\lambda_3}{dL}\right]\right] \tag{5.17}$$

$with$

$$\lambda_1 = \frac{L}{L_0}$$
$$\lambda_2 = \frac{r-\frac{t_b}{2}}{r_0-\frac{t_0}{2}}$$
$$\lambda_3 = \frac{t_b}{t-0}$$

$$F_C = -k_f(F_G + F_B - F_S)sgn(\dot{L}) \tag{5.18}$$

$$F_S = V_{sleeve}\frac{1}{E_s A_s^2 n^2}\frac{4\pi^2 P^2 B^2}{(2\pi N)^4} \tag{5.19}$$

Notable points include the reductive nature of all the additional terms. Including the Coulomb friction, which comprises the other force terms and a friction factor, k_f. Which is experimentally derived to fit and correct for the internal material friction. This friction, mentioned previously, is a contributing factor to the complexity in modelling PAM behaviour. The two PAM forces for the antagonistic system were then linked to the output angle θ through the moments about a pivot which forms the joint, then a second-order dynamic equation.

Overall, the modelling of these subsystems and the Pneumatic artificial muscles themselves could be considered developed. As mentioned previously, while no methodology has been definitively adopted, it is plain that a structure exists. The focus can therefore be considered to have shifted from the muscles themselves to the systems into which they are embedded. It must be noted that significant progress in the form and operation of PAMs will require continued modelling development. However, for the application presented in the form of morphing structures, the current orthodoxy has been proven reliable. The systems surrounding the muscles are highly adaptive, allowing the range of applications. It is these applications need an approach specific to aircraft and in particular morphing aircraft.

5.2.1 System Identification

Alongside the necessary model validation, it was decided that a process of frequency response would be undertaken. It was noted that the model in and of itself may not provide a reliable bases for development beyond the scope of this work. The addition therefore of a system identification methodology would support the model as development of the span-wise morphing concept developed. The production of a simplified model variant was also an aim of this process as the literature models can be computationally intensive.

Single Frequency Responce

It was decided that a single joint dynamic control would be the most effective method for initial control. The mechanical design for the joints themselves is relatively known in literature but a few features are notable from the perspective of individual joint control. The antagonistic nature of the joint results in markedly different behaviour to the unconstrained muscles. In a context of an applied constant weight or other controlled loading situation, variables such as contraction length, internal pressure, bladder stresses, and diameter are predictably independent or dependent. Resulting in a static case. In a tension or bidirectional force connecting mechanism PAMs in a pair apply a noticeably dynamic load. This effects the performance of the muscles, as noted in 5.2, reducing operating characteristics. Similarly, these must be taken into account in a control context.

The flow rate is determined by the proportional control valve, as shown in the model, which is then output to both PAMs. This connection, also shown in figure 5.7, acts as both an inlet and outlet for the PAM. The muscles themselves are affixed via threaded endcaps to a mounting plate and then to the bell crank via eye fixings, allowing for the degrees of freedom required to avoid overstraining the system.

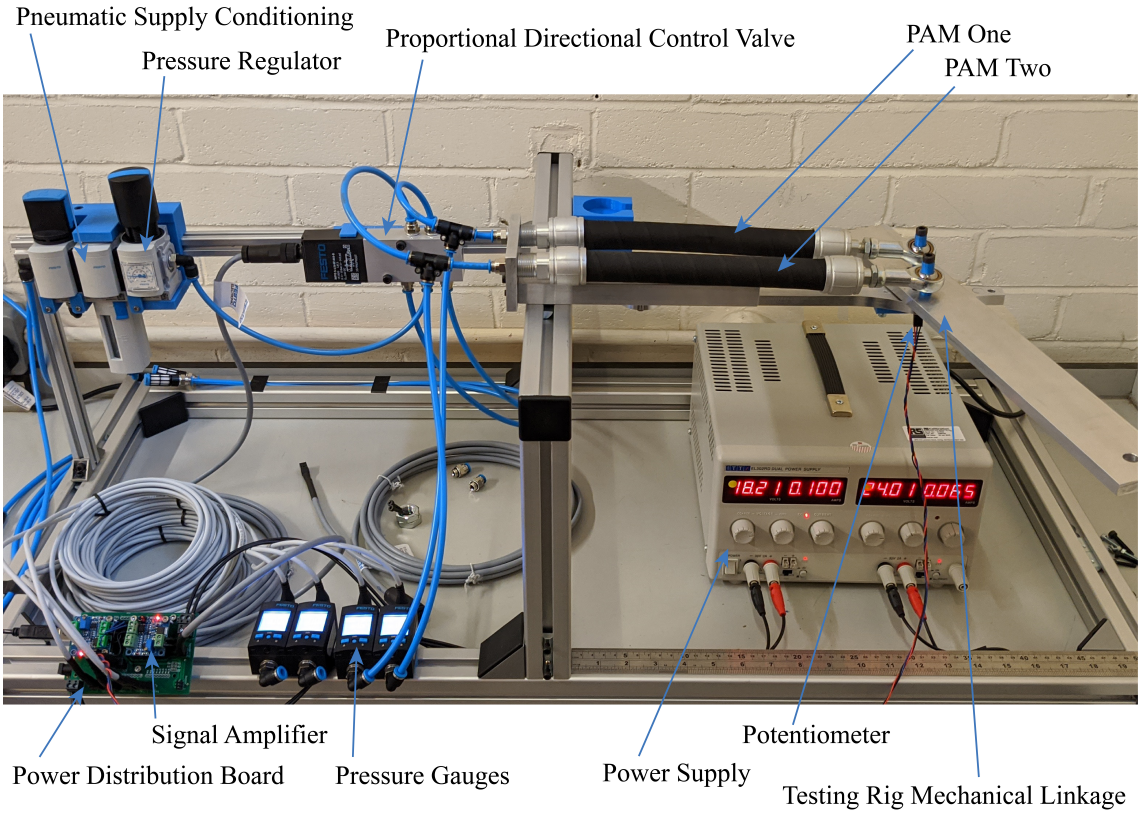


Figure 5.7: An image of the electro-pneumatic setup used for model validation and the process of frequency response system identification. Not shown is the computer providing the voltage input and recording the response. It should also be noted that this equipment rig has duplicated items for the two joint actuation of the full span-wise morphing concept.

The underside of this joint has an embedded potentiometer providing the feedback to the microprocessor. The microprocessor itself utilises amplifying circuits to

Table 5.1: Festo Pneumatic artificial muscle (PAM) Fluidic Muscle DMSP/MAS physical characteristics as used in validation of the proposed model and frequency response model development.

Pneumatic artificial muscle	Nominal length (mm)	Bladder Dia' (mm)	Sleeve Dia' (mm)
DMSP-10-210N-AM-CM	210	10	13.64 ±0.25
DMSP-10-150N-AM-CM	150	10	13.64 ±0.25
DMSP-10-130N-AM-CM	130	10	13.64 ±0.25
DMSP-10-100N-AM-CM	100	10	13.64 ±0.25
DMSP-20-200N-AM-CM	200	20	24.40 ±0.25
DMSP-20-130N-AM-CM	130	20	24.40 ±0.25

provide the control signal required by the PCV. The PAMs used in these tests were Festo Fluidic Muscle DMSP/MAS. Each has a working length of 300mm and an external sleeve diameter of 20mm. PAM details used in modelling are outlined in Table 5.1.

An initial set of measurements was taken with a sinusoidal voltage input of amplitude 5V about the median voltage for the control valves. Also carried out was the same test, but at a range of operating pressures up to a maximum of 6 Bar, defined by the maximum working pressure of each PAM. These are shown in table 5.1; note, the standard units for the PAMs and pneumatic equipment is bar equivalent to 100 kPa. This range of pressures and the effect on the PAM joint actuation is perhaps best exemplified in figure 5.8; shown with 20mm diameter muscles. The antagonistic nature of the joint results in the angular deflection of the joint being directly proportional to the operating pressure. Similar to linear actuation, in which the contraction length is related to the contraction strain.

The implications of this in relation to the span-wise morphing concept are particularly significant. Maximum span morphing is entirely dependent on this angular deflection. It is evident from these results that the deflections indicated during the development were not applicable. This is due to the antagonistic PAM, which extends as a result of the active muscle's contraction and exhibits a significantly increased resistive force than predicted. The result is a reduced actuation strain.

As the forces produced by the PAMs are related to a number of characteristics on the muscle design re-evaluation would be required for their application in situation where these characteristics, and by extension the force, are impacted due to the nature of the concept objectives. In the case of the span-wise morphing concept the primary effected characteristic is PAM volume; more significantly length. Change in the length of the PAM due to the pressurisation of the bladder

It can be noted from equations 5.17 and 5.19 that both sleeve volume and internal-bladder volume proportionally affect the force of the active PAM. The application of these muscles to actuate the elbow joint of the concept requires them to be embedded inside the wing box muscle volume is noticeably restricted. It is therefore clear that the critical restriction on the span-wise morphing concept is the volume of the PAMs. The implications of these results are discussed as part of the conclusion section 5.4.

Regarding the actuation characteristics of the single joint system, a noticeable hysteresis is exhibited. Apparent in figure 5.9 and figure 5.10 it is most visible in the former. Relating the control valve input to joint angle through the range of pressures tested, it is clear the dependency of the system on its history is consistent.

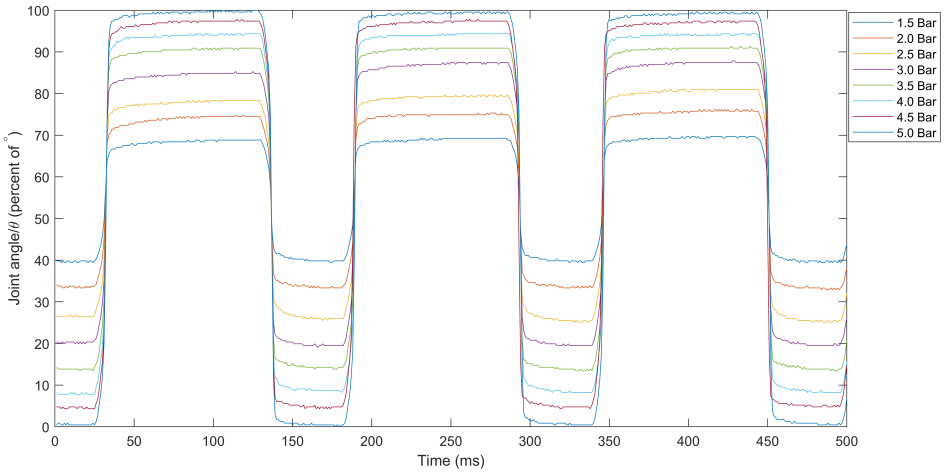


Figure 5.8: A comparison between the single pneumatic artificial muscle (PAM) joint actuated at different operating supply pressures. Shown is the measured joint angle as a percentage of the maximum angular deflection measured. This is presented as a result of a sinusoidal voltage input of 0.1 rad/s.

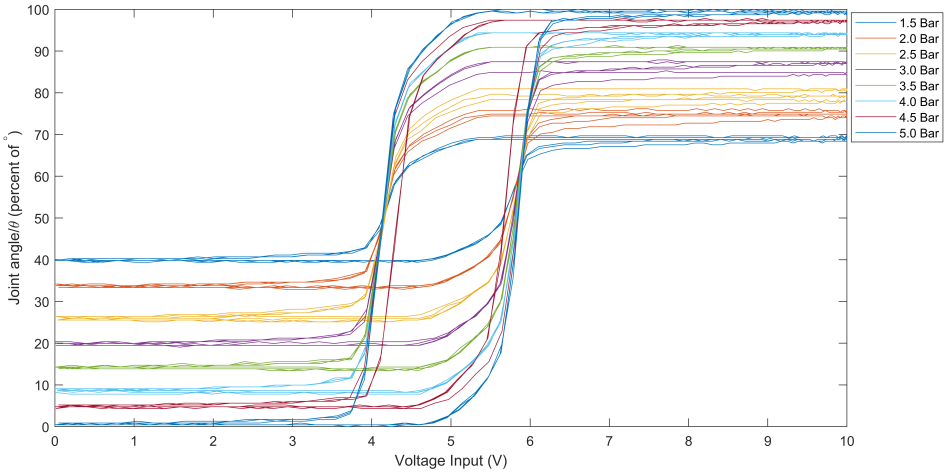


Figure 5.9: A similar comparison to figure 5.8. Shown against the voltage input to the proportional control valve. Of note is the range away from the median voltage 5V with a shallow gradient.

This consistency is seen in both the shown cycles and across the operating pressures. In comparison between the sinusoidal cycles, excluding visible anomalies, the joint angles are consistent to $\pm 0.5°$. The anomalies referenced are resultant from factors such as the potentiometer wire interacting with the structure of the test bench, external perturbations due to observation of the actuation, and noise that could not be filtered. The consistency in the joint angle profile as a result of the voltage input can be attributed to the manufacturer's tolerances for the PCV.

At a pressure of 5 bar figure 5.10 shows the dependency of the actuation on the interaction between the antagonistic PAMs. Over the three input cycles shown, an inconsistent behaviour can be observed. The internal pressures in each PAM can be

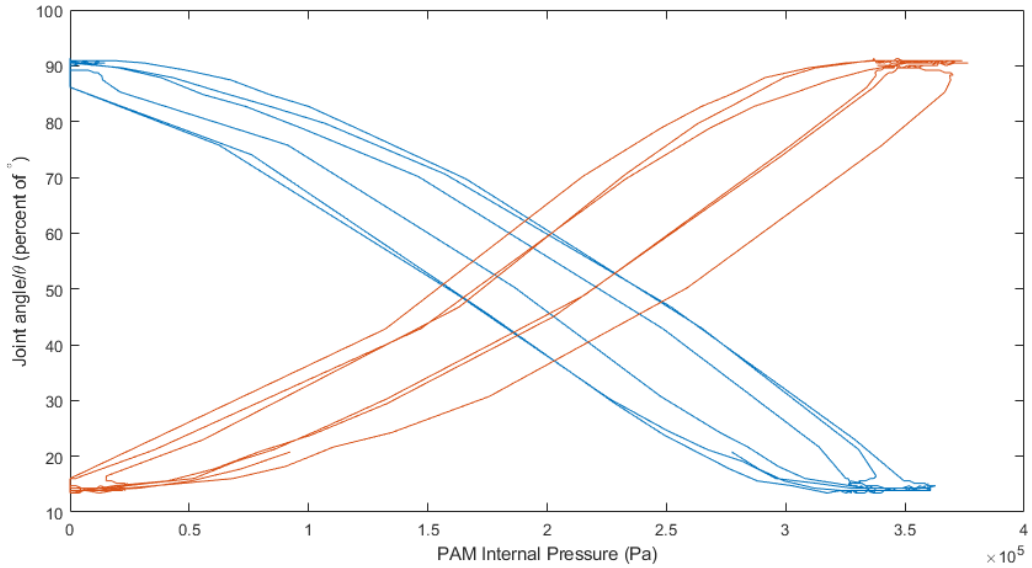


Figure 5.10: A plot showing the Internal pneumatic artificial muscle (PAM) pressure during the actuation period described in figure 5.8. Significant to note is the cycle formed by the pressure in the individual PAM and the inconsistent nature.

seen to increase and decrease at different rates over the cycles. However, as stated before it is the combined resultant force between the pair that effect the angular output. These inconsistencies, therefore, can be considered inconsequential. Indeed, at alternate operational pressures a greater variation in pressure can be observed. This lack of effect on the output can be observed by noting that in a cycle with a decrease pressure in PAM A, a similar decreased pressure is also observable in PAM B. The difference in the summation of the forces is therefore equal to other cycles.

As the technical documentation for the components specified, there is a significant response-less region. Input voltages outside a centralised voltage range $3V < input < 7V$ have a negligible effect on PAM actuation. While this was expected, an effect on system performance was unforeseen. The microcontroller, via a signal amplifier, was used to drive the PCV. This controller runs an 8-bit system, resulting in voltage step increases to the PVC. The total number of steps is therefore limited to 255. When this was used across the full 10V range, it resulted in a voltage-step resolution that was detrimental to the system's operation. This was corrected, and the voltage range was limited to 4V or less in subsequent system development.

Frequency Responce

Frequency response testing consisted of a sinusoidal input signal amplitude 5V and amplified producing a system input voltage range from $3-7$V. As the microcontroller produces a standard 8-bit PWM signal to the amplifiers, this voltage is stepped to 255 increments. The frequency ranges used were 0.1 rad/s to 100 rad/s. The lower bound of the frequency range was determined by the lowest angular rate measured in the avian testing of section 3.5. The lower limit was also chosen to represent a low manoeuvre speed. The upper limit ranges to the theoretical limit of the PAMs. This limit is determined by the mass flow rate achievable by both the flow supply

and the rate achievable by the PCV PAM side orifice. It should be noted that the mechanism is not the limiting factor in actuation frequency, as the amplitude of the PAM and subsequent angle deflection decrease with frequency.

The experimental system setup for these frequency response tests, displayed in figure 5.7 was identical to the system used for the previous single frequency actuation. However, the attached laboratory pneumatic system was regulated down to an input pressure of 3 Bar. This pressure was selected as it produces a good compromise between the range of motion achieved by the PAMs at a higher pressure and a manageable force output to reduce angle feedback errors caused by material deflection. This pressure is set using the same indicators that were used to measure the individual PAM pressures to provide a consistent gauge pressure.

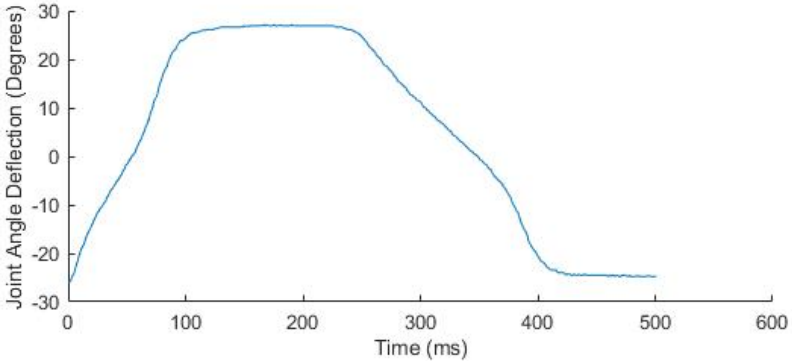
Measured at a rate of 50 Hz, were the pressure in each individual PAM and the resultant angle of joint deflection. Shown in figures 5.11 are a range of representative cycles at each frequency. A time period of 5 seconds is shown as a common x-axis to allow frequency comparison. These results are detrended to account for the shifting of the actuation midpoint. As the amplitude of actuation decreased, the point about which the actuation centred tended towards the positive angular maximum. A raw data plot shows the actuation shift immediately after power is applied. At this point, despite the PCV being in an unpowered state, the negative angled PAM is retracted resulting in the joint being initially at its limit in this direction. Despite this the actuation tend to the positive maximum. Given that the joint actuation amplitude is between 5 and 1 degrees at this frequency, the situation is likely never to be in demand. However, this shift renders the joint mechanism essentially inoperable at these frequencies.

Similarly to this tendency is an oscillation of this actuation midpoint that can be observed in figure 5.11g through 5.11k. This oscillation was not removed during the data detrending conducted and no filtering was conducted. The amplitude of this motion can be seen to vary across the frequencies but does not exceed ± 2 degrees and averages at 1 degree. This could therefore be present at lower frequencies and not observable due to the increase in overall amplitude and the errors involved. However, in comparison to the overall trend this movement is negligible particularly at the low frequencies at which the joint will operate.

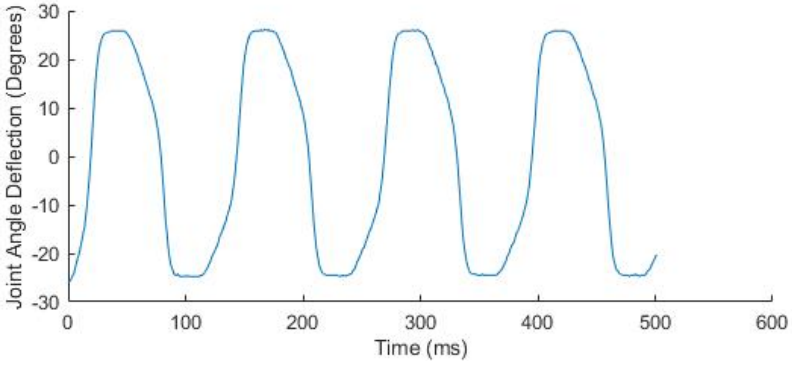
The same process was carried out with the positive PAM retracted in the system's initial position. The same tendency toward the positive maximum was observed, leading to the conclusion that the shift is due to the physical setup of the system. Due to the nature of antagonistic PAM joints the number of variables that could cause this imbalance and it would be impractical to attempt to eliminate each one. It is estimated, however, that the pipe losses between the PCV and PAMs have the greatest influence. Factors such as pipe length, internal cross-section and surface roughness are all factors that can be effectively managed to mitigate the issue. In the application for the span-wise morphing concept, two factors negated the requirement to manage the shift in actuation midpoint. The low-angle amplitudes mean that the advantages of span morphing would become negligible. While the high frequencies are rarely called for in flight, as explored in section 3.

As a result of the two tendencies, oscillation and drift, combined with significant decrease in angular deflection. Frequencies greater than 15 rad/s were not viable for effective control. The low angles and subsequent decrease in effective wing morphing were not acceptable with the compromises of more intensive control methods includ-

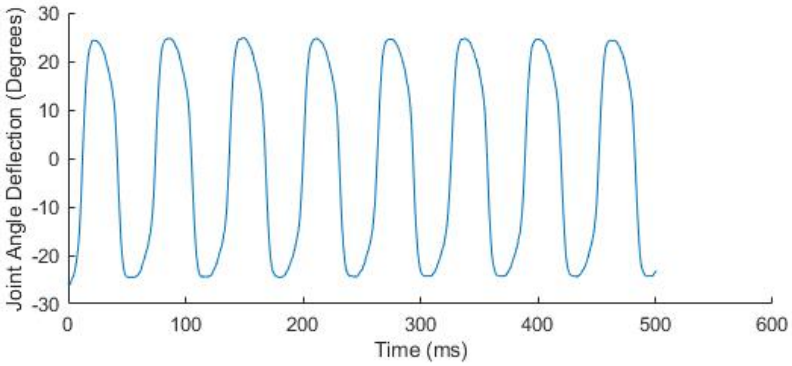
ing nonlinear methodologies. Data sets from frequency ranges 0.1 rad/s to 10 rad/s were considered for state-space control and less intensive nonlinear control. However, these were found to produce models which could not maintain accuracy across the range of frequencies. Alternatively, transfer function estimation was found to allow a greater range of operating conditions to be modelled. It was also considered that these would be less computationally intensive than state-space and more effectively altered to make them viable for similar joint concepts. Transfer function estimation has significant literature covering varied applications and an instrumental-variable approach as outlined by Ozdemir et al [168]. This was used for all model estimations as part of a nonlinear least squares algorithm.


Joint Angle Deflection (Degrees)
30
20
10
0
-10
-20
-30
0
100
200
300
400
500
600
Time (ms)

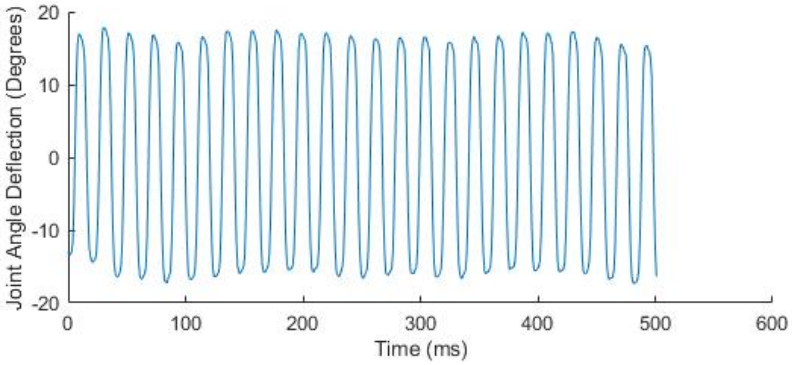
(a)


Joint Angle Deflection (Degrees)
30
20
10
0
-10
-20
-30
0
100
200
300
400
500
600
Time (ms)

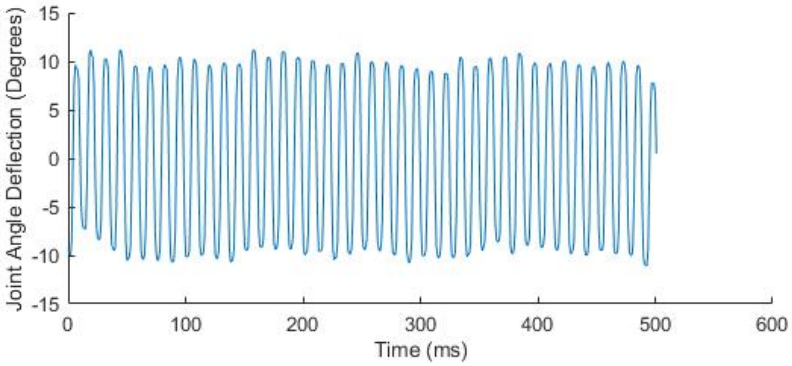
(b)


Joint Angle Deflection (Degrees)
30
20
10
0
-10
-20
-30
0
100
200
300
400
500
600
Time (ms)

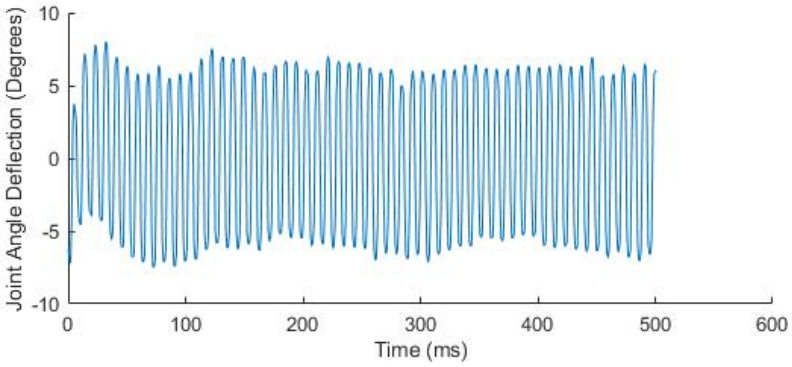
(c)


Joint Angle Deflection (Degrees)
20
10
0
-10
-20
0
100
200
300
400
500
600
Time (ms)

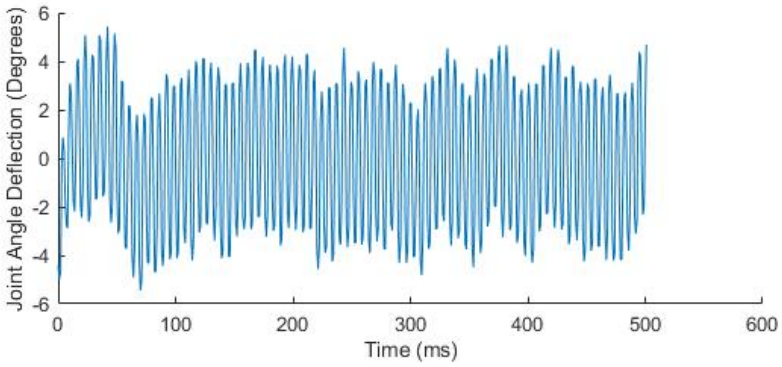
(d)


Joint Angle Deflection (Degrees)
15
10
5
0
-5
-10
-15
0
100
200
300
400
500
600
Time (ms)

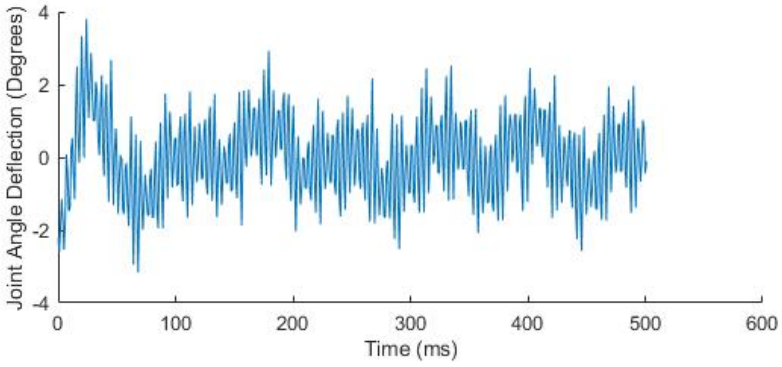
(e)


Joint Angle Deflection (Degrees)
10
5
0
-5
-10
0
100
200
300
400
500
600
Time (ms)

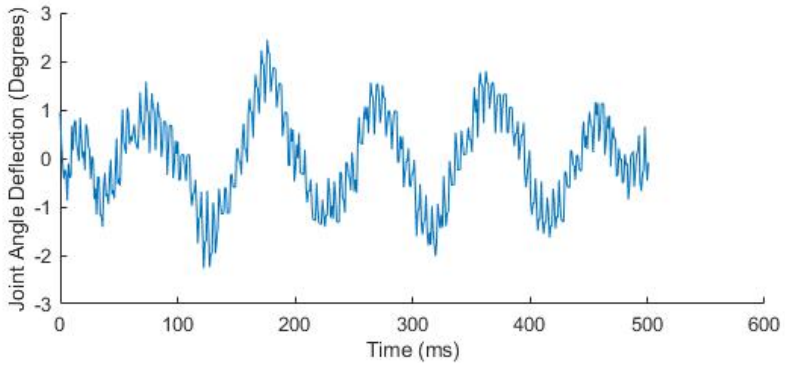
(f)


Joint Angle Deflection (Degrees)
6
4
2
0
-2
-4
-6
0
100
200
300
400
500
600
Time (ms)

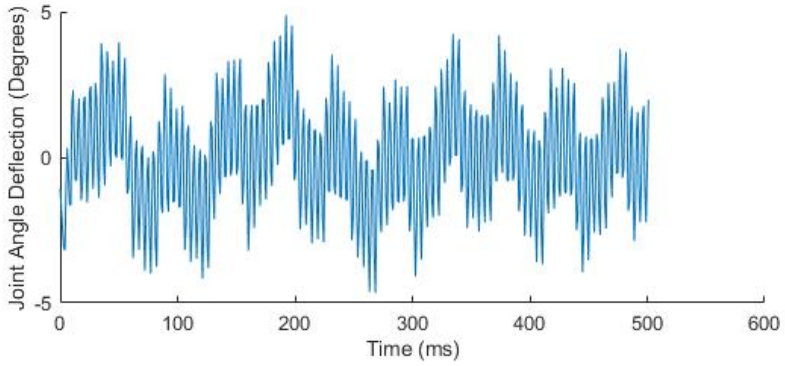
(g)


Joint Angle Deflection (Degrees)
4
2
0
-2
-4
0
100
200
300
400
500
600
Time (ms)

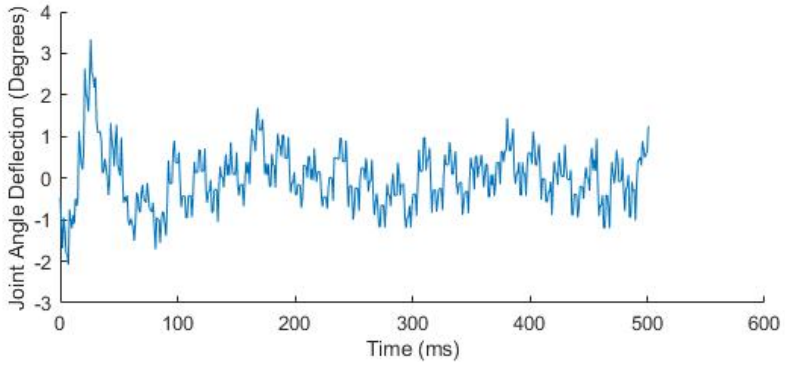
(h)



(i)



(j)



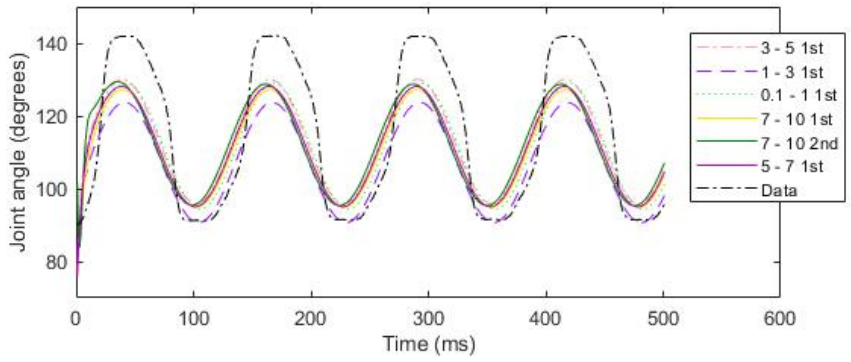
(k)

Figure 5.11: The joint angle response to a sinusoidal voltage input at the following frequencies: (a) 0.1 rad/s, (b) 0.5 rad/s, (c) 1 rad/s, (d) 3 rad/s, (e) 5 rad/s, (f) 7 rad/s, (g) 10 rad/s, (h) 15 rad/s, (i) 25 rad/s, (j) 50 rad/s, and (k) 100 rad/s. A constant amplitude was input; however, the resulting data was detrended over the 5 seconds shown.

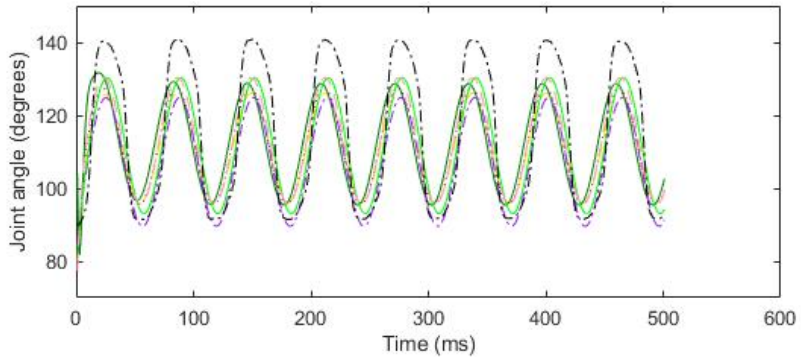
In figures 5.12 the output of five models are shown against the input data for the model estimation. The transfer function itself is shown with each plot. These differing models are due to the estimation algorithm's input data. It was determined at an initial stage that inputting all the data collected simultaneously resulted in errors. These were attributed to the nonlinear nature of PAM actuation, particularly in antagonistic joint configurations. Variations in frequency as low as 5 rad/s in the input data could result in model estimations exhibiting these errors. The five models represent models based on individual data sets collected at a single operational frequency. All shown are single pole transfer function models. The test stand data was collated into a bode plot in order to compare to model outputs. The result of this can be seen in figure 5.13. The form is a typical representation of a first order model and it was found the estimated first order models matched more consistently over higher order functions.

Figure 5.12a is based on the data collected at 0.1 rad/s and this original data is shown against the output of each of the other estimated models. The output of the system at these low frequencies is markedly different to those of the higher. The result is that the transfer functions derived perform less accurately for the low-frequency output. While the models are more consistent than at higher frequencies, none replicate the higher amplitudes that are produced by the PAMs. This under-estimation is a critical failure for this method of modelling the system. The increased actuation strain of the joint and morphing concept provides control and efficiency advantages and inaccuracy in this area makes the model unsuitable at these low frequencies. An argument could be made that the low angular rates represented at this frequency would seldom be exhibited in the application of the joint in a morphing wing. This is consistent with the increased control surface rates commonly required for MUAVs but may not be directly comparable to a full wing morphing surface. A good comparison could be made with the kinematics of the avian and the rates employed in biological flight. This is conducted in the context of the control system in section 5.3 where all the aspects of the PAM actuation is compared to in vivo captured avian kinematics.

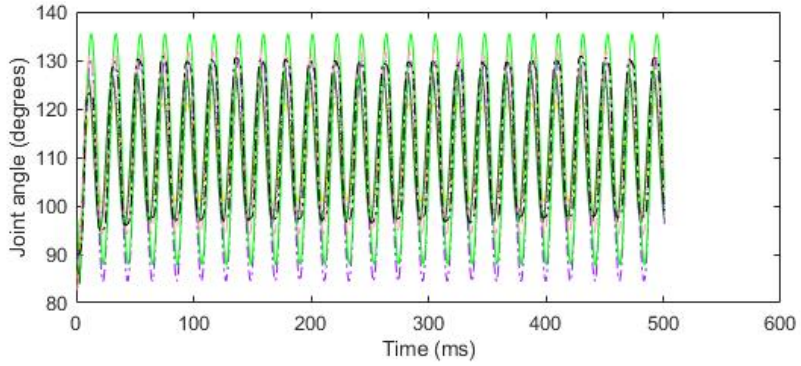
An input of 1 rad/s to 3 rad/s produces a similar output from each model. The notable difference is a reduction in consistency between the models. Figure 5.12c, representing the model output at 3 rad/s, exhibits a consistent tendency that becomes apparent at increased input frequencies. Models based on low-frequency data sets, in this case 0.1 – 1 rad/s, start to overshoot the experimental PAM amplitude at higher input frequencies. This is particularly evident in figure 5.12d where the model based on results at 1 rad/s to 3 rad/s overshoots 50% and lower models have been omitted as they could not be plotted with sufficient detail.


Joint angle (degrees)
Time (ms)
3 - 5 1st
1 - 3 1st
0.1 - 1 1st
7 - 10 1st
7 - 10 2nd
5 - 7 1st
Data

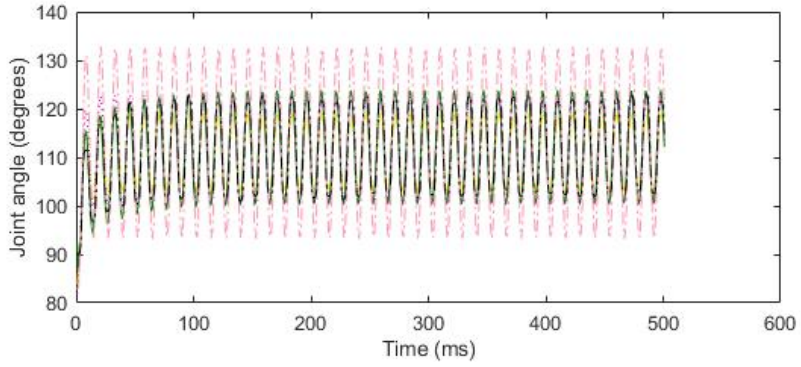
(a)


Joint angle (degrees)
Time (ms)

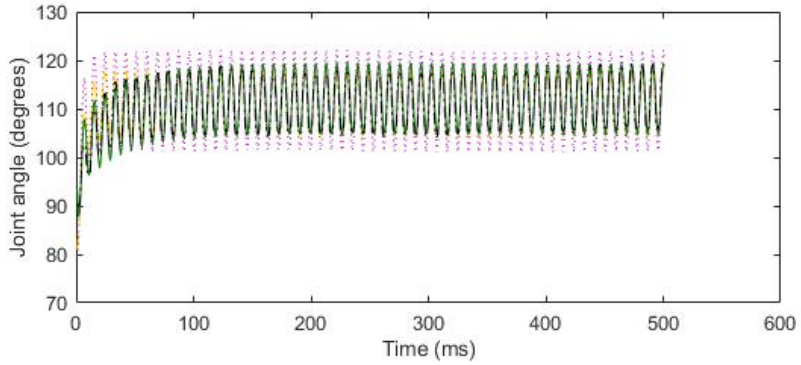
(b)


Joint angle (degrees)
Time (ms)

(c)


Joint angle (degrees)
Time (ms)

(d)



(e)

Figure 5.12: Presented are the models estimated from the PAM sinusoidal response from each of the following frequency ranges. (a) 0.1 rad/s to 1 rad/s, (b) 1 rad/s to 3 rad/s, (c) 3 rad/s to 5 rad/s, (d) 5 rad/s to 7 rad/s, and (e) 7 rad/s to 10 rad/s. Plotted at each frequency range is the output from each derived model against the following input frequency. (a) 0.5 rad/s, (b) 1 rad/s, (c) 3 rad/s, (d) 5 rad/s, and (e) 7 rad/s.

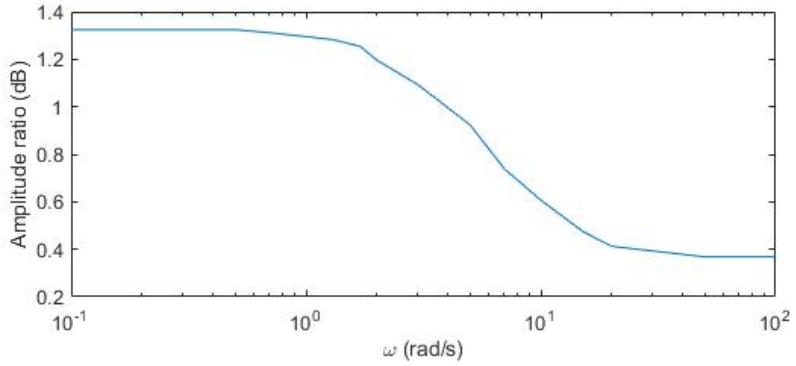


Figure 5.13: Bode plot of the frequency response system identification.

Models based on ranges 5 rad/s to 10 rad/s are shown to have a significantly increased accuracy and precision at their respective frequency ranges. At the same time, performing similarly at the lower bounds examined within the scope of the joint and its applications. The overall application of these models is limited. As discussed previously the modelling of PAMs themselves is nonlinear and this frequency response concurs with this characteristic. The limited range of frequencies to which each transfer function can be applied is consistent with a system with inherent nonlinearity. A mechanical joint featuring PAMs in an antagonistic pair is not suited for limited control methodology. However, the accuracy of each model within its limited range has its applications in the control of the morphing concept presented. While avian vary angular rates to suit the situation, aim, and environment in the particular manoeuvres and operations discussed in chapter 3 consistent angular movement was observed. Extended through to the span-wise morphing concept, this is the basis of further application into the use of these models.

5.3 Control System

As discussed previously in section 4.1 a three member system is used as an approximation of the avian limb. An available motion specification was three degrees of freedom to allow appropriate wing postures to be achieved. These three degrees allow the wing tip, which during derivations and calculations was referred to as the end effector, to be theoretically located at any required location. Theoretically limited by the sum of the member length, and practically additionally limited by the restricted angular rotation range of the joints.

The addition of the third member, for an increased span over fewer members, presented an issue from a control point of view. The Kutzbach criterion defines the mobility of a system and states that the system is under-constrained if the number of independent input criteria for the end effector is not equal to or greater than the degrees of freedom/mobility. The result is in order to fully define an end effector location and by extension a wing position, a third variable is required.

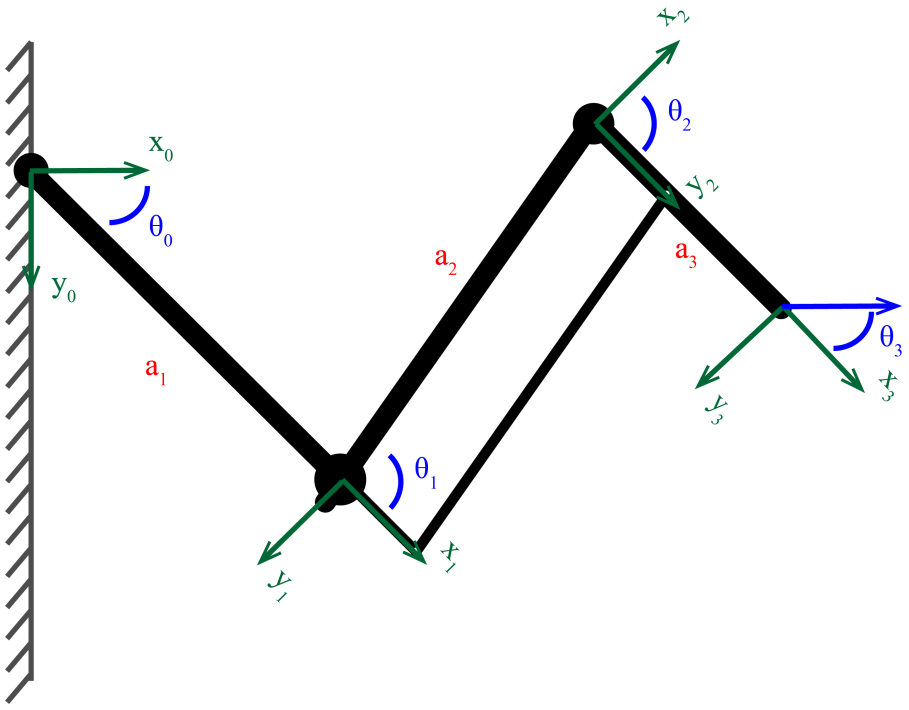


Figure 5.14: A visual representation of the notation used to define the span-wise morphing concept for application of inverse kinematics. Each linking member is denoted a_n with n the end effector joint number. The coordinate systems used are also represented and similarly subscripted in relation to joint number.

Variable	a_1	a_2	a_3	θ_0	θ_1	θ_2	θ_3
Value (Range)	240mm	270mm	190mm	0 - 90	0 - 180	0 - 180	0 - 90

Table 5.2: Values for the span-wise morphing concept proposed following the notation defined in figure 5.14.

This increase in input variables introduces an advantage over alternative rotating member morphing concepts. Whilst the third variable can be of arbitrary definition

in a continuation of the avian flight mechanics capture analysis, this variable represents a similar advantage avian exploit in flight. Cartesian coordinates, with x and a reference value y, can be taken for the longitudinal direction. The introduction of the third variable allows control over the end effector rotational angle about the z-axis. This angle, defined as theta, can be directly related to the sweep angle. In the general system case it is equal to the sweep angle of the final member a sub 3 but in the specific case of the span-wise morphing concept presented theta can also be used to derive the overall sweep of the wing. It should be noted that due to the parallelisms inherent in the simplification of the mechanical mechanisms used these two sweep angles are commonly equal.

Exploration of multiple version of a control system was conducted. The requirement for sweep control could be considered unnecessary in limited applications and a potential source of manual or system error. A single variable input for the system allows for simplified control of the wing. It also allows for a more analogical application of avian flight data in the replication of flight manoeuvres. This single input was determined to be the span length or semi-span length. A quasistatic set of kinematic equations in addition is therefore a requirement for useful application of the overall system.

Inverse kinematics for this morphing concept was completed through manual analysis of the members and joints. Numerous methods were considered. These were all deemed unnecessary due to the nature of the mechanism. Several steps were taken during the mechanical development to enable a non-extensive process. This included the joint type as simple one dimensional joints and a position inline with linking members.

The coordinate systems are related to the geometry of the previous linking member from the rigid joint. Detailed in figure 5.14 is the related notation. The inverse kinematic equations follow this in order of computation effectively from the end effector to the rigid body. Input; x_3, y_3 and, θ_3, the position of the wrist joint is established in (5.20).

$$\begin{aligned} x_2 &= x_3 - a_3 c(\theta_3) \\ y_2 &= y_3 - a_3 s(\theta_3) \end{aligned} \tag{5.20}$$

In relation to the position of the wrist joint and its coordinate system, the derivation of θ_2 the secondary actuated joint can be completed. Via the assumption of the member geometry a value, Z_1 , for the a_1 and a_2 member angle can be ascertained. Equations, (5.21) and (5.22). An assumption was made regarding the members' relationship in order to reduce the variables. This process assumes the members a_1 and a_2 are constrained at an angle less than parallel. This is the case for the span-wise concept as presented but it should be noted as a possible cause for error in any future development.

$$r_{12} = \sqrt{x_2^2 + y_2^2} \tag{5.21}$$

$$Z_1 = c^{-1}\left(\frac{r_{12}^2 - a_1^2 - a_2^2}{-2a_1 a_2}\right) \tag{5.22}$$

$$\theta_0 = \theta_3 \tag{5.23}$$

$$\theta_1 = 180 - Z_1 \tag{5.24}$$

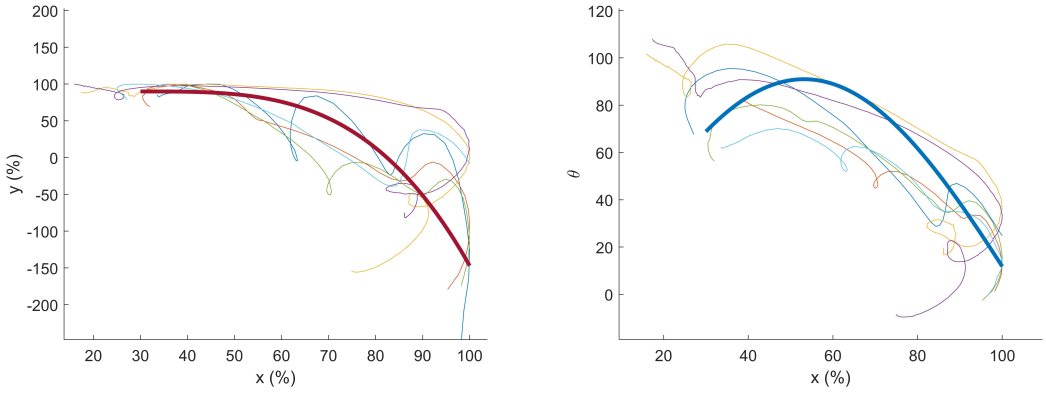
These simplified equations allow a computationally light response to manual input. However, and perhaps more significantly, this system allows for a more concise control approach. System specific values for joint angles and their subsequent motion and aerodynamic and stability impact, are not required. The total area within which the end effector can be located is highly dependent on the rotational range of the individual joints. The most impactful on the x span position is the shoulder. In an ideal mechanical situation theta the shoulder angle would range from +45 to -45 corresponding to perpendicular with the body of the aircraft to parallel. In the context of high manoeuvrability, high velocity aircraft forward swept wings, in this case greater than +45 could also be considered. Dictated in the inverse kinematics, it can be seen that the elbow joint thi has a less significant impact on the range of motion of the end effector. This can justify any mechanical shortcomings in the physical design due to the additional constraints of parallel system integration.

5.3.1 Biomimetic application

Presented in this section thus far is what could be considered a generic mechanism for control of the morphing wing. Used is a combination of both the dynamic PAM joint control and the inverse kinematics for wing tip positioning and an accompanying direct kinematic model for manoeuvre simulation. These allow common inputs, wing tip position and angle of attack, to be used for system level control. However, there is a requirement for a higher level of control which removes the requirement for system level interaction. The proposed additional set of equations allowing this is based upon the joint relationships measured during the avian kinematic capture in section 3.5. Replication of these relationships allows the concept to utilise the unique motion characteristics of the avian and allow adaptation based on manoeuvre and behaviour analysis collected from motion capture. The primary motion of the concept is the extension in the span-wise direction. This was taken forward and the each of the other input variables defined in relation to the span.

A number of flight modes were explored in chapter 3 and as the full extension and retraction of the wing occurs as part of each flight, it would be impractical to incorporate each one. These full extensions are most common in the take-off of the bird from a perch, as a method of stability on an unstable perch, and during ground locomotion. It was observed that in each of these instances a three-dimensional motion was exhibited. In application to the span-wise morphing concept the two-dimensional reduction of the movement was considered. This reduction simply omitted the z-axis and calculated joint angles based on the span and chord motion.

Complicating matters further there is an argument to similarly including partial extensions and retraction when considering the motion, as opposed to the full. Any control system based on the avian kinematics measured will be required to operate full wing actuation. However, it is reasonable that the partial actuation shown in flight could be extrapolated for the control through the entire range of motion. It was considered that the kinematics captured mid-flight, as opposed to a full extension from rest at take-off or similar, may benefit the control of the span-wise morphing



(a) (b)

Figure 5.15: (a) Avian motion capture data showing the chord-wise y positions of the wing tip as a percentage of the maximum y position. Against the x position of the wingtip, similarly as a percentage of the maximum value for span position. Also shown is the derived curve used to approximate the relationship between the two variables. (b) Presented as the angle of attack against the span-wise position x. Similarly shown is the curve used to define the angle of attack θ as a function of span.

concept to a greater extent. Several reasons for this are evident. While mid-flight the aerodynamic consequences of perturbations are increased due to the high airspeed. This could result in the more aggressive actuation used at low or no airspeed causing instability in the flight of the span-wise morphing concept. During flight, the motion of the wings has a significantly different effect on the centre of gravity as compared to perch or ground-based motion.

A compromise was made between the two kinematic data types. The full retraction kinematics explored in chapter 3 are more numerous. This is due to the proportion of its usage during flight and the relative ease of capturing extensions on take-off. A great certainty as to the reliability of the measurements can be taken for the average of all the full extension kinematic data collected. While the motion employed immediately during take off can be considered in flight with all the implications suggested previously. This is despite the bird still being in contact with the perch for a portion of the capture. Therefore, the averaging of the full extension and retraction kinematics was the basis for this proposed control system. This compromise in motion capture selection is a clear area for further development. The development of flight mode-specific control is of particular interest in further research.

The proposed input to the system is the span-wise position x_3 in relation to the x_0 coordinate system. The two variables which are to be made dependent are y_3 and θ_3. A summary of the take-off avian data is shown in figure 5.15a. The plot details the y position of the wing tip end-effector against the span-wise position x. These individual motion paths are constant despite the difference in flight conditions. The initial position of the wing tip is, as expected, the most repeated portion of the motion. While the wing is tucked into the body, the wing tip is restrained in its movement. Two paths start at a greater span. This is due to poor motion capture data at the start of the wing extension as opposed to any change in the manoeuvre

itself. The gradient of the initial movement starts low before increasing in general exponentially. The varied nature of the latter stages of the extension would require an increased number of captures to make any general conclusions. However, with the relatively minor impact on overall performance and the nature of bio-inspired design not being a direct copy of nature, a limited set was decided to be sufficient for the control system. Plot in figure 5.15a is the curve derived from the available data. The curve is characterised through the exponential equation 5.25. This curve proved to provide the best approximation between the low gradient and high gradient sections of the extension. Polynomial and similar curves less adequately represented both characteristics.

$$y = -4 \times 10^{-5} x^{3.386} + 106.5 \tag{5.25}$$

The angle θ_3 the angle between the x_0 and x_3 axis' is the second inverse kinematic input proposed to be controlled via avian behaviour. This angle can be effectively taken to represent the angle of attack for the semi-span of the wing. Due to the linked elbow and wrist joint the angles θ_0 and θ_3 are equal. The selection of this as a dependent variable allows further simplification of the system through the omission of any further equations linking the variables. In a similar process to the y variable, figure 5.15b exemplifies the relationship between the x span position and theta. These were again taken for the previously mentioned bird flights. These plots show a more defined profile for the motion. Each flight consistently used a curved profile at the start and end of each movement. Whilst the central portion of the motion can be considered more or less linear. The motion capture does show a repeated pattern; however, there are several notable exceptions. The beginning and end of each motion are not consistent, while the curve is similarly undefined in terms of x-value position. In a similar fashion to the y-position plots, the theta angle does exhibit a highly repeatable gradient against the span position. This can therefore be the feature from which the dependency can be derived.

It was decided not to relate the two variables linearly. A linear relationship would compromise the accuracy at the maximum and minimum retraction positions where the curved profile is most pronounced. A polynomial-based equation was considered, and it was found that at the 3rd order or greater, a reasonable curve was produced. However, these tended to produce low theta angles at lower x position values. This was deemed too significant a deviation to be considered. The equation 5.26 was produced from a sine-based curve fit. This provided the most reliable fit over the full range of span values. However, in plot 5.15b, it can clearly be seen that this is a compromise over the range too.

$$\theta = 91 \sin(0.02175x + 0.8365) \tag{5.26}$$

The method by which both of these dependencies were derived is fundamentally variable. The curves presented as a solution in this case are suited for this type of structure actuation. However, it is clear that the method is easily applied to differing situations. A similar process could be undertaken, using the same methodology, for wing twist, camber, and chord length. In the span-wise morphing concept, this technique could be utilised to effectively control wing sweep by analysing avian species such as the Swift, which extensively use sweep angle in flight.

5.3.2 Control validation

In a similar method to the single joint experimentation explored in section 5.2.1 a rig was constructed to validate the controlled system. Two actively controlled joints and a single passive joint were constructed from an aluminium plate with initial weight reduction included for validation purposes. In previous loadings with each muscle at 6 bar elastic deformation of the members was observed. It was predicted that deformation within the material strength would affect the angle feedback causing instability. This was mitigated with the application of a high-grade 7071 alloy. The pneumatic artificial muscles themselves were mounted in orientation to their respective joints through embedded threaded fittings.

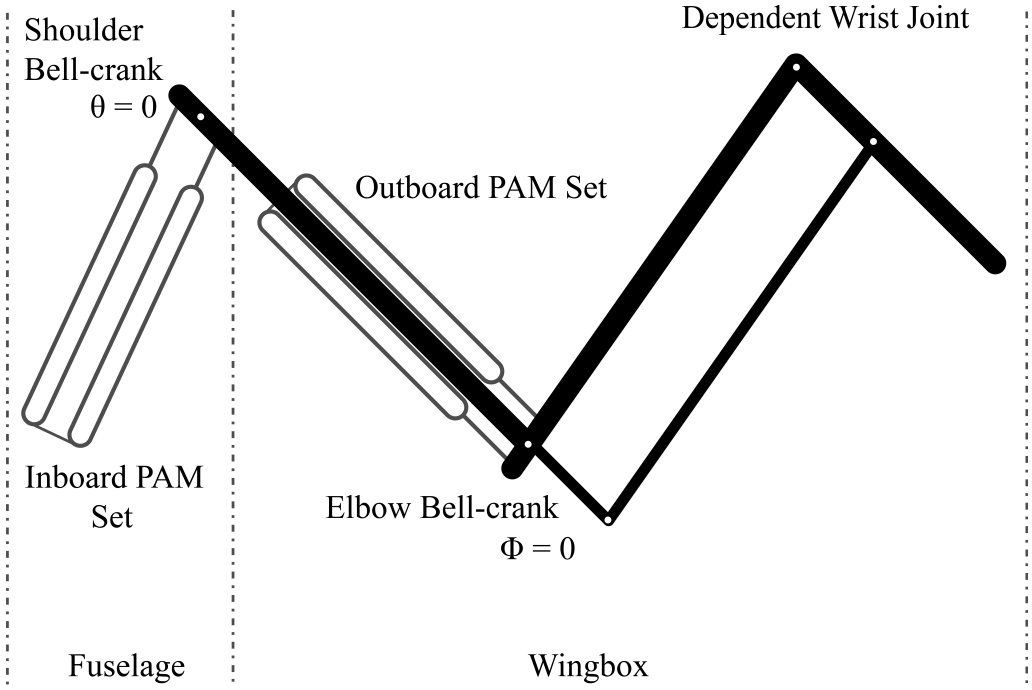


Figure 5.16: A diagram detailing the mechanical layout for the control system testing. Shown are both pairs of pneumatic artificial muscles (PAMs). Each actively actuates their respective joints, with the outboard pair passively actuating the final wrist joint. Note this diagram does not represent scale.

The inboard PAM set, shown in figure 5.16, are intended to housed within a fuselage to mitigate aerodynamically adverse structural elements required for their containment. It should be noted that the angle about the z-axis that the PAMs form with the neutral position of the actuated member is critical mechanically. However, this can be obviated through the mechanical linkage connecting the PAMs to the joint. As such, the position of the inboard pair in figure 5.16 shows a possible configuration. Whereas, the setup detailed in figure 5.17 and shown in figure 5.18 is rotated toward the fore as this equipment was also intended for wind tunnel use and space limitations caused interference with the wing body.

In the setup image the structural fuselage analogue is visible supporting the structural members and housing the inboard PAMs. This serves only as a stand-in for an airframe mounting. The overall setup is similar to that of the single joint

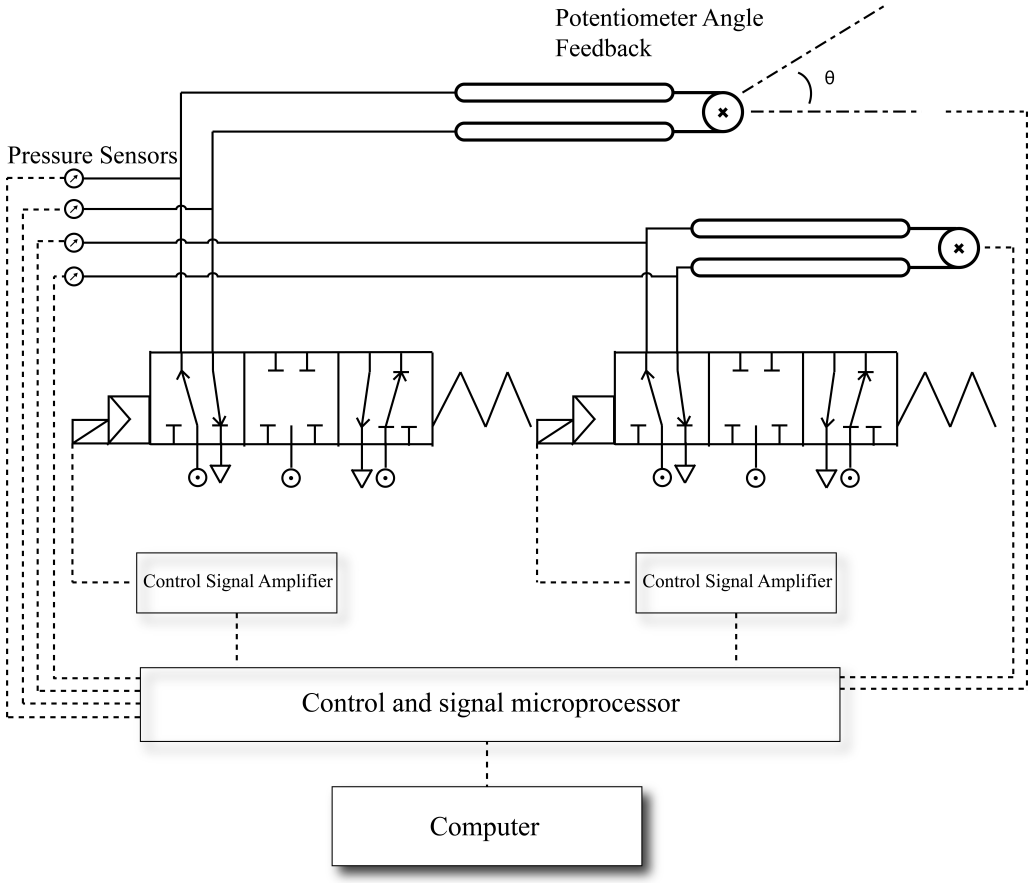


Figure 5.17: An overview of the electro-pneumatic system for the span-wise morphing concept. Featuring the pneumatic system outlined in ISO 1219-1:2012 symbols, the electronic system overview, and the feedback system overview.

experimental rig shown previously. Accommodations were made for the second joint via the inclusion of a replicated set of support equipment. Pneumatically, both muscle pairs are connected to a proportional control valve (MPYE-5-1/8-HF-010-B) and individually pressure transducers (SPAU-P10R-T-G18FD). Electrically, both muscle sets were connected to a common power sources and for data singles a common microcontroller. The control loop described in the previous section was run separately on a computer to allow data collection, monitoring, and adjustability. An overview of the physical system as proposed for the test and application in the span-wise morphing concept is shown in figure 5.17. The significant differences from the single joint testing is the duplication of the PAM support components: the PCV, Pressure sensors, and control signal amplifier.

A sinusoidal input was used to validate the individual joint's closed loop control methodology chosen and the structure's open loop control system developed. The control system can only be considered quasistatic due to the initial basic implementation of the inverse kinematics. As a result, the input value was of desired span length, with the output being the two joint angles. While the inverse kinematics used three inputs based on the span length, as detailed in section 5.3.1. In order to explore the versatility of the mechanism tests with different muscle parameters were tested. The system was run at 8 bar with two pairs of 10mm diameter blad-

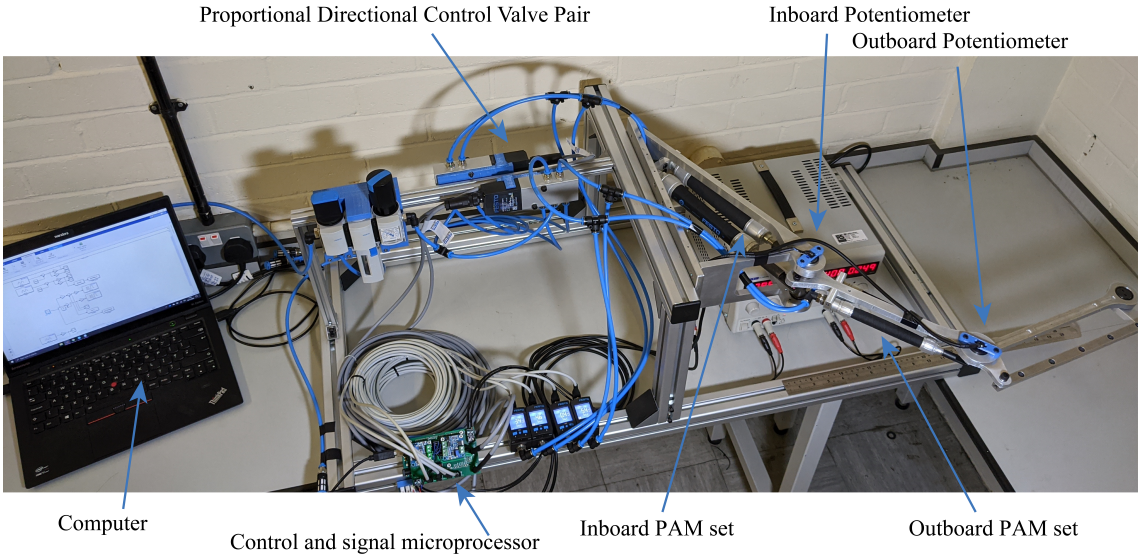
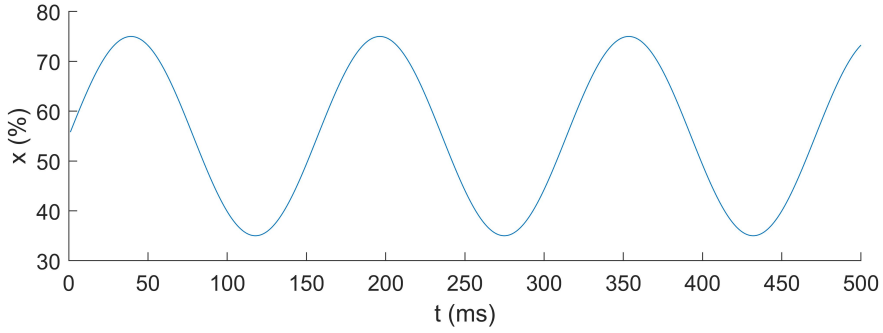


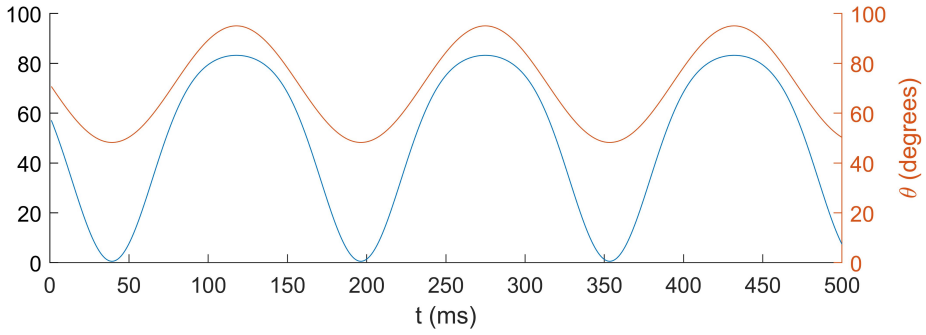
Figure 5.18: An image of the complete setup used to validate the control system in a passive environment. Labelled are the additional components which make up the three-jointed system as opposed to the single-jointed pneumatic artificial muscle control setup. Note that none of the aerodynamic surfaces of the span-wise morphing concept are present during these tests.

der PAMs. While a second configuration with the outboard joint using the same 10mm pair, while the inboard joint used the 20mm valiant; this was conducted at 6 bar. This 6 bar was used due to the upper pressure limit of the 20mm PAMs. A configuration with a 20mm pair at the outboard position could not be achieved as the length of the larger pair could not be accommodated in the structure design. This is considered more thoroughly as part of the wind tunnel testing in chapter 6. The full set of results for this 6 bar test is shown in figure 5.19, over a range of three representative cycles. The first point of note is the reduced input amplitude. It was noted after analysis of the avian motion capture that solely in the extension manoeuvre, the wing does not reach full retraction. This is due to taking the reference point at the centre of the body which obviously does not retract in the same manner. Similarly, it is only in further actions, such as a flapping stroke, that the avian extends past approximately 75% span. These were therefore restricted for this test of the extension exclusively.

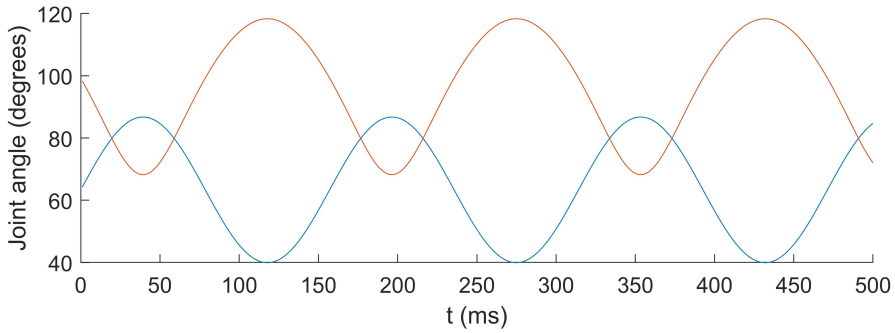
The following control stage includes calculating the dependent variables according to the biomimetically derived curves. As discussed in a previous section, the curves that define the relationship between the variables are the so-called 'best fit' for the data collected. This can therefore be considered the more adaptable section of the control system. Far from presenting a negative to the control of the span-wise morphing concept, this allows greater flexibility in the application of this methodology. The figure 5.19b presents the output of the particular variables defined for this concept. The variable y_3 is characterised by a broad peak and a narrow trough. This is typical due to the exponential relationship to the input variable. However, given the nature of the avian motion capture it is perhaps an understated response as the data showed a significant exponential y position change during retraction. It can be considered, given the nature of novel concepts, that an understated response



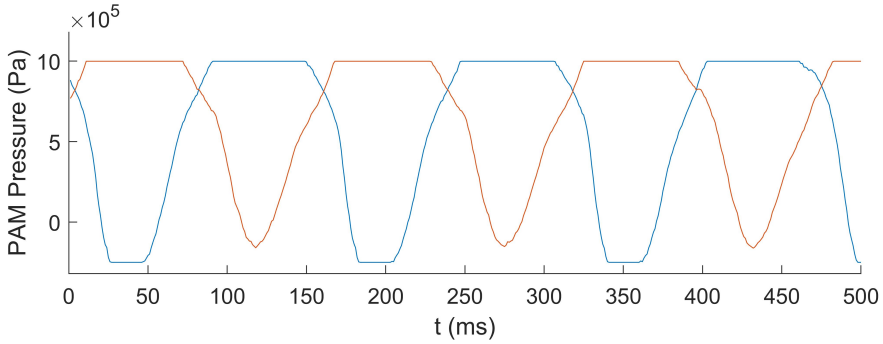
(a) System input, span length as a percentage of maximum span length.



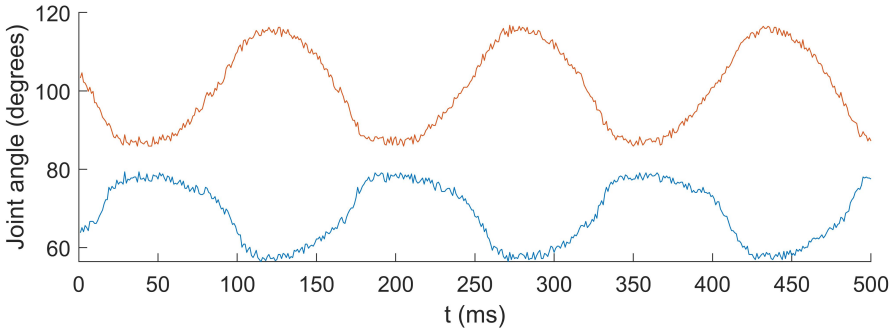
(b) Dependent variables, y_3 blue, θ_3 orange.



(c) Inverse kinematic output, θ_0 blue, and θ_1 orange.



(d) Measured Pneumatic artificial muscle (PAM) pressure, leading PAM in orange, trailing PAM in blue.



(e) Measured Joint angles, θ_0 blue, and θ_1 orange.

Figure 5.19: Presented are the outputs at each stage of the control system these form the input to the subsequent stage. (a) the system input; span position as a percent of maximum span, (b) the output of the dependent variables based on avian derived relationships, (c) inverse kinematic output joint angles, (d) resultant measured PAM pressures, (e) measured joint angles produced by the concept.

may be preferable at this stage. The flexibility in the equations allows for further development if necessary.

The variable θ_3 is also shown in figure 5.19b. Based on a sinusoidal curve out phase with the input a more standard output is presented in comparison to the y_3 value. Another phase shift can be observed in the subsequent stage of the control system, shown in figure 5.19c. This figure shows a plot of the 'shoulder' angle and 'elbow' angle, θ_0 and θ_1 respectively. The phase change in θ_0 is due to the axis change required for the kinematics as the reference datum changes for application to the muscles. This effectively sets the two joints out of phase. The opposing arrangement of the artificial muscles in each joint explains this system's output.

The feedback angle shown in the final plot in figure 5.19 makes clear a limitation in the system made clear by early joint angle validation testing. The primary limit on the muscles is force and when arranged antagonistically the opposing force reduces the operation angle range. A comparison between the desired angle from the avian results/ kinematics and the measured output angle shows a noticeable difference in amplitude. An approximate average of 55% reduction in actuation strain can be observed when driven to the same joint deviations as measured from the avian used for the system.

However, mimicking avian manoeuvre behaviour precisely is only of benefit if the result is improved flight performance over current morphing UAV and MUAV concepts. The control system in comparison with existing concepts gives a similar indication of performance. Chapter 6 explore the aerodynamic implications of avian based control. However, it is clear from the validation testing while the amplitude is not achieved the output is defined. Each of the joint angles matches closely in phase with the input demanded of the kinematics. The output span is therefore matched through the use of a biomimetically derived quasistatic control system.

5.4 Wing Control Conclusion

In this chapter, the avian wing span-wise morphing concept was modelled, and with the application of inverse kinematics, a control system is derived to allow simplified span-length positioning. Similarly, the desired wing area was also presented as a possible input for the system. The model is based on PAM force models to model the pneumatic system driving each joint individually. The mechanical system of each joint is subsequently used to produce a direct kinematic model for wing tip position, and the inverse was determined for control. The validity of both the model and system was experimentally tested on a fixed semi-span prototype rig of the morphing concept. Feedback is then introduced. Potentiometers are embedded into each joint to provide joint angle feedback. A method for frequency response system identification was presented for applications in deriving an experimentally derived model. This method showed limited success in the application case of pneumatic artificial muscles due to their highly nonlinear characteristics. It was shown however, that over a narrow range of applied frequencies a relatively simple first order transfer function could provide an adequate estimation of the system response. The control system based on joint angle was deemed to be too low-level for meaningful control. A method for defining dependent input variables to a single span length variable was presented. These dependent inputs would be defined through the relationships observed in similar avian flight manoeuvres. The kinematics used in the wing joints of avian were presented as measured using motion capture, and the dependent variables were defined. While the span-wise morphing concept cannot match the full physical range of motion exhibited by the avian studied, the control of the wing was successful. A system was presented with a single span-wise input that would reliably and accurately control the span-wise morphing concept.

Chapter 6

Wind Tunnel Experimentation

In the previous two chapters, which presented the design of the span-wise morphing concept, the aerodynamic performance of the lifting surface was explored computationally. The control of the concept also developed in a purely unloaded case. This chapter looks at the performance of the concept under load. Outlining both the morphing in the measurement of surface deflection and the lifting surface aerodynamic characterisation, looking to validate the CFD programme.

A static distributed loading was applied to the prototype structure based on the loading found from computational experimentation. The actuation was then measured both internally via embedded absolute encoders and externally using stereographic imaging. This also provided insight into the previously unknown three-dimensional motion of the concept. The motion recorded is then compared to the measured motion of the avian explored in section 3.5. Notably, the behaviour of the joints during overshoot. This subsequently allows conclusions to be drawn regarding the applicability of the bio-inspired control and motion of the concept.

Once the concept's performance was validated through simulated loading, a programme of wind tunnel testing was carried out. The implementation of an aerodynamic lifting surface to cover the actuation mechanism of the concept is presented. This follows the aerodynamic profile defined in section 4.1. The prototype produced is evaluated against surfaces set forth in the current literature. The concept prototype with an aerodynamic lifting surface then undergoes a series of static wind tunnel tests to produce the respective polars to determine aerodynamic characteristics. Comparisons are then made in reference to biomimetic literature data and the CFD results of the concept. Quasi-static measurement is then undertaken to ascertain the unsteady response of the flow due to the actuation of the concept. The nature of morphing concepts is inherently variable with respect to time and a series of results looking into the span-wise response is also presented.

6.1 Structural Testing

Biomimicry is commonly found at the forefront of modern engineering design. This is perhaps most true for the development of small uncrewed aerial vehicles, where aeronautical design is unrestricted from traditional constraints. Uncrewed vehicles have also served as the platform on which to prove such concepts for integration into piloted platforms [6]. Subsequently, the number of biomimetically derived concepts has increased. The reasons are perhaps obvious: the opportunity to improve effi-

ciency through material and surface optimisation [142] [25], increased performance via improved control authority [24] and bio-inspired flight profiles, amongst others [143] [144]. In this section, the development of a biomimetic UAV concept will be approached from the field of morphing structures. These structures allow the alteration of the aerodynamic shape of the vehicle on mission to suit the flight regime. When applied to the wing of an aircraft, advantages can range from reduced drag to increased stability or control, and it is an area with a significant number of morphing concepts. Presented here is the application of a span-wise morphing concept as the basis for the structure of a small uncrewed aerial vehicle. In this section, the structure is optimised through the study of macro-structural avian anatomy. The lifting surface morphing is then achieved via pneumatic artificial muscles (PAMs), and the performance is characterised in the context of a UAV application.

When considering the application of a morphing structure in the airframe of a proposed aircraft one of the primary specifications relates to the consistency of the structures deflection. This is perhaps more acute when related to morphing lifting surfaces. The geometry of the lifting surface directly affects the dominant aerodynamic forces generated and therefore so does, by extension, any morphing. Obviously, this is the intention in most concepts, and so the change in aerodynamic forces is desired. However, with any controlled system, there is a steady-state error. This can arise from the control itself or the structure, both of which therefore need to be quantified for the application of any proposed concept. The compliant nature of actuated structures typically results in a structure with reduced stiffness. However, this is not given, and particularly in recent proposed system concepts, this reduced stiffness may only be present in a single axis, thus allowing for it to be compensated with other structural elements. However, there is still an increased emphasis on aeroelastic effects [169] as a result of this lower stiffness. It may be considered that the primary mechanism for precise repeated motion is the driving actuation system. Pneumatic artificial muscles are continually considered for morphing concept applications in UAS [170]. While more commonly applied industrially in manufacture and robotics a high specific strength has resulted in suitability for morphing structures where reduced weight at the point of use, such as a structure in motion, is desirable. Typical of actuation development much has been discussed in the modelling and control of these actuators. Literature has also investigated reliability and fatigue characteristics [171]. Similarly, predictive methodologies have been developed to assess the accuracy of the PAM-based actuation system in a morphing lifting surface [172]. This employed fibre Bragg grating sensors to monitor PAM deflection, which is not applicable in a joint actuation system such as the span-wise morphing concept. However, it is clear that the aerodynamic loading cannot be neglected. Similar, large surface area deflecting lifting surface concepts have been evaluated with respect to these quasi-static forces [173]. In particular, a case of a Z-shaped structure exhibiting a span motion coupled with an out-of-plane motion similar to a gull-wing. The structure was evaluated via simulation whereby the motion of the structure was modelled via a Craig–Bampton vector synthesis method. The aerodynamic forces were subsequently derived via an unsteady vortex lattice method. Proven to be an effective holistic methodology this does not, however, represent the minor perturbations inherent in an imperfect mechanism.

The span-wise morphing concept consists of three linked members analogous to the skeletal structure of the avian wing [174]. Each joint exhibits one degree

of freedom, on the same plane, providing the end effector with three degrees of freedom. In this instance, the end effector relates to the wing tip, as such providing the concept with lateral span and chord motion in addition to rotation about the vertical axis, resulting in an effective wing sweep. The motion of the concept is under-constrained and so an effective relation between the joints is required. While a simple ratio is considered for the concept it is found that the avian, from which the linked members are derived, does not exhibit this motion. Analysis of avian motion capture data indicates an interrupted joint rotation for the extension of the wing structure. This forms the basis of a UAV system designed for effective span-wise control of the lifting surface. The structure impacts the aerodynamic and stability characteristics of any proposed aircraft into which it is incorporated. The joint relationships and the effectiveness of their actuation therefore play a significant role in achieving increased effective aircraft control, particularly in the structure's quasi-static response to span changes in flight, where the lifting surface itself is applied to affect control in roll and pitch.

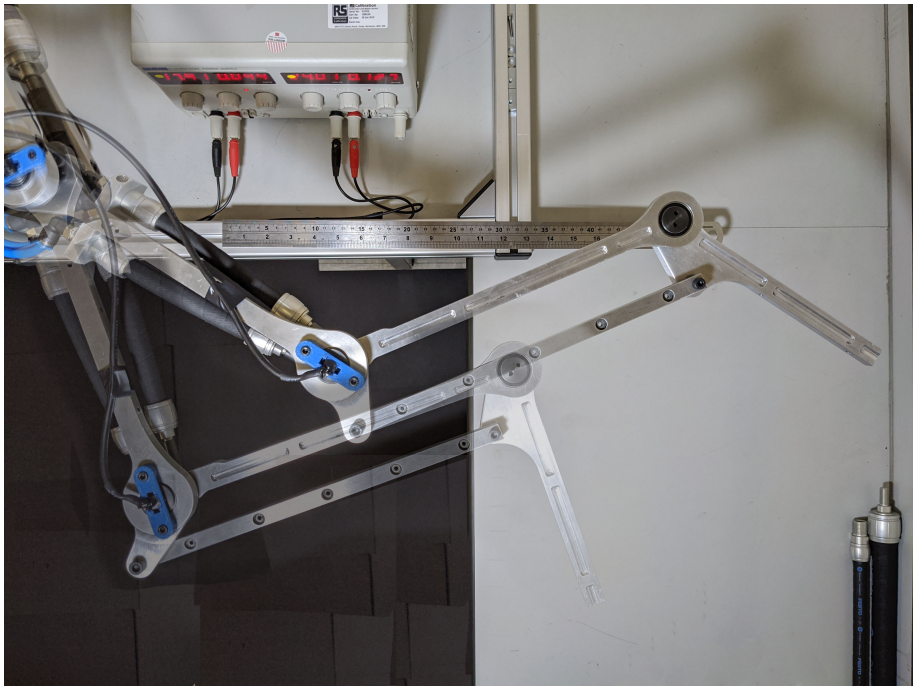


Figure 6.1: Span-wise morphing structure in a fully extended position and retracted overlaid. Each pneumatic artificial muscle (PAM) antagonistic pair is visible actuating each respective joint.

The proposed wing structure utilises this concept for an internally driven skeleton, shown in figure 6.1. The member lengths impact the morphing performance of the structure. To achieve a lifting surface area change sufficient to impact the performance of the vehicle a study was conducted into the avian skeleton on which the concept was based. Data collected and collated [132] was applied in an optimisation process to produce member lengths for the structure. This morphing structure was subsequently manufactured. Pneumatic artificial muscles actuated both the analogous 'shoulder' and 'elbow' joints through an antagonistic bell-crank mechanism. The motion-captured relation between the three joints was applied to the structure. The pneumatic muscles themselves are presented and sized to reproduce both the

simple ratio and biomimetically derived motion. Mechanical geometry is also assessed as a contributing factor to the motion and the wrist actuation via a parallels mechanism is further developed in relation to the biological captured motion. However, the aspect with the greatest effect on the structure's motion is the specification of the pneumatic system. These contributing factors are presented and applied as variables in the structure's performance.

The structure achieved an angular range of motion of 45° and 30° in the 'elbow' and 'shoulder' joints, respectively. A process to determine the deflection of the wing structure was undertaken. The contributing variables to the motion of the structure independently analysed as to the impact on the performance of the structure. Photogrammetry and static laser 3D scanning produced an evaluation of the prototype in terms of span and area morphing percentage. As well as factors resulting from the two joint motion types such as deformation under load and morphing consistency. Overall, a 38% span reduction was observed in line with similar concepts and the original span-wise morphing concept. While the biomimetically derived motion of the joints found to contribute to the reduction in out-of-plane deformation in the quasi-static response of the structure.

6.1.1 Position Experimental Setup

Stereo-photogrammetry-based metrology was the measurement technique employed as the external validation tool for the morphing concept. The concept being static resulted in a more repeatable setup across span-wise actuations. Thus, increased precision could be achieved via a visual measurement system as opposed to range-finding systems producing point clouds. Visual-based metrology can also exhibit a measurement rate in excess of $2 \times 10^5\ Hz$ providing insight into the dynamics of the objective system. Two Photron Fastcam Mini UX50 cameras were mounted together to provide the stereo setup, at an angle from the normal plane of the subject of 12.5^o. These were triggered simultaneously and synchronised through all recordings. As the cameras were static and frames taken synchronously, only a single calibration was required to adjust for discrepancies in the rig and lenses. Fixed prime 100mm lenses were set up fully closed down at an F24 aperture, providing the greatest depth-of-field possible for this system. Increased depth-of-field in this instance ensured points of interest on the concept that were set back from the focal plane did not become unfocused, decreasing accuracy in determining position. At a stand-off distance of $606mm$ the controlled volume comprised $40mm \times 50mm \times 50mm$. A small volume, as used here, provides the resolution required to distinguish both the hysteresis and small perturbations immediately following the concept actuation. It was therefore employed for the capture of the structure outboard point, which can determine the true pose of the system via the same kinematics/inverse kinematics which drive the joints. To provide contrast in the surface of the material high contrast markers were positioned on the end of the outboard member. These were black and white two dimensional paper marks as it is the contrast between the colours that is tracked as opposed to the colour or marker material itself. These are labelled in figure 6.2 along with the cameras as configured for the tests looking at the wing tip.

Alongside the static and quasi-static performance of the morphing concept alone it was considered necessary to identify the positional performance of the concept while loaded. As stated previously the pose of the concept impacts the platform

area of the lifting surface. Whilst it is tempting to treat this dependency as proportional the nature of the aerodynamic surfaces to cover the concept result in a relationship difficult to quantify outside of the wind tunnel. The overlapping or morphing surface components result in both span-wise and out of plane geometric changes which are not consistent across the full span change. There is therefore potential for this to be highly non-linear and potentially dependent on uncontrolled variables. Temperature effecting the elasticity of flexible polymers is one example of an uncontrolled variable which could significantly vary and change the lift produced by the surface across different span extensions. A mitigatory process for the impact of these differences in pose is to quantify the likely deviation under the aerodynamic load. However, the difficulty presented here is in simulating the load. While the ideal case would be to load the model using an intended lifting surface aerodynamically, this presents an issue in measurement. The lifting surfaces considered as part of the concept presented in 6.2.1, obscure the internal members resulting in position measurements being obviated to the surface itself. While applicable, this would not allow a distinction to be made as to the base structure's repeatable motion. Static loading was therefore achieved via weights distributed across the structure. Point masses were applied on each structural member representing the distributed load transferred to that section of structure through the lifting surface. A setup of cradles and load actuators was considered, however, discounted because the concept's actuation did not allow a consistent distribution of the load. Applied weights for simulating loading have the notable disadvantage of affecting the system inertia. As a result, no quasi-static testing was conducted under simulated load.

The concept test rig consists of the span-wise morphing concept rigidly affixed to an extrusion frame in turn bolted to the measurement reference ground. While under simulated static load the concept was inverted. The reference axis was set via the model positioning. The span axis was set by ensuring the aluminium extrusion of the concept and camera rig were parallel. As the pneumatic artificial muscles (PAMs) are rigidly set at their respective angles in relation to this extrusion the span motion is by default aligned, thus the cameras are set too. This axis is set at a level via reference to a laser level. The longitudinal axis along the concept fuselage was not mechanically fixed and therefore exhibited a quantifiable error. This was adjusted by realignment within the meteorology post-processing software. However, it should be noted that this was achieved via the use of the markers themselves. Three markers on one face of the concept, shown in figure 6.3, were set up for this purpose. The assumption was made that the component surface, on which these markers were adhered, were vertical and parallel with aforementioned laser level thus ensuring the span-chord and span-out-of-plane planes were perpendicular. While, this was brought to within an acceptable tolerance this could not be measured and so the error is not quantified. This was also considered the largest source of error in the measurement process due to the systematic nature of the camera and related software. An angular error of $\pm 0.5^o$ was therefore taken representing the maximum machining error in the part. However, it should be noted this applied exclusively to the axis displacement results which are derived from the overall displacement which itself is not included in this assumption.

Calibration was the term given by the software for the process of removing lens and angle distortion. This also included the photogrammetric process of calculating the unknowns in each projected view of the cameras. Commonly completed in more

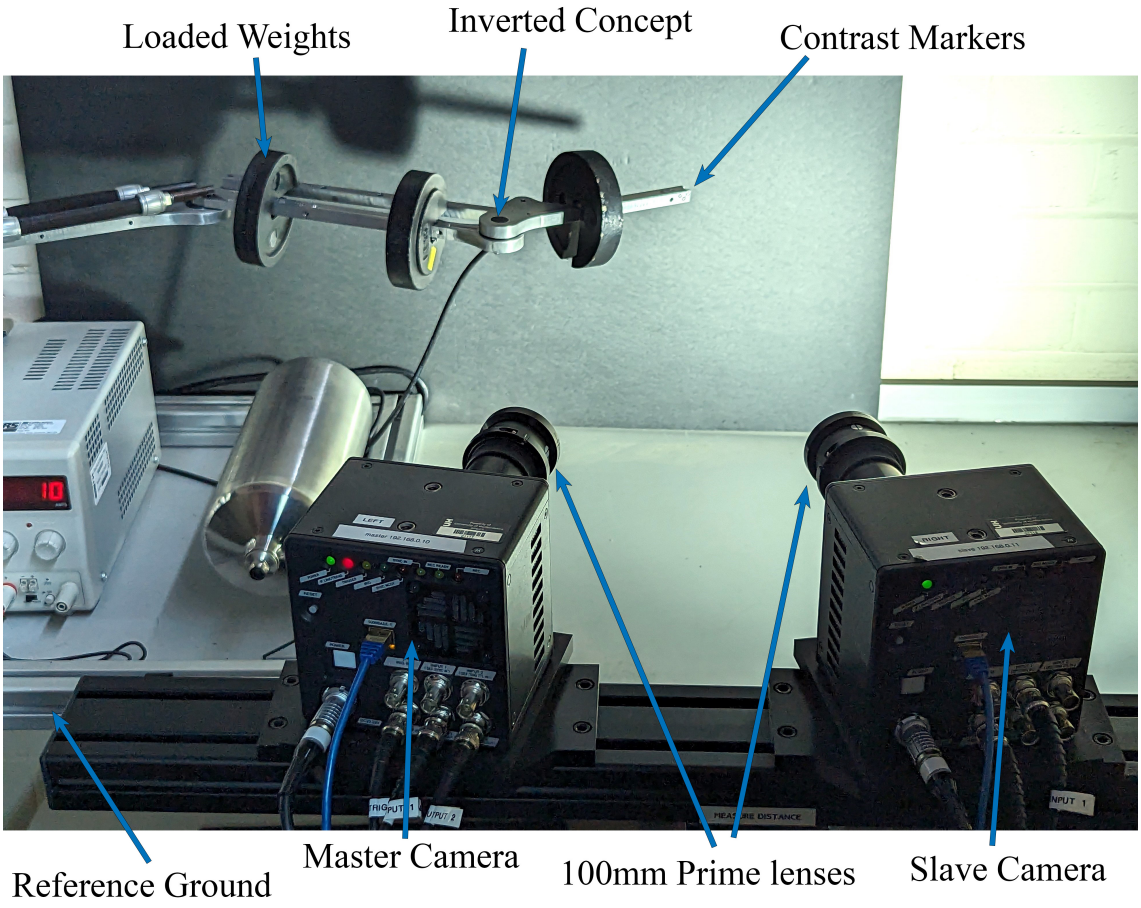


Figure 6.2: The stereo high-speed camera setup shown with the simulated morphing concept loading. These cameras were run at 500 Hz and configured here to track the wing tip position within a capture volume of 40 mm x 50 mm x 50 mm. Visible on the concept are contrasting white and black markers this contrast allowing increased accuracy in identifying the concept's position.

manual photogrammetry with a chequerboard pattern of known dimensions this was not used in this case. A coded board was used, that is a board with coded shapes identifiable via computer vision. The industrial metrology software used recalled the required known physical dimensions based on this code unique to each size of calibration board. This is known to reduce systematic error often found in the process of photogrammetry as the positioning and interpretation of calibration objects is subjective.

6.1.2 Concept Precision

To characterise the concept's ability to repeat a retraction and extension cycle the end-point was measured in reference to a starting position. This initial position represents the PAMs being brought to their extended configuration from a depressurised state. Whilst allowing the difference in start-up and normal cycle behaviour to be identified, this also provided a reference position from which to measure deflection of subsequent cycles. A value for deflection could then be ascertained from

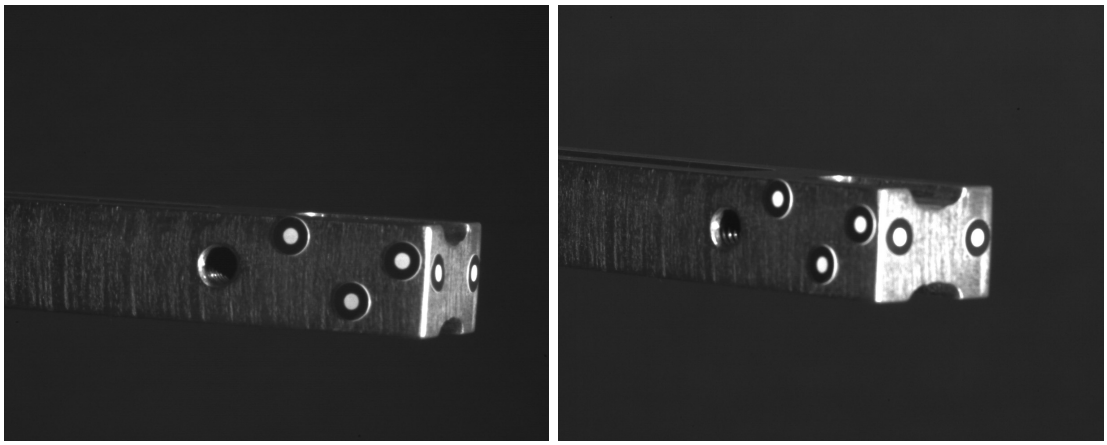


Figure 6.3: Left and right camera views as calibrated for the wing tip measurement volume. Each view depicts the wing tip in the non-inverted orientation, as taken unloaded, with the contrast markers in place.

the average values measured across the five tracked points on the concept for each cycle. Via the process of photogrammetry the total displacement is derived from the angels measured in the projected view. Thus, the global coordinate position of the markers in the cycle must be found from this and in reference to the aligned axis. As presented in table 6.1, where the x-axis represents the span-wise direction, the y-axis out-of-plane, and the z-axis the longitudinal axis.

To obtain a representative sample, the concept was set via a previously developed position control system, to target a quasi-static sinusoidal wing span length. This allowed a set of post-cycle positions to be collected within a single camera save, eliminating the risk of averaging dissimilar data. The sine frequency was set at 1 rad/s with the cameras triggered via this system at the peak/maximum extension. Due to camera hardware limitations, the sample size was 500 cycles. Mean averages derived from the unloaded sample are presented in table 6.1 with the overall average displacement of 1.2656 mm. Representing 0.14% chord length of the concept this is indicative of a repeatable span-wise morph. Notable is the distribution of displacement magnitude across the components. The axis out-of-plane dy exhibits the least deviation across the sampled cycles and similarly shows the lowest maximum measured deviation of 0.3973 mm. This is the axis along which the concept has no intended motion so this is perhaps expected. As part of the joint mechanisms within the span-wise morphing concept the the joints contain disc springs designed to resist motion in this axis. Arguably the more significant direction of motion is dx the span-wise motion which showed a mean average deviation approximately half the overall displacement and 0.07% of the semi-span length. However, the maximum represents 0.13% deviation as a percentage of semi-span and given the distribution the cycle on which these present is essentially random. A span difference between the two semi-spans must therefore be considered to be a maximum 0.27%.

In the case where $dz = 1.0393$ mm that is the longitudinal axis in line with the body of the concept aircraft. It can be determined that the axis exhibits an increased deflection over dx when related to the intended motion in line. The chord motion of the wing tip is directly related to the span via the aforementioned biomimetic extension control for the concept. Dependent on PAM actuation pressure the chord

motion can be approximated for this series of cycles as 200 mm. The resultant relative error in repeated position is 0.52%. It is arguable that this is not a direct comparison, however, it highlights the difference in accumulated error in the actuation system. It is hypothesised that the error in this axis is due to the primary joint responsible for the dz being the 'shoulder' joint, the inboard joint. This, with an increased moment to the centre of mass, could result in this noticeably higher position error.

The wingtip position error in the loaded quasi-static case is similar with values representing an insignificant change over those observed on the unloaded concept structure. These are summarised in table 6.2. The overall trend in these values does represent an increase in position error. The most significant of which is in the maximum deflection for the y out-of-plane axis approximately doubling. As this is the loading axis this is perhaps as expected but still leaves the position error for the axis in relation to the span motion at 0.1%.

It was noted in avian kinematics experimentation, summarised in previous literature [174], the apparent un-importance that motion in the dz axis is regarded in the behaviour of avian wings. In the span extension of avian wing an overshoot was observed, ranging up to 23.2% of the overall joint angular motion during span extension. It was concluded that this typically negative feature of quasi-static response was offset by the decrease in rise time it facilitated in the span axis.

The quasi-static response is plotted in a series of plots under figure 6.4. The aforementioned z-axis motion here exhibits the overshoot found in the avian motion. The overshoot is not as significant as observed in the biological wing at approximately 2 mm or 0.2% as opposed to 23.3%. This leads to the conclusion that the concept is currently underperforming in terms of rise time and time to steady state. This would seem to suggest that the concept is too conservative in its performance at the detriment of quasi-static response.

Table 6.1: Wing tip error observed in the unloaded concept across n = 500 cycles. Span-wise morphing concept was actuated as pressurised at 6 bar. Error referenced to an initial position

Displacement Direction	Minimum (mm)	Maximum (mm)	$\bar{x}$ (mm)	σ (mm)
d	0.204	2.560	1.265	0.573
dx	0.050	1.327	0.604	0.272
dy	0.001	0.397	0.170	0.163
dz	0.004	2.184	1.039	0.653

Table 6.2: Wing tip error observed in the loaded concept across n = 500 cycles. Span-wise morphing concept was actuated as pressurised at 6 bar. Error referenced to an initial position

Displacement Direction	Minimum (mm)	Maximum (mm)	$\bar{x}$ (mm)	σ (mm)
d	0.213	2.666	1.237	0.525
dx	0.023	1.219	0.712	0.339
dy	0.013	0.906	0.345	0.232
dz	0.076	2.546	0.857	0.524

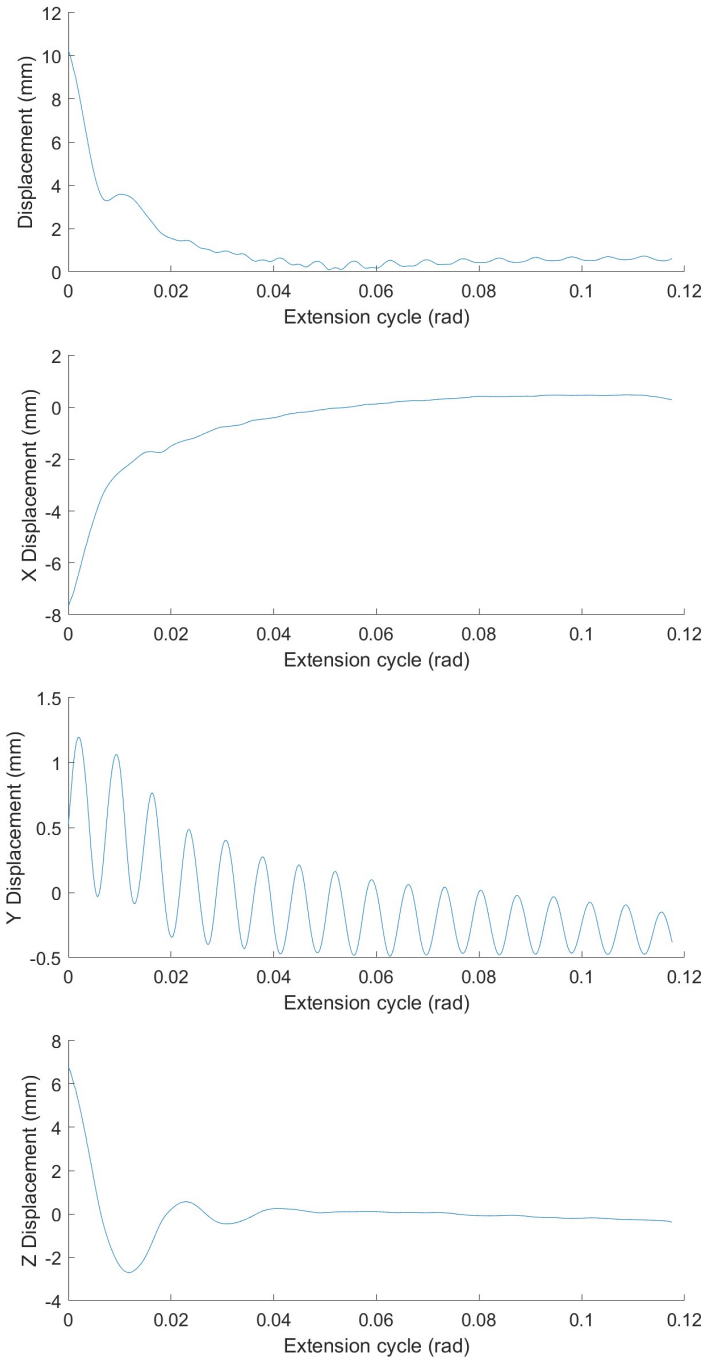


Figure 6.4: The quasi-static system response at the approach to a steady state after a 1 rad/s sinusoidal span position input. Plotted against the extension cycle angle where the datum represents 1 rad from the input signal for maximum extension. Note only the final 10 mm of the motion is shown due to the limitations of the cameras used.

The quasi-static response for the span-wise morphing concept is evaluated under simulated static aerodynamic loading. The concept is prototyped with structural members forming the basis of the morphing actuation system. This actuation is measured both for a quasi-static position and quasi-static displacement via external photogrammetry-based metrology. The morphing concept exhibits actuation in both the span and chord axes. This is achieved through a three-jointed mechanism

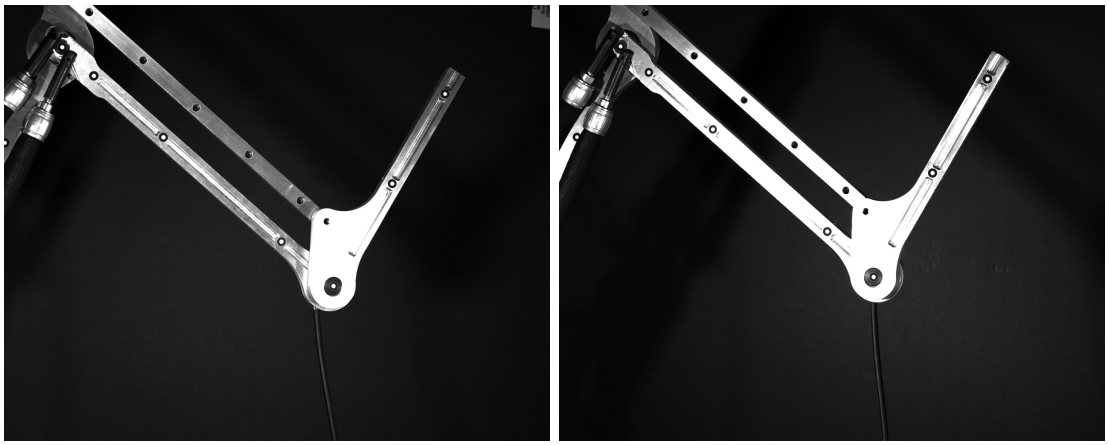


Figure 6.5: Left and ring camera views as calibrated for the full concept measurement volume 400 mm x 300 mm. Also note the contrast markers in place on the members and on the joint axis'.

analogous to an avian wing. Actuation of the two inboard joints is affected by an antagonistic pair of pneumatic artificial muscles (PAMs) acting to produce an angular displacement.

In the quasi-static case is presented for both the unloaded and the static aerodynamic loading case. The wing tip position of maximum extension is evaluated for a change in displacement over consecutive morphing cycles. These cycles represent a significant span reduction and extension. It was observed over a series of 500 cycles that the concept presented a maximum displacement of 0.28% the extended semi-span length. Perhaps of more note is the maximum deviation in the span axis directly impacting the primary direction of intended morphing. This value for deviation was found to be 0.07% the semi-span and considered negligible in terms of direct effect on planform area. However, it is noted that any indirect effect on aerodynamic performance such as impact on pressure distribution is not considered in this evaluation; further characterisation is required.

The quasi-static case is presented for only the unloaded but not the static aerodynamic loading case. It is noted that the simulated static loading is not suitable for a quasi-static evaluation. It is proposed that this would require computational simulation as any physical method for applying a quasi-static load would not be feasible with this amount of concept motion. In comparison to the avian motion data from which the concept is derived, it is concluded that the concept is underperforming, that is to say, the conservative errors in the response could be increased to improve position response in relation to time.

6.2 Wind Tunnel Methodology

The tunnel used throughout the experimentation of the span-wise morphing wing was the University of Hertfordshire's 5 ft x 6 ft research tunnel; a rectangular cross-section open return tunnel. As is common for this generation of tunnel in a higher education institution, this tunnel has been retrofitted both with an updated drive system and a measurement system. While the drive system was replaced previously, the measurement system was set up for the morphing concept programme. The validation of this setup and quantification of it's error was required and forms part of this chapter.

The model upon which the wind tunnel testing took place was based on the physical structure manufactured as part of control system validation in chapter 5. The structure, originally scaled to typify a small fixed-wing UAV, represents an appropriate scale for testing, allowing interpolation to both larger scales, such as large UAS, and smaller scales looking towards micro-UAS, which are finding increased application alongside the miniaturisation of other mission technologies.

6.2.1 Concept Lifting Surface

Stiff yet compliant feathers found on most avian species, including those on which the span-wise morphing concept was based, represent an ideal in terms of bio-inspired design. Actuating structures applied in aircraft are often required to compromise on the material of the sub-structure. These can be compliant to the actuation providing a morphing structure with the inherent performance advantages, such as reduced aerodynamic impact. Alternatively, they can be structurally rigid, with suitable resonance characteristics and reduced aerodynamic-induced flutter. These represent opposed characteristics in a structure, and as such, a significant amount of literature can be found presenting concepts to meet this compromise [113]. Indeed, the greater a concept's morphing magnitude, the less suitable traditional systems, such as aluminium-based semi-monocoque structures, become. While no solution has been widely adopted, one is prevalent in biology, notably in avian biology. Thus, the problem of producing a structure, material, or skin alongside a morphing system has been commonly approached with biomimicry.

C. Thill et al summarised current approaches in biomimetic skin in 2008 [113]. Identified as skins with potential were elastomer materials, auxetic materials, and smart structures. Elastomer materials are perhaps the first solution one would propose for this problem. Some of the most mature adapted structures propose elastic skins [97], while the methodology is still employed by emerging concepts [175]. These address a second specification arising from the nature of biomimetic concepts. That is the inherent complexity derived from the highly three-dimensional motion of avian. Thus, statures featuring what might be referred to as compound curves in reference to geometry but results in what has been referred to as poly-morphing when in reference to the requirement to deform in compounding directions. While this highlights the problems encountered when elastic material is applied, the span-wise morphing concept presented here consists exclusively of skin deforming unidirectionally at any given point.

Aside from multi-directional morphing requirements elastomers are considered largely unsuitable for increased strain applications. Where elastic material can ex-

hibit buckling resulting in aerodynamically disadvantageous skin deflections. Auxetic materials, which exhibit a negative Poisson's ratio have been highlighted as applicable to morphing structures. These materials are in themselves biomimetic, having been observed in mammalian skin [176] and cork, which has a Poisson's ratio of approximately zero. Artificial auxetic materials are typically cellular in nature, with more structurally complex lattice structures also being developed [177]. The advantage of this is a variable ratio and increased curvature in the structure.

A previously proposed aerodynamic structure referred to as a skin was presented in chapter 3. The concept consists of a self-supporting internal structure typical of a small UAV. These internal members also facilitate and are specified for the loading of the pneumatic actuators. This is the critical loading case, and therefore, the members require no additional structure to support the aerodynamic load. The main aerodynamic structure is therefore only required to support the distributed pressure across the body and in the proposed concept consisted of fused deposition modelling (FDM) or fused filament fabrication (FFF) produced components. The argument made regarding the use of a load-bearing internal structure is in allowing the skin to be specified primarily towards the juxtaposed characteristics of stiffness and compliance. This results in an aerodynamic surface that better aligns with the actuation of the wing or structure.

Recent advances in additive manufacturing technology provide the opportunity to produce flexible polymers in geometries required for application in large percentage surface morphs. Polymers which exhibited an increased elastic deformation before yield were previously only viable in limited manufacturing processes such as injection moulding. These processes imposed limitations on the geometry that could be achieved in the part from requirements such as cooling or critically mould release requirements. These are not critical in FDM manufacturing, masked stereolithography apparatus (MSLA), or selective laser sintering (SLS) common additive manufacturing techniques. Previously flexible filaments could not be used within deposition systems employed in FDM machines. However, given the rapid advancements seen due to projects such as Reprap components with these properties can be produced.

The span-wise morphing concept consists of three actuated joints at which point the aerofoil thickness is approximately 70mm. The axis of each joint can be taken at one-fifth the chord length or approximately 50mm. Joint angular defections of up to 60^o result in a maximum skin point defection of 73mm. This is taken on a leading edge point rotating about the wrist. The deflection requirement for the skin largely excludes material solutions with simple structures. Materials exhibiting elastic deformation over the required surface element length change, up to 60% for the leading edge wrist joint in the proposed morphing concept, also exhibit this yield below the aerodynamic pressure found through initial analysis of the concept. These are likely to deform during normal flight conditions.

An arguably more traditional approach to skin deflection is the application of overlapping or nesting stiff geometry. This is widely employed throughout industrial applications as a mature technology to cover the motion of trailing-edge-based high-lift systems, as a typical example. When applied in a cylindrical form commonly referred to as telescoping this method can be both passive and provide higher percentage surface area changes than the aforementioned flexible structures. Due to the rigid material they are also typically less subject to buckling during actuation. In

the case of the span-wise morphing concept overlapping skin panels also proved more viable to reliably manufacture as the FDM rapid prototyping technology requires less specialised equipment than flexible polymers.

Acrylonitrile Butadiene Styrene (ABS) FDM produced panels comprised the leading edge structure of the wind tunnel model, depicted in figure 6.6. The primary panels form the leading edge each corresponding to a section of the actuated structure to which it is mounted. In figure 6.6 the left member connects the first and second joint. The second joint itself, which is analogous of the avian elbow, is spanned by the first section of telescoping panels; comprised of the blue abs in the figure. The central member of the figure between joints two and three is swept forward in all actuated states. It also houses the mechanism by which the actuation force is linearly transferred to the third joint, this joint is similarly analogous to the avian but of the wrist joint. Outboard of the wrist joint is the wing tip member this is a single skin panel which extends beyond the internal support structure. The sizing of this panel poses another area of compromise. The leading edge of the section actuates upwards of 90^o between tangential and parallel to the flow. Increasing the span of this section proportionally increases the percentage span change of the concept at a higher rate than the other two members. It is therefore logical that this section span be increased until limited by another factor namely structural stiffness. The aerodynamic implications for this extended wing section are to be explored in this section in reference to the change in lifting surface area that the section affects. The panel prototyped here represents the proportional size of the section, in relation to the other two sections, as derived from examination of the avian in chapter 3. The section is also entirely ABS as no overlapping composite components are needed due to the wing taper allowing the necessary clearance with the inboard structure.

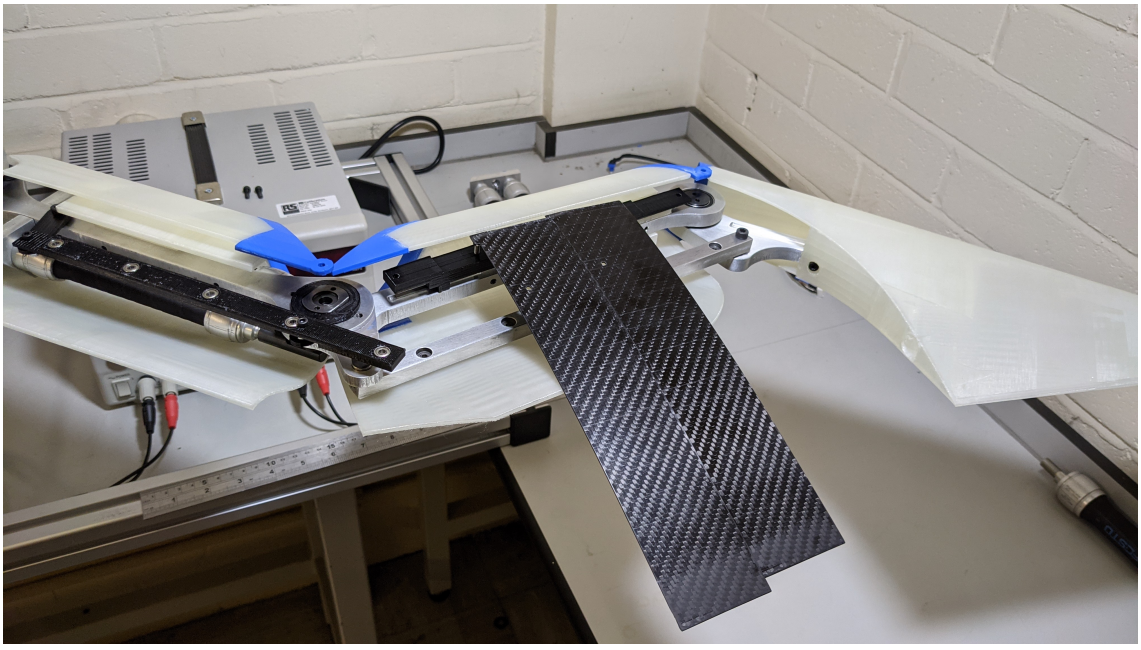


Figure 6.6: The span-wise morphing concept with a lifting surface leading edge attached. Also shown are two trailing edge carbon fibre plates or 'feathers'. Linking mechanisms, comprising one aluminium and two ABS members, for both the wrist joint and feather actuation can be seen.

The composite structure comprises ten carbon-composite plates to form the up-

per surface and trailing edge of the aerofoil skin. Both the inboard and mid-sections of the concept presented a section of the trailing edge with an overlap greater than 100mm which would require a material surface are change $> 60\%$ give the proposed section lengths defined by the avian-based member lengths. A similar problem as in the leading edge and outside the scope of most flexible material with suitable rigidity, particularly with the reduced cross-section present at the trailing edge. However, this reduced thickness at the trailing edge proved conducive to telescoping or overlapping geometry, again similar to the leading edge. The thickness necessitated a composite material with decreased strain under load and resistance to bending. Each plate consists of a 1.5mm thick bidirectional layup and makes up four fifths of the aerofoil chord. A more unidirectional material layup was considered more suitable however for a tunnel model this was forgone to reduce manufacturing complexity. Optimisation of the structure for weight and integration into an airworthy vehicle was not conducted as the skin concept presented at this scale was considered impractical due to the mechanisms that were considered to become more efficient as the concept was scaled up. To ensure the plates overlapped correctly and the upper surface of the wing skin remained cohesive, the plates were passively actuated. Two parallel bar mechanisms comprised of ABS FDM-produced parts are attached at approximately two-fifths of the chord from the leading edge. This resulted in a pivoting motion about the leading corners of the plates which were pin jointed to the leading edge components. This can be seen in figure 6.7 where both the pins can be seen on the upper surface of the concept when fully assembled.

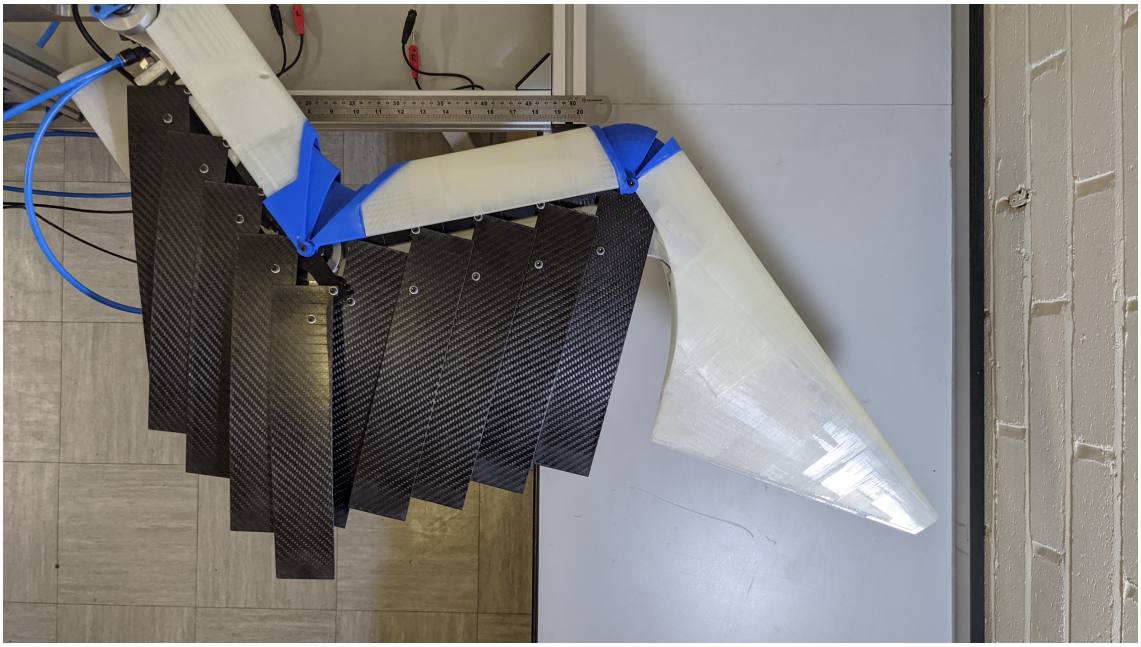


Figure 6.7: The span-wise morphing concept with lifting surface assembled, including leading edge and carbon composite upper-surface and trailing edge. Presented in mid-actuation approximately 550mm semi-span.

This motion in the composite plates keeps them perpendicular to the wing span-wise direction. Aside from the overlap, this forced perpendicularity allows the trailing plates to result in a more consistent chord length across the range of span lengths.

In the case of a pivoting wing increased sweep results in the chord length parallel to the flow similarly increasing. Similarly, the aerofoil section experiencing the flow becomes elongated longitudinally, notably negatively impacting the result of sheer forces on the overall drag resultant from the wing. This aerofoil section distortion coupled with the changing aspect ratio can also lead to unpredictable aerodynamic behaviour that the parallel plates mitigates.

Overall the wind tunnel model presents a maximum semi-span of 900mm with a nominal chord length at full extension of 305mm. This chord length increases with span retraction to 404mm as measured parallel to the flow. The concept prototype exhibits a span-wise morphing actuation of 315mm between the position of the wing tip in an extended and retracted state. This deflection is comprised of an angular deflection of 25 degrees at the first shoulder joint, 35 degrees at the second wrist joint, and 35 degrees at the third wrist joint. These values are notably reduced from those measured during actuation of the internal structure alone.

6.2.2 Wind Tunnel Setup

The concept prototype was positioned within the 1.52m by 1.83m working section of the open-return tunnel 2.44m aft of the inlet cone. The wing itself was radially bolted to a mounting plate itself inline with the tunnel ceiling. This plate formed the first component of the balance stack developed as part of this wind tunnel programme. Above the tunnel ceiling plate was mounted in turn: the yaw action bearing system, connecting plate, balance, and tunnel structure plate. All specified to $0.1mm$ defection under the balance maximum load. The balance stack was installed to an angular deviation of $30'$ arcminutes between the tunnel centre line and balance measurement axis. The balance comprised six axes each with a full bridge strain gauge. Calibrated externally the balance was rated to an accumulated error of $\pm 0.05\%$ of the axis force loading. Axis loading consisted of z-axis $500N$, y-axis $200N$, and x-axis $200N$. While the moment about each axis could be loaded to a maximum of $20Nm$. The tunnel coordinate axis was defined as depicted in figure 6.8 where the positive y-axis represents the lift generated normal to the longitudinal axis of the tunnel and the negative x-axis the drag parallel to the flow. Amplification of the individual axis signal was completed via a combined exciter/amplifier and AC/DC converter (BX8-HD44). $11.4kHz$ first order input filtering was also processed by the amplifier. Digital filtering was also conducted within the hardware this was configured as required throughout the experimentation.

Input filtering is used in particular to remove an increased level of background noise during the acquisition of some polars. This background vibration was likely reaching the balance through the tunnel structural frame to which it was bolted. Resources had not allowed for any additional physical dampening between this frame and the balance stack. During normal operation, the physical damping was sufficient to remove vibration from the tunnel drive system, for example. However, there was an unforeseen higher frequency vibration source in the compressor used for the concept's pneumatic supply. This was a permanent fixture system for the building in which the tunnel operated and the compressor unit was housed adjacent to the room. When operating a 0.23 N amplitude oscillation was observed in the filtered output from all axes. Significant, as this resulted in a force measurement approaching 50% some of the lower force readings. It was proposed that a process for post-processing

the measurements would remove this noise.

A majority of the components, predominantly pneumatic, comprising the actuation system were operated outside of the tunnel, as a representative of the fuselage-based position intended when integrated into a UAV application. This was achieved through a hole in the tunnel ceiling. This hole with the pneumatic lines in place was then sealed to prevent flow from being drawn into the tunnel. However, due to the nature of the yaw rotary mechanism in the tunnel, the only viable method for mounting was with the first joint, PAMs, and supporting structure in the working section. It is the intention of the concept that these too are to be housed within a fuselage structure, thus reducing the impact of the mechanism on the flow. This axle, aluminium plate, and connecting members can be seen in figure 6.8 alongside the shoulder muscles and blue pneumatic tubing.

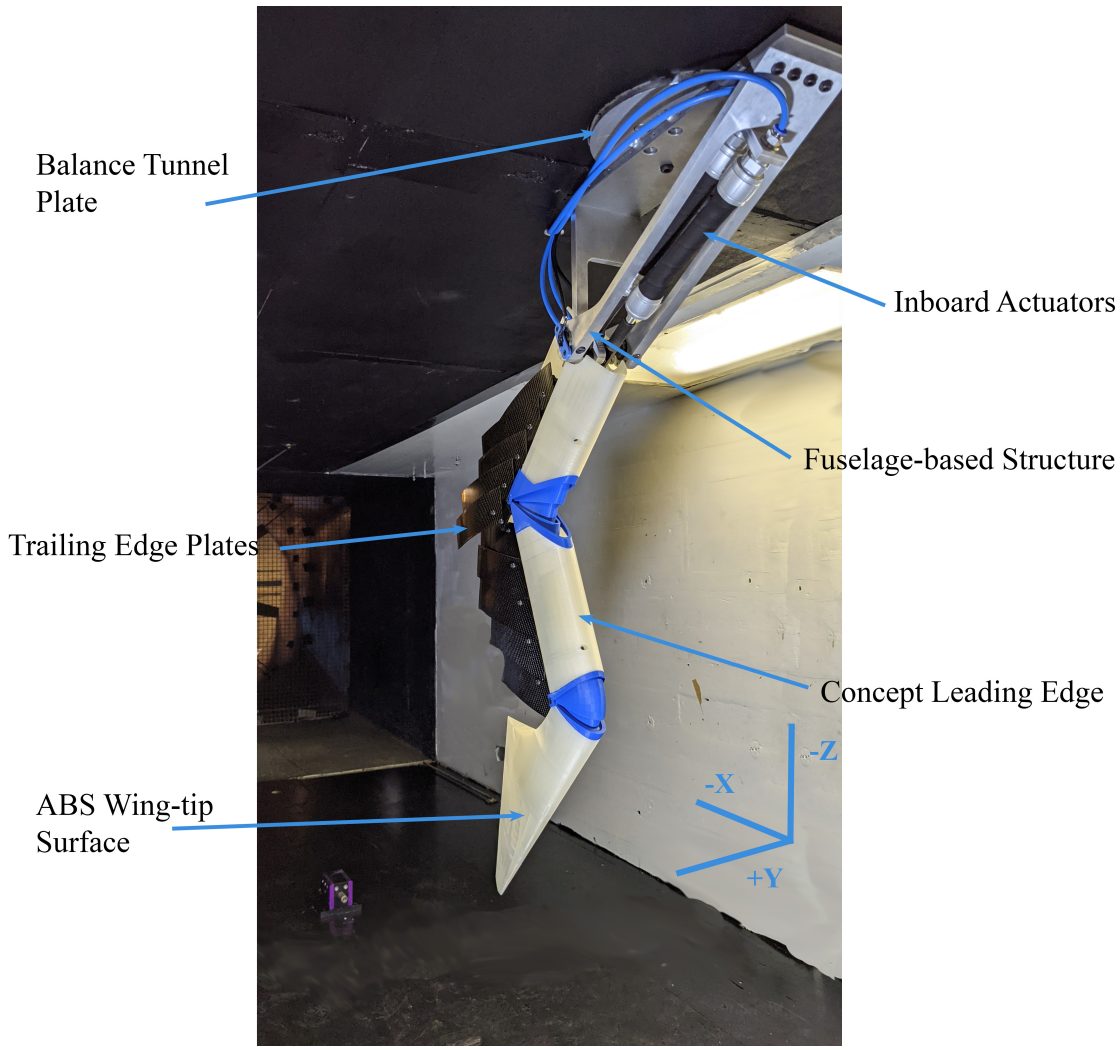


Figure 6.8: Prototype of the span-wise morphing concept as configured in the wind tunnel working section. Projected onto the image are the coordinate axis of the balance. Note that the wing is mounted vertically from the balance situated on the ceiling of the tunnel.

It was considered non-ideal to expose the fuselage-based aluminium structure to the flow. The geometric complexity was assumed to produce uncharacterised and potentially unstable effects on the flow over the body. In addition the exposed

tubing is not fixed rigidly to the frame and could therefore move laterally. A fairing was proposed for the mitigation of these effects. It was determined that the size required would be disproportionate to the model to be housed. The fairing was required to contain the structure, a portion of the wing when retracted, and the tapering required to ensure flow adhesion to the surface for a predictable attachment behaviour. This dimension was found to be approximately $700 - 800mm$ in line with the flow. The assembly at this length was found to contact the tunnel walls at 49^o wing angle of attack but more pertinently encroach within the wall clearance envelope at only 15^o incidence. Similarly, at angles of incidence over 5^o the fairing would produce significant blockage effects in the tunnel given both its length and height in the z-axis. These two effects combined would require a similar level of post-measurement tunnel correction to running without the fairing in place. The additional covering over the shoulder joint mechanism was therefore neglected for the tunnel programme. A process based on semi-span correction methods was employed to mitigate the body impact within the tunnel. Blockage effects were addressed by accounting for the effective acceleration of the flow caused by the model occupying a finite portion of the test section, represented through a solid-blockage correction based on the model's projected frontal area, such as equation 6.1.

$$\Delta\left(\frac{q}{q}\right) = k\frac{A_m}{A_t} \tag{6.1}$$

Where A_m and A_t represent the models projected area and the tunnels cross-sectional area, respectively. k represents the empirical blockage coefficient dependent on model geometry. Additional wake-blockage calculations were also completed to represent momentum loss in the model's wake, following the methodology set out by Barlow [178].

The root of the semi-span as it attached to the inboard PAM structure, forms a gap. The forces acting on the structure itself were removed using an independent series of measurements with the structure alone present in the tunnel. However, the interference of the structure and the gap it forms at the root of the semi-span were accounted for through potential theory. Typically in semi-span testing a structure is used to move the model way from the tunnel wall and out of the boundary layer. This is sometimes called a peniche. The interference of this peniche is modelled as a horseshoe vortex [179]. However, it has been shown a gap of 4δ, where *delta* is the boundary layer thickness, can remove the need to account for the interference via the horseshoe vortex [180]. As the boundary layer thickness for this tunnel was not known a boundary layer growth equation was used.

$$\delta = \frac{0.38\,x}{\mathrm{Re}_x^{1/5}}, \tag{6.2}$$

Based on a turbulent velocity profile

$$\frac{u}{u_\infty} = \frac{y}{\delta}^{\frac{1}{7}}$$

.

The boundary layer thickness was found to be 20 mm and so the inboard PAM structure extended from the wall 80 mm. However the presents of the gap at the wing root will result in wingtip vortices forming adding additional circulation around the

PAM structure that leds to an increase in the induced angle of attack. The method set out by Skinner et el. [179] was followed to correct the angle of attack.

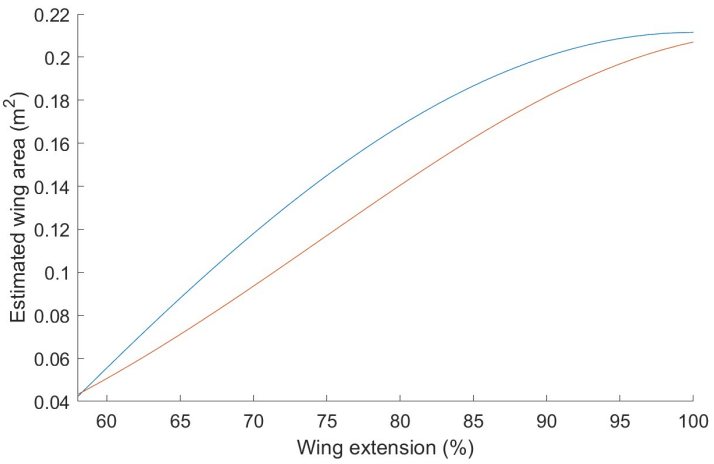


Figure 6.9: Wing area change as a function of variable wing span. Shown in blue is the area change given a 2:1 joint angle ratio as assumed in previous chapters. In orange, the area change derived from the avian motion is applied to the span-wise morphing concept.

In the case of the quasi-static testing it was found that a suitable testing methodology also significantly reduced experimental run time. The force measurement system used for both sets of experiments is capable of 1000 Hz sampling. However, quasi-static results were collected at 100 Hz as the actuation rate and control system data logging were limited to 10 Hz due to the data transfer protocol used and the number of measured parameters. To collect the aerodynamic response as a result of quasi-static span change, the concept was actuated in sinusoidal motion according to the set span length. This cyclic motion could then be repeated over a period of 120 cycles or approximately half an hour at a representative 0.2 rad/s; this actuation speed had been applied in the motion characterisation in section 6.1.2. The concept parameters measured during the quasi-static tests were the same as stated previously in chapter 5. It consists primarily of the internal PAM pressure and the internally measured joint angle. External position measurement was considered and would have been conducted with the same stereo camera setup as in the initially completed on the concept. However, the tunnel used did not possess clear working section walls and could not facilitate their use. Similarly, the placement of the cameras within the tunnel was disregarded as flow disruption was very likely due to the limited working section size.

Temporal synchronisation was completed during post-processing as no facility was available to conduct this inherently in the data capture. A common-event-based synchronisation methodology was used for the three separate times the quasi-static-sine test was carried out. The event consisted of an impact to the inboard member of the concept (a_1) this made a reference on both the potentiometer log and the balance; typically most noticeable in the $-z$ axis. The spike in measured angle of the former had an average rise time of 0.1s this sensor ran at the lowest measurement frequency of the two so this time was taken as the synchronisation error. The measured output of the balance and concept data logger once synchronised was split into its component cycles according the input signal to the control system.

This represented a sign change in the signal input. An identical process of stinger corrections to that of the static method was applied.

6.3 Static Performance

It was intended that the tunnel results collected be evaluated in comparison with the previously collected CFD results and those published as part of the development of similar morphing concepts. Force measurements allow this to a limited extent but it is the non-dimensional coefficients which allow a greater range of conclusions to be drawn from these comparisons. As noted previously, the characteristic area term has a novel consideration when applied to morphing concepts with significant area deflections. This is represented in the equations' notation used to derive the coefficients.

$$C_{L,ext} = \frac{2L}{\rho v^2 S_{ext}} \tag{6.3}$$

$$C_{L,mxt} = \frac{2L}{\rho v^2 S_{mxt}} \tag{6.4}$$

$$C_{L,rxt} = \frac{2L}{\rho v^2 S_{rxt}} \tag{6.5}$$

Where S represents the semi-span's exposed planform area. Subscript S_{rxt} denotes the concept in a fully retracted state, S_{mxt} a state where span falls in the midpoint of the range, and S_{ext} a fully extended state.

As the concept prototype was deliberately sized to an applicable scale for UAV implementation, evaluating the force at the balance provides some good insight into any implementation. Arguably, the most intuitive method for the evaluation is against the angle of attack (α). In figure 6.10 plots (a), (b), and (c) show the three forces of most interest, lift, drag, and pitching moment, respectively. In these static polars at $350,000$ Reynolds number the maximum lift force observed is shown to be 10.2 N in the extended case reducing to 9.05 N at mid-extension finally reducing again for the retracted configuration at 8.9 N. This is perhaps an entirely predictable order and demonstrates further confirmation of a morphing structure's ability to affect a change in its own aerodynamic performance. Total lift in a wing of this scale is low in comparison to non-morphing equivalents. Typical UAVs at this scale range 1 kg $-$ 20 kg are limited in civilian applications by vehicle weight limits in most classes. Clearly, the lift here restricts the concept's integration to aircraft on the lower end of this range. However, the estimated weights of a pneumatic system make this actuation method unlikely to be viable within the weight ranges indicated by these static tests. Earlier CFD coefficients applied to the tunnel flow conditions and prototype wing area at full extension indicate a semi-span lift 22 N approximately double that observed in these static tunnel polars. Consistent across all three presented forces/moments is the reduced difference between the retracted and mid-extension forces against the corresponding mid to full extension difference. Particularly noticeable in drag when the former varies by ± 0.2 N and the later upwards of 1.3 N.

Drag force values are also significantly increased over those predicted. This difference is perhaps less unexpected as the simplified geometry used neglected

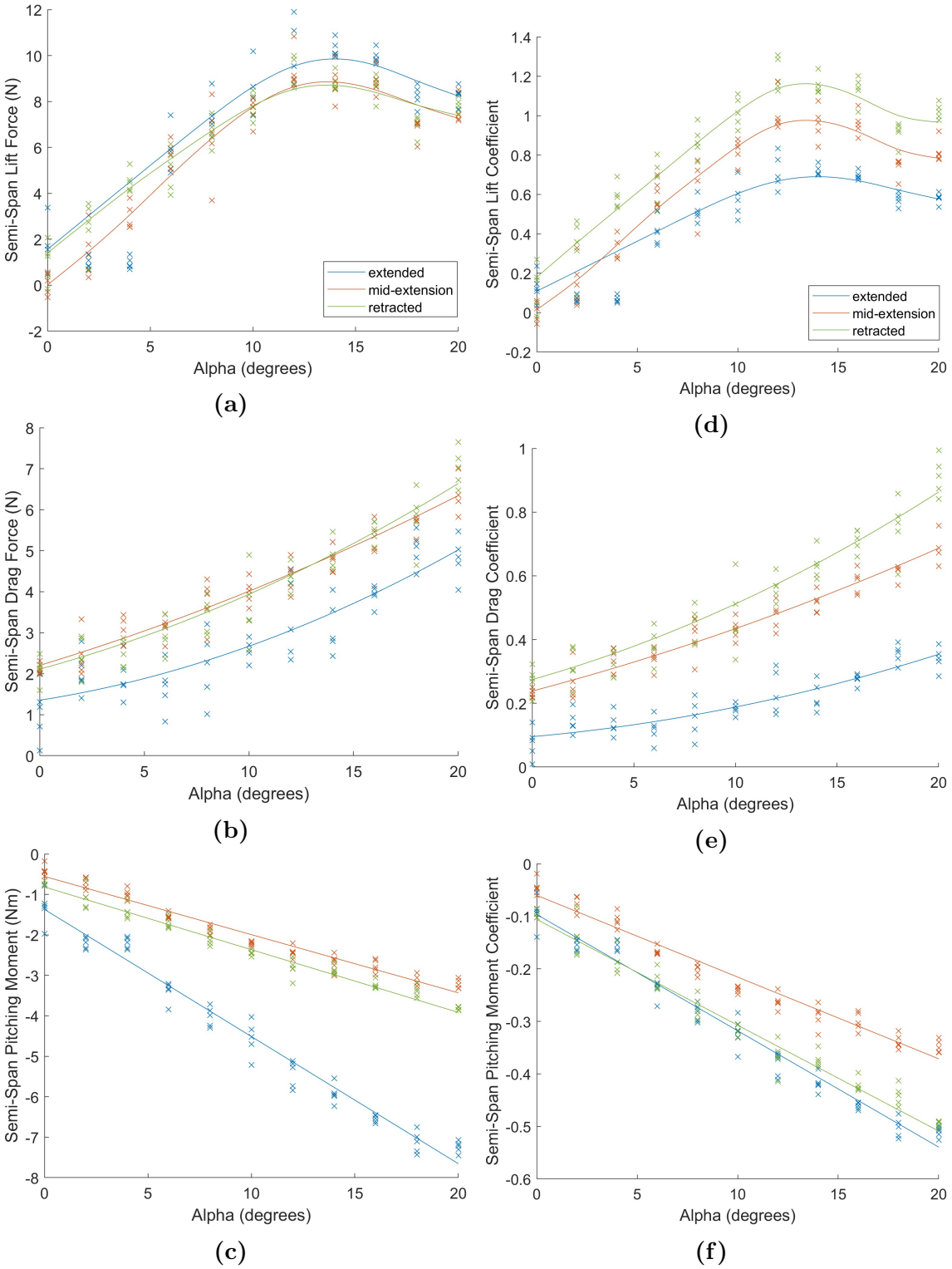


Figure 6.10: Lift (a), drag (b), and pitching moment (c) force polars for the span-wise morphing concept at 350,000 Reynolds number. Plotted for each is the measured and corrected values for full extension, full retraction, and mid-extension held at 50% deformation. Plots (d), (e), and (f) present the equivalent coefficient. Also represented here are the points collected over 12 runs.

components like fastenings, smaller actuation components, and surface defects or computational efficiency. These are most pertinent to the profile or pressure drag induced on the prototype as bolted connections were required on the upper surface. It is expected these caused limited separation, vorticity or other parasitic effects leading to this increased drag. Although, visualisation of the flow around these was not feasible due to limited seeding techniques available. Additive manufacturing, particularly FFD, is known for poor surface roughness. Viscus effects on the model surface are unlikely a major contributing factor to this drag due to the scaled small surface area effect. However, in a retracted state this 'wetted' surface area in proportion to span does increase. This may lead to a noticeable discrepancy in the difference between extensions in the CFD and tunnel results likely to be made clear with accounted characteristic area in the coefficients.

Variation between extensions is similarly evident in the pitching moment. The steep negative gradient here for the extended profile against the shallow gradient of the more retracted is attributed to the avian-based motion. The extension motion immediately proceeding full extension is weighted, and more greatly contributed to by the, elbow-wrist joint. This has an increased impact on span as a function of effective chord due to the swept back and forward inner two members.

Evidently the most significant aspect of these results is the reversal of extensions in the calculation of coefficients. In figure 6.10 plots (d), (e), and (f) show the derived coefficient for each of the observed forces and moments. While the values across the plot themselves fall within a nominal range for similar wings. The fully retracted state presented the highest lift coefficient which is somewhat counter to expectations. It is important to note when drawing conclusions from this change in lift characterisation that these polars were collected on different runs. While the flow conditions such as temperature and ambient atmospheric pressure are within $\pm 10\%$ of each other they cannot be ruled out. These are largely corrected for in the calculation for the coefficient but it was determined that the maximum deviation observed in the flow conditions could not account for the change seen in the coefficients. It is therefore concluded that the primary mechanism for this reversal is in the change of characteristic area S_{rxt}, S_{mxt}, and S_{ext}. Note from the plot figure 6.9 the control system behind the motion is not targeting a linear rate of area change rather a second order polynomial. This explains the separation differences. Across the force and coefficient plots the retracted (rxt) and mid-extension (mxt) separate a greater coefficient amount against the y-axis than between the mxt and extended (ext) wing. The explanation behind this lies in the fact that the rate of change in the rxt-mxt span region is greater than that in the range for mxt-ext. This applied proportionately in the equations deriving the coefficient leads to this unequal separation.

As for the apparent reversal in the span extension effect in the coefficient versus force. The conclusion drawn is largely based on which parameters of the wing design impact most significantly on aerodynamic performance. In this instance the increase in area with extension is resulting in an increase in lift force despite an adverse decrease in C_L as the span morphs to the extended configuration. It is therefore likely that the area change is the single design parameter with the largest impact on lift force generated by the surface. Although, this may be evident the validation here justifies this morphing for large aerodynamics changes over others previously investigated for applications, such as increasing efficiency via drag reduc-

tion for which this concept is not optimised. Conversely to the more predictable manifestation of area changes, the C_L and pertinently ${}^{\delta C_L}/_{\delta\alpha}$ is found to be lower for the extended wing. The extended wing exhibits an aspect ratio of 2.25 reduced to 1 in the retracted state. Looking at equation 6.6 both of these C_L based values are opposite of those predicted numerically.

$$\frac{\delta C_L}{\delta \alpha} = \frac{a_0}{1 + \frac{a_0}{\pi AR}} \tag{6.6}$$

Where a_0 in 6.6 represents the lift curve slope of the infinite wing. In this case the higher aspect ratio wing exhibits the lower ${}^{\delta C_L}/_{\delta\alpha}$. This is all under the assumption that the value for a_0 remains the same across each extension. This is not the case given an evident change in chord. Values for the aerofoils at stations from the wing root were not simulated in XFoil in chapter 4. Thus, we have no estimate for the change in a_0 against span-wise extension. However, looking at the relationship in the C_L results we can predict the correlation between each of the two must be negative. Its perhaps evident that this represents a non-ideal when looking to maximise manipulation of aerodynamic lift. The conclusion that therefore can be drawn that the aerofoil changes induced by the surface morphing during retraction need future development. Primally, it is predicted the geometric factor most contributory is the effective increase in chord.

6.4 Quasi-static Performance

The quasi-static results derived from the sinusoidal wind tunnel test were intended to provide insight into the relationship between span and the aerodynamic components. There was also interest in observing and quantifying any delay, constructive interference, or other quasi-static behaviour. These were expected to result from the overshoot allowed in the concept, following examination of avian structural quasi-static behaviour.

To extract any clear information from the 120 cycles captured, a methodology was employed to split and overlay each cycle in reference to the input command to the control system. In this instance, the cycle start was taken at the mid-extension on the retraction. The wing would retract fully before extending, and then partially retract once more. This allowed for the quasi-static behaviour at each span extreme to be better visualised. Figure 6.11 presents six plots pertaining to the quasi-static response in each of the aforementioned axis; here plots (a), (b), and (c) show the cycles overlaid for lift, drag, and pitching moment, respectively. These are plotted against cycle time in seconds, where each cycle is approximately 31.5 s. Time in seconds is used here as opposed to cycle angle in radians to better relate to applications such as a vehicle manoeuvrer. In figures (d), (e), and (f), a mean average is plotted with error bars for the standard deviation.

In the quasi-static measurements, the lift force exhibits a largely predicted force profile. The quasi-static response shows a noticeable delay. The delay is most evident at the limits of extension, where an average delay of 2.1 second and 1.0 second can be seen at maximum retraction and extension, respectively. Note also the increased standard deviation at these limits as compared to the mid-extension regions. This might initially suggest a deviation in the actual position compared to that commanded. However, in section 6.1 this was shown to be negligible under a static load.

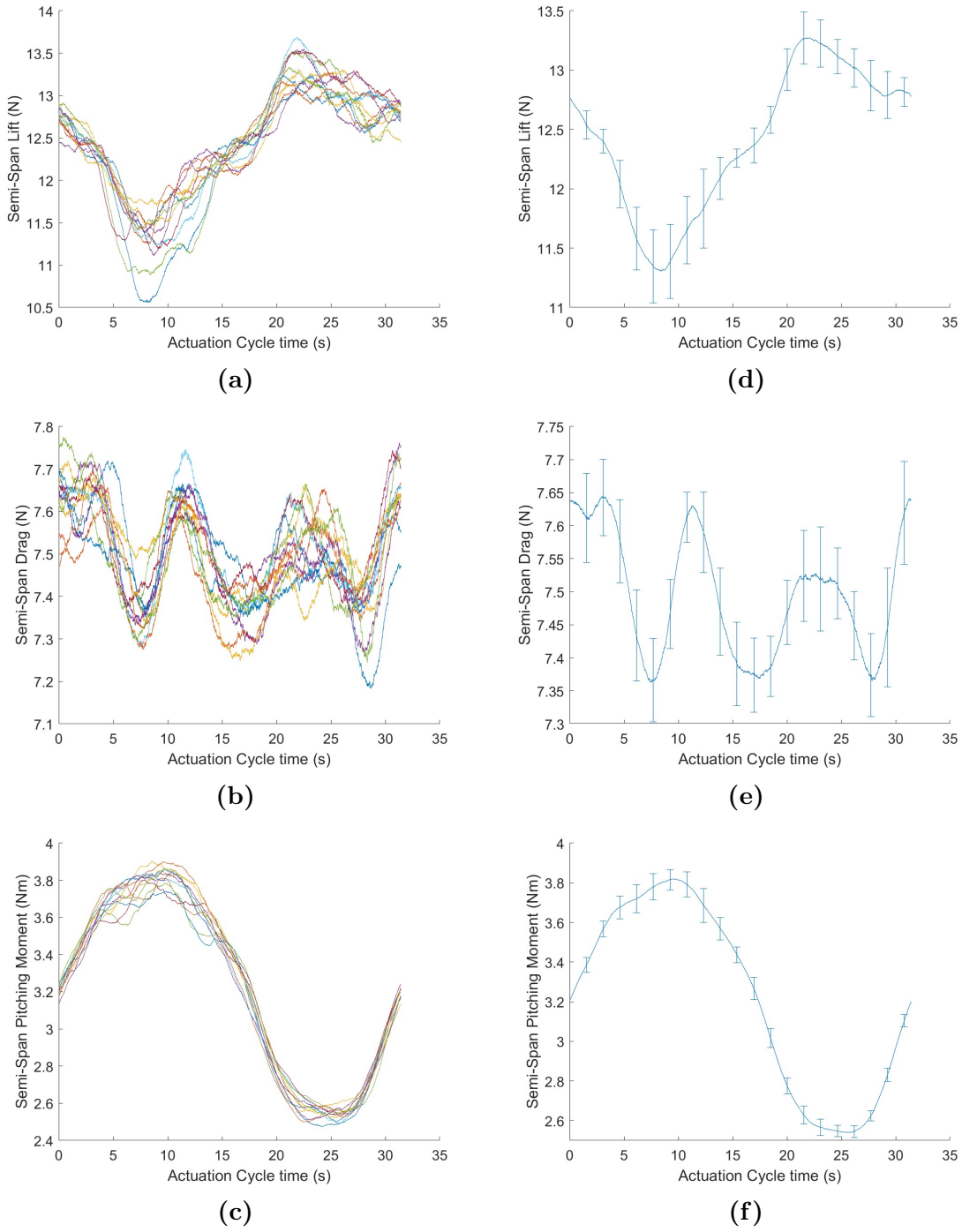


Figure 6.11: Lift and Drag force measured during cyclical extension and retraction of the concept at 350,000 Reynolds number. Plots (a), (b), and (c) present the forces acting on the concept against cycle time. A representative sample of the 120 cycles are shown for clarity. Plots (d), (e), and (f) show the calculated average of these cycles against cycle time. Also shown is the standard deviation presented as bars at 1.5 s intervals.

It is therefore concluded that this behaviour is a result of the aerodynamic surface itself deforming under the load. PLA is a relatively stiff polymer in comparison with others formulated for FFM. The structures themselves are likely geometrically

compromised due to the limited areas available for attachment to the aluminium structure of the concept. This limited area is a result of the requirement to provide adequate clearance for the mechanism driving the active trailing edge. The PLA leading edge and wing tip components are thus cantilevered and may be deflecting at the limits of the actuation due to the accelerations. This in turn resulting in an inconsistent value for the lift generated. This increase in standard deviation is evident across all of the forces measured and this is to be expected if it is the surface structure exhibiting some defection.

The drag force plotted in 6.11 (b) and (e) is more variable across the span lengths than lift or pitching moment. While this can be largely attributed to the aforementioned skin deflection the mechanism is not well understood. Lack of appropriate visualisation methodologies has limited the conclusions that can be drawn here. It is likely given the consistency of a high standard deviation across the whole cycle that the surface may be changing between cycles else oscillating with a period longer than the actuation cycle itself.

During the cycle, the drag force peaks 3 times. One peak is perhaps as expected, the point of maximum extension at approximately 22.5 s. This is the point with the maximum surface area exposed to the flow, and thus, drag resulting from both viscous and pressure effects will be increased. This peak in drag is also less abrupt or rather extended across a longer period of time due to the commanded input. It is notable that the peak here is decreased in magnitude in comparison to the two others suggesting the dominant mechanism for the drag in this instance has less overall impact. The other two peaks are presented at 0 s otherwise 31.5 s and 12 s. These sections of the cycle align with the periods just before and immediately following full retraction. However, notably not including the retracted state itself. The change in wetted area between the retracted state and this state is negligible. Similarly, the change profile between the two states is not significant enough to result in the perturbation seen in the drag force. Drag resultant from interference effects is likely the aerodynamic mechanism behind these peaks. The two inner members a_1 and a_2 form a sweep aft then forward in turn. The resulting 'v', it can be argued, will produce a variable magnitude of drag dependent on constructive effects as the angle between the members varies during actuation. This is something to be further investigated as it will be present regardless of the wing surface skin and is inherent to the three-member morphing concept.

Figures 6.11 (c) and (f) give the pitching moment against time. Most noticeable in the moment response is a significantly increased correlation to the span over the preceding two axes. This is inversely proportional to the span length of the wing and presents dynamically with no measured delay to the commanded input. Additionally, the standard deviation across the full set of runs decreases with lift and drag force. One conclusion that can be made in light of this is that the effect of the extension change on pitching moment is strong and predictable. The span-wise morphing concept here results in a 40% change in the overall pitching moment across the actuation. This indicates that this mechanism is a valid method for controlling aircraft pitch, thereby mitigating the need for other control surfaces. Indeed, other morphing concepts, that also change their sweep, have concluded that the pitching moment is the primary result of span morphing.

Chapter 7

Conclusion

In summary, this dissertation explored actuation technologies in an application for micro-scale morphing aircraft. This was implemented via a significantly morphing structure based around a primary span-wise change in wing area; a secondary sweep-based change in wing profile was also achieved.

An initial exploration involved a literature review, examining existing actuation systems suitable for such applications. This survey aimed to identify and understand the various technologies to facilitate subsequent comparisons with bio-actuation structures. Within the literature, a variety of actuation technologies emerged, each with distinct characteristics and applications. The section proposed a systematic methodology for comparing these artificial actuation systems with biological counterparts, aiming to distil essential characteristics for engineered systems from avian pectoral muscles. However, a notable challenge arose during the comparison between collated actuation systems and avian muscles, as these biological structures are fundamentally designed for different applications. Acknowledging this, the study shifted focus to identifying gaps in existing literature, particularly concerning the span-wise kinematics of avian wings. Recognising the dearth of information, the conclusion drawn from the literature resulted in a proposed program of experimental kinematic motion capture to bridge these knowledge gaps.

Infrared (IR) based motion tracking was identified as the most suitable technology for obtaining in vivo joint and member kinematics from avian. The subsequent experimental method involved the application of physical markers to capture point positions during wing expansions and retractions with the accuracy required to determine joint angles within the tolerance to which the concept will operate. The acquired data formed the basis for defining relationships between span-wise motion and individual joint motions. This analysis led to the formulation of mathematical expressions modelling the connections between each joint, providing a deeper understanding of avian wing dynamics. Conclusions were drawn not only from mechanical perspectives but also from dynamic observations during avian wing extension and retraction manoeuvres.

The application of this motion data was a proposed span-wise morphing concept, inspired by the avian wing mechanism. Following the conclusions in the literature review, the concept employed pneumatic artificial muscles to actuate a three-joint mechanism. The structure itself was developed based on findings in the field of biomechanics, specifically the literature surrounding ligament-skeletal anatomy of the avian wing. A two-dimensional implementation of this mechanism, commonly

referred to as the twin parallels mechanism, was determined to allow extended span-wise motion with a reduced number of actuated joints. An aerofoil, designed for controlled morphing, was introduced and evaluated using Computational Fluid Dynamics (CFD). The CFD results provided validating indications of the proposed wing design's suitability for a fixed-wing UAV role. However, the dynamic nature of the concept necessitated caution in interpreting these results. The conclusion drawn was that, while CFD simulations offered valuable insights, further validation through wind tunnel testing was needed to assess the performance and stability of the proposed span-wise morphing concept. Particularly surrounding the dynamic behaviour during morphing.

To address this need for validation, a prototype specified for wind tunnel testing was developed. The concept was manufactured as a semi-span at a scale applicable to common micro to small UAVs but that would also fit both commercially available PAM actuators and within the subsonic wind tunnels accessible within the University of Hertfordshire.

The structure formed three aluminium members connected via single-axis bearing joints all along the same plane. Direct kinematics was used to characterise the range of motion that could be achieved with the structure. Joint angles used for this estimation were those exhibited by the avian in captured motion. This indicated a retraction from the 900 mm extended prototype to 225 mm retracted; a predicted 75% reduction in semi-span length. However, this was found to be an overestimation. The PAM actuators were implemented in antagonistic pairs via a bell crank mechanism to each of the two actuated joints, the third joint driven by the twin parallels mechanism of the second joint. An initial programme of tests was carried out to characterise the muscles in this configuration. When antagonistic, the muscles' actuation strain was reduced due to the opposing load required to overcome the mechanism's stiffness imposed by the opposing PAM. While this was expected, through integration testing, it was found that the scale required for the prototype in the wind tunnel required PAMs with a reduced nominal length and cross-section over those predicted. The consequence is that the PAMs both had reduced percentage strain and exhibited a further reduction in strain length as a result of the reduced force available to extend the antagonistic PAM.

Development of a model for the concept and then a controller was undertaken. The model derived from literature was found to reliably estimate single joint behaviour. However, a less computationally intensive model was sought for potential inclusion on a microcontroller or single-board computer. The prototype was used as the basis for a frequency response method for determining a function capable of predicting behaviour to some extent, to operate as a viable replacement for the internal friction-based model. The results of the methodology showed that most frequency response-based models were limited but accurate at some actuation frequencies. A system for control of the single PAM joint and the combined three-joint structure was implemented via a microcontroller and proportional compressed air control valves. Closed-loop feedback was completed with mechanical potentiometers embedded within the joints. A proportional, integral, derivative controller, employed from literature, also looking at control of antagonistic PAMs, was used, and a validation process was undertaken with the model. This setup aimed to provide empirical data directly comparable with the modelled dynamics, emphasising the concept's dynamic nature and capturing motion and deformation during morphing.

This led to a series of experiments looking to measure the structural response of the prototype. Stereo-photogrammetry-based metrology was used to track the wingtip position relative to a fixed axis. This allowed conclusions to be made regarding the consistency of the actuation across cycles. Alongside this, the full concept was measured using the same external methodology. This allowed measurement of the joint angles in motion, providing a means of validation against the internal potentiometer-based measurements from the control system. It was found, in both an unloaded and a loaded case, that the error in wingtip position did not exceed 1% of the chord length. The maximum error was found to occur in the longitudinal axis and was attributed to the angular error in the joints. However, the conclusion was that the error would have a negligible effect on the wing's aerodynamic performance.

Finally, a programme of static and quasi-static wind tunnel tests was undertaken. These aimed to both validate the aforementioned CFD results for the concept and demonstrate its viability for further development in a UAV application. All testing was conducted in a semi-span wall-mounted configuration in the University of Hertfordshire's 5 ft by 6 ft open return tunnel. Static results were recorded at a Reynolds number of $350,000$ to best represent the proposed UAV use case and remain within the tunnel's limits. Three span extensions were examined, extended, retracted, and a span length midway between the actuation limits.

It was found that the lift performance was significantly below that which was produced in the CFD simulations. The coefficients presented 60% lower than the CFD in the extended case. However, in both the retracted and mid-extension configurations, the lift coefficient was increased over the simulation. The conclusion for the UAV application was that the lift generated for these flow conditions were not sufficient to maintain flight given the predicted weight of an aircraft of this scale, particularly when including the pneumatic systems required for actuation. It was proposed that the increased wing area required to mitigate this issue would better suit a UAV of a scale greater than that tested. The drag force measured in the tunnel was higher than that of the simulated prototype across all extensions. This was largely attributed to the reduced detail in the CFD model, required to keep the computational cost low. This detail, including fasteners and the mechanical linkages, would have increased the profile drag on the wind tunnel model. A significant pitching moment change was noted and attributed to aspect ratio changes, along with sweep. The quasi-static series of tests was conducted with a sinusoidal span length input, across the full extension, to the controller. The primary conclusion taken from these quasi-static results was in relation to the pitching moment. It was found to exhibit a low standard deviation, suggesting a correlation which proves this is a viable method of affecting vehicle pitch control. While the CFD results showed promise, the conclusion underscored the importance of a comprehensive approach, suggesting that further wind-tunnel testing is a crucial step in validating and refining the proposed biomimetic adaptive structure.

7.1 Continued work

While this span-wise morphing concept has been proposed for an uncrewed aerial vehicle (UAV) application, this does little to narrow down the intended remit. Applications for uncrewed aerial systems are seemingly being proposed at a rate exceeding the development of the adaptive systems they are intended to address. However, the

key term highlighted within the field in recent years is 'adaptive'. This applies to the concept form and, subsequently, to the use case. However, a limitation imposed by the scale of the concept was identified here, derived from the availability of the PAMs. This is not necessarily a detriment, as previously noted, the minimum useful size of the muscles correlates with a UAV scale that inherently contains the systems to power the muscles. Therefore, an approximate minimum concept size can be considered 2m wing span at full extension.

Further development is therefore towards adapting the concept to a span lower than this limit. While PAMs have been developed and operated below the approximately 150mm nominal length of those used in the presented concept, the systems are not inherent to this scale of aerial vehicle; notably, a source of pneumatic power. Overwhelmingly, these UAS are solely electromechanical, with approaches to battery storage being developed in parallel to those in automotive and similar fields. Thus, it becomes applicable to more situations and increasingly capable in areas where it is already applied. The span-wise morphing concept derived from this research uses typical electromechanical actuation; the advantage of these inexpensive systems allows for a decreased time-to-prototype. In addition, the reduced scale has allowed a full vehicle to be produced.

The novel avian motion, morphing structure, and control presented in previous chapters are employed in this electromechanical (EM) span-wise morphing concept. System integration surrounding the proposed servo-driven actuation is complete as of publication. The proposed future work here is further computational, followed by experimental, aerodynamic testing.

Appendix A

Avian Motion Capture Tables

This appendix contains the filtered avian motion data in the original coordinate axis and original origin. This origin is arbitrary and was set as part of the camera system automated calibration process as the middle a lowest point of the valid capture volume. As the validity was set automatically by the system based on manufacturer recommendations this did vary and was thus compensated for in the analysis of the capture data. However, the average position tended to be the middle of the volume hence the presence of negative values for the vertical axis z. The axes X and Y represent the lateral axes however as the direction of travel between each flight changed no general statement can be made of the representation for these two axes.

The tables below contain the data for each marker placed on the avian wing. Three markers were used per semi-span. Placed on the leading edge of the primary feathers, wrist, and Elbow. These in the table are given a designation P - port, and S - starboard to denote the side of the avian. The marker Spine-F, forward, is also given as this formed the basis for some of the matrix rotation done in the main body of the text. The table caption notation is as follows: Avian specimen, trial number, capture session number, frame start and end. The frame start and end is given in reference to the full set of data provided in the digital complement to this document.

Table A.1: Common Buzzard - specimen: CB, Trial 2, Capture session 2, Frames: 1535-1625

Frame	Primary_P			Wrist_P			Elbow_P			Elbow_S			Wrist_S			Primary_S			Spine_F		
	X	Y	Z	X	Y	Z	X	Y	Z	X	Y	Z	X	Y	Z	X	Y	Z	X	Y	Z
1535	-166	1169	1549	-23	1327	1532	55	1329	1670				330	1332	1552	482	1208	1623	147	1335	1672
1536	-170	1195	1542	-17	1338	1504	62	1331	1637				318	1344	1529	489	1232	1617	150	1328	1642
1537	-174	1226	1534	-9	1347	1476	70	1331	1602				322	1352	1491	493	1261	1612	152	1322	1613
1538	-176	1261	1522	-1	1352	1449	78	1330	1568				327	1358	1459	495	1295	1603	156	1315	1583
1539	-175	1297	1508	6	1352	1419	86	1327	1534				335	1363	1429	496	1332	1588	159	1308	1554
1540	-183	1336	1500	13	1350	1388	94	1323	1500				345	1365	1403	497	1368	1565	161	1300	1526
1541	-179	1363	1471	16	1345	1357	100	1315	1467				354	1363	1379	499	1398	1534	164	1293	1497
1542	-178	1380	1437	19	1340	1326	105	1307	1438				362	1359	1357	505	1418	1499	167	1286	1467
1543	-180	1387	1402	18	1332	1296	108	1299	1410				369	1354	1334	515	1428	1462	170	1278	1439
1544	-185	1388	1369	14	1322	1269	112	1292	1383				375	1349	1310	529	1431	1425	173	1270	1410
1545	-191	1383	1335	8	1313	1242	114	1285	1357				381	1343	1286	545	1425	1391	175	1263	1382
1546	-199	1373	1300	3	1304	1216	115	1278	1331				387	1337	1262	562	1415	1354	178	1256	1353
1547	-208	1359	1265	-4	1297	1190	113	1271	1305				394	1330	1237	579	1401	1321	181	1250	1325
1548	-216	1342	1229	-10	1289	1166	112	1263	1277				401	1320	1214	596	1385	1283	184	1243	1297
1549	-224	1321	1192	-16	1278	1145	110	1256	1248				409	1308	1189	612	1366	1245	187	1238	1269
1550	-230	1297	1154	-20	1266	1124	110	1249	1218				418	1295	1165	626	1343	1206	190	1233	1240
1551	-235	1271	1115	-20	1252	1098	110	1240	1187				428	1284	1138	640	1318	1167	194	1229	1211
1552	-238	1244	1075	-20	1237	1070	111	1231	1156				438	1271	1109	651	1292	1128	199	1224	1182
1553	-239	1216	1036	-21	1221	1040	111	1222	1126				447	1257	1079	660	1267	1088	203	1221	1153
1554	-237	1188	997	-21	1205	1008	112	1214	1095				456	1243	1047	667	1240	1047	206	1217	1124
1555	-233	1160	957	-22	1189	975	112	1207	1065				465	1228	1014	672	1215	1005	209	1215	1096
1556	-227	1134	916	-20	1175	941	111	1199	1034				473	1213	981	676	1193	963	212	1213	1067
1557	-220	1110	875	-15	1161	907	111	1192	1005				477	1197	947	676	1172	918	215	1211	1037
1558	-209	1087	832	-10	1148	873	112	1185	975				479	1184	911	675	1153	875	217	1209	1008
1559	-199	1069	791	-4	1137	839	114	1179	945				479	1172	876	674	1136	833	219	1208	979
1560	-187	1053	750	3	1128	805	117	1174	916				478	1164	840	669	1121	794	221	1206	950
1561	-175	1042	711	11	1122	771	121	1168	886				476	1159	804	666	1107	753	223	1205	921

Table A.1: CB T2 C2 1535-1625

Frame	Primary_P			Wrist_P			Elbow_P			Elbow_S			Wrist_S			Primary_S			Spine_F		
	X	Y	Z	X	Y	Z	X	Y	Z	X	Y	Z	X	Y	Z	X	Y	Z	X	Y	Z
1562	-149	1029	654	18	1120	736	124	1164	858				473	1157	769	658	1094	716	225	1204	891
1563	-138	1026	618	27	1121	703	126	1163	830				470	1157	734	650	1085	680	227	1204	861
1564	-129	1026	584	34	1124	672	130	1161	802				465	1161	699	644	1081	647	229	1203	831
1565	-123	1029	556	41	1132	643	130	1164	775				460	1167	665	636	1080	616	232	1203	800
1566	-118	1036	534	45	1144	614	133	1168	748				454	1174	636	637	1086	591	234	1203	768
1567	-125	1049	522	47	1157	583	135	1173	718				449	1184	608	633	1094	569	237	1203	735
1568	-126	1060	504	49	1172	551	139	1179	689				444	1196	580	634	1106	553	240	1203	704
1569	-127	1073	491	51	1187	519	142	1186	657				425	1215	524	635	1118	539	243	1202	672
1570	-122	1086	471	54	1203	491	147	1195	625				421	1225	495	635	1131	529	246	1201	640
1571	-119	1099	460	59	1217	464	153	1202	592	356	1214	601	418	1233	462	635	1147	518	249	1199	608
1572	-119	1119	450	65	1227	440	160	1208	559	354	1219	569	430	1235	454	636	1166	509	253	1198	577
1573	-127	1145	452	73	1233	416	169	1214	525	351	1224	535	429	1244	422	635	1189	499	255	1196	546
1574	-124	1169	440	82	1235	389	176	1216	492	348	1227	503	429	1252	389	633	1214	488	258	1194	516
1575	-120	1193	425	88	1237	358	185	1217	460				431	1259	359	630	1242	473	261	1192	487
1576	-116	1213	406	93	1237	325	191	1215	428				435	1264	331	626	1268	451	263	1189	458
1577	-112	1227	382	97	1236	292	198	1211	399				441	1267	305	623	1289	425	265	1187	428
1578	-109	1235	358	100	1232	260	201	1206	371				446	1268	281	623	1305	396	268	1184	398
1579	-107	1239	333	100	1226	230	202	1202	345				452	1267	256	627	1315	366	270	1181	368
1580	-108	1239	307	98	1219	202	203	1198	319				457	1265	231	633	1320	334	272	1178	339
1581	-110	1237	280	96	1213	174	202	1194	293				462	1263	206	642	1322	301	274	1175	310
1582	-114	1233	253	92	1208	147	201	1190	267				468	1261	180	652	1320	267	276	1172	281
1583	-118	1227	223	88	1204	120	198	1187	239				473	1258	153	664	1317	232	278	1169	253
1584	-124	1219	192	83	1201	95	194	1182	211				479	1254	127	676	1313	193	280	1167	225
1585	-130	1207	158	77	1197	70	192	1179	182				486	1248	99	689	1306	153	282	1165	198
1586	-137	1191	121	70	1190	48	190	1172	151				494	1241	72	702	1298	112	284	1163	171
1587	-145	1173	81	65	1179	26	189	1166	121				504	1233	44	714	1287	69	285	1161	145
1588	-151	1155	38	62	1168	0	189	1161	91				513	1225	16	724	1275	26	287	1160	119

Table A.1: CB T2 C2 1535-1625

Frame	Primary_P			Wrist_P			Elbow_P			Elbow_S			Wrist_S			Primary_S			Spine_F		
	X	Y	Z	X	Y	Z	X	Y	Z	X	Y	Z	X	Y	Z	X	Y	Z	X	Y	Z
1589	-154	1137	-6	62	1158	-31	189	1157	61				522	1218	-12	731	1262	-19	289	1160	91
1590	-155	1122	-52	62	1148	-63	187	1153	32				528	1214	-42	735	1251	-61	291	1160	64
1591	-153	1109	-97	62	1139	-95	187	1150	2				533	1211	-73	737	1241	-104	293	1160	36
1592	-149	1098	-142	62	1133	-128	187	1145	-28				537	1208	-103	738	1233	-146	294	1160	9
1593	-144	1088	-186	64	1130	-161	187	1142	-58				539	1206	-134	737	1225	-187	295	1162	-18
1594	-137	1080	-231	67	1128	-193	187	1139	-86				540	1204	-166	735	1219	-226	295	1164	-45
1595	-129	1072	-276	70	1128	-225	189	1137	-114				539	1205	-198	732	1214	-264	295	1167	-72
1596	-121	1068	-320	72	1130	-255	189	1138	-141				537	1207	-230	729	1210	-300	295	1170	-99
1597	-112	1069	-362	74	1134	-286	189	1141	-169				535	1211	-261	724	1207	-335	295	1172	-126
1598	-101	1070	-407	76	1140	-315	190	1144	-196				532	1216	-292	720	1205	-369	294	1172	-150
1599	-92	1077	-447	78	1148	-343	190	1147	-223				528	1223	-321	713	1204	-402	294	1173	-176
1600	-84	1090	-483	80	1159	-370	190	1149	-249				522	1232	-349	706	1206	-433	294	1177	-202
1601	-79	1106	-515	82	1171	-397	191	1152	-274				516	1241	-375	699	1210	-461	293	1179	-228
1602	-76	1124	-540	84	1185	-420	191	1156	-298				509	1250	-398	692	1219	-485	293	1183	-254
1603	-75	1140	-562	86	1202	-443	191	1162	-322				501	1261	-419	686	1229	-506	292	1187	-280
1604	-74	1154	-580	88	1219	-463	189	1170	-343				494	1272	-439	682	1239	-522	293	1191	-307
1605	-75	1167	-596	91	1237	-483	189	1178	-365				486	1283	-458	677	1248	-536	292	1196	-333
1606	-75	1179	-610	93	1255	-501	189	1187	-387				479	1295	-478	673	1255	-548	292	1201	-360
1607	-76	1191	-620	98	1273	-519	190	1199	-408				472	1307	-500	670	1262	-557	291	1207	-386
1608	-77	1203	-627	104	1288	-536	192	1211	-430				465	1318	-522	668	1269	-563	292	1211	-413
1609	-80	1215	-633	111	1299	-553	195	1226	-452				458	1330	-545	666	1276	-567	292	1216	-440
1610	-82	1229	-637	119	1308	-574	201	1240	-476				451	1342	-568	664	1285	-567	293	1221	-466
1611	-83	1243	-639	127	1314	-597	207	1252	-500				446	1352	-590	661	1296	-565	290	1225	-489
1612	-84	1259	-642	133	1322	-622	215	1265	-526				442	1360	-611	657	1310	-561	292	1228	-518
1613	-84	1277	-644	138	1331	-650	223	1275	-552	363	1293	-547	440	1365	-629	649	1330	-559	292	1231	-541
1614	-83	1295	-647	141	1337	-678	229	1282	-579				440	1369	-649	642	1352	-559	291	1235	-564
1615	-82	1312	-655	140	1341	-707	235	1286	-607				441	1371	-669	633	1376	-564	291	1238	-588

Table A.1: CB T2 C2 1535-1625

Frame	Primary_P			Wrist_P			Elbow_P			Elbow_S			Wrist_S			Primary_S			Spine_F		
	X	Y	Z	X	Y	Z	X	Y	Z	X	Y	Z	X	Y	Z	X	Y	Z	X	Y	Z
1616	-81	1327	-665	138	1340	-733	237	1286	-634				443	1373	-689	626	1400	-574	292	1241	-614
1617	-83	1339	-679	133	1338	-757	237	1284	-660				445	1374	-712	622	1419	-589	293	1243	-640
1618	-86	1348	-693	128	1336	-779	233	1281	-684				449	1375	-733	623	1432	-608	294	1245	-666
1619	-91	1355	-708	120	1334	-799	229	1279	-707				455	1375	-756	628	1440	-628	295	1246	-693
1620	-97	1359	-726	112	1333	-818	223	1276	-728				463	1374	-779	637	1444	-651	296	1247	-718
1621	-106	1361	-746	104	1334	-836	217	1273	-749				473	1372	-800	650	1441	-675	295	1248	-742
1622	-116	1360	-772	94	1334	-853	211	1268	-770				483	1370	-820	664	1435	-705	293	1251	-763
1623	-126	1355	-803	84	1333	-870	207	1265	-791				493	1368	-840	679	1429	-737	292	1253	-784
1624	-137	1350	-840	74	1329	-886	199	1261	-817	405	1287	-820	502	1367	-860	694	1421	-773	291	1253	-805
1625	-147	1345	-881	64	1323	-903	195	1260	-844	411	1284	-844	510	1366	-880	707	1414	-810	291	1252	-829

Table A.2: Common Buzzard - specimen: CB, Trial 3, Capture session 2, Frames: 7288-7389

Frame	Primary_P			Wrist_P			Elbow_P			Elbow_S			Wrist_S			Primary_S			Spine_F		
	X	Y	Z	X	Y	Z	X	Y	Z	X	Y	Z	X	Y	Z	X	Y	Z	X	Y	Z
7284				-581	1123	2568	-450	1160	2658	-228	1171	2679	-83	1155	2637				-357	1173	2689
7285				-568	1104	2535	-448	1149	2624	-220	1159	2646	-77	1130	2603	116	1074	2623	-351	1169	2655
7286				-556	1085	2501	-445	1139	2590	-212	1148	2612	-74	1106	2571	113	1033	2587	-346	1166	2620
7287				-544	1067	2468	-441	1130	2556	-207	1137	2579	-71	1083	2536	107	992	2552	-341	1163	2584
7288	-719	916	2411	-532	1050	2434	-436	1120	2522	-201	1127	2546	-71	1062	2500	98	955	2515	-336	1160	2549
7289	-695	885	2379	-520	1035	2400	-431	1113	2489	-198	1119	2515	-73	1045	2463	84	921	2477	-331	1157	2514
7290	-669	858	2347	-509	1021	2365	-425	1105	2456	-194	1111	2482	-76	1030	2424	67	891	2437	-326	1154	2479
7291	-641	837	2313	-498	1010	2330	-420	1100	2423	-191	1105	2451	-80	1020	2384	49	868	2395	-321	1150	2443
7292	-614	821	2278	-488	1002	2294	-414	1095	2390	-188	1100	2418	-85	1015	2343	31	853	2352	-316	1146	2407
7293	-590	812	2241	-478	997	2257	-409	1091	2358	-186	1096	2385	-90	1013	2301	17	844	2308	-311	1141	2370
7294	-569	809	2204	-470	996	2219	-403	1088	2325	-183	1094	2352	-94	1015	2260	8	842	2266	-306	1136	2334
7295	-554	812	2167	-461	999	2180	-396	1086	2292	-180	1094	2318	-97	1021	2219	2	844	2227	-301	1131	2297
7296	-545	819	2131	-454	1006	2140	-390	1086	2259	-177	1094	2283	-99	1029	2180	5	852	2192	-295	1126	2261
7297	-542	829	2098	-448	1017	2098	-384	1085	2225	-173	1095	2246	-100	1038	2141	12	862	2161	-290	1120	2224
7298	-543	843	2069	-443	1029	2057	-378	1087	2189	-170	1096	2209	-99	1049	2101	21	875	2136	-285	1114	2187
7299	-548	860	2044	-437	1042	2017	-371	1088	2155	-166	1098	2170	-98	1060	2062	31	892	2115	-280	1107	2151
7300	-554	881	2020	-432	1055	1978	-364	1089	2117	-163	1099	2131	-95	1070	2021	41	912	2095	-275	1100	2114
7301	-561	904	1998	-426	1068	1939	-357	1090	2079	-161	1099	2092	-92	1079	1979	52	936	2076	-270	1093	2078
7302	-569	929	1977	-420	1080	1902	-349	1090	2040	-160	1099	2053	-88	1086	1936	62	963	2057	-265	1086	2042
7303	-575	957	1954	-415	1089	1867	-341	1089	2001	-158	1098	2013	-82	1092	1895	71	994	2036	-260	1078	2006
7304	-579	987	1929	-408	1096	1833	-332	1086	1961	-157	1095	1973	-74	1098	1855	80	1026	2012	-255	1071	1970
7305	-580	1019	1903	-401	1100	1797	-324	1082	1920	-154	1091	1932	-65	1103	1817	86	1058	1984	-251	1064	1935
7306	-580	1051	1873	-395	1101	1761	-316	1076	1880	-152	1086	1894	-55	1107	1781	92	1088	1952	-246	1056	1900
7307	-579	1079	1839	-390	1102	1724	-309	1069	1840	-150	1079	1857	-44	1110	1746	100	1114	1916	-240	1049	1865
7308	-578	1102	1800	-385	1099	1686	-303	1061	1803	-147	1071	1820	-37	1109	1717	109	1134	1877	-236	1041	1829
7309	-578	1116	1758	-381	1094	1649	-296	1055	1766	-143	1066	1783	-29	1107	1688	119	1146	1836	-232	1034	1795
7310	-579	1124	1714	-382	1086	1614	-291	1050	1731	-138	1061	1745	-22	1105	1660	132	1153	1793	-227	1027	1760

Table A.2: CB T3 C2 7288-7389

Frame	Primary_P			Wrist_P			Elbow_P			Elbow_S			Wrist_S			Primary_S			Spine_F		
	X	Y	Z	X	Y	Z	X	Y	Z	X	Y	Z	X	Y	Z	X	Y	Z	X	Y	Z
7311	-581	1125	1669	-381	1080	1577	-284	1046	1697	-134	1056	1707	-15	1101	1631	146	1154	1750	-223	1021	1725
7312	-586	1123	1623	-381	1074	1541	-279	1040	1663	-127	1049	1671	-9	1097	1599	161	1152	1707	-217	1014	1689
7313	-589	1119	1574	-382	1068	1506	-279	1032	1628	-119	1042	1634	-4	1092	1565	176	1147	1664	-212	1008	1654
7314	-593	1113	1526	-383	1062	1472	-277	1024	1592	-112	1035	1599	3	1085	1531	190	1140	1620	-208	1002	1618
7315	-596	1105	1479	-385	1055	1440	-274	1018	1556	-104	1029	1564	10	1077	1498	206	1130	1572	-203	996	1582
7316	-598	1094	1430	-387	1048	1409	-271	1013	1519	-96	1022	1528	18	1067	1463	219	1120	1527	-198	991	1546
7317	-598	1081	1384	-388	1039	1377	-268	1006	1482	-90	1016	1492	27	1056	1430	230	1107	1486	-193	985	1511
7318	-598	1065	1338	-386	1031	1344	-264	1000	1445	-83	1008	1458	35	1046	1395	243	1092	1441	-188	981	1475
7319	-597	1048	1295	-383	1022	1310	-260	993	1407	-76	1002	1422	44	1036	1360	254	1076	1399	-183	976	1439
7320	-595	1030	1253	-381	1012	1273	-256	987	1370	-69	995	1385	52	1027	1325	264	1059	1359	-177	971	1403
7321	-593	1011	1210	-378	1003	1235	-253	981	1333	-62	989	1348	60	1019	1288	273	1041	1317	-173	967	1367
7322	-589	994	1169	-377	994	1198	-250	976	1297	-56	983	1312	68	1011	1252	281	1024	1277	-169	962	1332
7323	-585	978	1128	-374	984	1159	-248	970	1261	-50	976	1276	77	1003	1215	288	1009	1236	-164	958	1296
7324	-581	964	1086	-371	977	1121	-246	964	1225	-43	970	1241	84	994	1179	295	996	1195	-159	955	1260
7325	-576	953	1047	-366	971	1082	-243	958	1189	-38	965	1204	92	986	1141	301	984	1155	-155	951	1224
7326	-571	943	1007	-361	964	1043	-241	952	1153	-32	960	1167	98	979	1102	306	973	1115	-150	948	1188
7327	-566	935	968	-357	958	1005	-237	947	1117	-27	955	1130	103	974	1063	311	963	1077	-146	944	1152
7328	-561	929	930	-352	953	966	-233	942	1079	-21	950	1094	108	969	1024	316	956	1039	-142	941	1116
7329	-556	924	892	-346	949	928	-229	938	1042	-16	947	1057	111	965	985	320	950	1002	-138	938	1080
7330	-551	920	855	-341	946	889	-225	935	1004	-12	944	1020	115	962	946	323	945	965	-133	935	1044
7331	-546	918	818	-335	944	852	-221	932	967	-7	941	983	119	959	907	326	941	929	-128	932	1008
7332	-541	917	782	-330	942	813	-216	929	930	-3	938	946	122	957	869	330	938	893	-124	929	972
7333	-536	916	748	-324	940	775	-212	927	894	2	936	910	124	956	831	333	935	857	-120	926	936
7334	-530	915	714	-318	939	738	-207	925	858	6	934	874	128	955	793	336	934	821	-116	924	900
7335	-525	915	680	-312	938	700	-202	923	822	10	931	838	130	954	756	340	933	786	-112	921	864
7336	-519	914	647	-306	938	663	-198	922	787	14	930	801	133	954	719	344	934	750	-107	919	828
7337	-515	913	615	-299	938	627	-193	921	751	18	929	765	137	954	682	347	935	715	-103	917	792

Table A.2: CB T3 C2 7288-7389

Frame	Primary_P			Wrist_P			Elbow_P			Elbow_S			Wrist_S			Primary_S			Spine_F		
	X	Y	Z	X	Y	Z	X	Y	Z	X	Y	Z	X	Y	Z	X	Y	Z	X	Y	Z
7338	-509	912	582	-294	938	590	-188	921	716	21	928	730	140	953	646	350	935	682	-98	915	756
7339	-505	911	550	-289	937	554	-183	921	680	25	927	694	144	953	609	354	934	648	-94	913	720
7340	-501	910	518	-284	937	519	-178	921	644	28	927	658	147	953	573	358	934	614	-89	912	684
7341	-497	910	486	-280	936	485	-173	920	609	33	926	621	150	952	538	362	932	581	-85	910	647
7342	-493	909	454	-276	936	451	-168	919	573	36	925	585	154	951	504	366	930	548	-80	909	612
7343	-490	908	421	-273	935	417	-163	918	537	41	924	549	159	950	468	371	927	515	-76	908	576
7344	-487	908	388	-271	934	383	-159	917	502	45	923	514	164	949	434	376	926	481	-72	907	539
7345	-484	907	354	-268	933	350	-155	916	467	49	921	480	168	947	400	380	925	448	-68	905	504
7346	-482	907	321	-267	932	316	-151	914	432	54	919	445	173	946	366	385	925	414	-63	905	468
7347	-478	906	287	-264	932	283	-146	913	397	58	918	410	178	945	332	390	925	380	-59	903	432
7348	-476	906	254	-262	930	250	-142	912	362	63	917	374	181	943	302	395	926	345	-55	902	397
7349	-472	905	219	-259	929	217	-138	911	326	67	915	339	186	943	269	399	926	311	-51	901	362
7350	-468	905	186	-254	929	182	-134	910	291	71	914	305	192	942	235	404	927	275	-46	900	327
7351	-464	905	152	-250	928	147	-130	909	256	75	913	269	196	943	200	408	927	240	-42	899	292
7352	-460	904	118	-246	926	112	-125	909	221	81	913	233	202	944	166	413	929	203	-38	898	257
7353	-456	904	85	-242	925	76	-122	907	186	84	912	198	207	944	131	418	931	166	-34	898	222
7354	-451	904	52	-237	924	40	-118	906	151	89	911	163	213	944	95	422	934	129	-30	897	188
7355	-447	903	19	-232	924	4	-114	905	117	93	911	128	218	944	60	426	936	92	-25	897	152
7356	-442	902	-13	-228	924	-31	-110	905	82	97	910	94	222	945	24	430	939	55	-22	896	118
7357	-437	900	-45	-223	923	-66	-106	905	47	102	911	59	226	946	-11	434	941	18	-17	895	84
7358	-432	897	-79	-219	923	-101	-102	905	13	106	911	24	229	947	-46	439	943	-20	-13	895	49
7359	-427	894	-113	-214	922	-136	-98	905	-22	110	912	-10	233	948	-82	443	944	-57	-9	895	15
7360	-422	891	-147	-210	922	-171	-94	904	-57	114	912	-45	236	949	-117	447	946	-94	-5	895	-19
7361	-418	889	-182	-206	921	-206	-91	903	-91	118	913	-80	239	949	-152	451	948	-132	-1	896	-53
7362	-415	887	-218	-202	921	-240	-88	903	-124	123	913	-114	243	950	-187	456	949	-170	3	896	-86
7363	-412	886	-253	-198	919	-274	-84	903	-159	128	914	-148	246	950	-221	460	951	-207	7	897	-120
7364	-409	884	-289	-195	918	-308	-81	903	-192	132	914	-182	250	950	-256	464	953	-244	11	897	-153

Table A.2: CB T3 C2 7288-7389

Frame	Primary_P			Wrist_P			Elbow_P			Elbow_S			Wrist_S			Primary_S			Spine_F		
	X	Y	Z	X	Y	Z	X	Y	Z	X	Y	Z	X	Y	Z	X	Y	Z	X	Y	Z
7365	-406	882	-324	-192	916	-342	-79	902	-226	137	914	-215	255	951	-290	468	954	-280	14	898	-187
7366	-403	878	-361	-190	914	-376	-75	902	-260	142	915	-249	258	951	-322	473	956	-316	18	900	-220
7367	-400	874	-397	-187	912	-411	-74	901	-293	146	916	-282	262	951	-356	477	956	-351	22	902	-253
7368	-396	869	-434	-184	910	-445	-71	901	-326	150	917	-315	266	952	-389	481	956	-385	26	903	-286
7369	-392	864	-472	-180	909	-478	-68	901	-360	155	919	-348	271	953	-423	485	954	-420	29	905	-318
7370	-387	859	-510	-177	909	-511	-66	901	-393	159	920	-380	276	954	-456	490	952	-456	32	907	-351
7371	-382	854	-547	-174	908	-543	-63	901	-425	162	922	-412	280	956	-489	493	948	-493	34	910	-382
7372	-376	849	-584	-171	910	-576	-60	902	-457	166	924	-443	284	959	-520	496	946	-530	37	913	-414
7373	-370	846	-622	-167	912	-609	-58	904	-488	169	926	-474	289	962	-552	498	946	-567	40	916	-446
7374	-363	842	-662	-162	916	-640	-55	905	-519	173	929	-505	293	965	-582	500	947	-604	43	919	-478
7375	-355	840	-701	-159	922	-673	-52	907	-550	175	933	-535	296	969	-613	501	951	-640	46	922	-509
7376	-347	839	-733	-155	928	-703	-49	910	-581	177	935	-564	299	975	-642	502	955	-674	48	926	-540
7377	-344	843	-772	-152	936	-733	-47	913	-612	180	940	-594	300	982	-672	503	960	-706	50	930	-571
7378	-339	852	-810	-150	945	-763	-44	917	-642	183	944	-623	301	990	-700	503	966	-735	53	933	-602
7379	-329	859	-848	-147	955	-791	-41	922	-672	185	950	-652	301	999	-728	504	971	-764	56	937	-632
7380	-323	869	-883	-145	965	-819	-38	927	-701	191	958	-679	300	1010	-757	503	978	-790	58	941	-663
7381	-321	882	-916	-142	975	-844	-36	932	-730	187	963	-710	299	1022	-786	503	984	-814	61	946	-694
7382	-318	898	-948	-139	986	-872	-33	939	-759	189	971	-739	299	1034	-814	501	990	-839	64	950	-725
7383	-314	911	-975	-137	997	-899	-32	947	-788	187	979	-763	298	1046	-842	500	998	-861	66	955	-755
7384	-313	927	-1001	-134	1008	-924	-28	956	-816	186	990	-790	296	1058	-870	499	1007	-884	70	961	-785
7385	-312	940	-1024	-129	1020	-951	-24	967	-843	184	1001	-818	294	1068	-898	498	1017	-905	72	967	-815
7386	-311	954	-1045	-125	1032	-979	-21	979	-871	182	1011	-846	291	1077	-927	495	1027	-924	72	972	-843
7387	-310	967	-1064	-120	1043	-1007	-16	991	-898	180	1021	-875	288	1085	-957	493	1037	-943	76	976	-875
7388	-308	981	-1084	-113	1053	-1037	-13	1003	-925	176	1030	-904	284	1092	-986	491	1049	-961	78	983	-907
7389	-307	994	-1103	-106	1063	-1067	-9	1015	-953	173	1039	-935	281	1099	-1016	488	1060	-978	80	990	-937
7390	-304	1007	-1118	-98	1072	-1098	-2	1026	-983	172	1048	-969	278	1106	-1045	485	1073	-996	81	994	-961
7391	-304	1023	-1137	-94	1080	-1128	2	1034	-1013	170	1055	-1000	274	1113	-1074	483	1086	-1013	82	999	-990

Table A.2: CB T3 C2 7288-7389

Frame	Primary_P			Wrist_P			Elbow_P			Elbow_S			Wrist_S			Primary_S			Spine_F		
	X	Y	Z	X	Y	Z	X	Y	Z	X	Y	Z	X	Y	Z	X	Y	Z	X	Y	Z
7392	-301	1038	-1154	-90	1086	-1156	9	1041	-1044	170	1057	-1029	271	1118	-1105	481	1099	-1032	84	1003	-1020
7393	-299	1053	-1171	-83	1093	-1186	13	1045	-1074	169	1061	-1061	270	1123	-1134	480	1112	-1051	88	1008	-1053
7394	-297	1068	-1189	-78	1100	-1216	17	1047	-1105	171	1063	-1091	270	1125	-1163	480	1124	-1072	89	1011	-1077
7395	-297	1082	-1208	-74	1104	-1245	20	1048	-1136	174	1066	-1124	273	1126	-1193	482	1134	-1094	89	1014	-1105
7396	-298	1094	-1228	-71	1108	-1272	21	1049	-1166	179	1064	-1149	279	1126	-1220	485	1144	-1118	90	1016	-1131
7397	-299	1106	-1252	-72	1110	-1298				186	1064	-1174	285	1126	-1247	490	1154	-1144	19	1048	-1193
7398	-303	1113	-1278	-75	1112	-1322	98	1020	-1193	193	1063	-1199	293	1127	-1273	497	1163	-1173	17	1047	-1220

Table A.3: Common Buzzard - specimen: CB, Trial 4, Capture session 2, Frames: 1581-1688

Frame	Primary_P			Wrist_P			Elbow_P			Elbow_S			Wrist_S			Primary_S			Spine_F		
	X	Y	Z	X	Y	Z	X	Y	Z	X	Y	Z	X	Y	Z	X	Y	Z	X	Y	Z
1580	-728	1017	2160	-559	1135	2076	-482	1121	2208				-223	1147	2104	-87	1068	2271	-405	1113	2214
1581	-734	1055	2143	-553	1142	2043	-474	1117	2169				-216	1153	2069	-84	1107	2251	-401	1104	2181
1582	-734	1092	2120	-546	1143	2010	-467	1111	2130				-209	1158	2037	-81	1146	2224	-397	1096	2148
1583	-731	1126	2090	-541	1142	1976	-460	1104	2092				-200	1159	2008	-77	1181	2190	-394	1088	2116
1584	-729	1154	2053	-536	1139	1941	-455	1096	2055				-192	1158	1980	-67	1206	2149	-389	1079	2083
1585	-730	1172	2012	-534	1131	1906	-450	1088	2020				-184	1153	1953	-54	1220	2105	-386	1070	2051
1586	-732	1180	1969	-534	1121	1872	-445	1082	1987				-176	1146	1927	-37	1226	2061	-381	1062	2018
1587	-736	1180	1925	-535	1112	1839	-439	1077	1955				-168	1140	1900	-18	1224	2017	-377	1053	1986
1588	-742	1175	1880	-539	1101	1807	-435	1071	1924				-161	1133	1871	2	1216	1974	-373	1046	1954
1589	-749	1165	1834	-543	1091	1777	-434	1062	1893				-154	1125	1841	22	1205	1931	-368	1039	1921
1590	-757	1150	1789	-549	1081	1747	-435	1052	1861				-147	1115	1813	43	1189	1887	-364	1033	1889
1591	-763	1129	1744	-555	1070	1720	-435	1043	1829				-138	1103	1784	59	1166	1850	-358	1027	1855
1592	-767	1105	1700	-559	1058	1693	-433	1035	1795				-128	1089	1755	77	1142	1808	-354	1022	1823
1593	-772	1076	1659	-559	1044	1665	-431	1027	1761				-116	1073	1727	92	1113	1767	-350	1016	1789
1594	-774	1045	1617	-559	1029	1635	-429	1019	1725				-105	1059	1697	106	1083	1728	-345	1012	1756
1595	-774	1013	1577	-557	1014	1602	-428	1010	1690				-94	1045	1663	118	1052	1687	-340	1008	1723
1596	-772	980	1536	-557	998	1567	-428	1001	1656				-83	1030	1629	127	1019	1647	-335	1005	1689
1597	-767	948	1496	-559	980	1533	-427	993	1622				-72	1011	1597	135	987	1604	-333	1001	1657
1598	-760	916	1456	-559	961	1498	-426	985	1587				-62	991	1560	140	954	1567	-329	998	1623
1599	-752	884	1417	-553	943	1461	-423	978	1553				-52	972	1523	142	924	1523	-325	996	1590
1600	-740	853	1377	-547	926	1426	-421	970	1520				-49	952	1485	142	893	1481	-322	994	1557
1601	-726	824	1337	-540	909	1390	-419	963	1486				-49	933	1448	140	865	1439	-317	992	1522
1602	-708	799	1297	-532	894	1354	-415	957	1453				-47	918	1408	136	839	1397	-313	990	1488
1603	-690	777	1258	-521	883	1318	-410	951	1420				-49	905	1369	129	816	1356	-309	989	1454
1604	-671	759	1217	-511	874	1283	-406	947	1388				-51	896	1330	122	797	1315	-305	989	1420
1605	-653	747	1177	-503	867	1249	-401	943	1355				-55	889	1292	114	782	1274	-301	988	1385
1606	-638	741	1138	-492	865	1213	-396	940	1323				-60	886	1254	106	773	1234	-297	987	1351

Table A.3: CB T4 C2 1581-1688

Frame	Primary_P			Wrist_P			Elbow_P			Elbow_S			Wrist_S			Primary_S			Spine_F		
	X	Y	Z	X	Y	Z	X	Y	Z	X	Y	Z	X	Y	Z	X	Y	Z	X	Y	Z
1607	-625	740	1102	-480	870	1176	-392	938	1291				-66	887	1225	101	771	1196	-292	987	1315
1608	-618	743	1069	-474	878	1140	-389	939	1259				-68	897	1191	98	773	1160	-287	986	1279
1609	-614	749	1039	-471	888	1105	-383	941	1226				-68	909	1155	100	780	1128	-282	985	1242
1610	-614	759	1013	-471	900	1067	-378	946	1190				-65	920	1119	104	791	1102	-278	983	1206
1611	-618	772	992	-471	915	1029	-377	948	1155				-62	931	1084	111	806	1080	-273	982	1169
1612	-624	788	975	-469	931	991	-373	953	1121				-57	943	1047	116	822	1062	-267	982	1130
1613	-629	806	960	-467	947	955	-365	957	1083				-52	954	1009	122	840	1047	-265	978	1097
1614	-632	827	946	-465	963	921	-360	961	1046				-46	967	969	127	862	1033	-260	974	1062
1615	-634	852	930	-459	977	889	-354	964	1009	-148	973	1032	-40	979	927	133	886	1018	-256	971	1026
1616	-636	879	913	-453	988	859	-348	966	971	-146	975	992	-34	991	890	136	912	1002	-252	968	992
1617	-635	906	894	-443	994	829	-341	966	934	-146	977	955	-30	1002	856	139	940	982	-249	964	957
1618	-633	932	869	-433	996	796	-334	966	898	-144	977	916	-26	1013	826	142	967	957	-244	960	923
1619	-630	952	841	-425	996	761	-328	966	862	-142	975	880	-24	1019	799	146	990	927	-241	956	889
1620	-627	966	809	-417	995	725	-321	964	827	-139	973	844	-24	1020	773	152	1008	892	-237	951	855
1621	-625	975	776	-412	994	689	-315	962	793				-26	1015	746	159	1020	855	-233	947	821
1622	-625	981	740	-410	991	653	-310	960	761	-131	967	776	-25	1009	715	168	1029	815	-230	944	788
1623	-626	983	703	-410	988	618	-305	957	729	-127	965	744	-22	1007	680	178	1032	774	-227	941	754
1624	-628	985	664	-412	985	583	-303	954	695	-121	962	709	-16	1004	642	189	1033	731	-224	938	721
1625	-631	985	622	-415	981	550	-302	951	662	-114	958	673	-9	1001	604	200	1031	688	-220	936	688
1626	-634	983	580	-419	977	518	-302	948	627				-2	998	567	210	1028	646	-216	934	654
1627	-637	979	536	-423	971	486	-301	946	592				8	992	531	220	1021	602	-212	933	621
1628	-639	971	491	-426	962	457	-299	943	557				18	988	495	230	1014	558	-208	931	588
1629	-640	960	446	-426	956	426	-296	939	522				28	984	461	238	1006	514	-204	931	555
1630	-640	947	401	-424	948	395	-294	935	487				38	978	426	247	998	469	-200	930	521
1631	-640	933	356	-422	940	363	-292	931	452				48	974	394	255	989	425	-197	929	489
1632	-637	917	310	-421	932	329	-290	928	418				58	968	363	260	979	385	-193	929	455
1633	-634	902	265	-421	923	295	-289	925	384				64	962	331	266	970	342	-190	930	423

Table A.3: CB T4 C2 1581-1688

Frame	Primary_P			Wrist_P			Elbow_P			Elbow_S			Wrist_S			Primary_S			Spine_F		
	X	Y	Z	X	Y	Z	X	Y	Z	X	Y	Z	X	Y	Z	X	Y	Z	X	Y	Z
1634	-629	888	220	-419	914	259	-289	922	350				67	957	298	272	960	298	-186	931	391
1635	-622	875	175	-417	905	223	-288	919	317				70	951	265	277	949	255	-184	932	358
1636	-614	863	129	-412	899	186	-286	916	283				73	945	232	279	937	211	-182	933	326
1637	-606	852	86	-407	893	149	-284	914	250				75	939	199	282	926	167	-179	934	294
1638	-597	842	43	-402	888	112	-281	913	216				77	934	164	284	915	121	-177	936	262
1639	-587	834	1	-396	885	76	-278	913	183				79	932	127	283	904	77	-175	938	231
1640	-576	827	-41	-390	885	40	-276	914	150				81	929	89	281	895	34	-173	941	199
1641	-566	822	-81	-384	887	4	-273	915	118				82	928	52	278	889	-9	-171	944	167
1642	-557	820	-121	-379	892	-32	-271	918	87				83	931	16	275	884	-50	-169	947	136
1643	-547	821	-159	-374	900	-67	-269	922	55				83	937	-20	271	883	-87	-167	952	104
1644	-539	825	-195	-370	912	-102	-266	927	25				82	946	-54	267	884	-122	-164	957	71
1645	-532	832	-228	-366	926	-136	-265	931	-5				82	957	-89	266	888	-152	-162	961	39
1646	-527	844	-257	-361	941	-168	-263	937	-35				82	970	-123	264	895	-179	-160	967	5
1647	-525	858	-283	-357	957	-199	-260	944	-66				81	984	-156	264	905	-200	-158	971	-28
1648	-523	871	-305	-352	974	-229	-257	954	-96				80	998	-188	265	916	-217	-156	975	-61
1649	-524	886	-321	-347	992	-258	-254	966	-127				78	1012	-219	267	928	-230	-153	980	-95
1650	-525	901	-335	-342	1009	-286	-250	978	-157				75	1025	-248	266	941	-239	-150	984	-128
1651	-526	919	-350	-337	1024	-312	-247	989	-188				74	1039	-278	264	955	-248	-148	987	-162
1652	-525	937	-363	-331	1038	-339	-241	1000	-220				73	1052	-309	262	971	-257	-145	991	-195
1653	-525	958	-376	-323	1048	-366	-233	1010	-253				72	1066	-340	261	992	-266	-142	994	-227
1654	-524	980	-390	-316	1056	-395	-225	1018	-287	-38	1032	-268	70	1078	-369	258	1013	-278	-139	997	-260
1655	-523	1002	-407	-310	1064	-426	-218	1025	-319	-41	1037	-304	68	1087	-395	255	1036	-293	-136	999	-292
1656	-520	1021	-425	-304	1071	-458	-211	1030	-352	-39	1040	-340	66	1094	-421	254	1058	-311	-134	1002	-323
1657	-518	1037	-446	-300	1076	-491	-205	1033	-383				64	1098	-445	254	1077	-333	-130	1003	-355
1658	-518	1049	-470	-296	1078	-523	-200	1035	-415				63	1099	-471	257	1093	-359	-128	1005	-387
1659	-518	1058	-494	-295	1078	-555	-197	1035	-445				65	1098	-497	262	1105	-388	-125	1007	-418
1660	-519	1064	-521	-296	1076	-586	-196	1035	-475				69	1096	-523	270	1114	-420	-123	1010	-448

Table A.3: CB T4 C2 1581-1688

Frame	Primary_P			Wrist_P			Elbow_P			Elbow_S			Wrist_S			Primary_S			Spine_F		
	X	Y	Z	X	Y	Z	X	Y	Z	X	Y	Z	X	Y	Z	X	Y	Z	X	Y	Z
1661	-522	1068	-549	-299	1075	-615	-196	1035	-504				76	1093	-553	281	1120	-454	-120	1012	-480
1662	-526	1069	-579	-303	1074	-644	-198	1034	-532				84	1091	-582	292	1124	-489	-117	1015	-510
1663	-530	1069	-613	-308	1073	-672	-199	1035	-562				92	1092	-610	305	1126	-526	-115	1017	-540
1664	-535	1064	-649	-315	1072	-699	-201	1035	-592				104	1092	-639	317	1126	-565	-113	1020	-569
1665	-539	1058	-687	-323	1067	-722	-203	1035	-622				115	1092	-669	329	1124	-606	-111	1023	-597
1666	-544	1052	-729	-329	1062	-749	-205	1034	-653				128	1091	-697	341	1120	-649	-108	1025	-625
1667	-546	1045	-772	-332	1055	-778	-206	1034	-685				141	1090	-726	350	1115	-695	-106	1028	-652
1668	-545	1036	-817	-330	1051	-811	-206	1034	-717				153	1087	-755	357	1110	-741	-103	1031	-680
1669	-547	1026	-861	-327	1047	-845	-206	1035	-750				161	1082	-784	360	1105	-786	-102	1035	-709
1670	-539	1017	-913	-326	1045	-880	-205	1036	-781				162	1081	-817	364	1101	-832	-99	1040	-737
1671	-533	1012	-961	-326	1045	-913	-203	1038	-812				161	1081	-852	365	1096	-877	-97	1044	-766
1672	-523	1011	-1009	-324	1048	-947	-201	1040	-842				159	1082	-885	361	1092	-914	-96	1049	-793
1673	-514	1016	-1058	-320	1051	-981	-202	1043	-872				157	1085	-920	358	1089	-954	-96	1054	-821
1674	-504	1023	-1104	-316	1054	-1013	-200	1047	-900				155	1090	-953	358	1093	-1001	-95	1060	-848
1675	-490	1029	-1145	-312	1060	-1045	-199	1049	-933				152	1097	-986	353	1096	-1039	-95	1067	-874
1676	-480	1041	-1187	-310	1068	-1076	-201	1055	-954				151	1104	-1018	352	1102	-1084	-93	1072	-901
1677	-473	1058	-1229	-307	1078	-1106	-200	1062	-982				149	1115	-1050	346	1107	-1120	-95	1079	-923
1678	-463	1073	-1265	-304	1090	-1134	-200	1070	-1008				148	1127	-1080	341	1115	-1156	-95	1086	-949
1679	-455	1090	-1297	-301	1105	-1161	-195	1075	-1032				145	1141	-1109	335	1123	-1189	-95	1091	-974
1680	-448	1109	-1326	-299	1122	-1186	-195	1083	-1057				143	1158	-1137	329	1135	-1220	-94	1099	-1000
1681	-444	1130	-1348	-296	1141	-1207	-198	1095	-1081				138	1176	-1163	322	1149	-1246	-94	1106	-1025
1682	-441	1147	-1367	-298	1157	-1220	-197	1098	-1102				132	1194	-1185	316	1165	-1267	-96	1113	-1050
1683	-443	1166	-1382	-291	1180	-1241	-194	1107	-1125				125	1210	-1203	312	1181	-1285	-91	1123	-1076
1684	-446	1181	-1393	-290	1201	-1255	-198	1123	-1146				118	1228	-1221	308	1197	-1299	-90	1131	-1102
1685	-447	1191	-1401	-288	1222	-1268	-199	1132	-1166				111	1247	-1240	305	1212	-1312	-90	1138	-1127
1686	-449	1201	-1408	-285	1242	-1280	-193	1147	-1183				105	1265	-1257	301	1226	-1320	-89	1147	-1153
1687	-451	1210	-1414	-281	1260	-1291	-191	1162	-1201				99	1283	-1276	299	1239	-1328	-88	1156	-1177

Table A.3: CB T4 C2 1581-1688

Frame	Primary_P			Wrist_P			Elbow_P			Elbow_S			Wrist_S			Primary_S			Spine_F		
	X	Y	Z	X	Y	Z	X	Y	Z	X	Y	Z	X	Y	Z	X	Y	Z	X	Y	Z
1688	-454	1219	-1417	-275	1275	-1303	-189	1178	-1219				93	1301	-1296	297	1253	-1334	-86	1163	-1202

Table A.4: Eurasian Eagle Owl - specimen: EEO, Trial 9, Capture session 3, Frames: 67-168

Frame	Primary_P			Wrist_P			Elbow_P			Elbow_S			Wrist_S			Primary_S			Spine_F		
	X	Y	Z	X	Y	Z	X	Y	Z	X	Y	Z	X	Y	Z	X	Y	Z	X	Y	Z
67	1893	-218	734	1809	59	809	1800	250	835	1638	582	836	1445	710	824	1267	895	737	1705	441	840
68	1850	-232	702	1780	43	789	1780	234	824	1617	575	827	1418	695	804	1237	867	703	1688	432	840
69	1805	-243	672	1749	31	769	1761	219	813	1595	567	818	1390	676	784	1207	835	670	1672	422	841
70	1760	-251	642	1717	21	750	1740	205	803	1575	557	809	1365	655	765	1179	800	640	1655	411	840
71	1713	-256	613	1684	13	733	1720	191	793	1555	547	801	1341	631	749	1152	762	611	1637	402	841
72	1664	-257	585	1652	6	720	1699	179	784	1536	537	792	1319	605	735	1127	720	585	1620	392	842
73	1614	-256	560	1620	0	708	1678	167	777	1518	526	785	1299	577	723	1104	676	561	1603	382	843
74	1562	-252	539	1588	-3	698	1658	157	770	1501	516	778	1281	549	713	1084	629	542	1585	373	845
75	1511	-244	521	1557	-7	692	1638	147	765	1485	505	772	1264	521	706	1066	581	527	1567	364	847
76	1460	-233	507	1525	-8	688	1618	138	761	1470	494	766	1248	494	701	1051	531	516	1550	355	848
77	1411	-218	498	1495	-8	687	1598	129	756	1456	484	761	1233	468	699	1039	480	511	1533	346	850
78	1363	-201	493	1466	-6	689	1579	121	753	1442	472	756	1220	444	700	1029	429	513	1515	336	851
79	1316	-180	494	1439	-3	695	1560	115	752	1428	461	753	1207	422	703	1021	381	521	1496	327	852
80	1272	-159	500	1415	-2	703	1542	110	751	1416	450	751	1195	403	708	1015	337	534	1477	317	852
81	1233	-139	513	1393	-1	715	1525	105	752	1403	439	750	1184	388	717	1010	298	551	1458	307	852
82	1197	-122	530	1374	-1	730	1509	101	754	1391	429	751	1173	376	728	1005	264	572	1438	296	852
83	1167	-109	552	1357	-1	746	1495	98	759	1379	421	753	1162	366	741	999	237	595	1418	286	851
84	1142	-99	576	1341	-2	765	1482	94	765	1367	412	756	1153	359	756	992	215	618	1397	275	850
85	1120	-94	599	1328	-4	785	1471	90	774	1355	403	762	1144	352	772	984	199	641	1377	264	849
86	1104	-95	623	1315	-6	805	1461	86	785	1343	394	770	1135	347	790	975	190	659	1356	254	847
87	1093	-103	645	1304	-8	826	1449	85	797	1332	385	780	1127	342	809	964	188	673	1335	243	845
88	1089	-116	661	1294	-11	848	1435	87	811	1320	374	791	1120	336	829	951	194	681	1314	232	842
89	1094	-132	672	1285	-14	869	1419	90	827	1306	361	803	1114	329	849	941	207	684	1293	221	839
90	1107	-151	680	1276	-17	889	1400	96	842	1292	345	815	1108	321	869	931	229	683	1272	210	835
91	1129	-170	686	1266	-15	909	1379	103	857	1278	328	827	1103	311	889	928	259	681	1252	198	832
92	1161	-192	696	1254	-10	928	1354	111	870	1263	308	839	1099	298	908	930	297	684	1232	188	831
93	1202	-212	715	1241	-3	947	1324	118	880	1248	286	850	1095	282	927	939	339	695	1212	175	827

Table A.4: EEO T9 C3 67-168

Frame	Primary_P			Wrist_P			Elbow_P			Elbow_S			Wrist_S			Primary_S			Spine_F		
	X	Y	Z	X	Y	Z	X	Y	Z	X	Y	Z	X	Y	Z	X	Y	Z	X	Y	Z
94	1246	-228	744	1223	5	965	1293	125	888	1233	264	858	1092	260	944	955	381	717	1192	163	825
95	1288	-237	782	1199	12	979	1261	130	892	1217	240	865	1083	233	957	972	415	746	1173	151	823
96	1323	-241	827	1170	12	987	1226	129	891	1199	218	870	1061	206	963	990	441	782	1155	139	821
97	1351	-239	875	1140	2	990	1191	123	887	1181	196	873	1031	188	965	1005	460	821	1137	127	819
98	1371	-233	922	1114	-16	989	1161	114	882	1160	177	873	1001	179	966	1016	472	861	1119	117	817
99	1383	-226	967	1098	-37	987	1132	100	876	1139	159	872	975	179	965	1021	481	903	1101	108	814
100	1387	-221	1009	1088	-61	985	1108	83	871	1116	144	869	952	187	964	1019	487	945	1084	99	812
101	1382	-223	1047	1085	-86	983	1088	64	866	1095	131	864	930	199	961	1008	491	985	1066	92	809
102	1371	-235	1076	1085	-109	981	1072	45	863	1071	122	858	911	215	957	988	493	1019	1049	84	804
103	1357	-255	1092	1087	-130	978	1058	24	860	1046	117	851	894	232	952	959	495	1043	1031	77	799
104	1345	-281	1095	1088	-148	974	1047	5	858	1023	115	843	877	249	945	924	500	1054	1014	69	793
105	1336	-309	1089	1090	-164	968	1038	-13	856	1002	114	834	862	263	936	886	507	1053	997	61	785
106	1327	-339	1076	1091	-180	960	1029	-29	854	982	116	825	846	273	925	846	515	1043	979	53	778
107	1315	-372	1060	1090	-197	951	1021	-44	851	963	119	815	830	279	912	807	523	1025	961	44	771
108	1300	-408	1040	1084	-215	939	1013	-58	847	944	123	805	810	283	899	766	530	1001	943	34	764
109	1280	-446	1018	1075	-234	926	1006	-70	844	924	126	795	788	284	885	724	534	974	926	25	759
110	1257	-484	993	1064	-254	911	999	-85	839	901	126	790	765	284	870	682	534	944	910	16	756
111	1231	-520	967	1051	-277	898	991	-107	831	876	124	787	739	282	854	640	530	913	892	7	753
112	1202	-554	940	1036	-299	883	982	-131	821	851	121	784	711	278	839	596	522	883	872	-3	751
113	1170	-585	913	1016	-322	868	971	-155	811	827	116	780	682	271	824	552	509	855	855	-12	752
114	1135	-615	885	993	-345	853	954	-178	803	804	110	773	652	263	810	510	495	827	837	-22	751
115	1099	-642	858	968	-368	838	935	-197	798	779	102	765	622	253	796	469	478	800	819	-31	751
116	1060	-668	830	941	-389	824	914	-214	792	757	94	760	592	241	784	428	459	774	801	-41	751
117	1020	-693	803	913	-410	810	892	-231	787	734	85	753	561	228	771	389	436	749	783	-51	752
118	978	-716	777	884	-431	797	870	-247	781	711	76	749	531	213	759	349	413	725	765	-61	753
119	935	-738	751	854	-451	784	847	-262	776	687	66	744	499	197	747	312	388	702	747	-71	754
120	890	-758	728	822	-469	770	824	-278	769	663	57	739	469	182	734	275	360	680	730	-81	756

Table A.4: EEO T9 C3 67-168

Frame	Primary_P			Wrist_P			Elbow_P			Elbow_S			Wrist_S			Primary_S			Spine_F		
	X	Y	Z	X	Y	Z	X	Y	Z	X	Y	Z	X	Y	Z	X	Y	Z	X	Y	Z
121	843	-775	707	790	-486	756	802	-294	765	640	48	734	441	165	722	240	331	659	712	-91	757
122	796	-790	687	757	-502	743	780	-309	760	616	38	728	413	146	709	206	300	639	694	-101	760
123	748	-803	666	725	-516	731	757	-324	754	594	29	724	386	126	697	175	268	619	677	-111	763
124	701	-812	646	690	-525	719	735	-337	749	572	18	720	359	104	686	145	234	602	660	-121	766
125	652	-818	627	656	-534	711	714	-350	745	552	8	717	335	81	678	117	198	584	643	-131	770
126	602	-821	610	624	-541	704	693	-363	741	534	-4	713	312	57	670	92	160	569	625	-140	773
127	553	-822	595	591	-547	699	672	-374	737	516	-15	710	290	32	664	68	121	555	608	-150	777
128	504	-819	583	560	-551	696	652	-385	734	499	-27	708	270	7	659	47	80	543	592	-160	781
129	456	-814	573	529	-554	696	632	-395	731	483	-38	705	252	-18	657	28	37	535	575	-169	785
130	408	-806	567	501	-555	697	613	-405	729	468	-48	704	236	-44	658	12	-6	530	558	-178	789
131	362	-795	566	474	-555	702	593	-413	726	454	-60	703	222	-67	664	-1	-50	530	541	-188	793
132	319	-783	568	449	-554	709	574	-421	726	440	-71	702	210	-88	672	-12	-93	535	523	-197	796
133	279	-770	576	427	-554	719	556	-429	725	427	-82	703	198	-107	683	-21	-134	544	506	-207	800
134	243	-758	587	408	-553	730	538	-435	727	415	-92	706	188	-123	696	-28	-171	558	487	-218	803
135	213	-747	601	391	-555	745	522	-441	730	402	-100	709	179	-136	710	-33	-203	575	468	-228	806
136	187	-738	617	377	-558	761	507	-444	734	390	-110	713	170	-147	726	-38	-230	595	449	-239	807
137	166	-731	634	366	-561	777	496	-449	742	379	-118	718	163	-156	743	-43	-253	615	430	-250	810
138	148	-727	651	355	-565	795	486	-452	748	369	-125	725	156	-163	759	-49	-269	637	411	-261	812
139	135	-726	667	347	-569	812	477	-456	758	358	-133	733	149	-169	776	-56	-280	658	391	-272	814
140	126	-728	681	340	-572	827	466	-458	767	348	-142	743	142	-173	793	-63	-286	676	371	-283	815
141	123	-734	692	334	-575	842	455	-458	779	338	-151	754	135	-177	809	-72	-286	690	351	-294	816
142	123	-740	700	328	-577	857	441	-456	791	327	-162	766	128	-181	827	-80	-280	699	330	-305	817
143	131	-748	703	321	-578	871	427	-453	804	316	-174	778	122	-184	845	-87	-267	705	310	-317	817
144	146	-757	705	315	-578	886	409	-448	817	304	-188	791	117	-189	865	-92	-245	708	289	-328	817
145	166	-766	705	306	-575	900	389	-443	828	292	-204	803	114	-196	886	-91	-218	710	270	-338	817
146	198	-778	708	296	-573	918	368	-438	841	279	-221	815	113	-204	907	-85	-183	715	250	-349	817
147	238	-788	717	283	-570	936	343	-434	852	266	-240	826	113	-215	928	-73	-144	725	230	-360	817

Table A.4: EEO T9 C3 67-168

Frame	Primary_P			Wrist_P			Elbow_P			Elbow_S			Wrist_S			Primary_S			Spine_F		
	X	Y	Z	X	Y	Z	X	Y	Z	X	Y	Z	X	Y	Z	X	Y	Z	X	Y	Z
148	283	-795	733	268	-568	954	316	-430	860	250	-259	836	111	-230	946	-53	-106	743	214	-369	816
149	329	-798	758	250	-566	971	286	-429	867	234	-279	844	108	-250	961	-32	-74	767	192	-381	817
150	371	-796	790	227	-567	983	256	-430	872	218	-299	851	95	-272	970	-7	-47	797	174	-392	817
151	406	-790	829	202	-573	987	228	-435	875	200	-318	857	73	-290	975	14	-28	828	156	-403	817
152	431	-783	868	179	-586	986	198	-444	876	181	-335	861	45	-298	978	32	-14	861	138	-413	816
153	448	-776	907	162	-603	983	172	-457	877	160	-351	865	16	-298	982	45	-3	896	121	-423	815
154	455	-774	944	150	-622	981	147	-472	877	139	-364	867	-10	-291	984	52	6	933	104	-431	814
155	456	-778	978	143	-643	978	126	-491	877	118	-375	867	-32	-280	984	50	11	970	88	-440	813
156	449	-790	1007	139	-664	974	109	-510	876	97	-383	866	-49	-267	980	37	14	1001	72	-447	812
157	438	-808	1029	138	-685	969	94	-530	874	76	-388	863	-63	-253	973	14	18	1021	56	-455	809
158	424	-833	1041	140	-705	962	82	-549	873	55	-392	859	-76	-240	965	-16	23	1031	40	-463	806
159	408	-862	1044	142	-724	954	72	-566	870	35	-394	853	-90	-230	954	-50	29	1030	23	-470	803
160	392	-896	1038	142	-742	944	63	-583	868	16	-394	847	-106	-223	943	-87	36	1022	6	-478	799
161	371	-930	1028	140	-759	934	54	-598	865	-2	-393	841	-125	-220	931	-126	41	1007	-10	-486	795
162	346	-964	1014	131	-775	923	45	-612	861	-21	-391	832	-144	-217	918	-167	44	988	-28	-494	791
163	317	-998	997	117	-793	912	37	-625	858	-43	-389	823	-164	-216	905	-209	45	967	-45	-503	788
164	285	-1031	979	100	-810	901	29	-637	854	-66	-389	815	-187	-217	894	-252	41	944	-62	-512	785
165	251	-1064	958	82	-829	890	20	-652	848	-89	-392	810	-212	-221	881	-297	34	922	-79	-521	785
166	214	-1098	937	61	-849	879	7	-673	839	-111	-396	808	-240	-228	871	-343	24	900	-95	-529	786
167	177	-1130	914	37	-869	870	-5	-692	830	-134	-402	805	-271	-236	860	-389	10	879	-111	-537	788
168	138	-1163	891	11	-889	861	-20	-713	821	-157	-409	802	-303	-247	851	-435	-7	859	-127	-545	790

Table A.5: Harris Hawk - specimen: HH, Trial 11, Capture session 3, Frames: 951-1073

Frame	Primary_P			Wrist_P			Elbow_P			Elbow_S			Wrist_S			Primary_S			Spine_F		
	X	Y	Z	X	Y	Z	X	Y	Z	X	Y	Z	X	Y	Z	X	Y	Z	X	Y	Z
951	1714	-151	418	1636	58	431	1667	180	427	1556	365	423	1421	400	403	1242	490	427	1625	276	451
952	1680	-164	404	1618	49	424	1650	170	421	1537	353	418	1401	386	400	1220	464	420	1610	266	449
953	1640	-175	391	1600	39	416	1633	159	418	1522	345	415	1381	371	397	1199	437	411	1595	256	448
954	1597	-185	378	1579	32	416	1615	148	419	1507	337	414	1363	358	395	1180	408	400	1578	247	448
955	1552	-188	368	1554	25	418	1600	139	420	1492	327	413	1347	346	393	1163	378	390	1562	237	449
956	1511	-186	361	1530	20	424	1586	130	423	1479	319	414	1335	334	393	1150	348	381	1545	227	450
957	1474	-179	360	1507	14	434	1575	122	428	1466	310	417	1326	321	398	1141	322	375	1527	216	450
958	1448	-173	362	1485	12	444	1563	115	435	1456	301	420	1318	307	407	1135	301	374	1508	206	449
959	1433	-170	366	1464	12	454	1550	109	444	1445	290	424	1310	294	418	1129	289	377	1490	195	448
960	1429	-171	369	1445	15	463	1534	106	455	1435	279	429	1302	281	430	1121	287	381	1469	186	447
961	1434	-176	375	1427	17	473	1513	103	465	1423	266	434	1292	267	443	1112	294	385	1451	175	445
962	1449	-184	385	1413	19	483	1489	100	474	1410	251	441	1281	254	455	1105	305	390	1432	166	443
963	1472	-190	401	1405	15	491	1464	97	482	1395	236	448	1268	240	467	1101	320	398	1415	156	441
964	1499	-192	425	1399	5	499	1438	93	487	1379	220	455	1252	227	478	1099	339	410	1397	148	441
965	1524	-187	457	1383	-9	508	1409	86	489	1361	205	460	1232	213	486	1102	363	428	1379	138	439
966	1540	-175	495	1363	-26	517	1380	76	487	1341	189	465	1212	200	494	1110	388	452	1362	129	438
967	1543	-160	532	1344	-47	519	1353	63	482	1319	176	466	1192	191	502	1122	406	482	1346	121	437
968	1533	-146	565	1327	-68	510	1330	46	472	1297	164	465	1175	191	507	1133	413	515	1329	112	436
969	1513	-142	590	1317	-86	492	1313	28	461	1277	155	460	1159	196	509	1138	407	545	1313	103	435
970	1490	-150	601	1314	-98	474	1301	9	450	1260	147	456	1144	203	505	1134	395	571	1297	94	433
971	1474	-171	602	1316	-104	459	1293	-8	441	1243	141	448	1130	209	497	1116	381	587	1281	85	432
972	1465	-201	591	1318	-108	452	1284	-21	436	1230	137	445	1118	207	489	1088	373	589	1265	76	430
973	1459	-236	568	1315	-115	448	1273	-32	434	1216	131	443	1105	205	481	1052	371	578	1249	68	428
974	1451	-270	535	1307	-125	442	1262	-42	434	1203	127	439	1093	202	473	1016	372	558	1234	60	426
975	1435	-300	498	1292	-139	431	1250	-51	435	1191	122	436	1081	200	466	980	369	529	1220	53	423
976	1414	-324	462	1276	-152	421	1238	-60	435	1177	118	432	1068	197	458	947	362	500	1204	44	421
977	1391	-343	434	1258	-166	415	1226	-69	436	1161	113	423	1053	191	453	917	349	474	1189	35	419

Table A.5: HH T11 C3 951-1073

Frame	Primary_P			Wrist_P			Elbow_P			Elbow_S			Wrist_S			Primary_S			Spine_F		
	X	Y	Z	X	Y	Z	X	Y	Z	X	Y	Z	X	Y	Z	X	Y	Z	X	Y	Z
978	1367	-360	414	1239	-180	411	1216	-75	435	1143	106	415	1037	183	446	887	333	454	1175	26	417
979	1344	-376	400	1221	-194	406	1206	-82	434	1125	98	410	1019	175	439	858	314	441	1160	17	416
980	1323	-391	391	1202	-207	402	1197	-88	429	1106	89	407	1000	166	431	829	294	433	1146	7	414
981	1300	-405	384	1183	-222	399	1186	-95	420	1087	79	405	978	156	424	800	274	427	1131	-3	413
982	1276	-418	376	1164	-236	395	1174	-102	406	1067	70	402	956	146	418	773	253	424	1116	-14	411
983	1250	-433	367	1144	-250	392	1157	-113	391	1045	59	397	932	135	411	746	231	422	1102	-24	409
984	1220	-448	357	1124	-261	387	1138	-126	383	1027	53	394	908	123	406	720	208	418	1088	-35	408
985	1187	-464	345	1102	-270	381	1116	-139	384	1009	44	392	884	109	400	695	184	414	1074	-45	407
986	1150	-481	333	1080	-278	374	1096	-153	385	990	32	390	860	93	395	672	158	409	1062	-55	408
987	1107	-496	322	1057	-286	368	1074	-167	387	974	23	389	837	77	389	650	129	404	1046	-66	406
988	1063	-508	313	1034	-294	363	1053	-180	388	960	15	389	816	59	382	631	99	398	1031	-77	406
989	1015	-516	306	1011	-302	359	1033	-193	388	947	6	389	798	38	377	615	69	390	1016	-86	410
990	968	-519	301	989	-310	358	1013	-206	387	934	-4	391	785	17	376	601	39	382	1001	-96	413
991	924	-515	298	970	-317	365	993	-219	386	923	-13	393	779	-4	377	591	11	374	986	-106	416
992	888	-509	298	952	-325	375	974	-232	386	913	-23	397	779	-19	385	585	-15	369	970	-117	419
993	861	-502	298	935	-332	385	959	-242	388	904	-32	401	778	-33	396	582	-37	368	952	-128	422
994	845	-498	300	918	-336	398	948	-249	394	895	-43	407	775	-48	408	581	-53	373	934	-141	424
995	839	-498	303	902	-338	413	938	-252	405	887	-55	414	769	-63	422	577	-62	384	916	-152	425
996	842	-501	306	888	-339	427	926	-255	417	878	-70	422	760	-78	435	572	-62	397	898	-163	427
997	853	-509	313	873	-341	442	914	-258	430	869	-86	431	750	-93	449	565	-55	412	880	-174	426
998	872	-517	323	859	-342	456	903	-260	442	858	-104	441	737	-108	462	560	-41	429	862	-186	426
999	896	-523	336	844	-344	470	891	-263	454	844	-122	448	722	-122	475	559	-21	451	846	-197	427
1000	926	-525	357	831	-350	480	877	-266	460	829	-142	456	706	-136	488	566	4	476	830	-207	427
1001	957	-520	384	820	-364	484	857	-270	458	813	-160	463	688	-149	498	585	30	507	814	-218	428
1002	983	-504	420	809	-379	488	836	-277	454	793	-178	468	668	-161	508	614	44	541	799	-227	429
1003	994	-484	462	795	-393	493	814	-284	449	772	-193	471	647	-173	515	643	42	578	784	-237	430
1004	987	-469	506	779	-410	493	792	-293	444	750	-204	471	629	-181	524	663	26	611	770	-245	431

Table A.5: HH T11 C3 951-1073

Frame	Primary_P			Wrist_P			Elbow_P			Elbow_S			Wrist_S			Primary_S			Spine_F		
	X	Y	Z	X	Y	Z	X	Y	Z	X	Y	Z	X	Y	Z	X	Y	Z	X	Y	Z
1005	964	-468	541	763	-429	489	771	-305	439	730	-212	469	618	-180	532	667	4	640	756	-254	431
1006	942	-486	561	750	-448	479	752	-322	435	713	-215	466	609	-176	537	651	-17	660	742	-262	432
1007	927	-519	568	743	-465	462	737	-339	431	699	-219	463	602	-167	535	623	-26	668	728	-271	431
1008	917	-564	562	741	-479	444	721	-358	429	687	-224	462	591	-164	531	587	-23	667	714	-279	431
1009	905	-613	543	744	-489	427	708	-376	427	676	-230	462	579	-167	524	547	-9	654	699	-288	431
1010	882	-657	511	744	-499	413	696	-394	425	666	-236	460	567	-170	518	506	3	629	686	-297	431
1011	852	-692	474	739	-507	402	686	-411	423	656	-241	459	555	-173	511	469	7	598	671	-306	430
1012	820	-716	437	730	-515	392	676	-427	421	642	-246	454	543	-176	505	435	4	568	657	-316	430
1013	791	-733	402	718	-523	385	669	-441	419	624	-250	446	530	-180	498	404	-4	541	644	-326	430
1014	765	-746	375	703	-532	378	661	-455	417	608	-256	442	515	-184	492	375	-16	518	631	-337	430
1015	740	-759	353	685	-542	372	653	-468	415	593	-265	441	495	-189	485	346	-30	499	618	-347	430
1016	716	-771	337	666	-553	365	645	-480	413	574	-274	440	473	-197	477	318	-45	483	604	-358	430
1017	693	-784	323	645	-566	357	636	-488	409	555	-283	438	450	-207	470	290	-61	468	591	-370	430
1018	668	-795	310	622	-581	349	625	-493	402	536	-291	436	426	-219	463	261	-80	456	578	-380	430
1019	640	-806	297	598	-595	341	612	-498	393	516	-299	434	402	-231	456	232	-100	444	564	-391	430
1020	609	-815	282	574	-608	333	595	-501	384	497	-307	431	378	-244	448	203	-123	433	551	-402	431
1021	574	-824	267	550	-621	325	576	-507	379	479	-316	429	353	-258	440	175	-149	421	539	-413	433
1022	535	-829	253	526	-631	320	558	-515	380	461	-326	428	329	-274	432	149	-177	409	526	-425	435
1023	493	-832	240	503	-638	319	539	-522	380	445	-336	427	306	-292	424	125	-210	399	512	-434	441
1024	449	-828	230	481	-643	318	522	-531	382	430	-346	427	284	-314	418	104	-245	391	498	-444	446
1025	405	-821	224	460	-647	319	509	-539	386	416	-357	428	267	-339	416	87	-283	385	484	-454	451
1026	363	-809	223	439	-650	327	497	-546	391	405	-368	430	258	-366	418	75	-322	382	470	-465	456
1027	328	-793	227	420	-650	340	486	-554	396	395	-378	432	256	-390	425	68	-359	385	454	-476	462
1028	301	-776	237	406	-648	359	475	-562	402	387	-389	438	258	-408	437	64	-392	393	439	-487	467
1029	282	-762	252	398	-648	381	465	-570	412	379	-399	445	261	-422	455	63	-418	406	423	-498	472
1030	272	-754	270	389	-650	407	455	-578	425	371	-411	453	260	-436	474	62	-437	421	404	-508	473
1031	267	-756	289	378	-652	432	445	-584	441	363	-425	462	256	-451	493	60	-447	436	386	-519	476

Table A.5: HH T11 C3 951-1073

Frame	Primary_P			Wrist_P			Elbow_P			Elbow_S			Wrist_S			Primary_S			Spine_F		
	X	Y	Z	X	Y	Z	X	Y	Z	X	Y	Z	X	Y	Z	X	Y	Z	X	Y	Z
1032	267	-769	309	364	-654	455	436	-591	459	354	-441	473	250	-468	512	57	-447	452	369	-531	478
1033	278	-789	328	346	-658	477	424	-597	476	344	-458	485	241	-488	529	54	-438	467	352	-542	481
1034	300	-811	349	325	-662	497	410	-602	492	333	-477	495	230	-506	546	55	-418	484	335	-553	484
1035	334	-830	375	303	-667	516	390	-606	505	320	-496	505	219	-523	564	63	-389	503	320	-563	486
1036	376	-839	409	282	-672	535	368	-609	517	306	-515	514	204	-533	580	82	-356	527	305	-574	489
1037	418	-833	452	264	-680	555	344	-614	528	289	-534	521	186	-537	593	111	-332	559	290	-585	493
1038	448	-818	501	254	-696	573	319	-620	537	272	-552	526	166	-540	602	145	-324	598	277	-596	495
1039	462	-798	554	248	-720	584	293	-629	541	253	-568	530	144	-540	605	172	-333	638	263	-606	497
1040	460	-780	605	243	-747	587	267	-644	541	233	-580	531	123	-540	603	185	-356	674	250	-617	499
1041	439	-773	648	239	-774	586	246	-664	537	215	-586	530	103	-540	596	177	-381	701	238	-627	501
1042	413	-785	677	234	-799	582	231	-688	531	200	-589	527	87	-539	586	153	-393	717	226	-637	503
1043	393	-814	693	229	-820	575	220	-713	524	187	-594	525	74	-538	574	117	-393	722	213	-648	505
1044	384	-859	700	226	-838	565	211	-736	520	176	-599	526	65	-536	563	74	-380	716	201	-658	507
1045	382	-916	695	223	-855	556	203	-756	520	167	-606	526	58	-533	552	29	-368	696	189	-667	509
1046	374	-976	673	220	-871	547	195	-773	521	158	-613	526	50	-531	545	-13	-361	666	176	-677	511
1047	354	-1031	638	216	-887	538	186	-789	526	149	-619	523	43	-528	542	-49	-363	636	164	-687	513
1048	325	-1075	599	208	-902	530	176	-802	531	134	-624	517	30	-531	537	-79	-370	611	152	-697	514
1049	292	-1105	562	197	-916	523	167	-815	537	117	-630	512	12	-539	531	-105	-380	594	140	-708	515
1050	259	-1128	536	183	-930	517	159	-827	541	100	-639	510	-10	-552	524	-129	-392	583	127	-719	516
1051	230	-1150	517	164	-944	511	152	-837	542	83	-649	511	-33	-566	519	-153	-406	576	116	-731	518
1052	204	-1169	506	143	-959	507	145	-846	539	66	-659	513	-55	-581	515	-178	-423	570	104	-743	521
1053	181	-1186	498	121	-975	505	137	-855	533	51	-668	515	-74	-595	513	-206	-444	564	93	-755	523
1054	157	-1202	490	100	-989	502	127	-865	522	31	-679	514	-94	-608	513	-235	-469	558	82	-766	526
1055	128	-1212	484	79	-1004	498	112	-877	510	15	-688	514	-113	-621	512	-265	-499	552	70	-779	528
1056	94	-1218	479	58	-1019	495	94	-891	501	0	-697	515	-131	-634	511	-292	-531	548	59	-791	531
1057	56	-1219	474	36	-1033	493	77	-903	506	-15	-708	516	-149	-646	511	-315	-563	542	47	-802	535
1058	16	-1217	472	16	-1044	491	60	-916	509	-27	-718	518	-163	-657	509	-336	-593	534	35	-813	541

Table A.5: HH T11 C3 951-1073

Frame	Primary_P			Wrist_P			Elbow_P			Elbow_S			Wrist_S			Primary_S			Spine_F		
	X	Y	Z	X	Y	Z	X	Y	Z	X	Y	Z	X	Y	Z	X	Y	Z	X	Y	Z
1059	-25	-1212	470	-3	-1052	490	43	-930	513	-42	-732	520	-176	-670	508	-353	-620	525	24	-824	547
1060	-67	-1206	470	-23	-1057	491	27	-943	517	-53	-744	524	-187	-686	511	-369	-645	516	12	-834	553
1061	-106	-1198	470	-41	-1060	496	12	-954	520	-61	-753	530	-197	-704	517	-381	-669	509	0	-846	561
1062	-143	-1191	473	-56	-1061	504	-2	-963	525	-67	-762	537	-207	-724	526	-390	-697	506	-12	-857	568
1063	-176	-1183	476	-68	-1060	517	-13	-971	531	-72	-771	544	-214	-745	542	-395	-724	509	-26	-867	575
1064	-203	-1178	481	-77	-1057	533	-20	-979	541	-77	-782	553	-216	-765	560	-398	-751	518	-37	-879	582
1065	-223	-1174	487	-85	-1053	552	-25	-985	552	-82	-795	561	-216	-785	578	-398	-771	535	-49	-892	589
1066	-235	-1173	495	-93	-1049	572	-29	-991	566	-88	-809	571	-213	-803	597	-400	-784	554	-64	-904	595
1067	-237	-1176	504	-102	-1044	594	-33	-995	581	-94	-824	583	-211	-819	618	-402	-786	573	-84	-913	598
1068	-229	-1184	514	-113	-1041	617	-37	-999	597	-102	-841	596	-210	-834	638	-404	-778	589	-99	-924	603
1069	-208	-1197	526	-126	-1038	639	-45	-999	610	-111	-858	609	-210	-849	658	-399	-759	606	-113	-937	607
1070	-174	-1214	540	-141	-1036	662	-57	-995	623	-122	-876	621	-215	-864	679	-388	-735	624	-127	-948	612
1071	-132	-1227	557	-156	-1036	684	-73	-991	635	-134	-895	633	-226	-876	698	-368	-710	645	-140	-959	617
1072	-84	-1225	579	-168	-1043	705	-94	-989	646	-149	-914	645	-244	-884	713	-339	-693	673	-153	-970	622
1073	-37	-1203	608	-179	-1057	722	-120	-990	655	-165	-931	654	-266	-891	727	-303	-685	705	-167	-980	628

Table A.6: Common Buzzard - specimen: CB, Trial 8, Capture session 3, Frames: 1505-1555

Frame	Primary_P			Wrist_P			Elbow_P			Elbow_S			Wrist_S			Primary_S			Spine_F		
	X	Y	Z	X	Y	Z	X	Y	Z	X	Y	Z	X	Y	Z	X	Y	Z	X	Y	Z
1505	163	-27	444	13	-4	640	124	22	588	168	129	562	81	190	616	208	101	427	111	82	580
1506	159	-33	444	10	-10	642	120	20	588	166	132	563	79	192	616	210	108	429	109	82	579
1507	158	-45	448	7	-16	644	116	18	588	163	134	563	76	194	617	211	115	431	106	82	577
1508	157	-57	451	3	-22	644	112	15	588	159	137	564	72	197	618	213	123	433	104	82	575
1509	155	-69	455	-1	-27	645	108	13	588	156	139	564	68	199	618	215	132	435	102	82	573
1510	155	-84	460	-6	-32	644	104	10	589	152	142	564	64	201	618	217	142	438	100	82	572
1511	156	-102	469	-11	-36	643	100	7	589	148	145	564	58	204	617	218	153	439	97	82	570
1512	155	-119	477	-17	-40	641	95	5	589	143	148	564	53	206	616	220	165	443	95	81	569
1513	153	-136	488	-22	-42	639	91	3	590	138	151	565	47	208	615	224	177	449	92	80	567
1514	150	-156	500	-28	-44	638	88	1	590	132	153	565	40	209	615	224	190	453	90	80	566
1515	144	-174	513	-32	-46	637	84	-1	590	127	153	566	34	210	614	224	205	459	87	79	564
1516	135	-192	526	-37	-47	637	80	-2	589	122	153	568	26	209	614	224	221	465	84	78	562
1517	124	-208	538	-41	-47	637	78	-2	589	116	152	570	19	207	614	220	236	470	81	77	561
1518	113	-222	552	-44	-47	639	74	-1	590	109	149	574	11	204	613	214	252	477	78	76	559
1519	102	-234	566	-48	-46	641	71	1	591	103	145	578	2	201	612	207	269	486	75	74	557
1520	91	-243	582	-51	-45	645	68	4	593	95	141	582	-7	196	612	198	285	497	71	72	555
1521	80	-250	598	-53	-43	650	65	8	594	88	135	585	-16	189	613	188	300	512	68	70	553
1522	70	-253	615	-55	-40	656	61	12	596	81	128	589	-25	181	615	176	309	527	64	69	552
1523	61	-253	632	-58	-35	663	57	17	598	73	121	593	-33	173	619	164	314	543	61	67	550
1524	55	-250	652	-59	-29	671	53	20	598	65	113	595	-41	164	624	152	316	561	58	64	549
1525	51	-243	675	-61	-22	679	48	25	598	57	104	598	-50	154	630	141	314	581	54	61	549
1526	52	-232	700	-63	-13	687	43	29	598	49	95	601	-58	144	637	131	310	605	50	57	548
1527	55	-217	728	-65	-4	695	38	33	599	40	86	603	-67	133	644	121	302	632	47	53	549
1528	62	-198	759	-68	6	701	33	37	599	31	77	605	-75	120	651	114	290	665	43	49	551
1529	69	-174	792	-70	15	708	27	41	600	22	67	607	-82	109	656	109	273	702	39	46	553
1530	75	-145	826	-73	24	713	20	45	601	15	58	608	-90	97	662	99	253	739	34	43	555
1531	78	-111	861	-77	32	718	12	47	603	8	50	610	-98	85	668	88	231	777	29	40	558

Table A.6: CB T8 C3 1505-1555

Frame	Primary_P			Wrist_P			Elbow_P			Elbow_S			Wrist_S			Primary_S			Spine_F		
	X	Y	Z	X	Y	Z	X	Y	Z	X	Y	Z	X	Y	Z	X	Y	Z	X	Y	Z
1532	74	-75	895	-81	37	722	2	48	605	1	43	612	-104	75	673	73	207	816	23	37	561
1533	62	-40	927	-85	39	726	-8	47	608	-7	38	614	-110	66	678	55	182	853	18	34	564
1534	42	-11	956	-89	38	731	-19	45	612	-15	34	618	-114	61	685	33	159	887	11	31	568
1535	20	5	979	-93	29	736	-28	41	617	-23	31	621	-118	61	693	9	141	916	5	29	571
1536	-2	11	996	-94	15	743	-35	36	623	-31	29	625	-119	66	701	-16	128	940	-2	26	575
1537	-19	5	1008	-94	-3	752	-39	30	630	-39	29	629	-120	74	710	-38	125	958	-8	24	579
1538	-30	-15	1016	-94	-21	762	-40	22	639	-46	30	634	-124	83	720	-56	133	972	-15	22	584
1539	-35	-46	1020	-92	-40	774	-42	13	646	-53	33	638	-117	96	728	-67	151	980	-23	20	588
1540	-37	-85	1021	-88	-59	784	-46	2	650	-59	37	642	-115	108	735	-72	176	983	-30	17	593
1541	-37	-132	1017	-83	-79	792	-52	-8	656	-65	42	647	-118	119	739	-72	208	979	-38	15	598
1542	-36	-183	1009	-77	-101	796	-59	-19	665	-72	46	654	-122	130	741	-69	243	970	-45	13	604
1543	-37	-236	997	-78	-121	797	-65	-31	671	-80	49	662	-128	140	742	-66	281	954	-53	11	609
1544	-41	-289	980	-82	-141	795	-72	-44	676	-87	55	669	-135	151	742	-69	320	933	-61	8	615
1545	-49	-339	959	-87	-162	791	-80	-57	681	-94	62	675	-145	161	742	-81	357	908	-68	6	621
1546	-64	-385	933	-92	-185	786	-87	-71	685	-101	70	679	-152	172	739	-104	391	881	-76	3	627
1547	-86	-425	903	-99	-209	778	-95	-84	687	-108	77	681	-160	184	735	-134	420	851	-84	1	633
1548	-111	-458	868	-106	-233	767	-104	-97	688	-116	84	682	-169	195	729	-166	444	817	-93	-2	641
1549	-138	-486	830	-118	-253	752	-113	-109	689	-126	90	683	-179	204	721	-201	460	780	-103	-4	649
1550	-167	-508	790	-134	-269	737	-123	-120	689	-138	96	685	-193	212	711	-235	471	741	-112	-6	659
1551	-197	-525	747	-151	-282	720	-133	-129	689	-150	101	686	-208	218	700	-267	474	700	-121	-9	669
1552	-230	-532	705	-169	-292	703	-144	-137	688	-163	104	686	-225	220	688	-298	470	659	-130	-11	680
1553	-265	-528	662	-190	-298	687	-157	-143	688	-177	107	686	-245	219	677	-332	460	620	-139	-14	691
1554	-302	-522	619	-212	-300	672	-170	-147	689	-191	107	686	-265	214	666	-370	441	584	-148	-16	702
1555	-340	-504	580	-235	-298	659	-182	-150	690	-205	106	687	-286	206	657	-407	414	553	-157	-18	714

Table A.7: Common Buzzard - specimen: CB, Trial 4, Capture session 3, Frames: 188-240

Frame	Primary_P			Wrist_P			Elbow_P			Elbow_S			Wrist_S			Primary_S			Spine_F		
	X	Y	Z	X	Y	Z	X	Y	Z	X	Y	Z	X	Y	Z	X	Y	Z	X	Y	Z
188	956	-20	387	744	-10	525	864	32	530	909	137	532	819	217	552	986	114	403	846	95	540
189	952	-26	385	742	-11	526	862	32	530	906	138	532	818	219	552	985	118	403	844	96	539
190	948	-32	383	741	-12	527	859	33	530	904	140	533	816	221	551	986	123	404	842	97	538
191	943	-41	383	739	-14	529	857	34	530	901	142	533	814	223	551	986	128	404	840	98	536
192	939	-50	383	737	-15	531	855	35	530	899	143	534	811	225	551	987	135	406	837	99	535
193	933	-61	384	734	-16	533	852	36	531	896	146	534	808	227	552	989	142	408	835	99	533
194	928	-72	386	732	-18	535	849	36	531	893	148	535	805	229	553	991	151	412	833	100	531
195	922	-84	389	729	-19	538	846	37	531	889	151	536	801	231	554	992	162	416	831	100	529
196	915	-96	394	725	-21	541	843	37	531	886	154	536	796	233	555	995	174	423	829	101	527
197	909	-108	400	721	-22	545	839	37	531	882	158	537	790	235	557	997	187	430	827	102	524
198	901	-121	407	717	-23	548	836	37	530	878	162	538	785	236	559	998	202	438	825	103	522
199	893	-133	415	712	-24	553	831	35	529	874	166	538	779	238	561	1000	218	448	823	103	519
200	884	-146	423	707	-24	556	827	34	527	870	170	539	773	239	562	999	234	459	822	104	517
201	875	-160	434	702	-24	560	823	32	527	865	174	539	766	240	563	998	251	470	820	105	514
202	864	-172	444	696	-23	563	818	31	527	861	178	539	760	240	564	995	269	481	818	106	512
203	852	-184	455	691	-22	565	814	31	528	855	181	541	753	241	564	991	287	493	817	107	509
204	841	-195	468	686	-20	567	810	32	529	849	182	542	747	242	563	985	304	504	815	108	507
205	828	-205	482	681	-17	569	805	34	530	842	182	545	740	242	561	978	321	515	813	109	505
206	815	-215	496	676	-15	569	802	37	533	835	179	547	734	243	559	969	336	527	811	110	503
207	801	-222	512	672	-12	570	799	40	535	828	177	549	727	244	558	959	350	539	810	111	501
208	787	-227	529	667	-9	573	796	45	536	820	174	551	720	244	559	948	362	552	808	112	499
209	773	-229	546	664	-3	577	792	49	537	813	170	551	713	242	563	936	372	567	806	112	497
210	761	-228	564	661	4	582	790	55	538	806	167	551	707	239	567	923	379	582	804	112	495
211	751	-224	582	658	12	588	787	61	539	799	162	552	700	234	571	911	382	601	801	112	494
212	743	-217	602	655	20	594	785	68	540	792	156	553	694	230	576	898	382	621	798	111	493
213	739	-208	623	653	28	602	782	75	541	785	150	553	688	224	582	885	380	644	795	110	491
214	738	-196	646	651	37	610	779	82	541	778	143	553	682	218	588	872	372	670	791	110	490

Table A.7: CB T4 C3 188-240

Frame	Primary_P			Wrist_P			Elbow_P			Elbow_S			Wrist_S			Primary_S			Spine_F		
	X	Y	Z	X	Y	Z	X	Y	Z	X	Y	Z	X	Y	Z	X	Y	Z	X	Y	Z
215	739	-181	671	649	47	618	775	89	541	771	137	552	676	211	594	858	361	699	788	110	491
216	744	-163	699	648	57	626	770	95	541	764	131	551	670	201	599	843	344	729	785	111	491
217	749	-141	729	647	67	633	764	101	542	758	124	550	665	192	605	827	324	760	781	111	492
218	755	-116	761	646	77	640	759	108	543	752	117	548	659	183	610	808	301	789	777	111	493
219	760	-87	794	645	86	647	752	113	544	752	113	544	654	174	615	788	276	818	772	111	494
220	760	-56	826	643	95	652	746	116	545	753	109	541	649	165	621	767	252	844	767	110	496
221	754	-23	857	642	103	656	740	117	548	751	107	540	645	158	627	743	230	867	762	110	498
222	740	4	884	641	107	658	735	117	551	748	106	541	642	153	635	720	214	885	757	110	501
223	722	24	908	639	104	658	729	116	555	744	105	544	641	151	643	698	204	901	751	110	503
224	704	36	925	637	93	659	723	114	559	739	106	548	642	154	652	680	199	914	745	109	507
225	689	38	938	636	79	663	717	110	564	732	108	554	645	159	660	669	199	924	739	109	510
226	678	28	947	635	64	669	711	106	570	725	110	560	648	166	669	665	208	931	733	108	514
227	670	5	950	634	48	676	704	100	575	718	113	568	652	174	676	671	222	937	726	108	519
228	666	-28	949	632	34	683	697	94	581	709	118	575	655	185	684	685	240	940	719	107	523
229	666	-69	944	630	20	692	690	87	587	701	123	583	656	197	690	703	262	940	712	107	528
230	667	-115	935	628	6	700	682	78	593	693	129	592	656	209	693	722	288	936	704	107	533
231	664	-163	920	626	-10	707	673	70	599	684	136	600	655	224	697	738	320	927	697	106	539
232	654	-208	898	626	-28	712	664	60	604	676	144	607	653	237	699	748	357	914	688	106	544
233	635	-250	873	626	-51	711	654	51	607	669	152	614	649	252	700	748	397	897	680	105	551
234	610	-286	844	621	-74	706	643	41	611	662	162	620	646	266	698	738	441	876	672	105	557
235	582	-317	811	606	-93	698	633	30	613	656	172	625	643	280	696	721	483	848	663	104	563
236	551	-342	775	590	-111	689	622	20	613	650	183	629	640	295	692	700	520	815	653	104	570
237	519	-362	737	574	-128	674	612	11	613	644	193	630	635	308	685	676	552	778	642	103	577
238	487	-374	699	558	-143	657	601	3	613	637	203	630	627	322	675	650	577	739	634	103	585
239	456	-380	660	541	-153	640	590	-4	611	629	211	630	616	335	664	625	595	701	624	103	594
240	424	-380	620	521	-158	623	578	-9	610	619	218	629	601	346	651	600	607	666	614	103	603

Table A.8: Common Buzzard - specimen: CB, Trial 7, Capture session 3, Frames: 780-866

Frame	Primary_P			Wrist_P			Elbow_P			Elbow_S			Wrist_S			Primary_S			Spine_F		
	X	Y	Z	X	Y	Z	X	Y	Z	X	Y	Z	X	Y	Z	X	Y	Z	X	Y	Z
780	1124	602	486	877	556	570	972	628	589	958	729	590	841	764	566	1079	773	498	920	678	593
781	1123	602	484	877	556	571	971	628	588	958	729	589	841	764	566	1078	773	495	920	677	593
782	1122	601	481	876	555	571	971	628	588	958	729	588	841	765	566	1077	772	493	919	677	593
783	1120	600	478	876	555	571	971	627	587	957	729	588	840	765	566	1076	772	491	919	677	592
784	1119	600	475	876	554	571	971	627	587	957	729	587	840	765	566	1075	771	489	919	677	592
785	1117	599	472	876	554	572	970	627	586	957	729	586	840	766	566	1074	771	487	919	676	591
786	1116	597	469	876	553	572	970	626	585	957	729	586	839	766	566	1073	771	485	918	676	591
787	1115	597	468	875	553	572	970	626	585	956	728	585	839	766	566	1072	771	483	918	676	591
788	1114	596	466	875	552	572	969	626	584	956	728	585	839	766	566	1071	771	481	918	675	590
789	1113	595	464	875	552	572	969	625	584	955	728	584	838	766	566	1070	771	479	917	675	590
790	1112	594	462	875	551	572	969	625	583	955	728	583	838	766	566	1069	771	478	917	674	590
791	1110	594	459	874	551	572	969	624	583	955	728	583	838	766	566	1068	771	476	917	674	589
792	1110	591	458	874	551	572	968	624	582	954	728	582	837	766	566	1067	771	475	916	674	589
793	1109	590	456	873	550	572	968	624	581	954	728	582	837	766	566	1066	771	474	916	674	589
794	1108	588	453	873	550	572	968	623	581	954	728	581	836	765	566	1065	771	473	916	673	588
795	1108	587	454	873	550	572	967	623	580	953	728	581	836	765	566	1064	772	472	916	673	588
796	1107	585	452	872	550	572	967	623	580	953	728	580	835	765	566	1063	772	471	915	673	588
797	1106	583	451	872	549	572	967	622	579	952	728	580	835	764	566	1062	773	471	915	672	587
798	1106	581	450	871	549	572	966	622	579	952	727	579	834	764	566	1062	773	470	915	671	586
799	1105	579	449	871	548	572	966	621	578	952	727	579	834	763	566	1061	774	469	915	671	586
800	1105	576	449	871	548	572	966	621	578	951	727	578	833	763	566	1060	774	469	914	671	586
801	1105	574	448	870	547	572	965	621	577	951	727	578	832	762	566	1059	775	469	914	670	585
802	1104	571	447	870	547	572	965	620	577	950	727	577	832	762	566	1058	776	468	914	670	585
803	1103	568	446	869	546	573	964	620	577	950	726	576	831	762	567	1057	777	468	913	669	584
804	1103	565	445	869	545	573	963	619	576	949	726	576	830	761	567	1056	779	467	913	669	583
805	1104	561	446	869	544	573	963	618	576	949	726	576	829	761	567	1055	781	467	912	668	582
806	1104	556	447	868	542	573	962	618	575	948	726	575	828	761	568	1053	783	467	912	667	581

Table A.8: CB T7 C3 780-866

Frame	Primary_P			Wrist_P			Elbow_P			Elbow_S			Wrist_S			Primary_S			Spine_F		
	X	Y	Z	X	Y	Z	X	Y	Z	X	Y	Z	X	Y	Z	X	Y	Z	X	Y	Z
807	1104	551	446	868	541	574	961	617	575	946	727	575	827	760	568	1051	786	467	912	667	581
808	1105	546	447	868	539	574	961	616	575	945	728	575	825	760	569	1049	790	468	912	666	579
809	1105	539	449	867	537	574	960	615	574	943	729	576	822	760	569	1047	795	469	911	665	578
810	1106	532	452	867	535	574	959	613	573	941	730	576	820	760	570	1044	801	471	911	664	576
811	1107	524	455	866	532	575	958	612	573	938	732	576	817	759	571	1040	807	473	910	664	574
812	1108	515	458	865	530	575	957	610	572	935	734	575	813	759	573	1036	815	476	910	663	572
813	1108	506	462	864	528	575	956	608	571	932	736	575	810	759	574	1032	823	479	910	662	571
814	1109	496	465	863	526	575	956	606	570	929	738	575	806	758	575	1026	832	483	910	662	569
815	1108	486	469	862	523	575	955	604	570	925	741	575	802	758	576	1020	841	486	910	661	566
816	1108	475	474	861	521	574	954	601	569	921	744	574	798	757	577	1013	851	489	910	660	564
817	1106	465	478	859	519	574	953	598	568	917	747	573	794	756	577	1005	861	492	910	660	562
818	1105	454	482	857	517	573	952	595	567	913	749	571	789	755	577	997	871	496	910	658	560
819	1102	444	486	855	515	571	951	592	566	909	751	570	785	753	576	988	881	499	910	658	558
820	1099	433	490	853	513	570	949	589	564	905	752	568	781	752	575	978	892	503	909	658	556
821	1095	422	493	851	512	570	948	585	562	901	753	567	777	750	573	967	902	507	909	657	554
822	1091	411	497	848	510	569	947	583	561	898	753	566	774	748	571	956	912	511	909	656	551
823	1086	400	500	846	509	569	946	581	561	894	752	565	770	746	569	943	922	515	908	656	550
824	1081	389	504	843	508	569	944	579	560	891	751	565	767	743	566	929	931	519	908	655	549
825	1075	377	507	841	507	569	942	578	560	888	748	565	764	740	564	914	939	523	908	655	548
826	1069	367	512	838	506	569	939	577	561	884	746	565	761	737	562	899	947	527	907	654	546
827	1062	357	517	836	505	570	937	577	562	881	743	566	758	733	561	882	953	531	906	654	544
828	1054	348	523	833	505	571	933	577	563	879	740	568	754	728	561	865	957	536	906	653	542
829	1046	340	530	830	505	573	930	578	565	875	735	568	751	723	562	848	960	542	905	652	540
830	1039	335	540	826	506	575	926	579	566	872	730	569	748	718	563	835	958	550	904	651	537
831	1031	331	552	822	508	578	922	581	567	869	723	571	745	711	564	827	954	558	903	650	536
832	1024	329	566	818	510	580	917	583	569	866	715	573	742	704	566	820	947	568	903	650	534
833	1017	329	584	813	512	582	911	587	571	864	706	576	739	697	569	813	941	580	902	649	533

Table A.8: CB T7 C3 780-866

Frame	Primary_P			Wrist_P			Elbow_P			Elbow_S			Wrist_S			Primary_S			Spine_F		
	X	Y	Z	X	Y	Z	X	Y	Z	X	Y	Z	X	Y	Z	X	Y	Z	X	Y	Z
834	1010	333	605	808	515	584	906	590	572	862	697	577	736	689	575	804	934	595	901	649	532
835	1004	340	630	803	519	589	899	595	573	861	689	578	735	679	579	796	925	614	900	648	531
836	997	349	655	797	523	592	893	599	574	861	680	578	735	669	585	788	914	636	900	647	531
837	991	361	688	790	526	596	887	603	574	861	671	579	735	658	591	781	900	662	898	645	530
838	981	377	719	784	529	600	881	607	574	862	662	579	736	646	597	777	883	692	896	643	531
839	970	397	756	779	533	603	876	611	575	864	653	580	737	634	602	775	862	723	895	642	532
840	955	418	791	775	535	604	870	615	577	864	643	580	738	623	609	775	836	755	893	640	534
841	935	441	825	771	539	611	866	620	579	862	634	580	740	611	617	776	807	788	891	638	537
842	911	465	858	768	541	614	861	619	578	860	626	581	741	599	628	776	774	820	889	636	540
843	884	489	888	766	544	619	855	617	579	856	619	583	743	586	641	775	740	849	886	634	543
844	853	509	914	766	545	622	850	615	581	852	613	585	745	574	655	773	704	876	883	631	547
845	823	523	935	767	548	634	846	612	584	847	608	588	746	562	670	768	668	900	880	628	551
846	797	530	951	767	553	647	842	608	589	843	604	592	747	551	685	760	637	920	876	625	555
847	778	533	966	769	555	661	838	604	595	838	599	596	748	542	701	748	612	936	872	621	560
848	768	527	976	773	555	674	834	599	601	834	595	602	748	536	716	735	594	950	868	617	565
849	770	517	985	777	551	687	831	593	609	831	590	608	747	533	730	724	590	964	864	614	571
850	778	501	991	783	545	699	828	587	616	828	584	615	745	533	743	715	599	976	859	609	576
851	789	479	994	790	536	711	826	580	625	827	578	623	742	538	755	706	617	985	854	605	583
852	803	451	993	797	524	721	824	572	633	826	571	631	738	548	763	695	638	990	849	600	589
853	819	419	989	805	511	730	822	563	642	826	565	641	732	563	770	683	659	990	843	595	596
854	835	384	981	812	495	738	821	553	650	818	566	650	726	582	773	669	680	985	837	590	603
855	852	345	970	820	478	744	820	542	658	805	575	660	718	604	775	653	701	975	831	585	610
856	869	306	955	827	459	748	820	531	666	789	587	669	709	627	775	635	721	960	825	579	618
857	885	265	936	833	439	750	819	518	673	773	599	679	699	650	774	616	740	942	819	573	625
858	898	224	915	838	417	750	819	504	679	761	607	688	688	671	771	596	759	920	812	567	633
859	909	185	889	842	396	748	818	489	683	752	611	698	676	689	768	574	778	895	806	561	642
860	917	147	860	843	375	745	815	474	687	743	617	705	664	703	764	551	796	868	799	554	650

Table A.8: CB T7 C3 780-866

Frame	Primary_P			Wrist_P			Elbow_P			Elbow_S			Wrist_S			Primary_S			Spine_F		
	X	Y	Z	X	Y	Z	X	Y	Z	X	Y	Z	X	Y	Z	X	Y	Z	X	Y	Z
861	921	113	828	844	353	736	812	459	689	731	622	709	651	711	760	528	814	838	792	548	659
862	920	82	792	842	332	725	809	446	691	721	626	712	638	718	753	503	832	806	784	540	669
863	914	56	752	835	312	708	805	433	692	709	628	715	623	722	743	478	850	772	777	533	680
864	901	36	709	827	296	692	798	421	693	697	628	716	607	722	733	453	868	737	768	525	690
865	881	22	663	816	285	677	790	410	693	684	627	717	590	719	720	427	885	702	759	518	701
866	855	15	613	800	276	662	781	400	694	671	624	718	573	712	708	401	903	666	751	511	712

Table A.9: Common Buzzard - specimen: CB, Trial 15, Capture session 3, Frames: 445-615

Frame	Primary_P			Wrist_P			Elbow_P			Elbow_S			Wrist_S			Primary_S			Spine_F		
	X	Y	Z	X	Y	Z	X	Y	Z	X	Y	Z	X	Y	Z	X	Y	Z	X	Y	Z
445	935	1181	540	780	1034	673	829	1151	675	773	1256	664	653	1230	674	847	1306	542	770	1178	670
446	938	1173	541	782	1029	675	827	1149	675	770	1256	665	649	1231	678	840	1313	543	769	1177	668
447	943	1163	542	784	1025	678	825	1147	674	766	1257	666	646	1232	680	833	1320	546	768	1175	667
448	948	1153	543	786	1021	681	824	1145	674	761	1257	667	642	1233	683	826	1327	548	767	1174	665
449	955	1142	547	786	1017	683	823	1142	673	757	1257	667	638	1234	686	818	1335	551	766	1173	663
450	962	1130	551	787	1013	685	822	1139	672	752	1257	668	634	1234	688	809	1344	555	765	1172	661
451	970	1118	557	787	1009	687	821	1135	670	746	1258	668	630	1233	690	799	1355	559	764	1171	659
452	979	1105	565	786	1004	688	820	1132	670	740	1258	668	626	1231	691	788	1366	564	763	1170	657
453	988	1091	575	784	1000	689	820	1128	669	735	1257	668	621	1229	691	777	1377	571	762	1169	656
454	995	1076	585	782	996	690	819	1124	669	730	1256	668	615	1226	691	764	1390	580	761	1168	653
455	1002	1060	596	780	992	691	818	1120	668	725	1254	668	610	1223	690	751	1402	590	760	1166	652
456	1007	1043	607	776	989	692	816	1117	667	721	1251	668	606	1219	688	736	1413	601	759	1165	650
457	1010	1025	618	773	986	693	815	1114	667	718	1248	668	602	1215	686	718	1423	612	758	1164	648
458	1011	1007	628	769	984	693	813	1112	668	715	1244	670	598	1210	684	699	1432	622	757	1164	647
459	1011	989	638	765	981	694	810	1111	669	712	1240	671	596	1204	681	679	1438	632	756	1162	645
460	1009	973	647	761	979	695	806	1110	671	710	1235	673	594	1199	679	660	1442	642	755	1161	643
461	1004	957	657	756	978	698	801	1110	673	708	1228	675	592	1192	678	641	1442	653	754	1160	641
462	999	944	667	751	978	702	796	1111	675	708	1220	678	591	1185	679	623	1438	664	753	1158	639
463	992	934	678	744	979	707	791	1111	677	707	1212	680	590	1177	680	607	1434	675	752	1157	637
464	982	926	690	737	980	714	784	1113	678	707	1203	682	590	1169	684	594	1426	688	750	1155	635
465	973	921	704	729	983	721	777	1114	680	708	1193	684	589	1159	688	585	1416	703	749	1153	634
466	962	921	721	720	987	729	770	1116	681	708	1184	685	590	1149	694	578	1405	721	748	1152	633
467	951	924	741	711	992	737	763	1118	681	708	1174	686	591	1137	701	573	1390	740	747	1150	632
468	940	931	765	700	998	745	755	1119	681	709	1163	686	593	1126	707	572	1375	764	746	1147	631
469	928	943	791	690	1005	752	749	1123	682	709	1153	686	595	1114	714	575	1357	791	744	1144	629
470	917	955	819	679	1011	759	741	1124	681	710	1143	686	598	1102	719	580	1336	821	742	1141	627
471	908	964	847	669	1018	765	733	1124	681	718	1136	690	601	1090	724	588	1312	854	740	1138	626

Table A.9: CB T15 C3 445-615

Frame	Primary_P			Wrist_P			Elbow_P			Elbow_S			Wrist_S			Primary_S			Spine_F		
	X	Y	Z	X	Y	Z	X	Y	Z	X	Y	Z	X	Y	Z	X	Y	Z	X	Y	Z
472	901	972	874	659	1025	771	727	1124	682	728	1132	695	604	1078	729	598	1284	888	737	1134	624
473	895	977	902	650	1031	775	721	1123	683	736	1128	700	607	1068	733	608	1252	921	734	1130	622
474	891	981	928	641	1036	778	717	1121	686	740	1124	703	608	1060	736	616	1216	952	730	1125	621
475	888	982	953	636	1039	779	713	1118	689	741	1119	706	609	1053	741	619	1177	979	727	1121	620
476	887	982	976	635	1039	782	710	1114	693	739	1115	708	608	1050	746	618	1141	1003	723	1116	620
477	886	979	997	640	1034	786	708	1110	697	735	1111	710	603	1053	756	609	1110	1020	719	1111	620
478	887	974	1017	649	1027	791	706	1104	702	728	1107	711	598	1060	766	596	1091	1033	715	1107	620
479	888	966	1033	660	1017	798	706	1098	707	720	1103	712	592	1069	777	578	1084	1042	711	1102	622
480	891	956	1047	674	1006	806	705	1091	712	710	1100	713	588	1081	788	560	1093	1048	707	1097	624
481	894	944	1057	688	995	814	706	1083	717	700	1097	715	583	1095	796	545	1115	1052	703	1092	628
482	898	929	1063	703	984	824	706	1075	723	688	1095	716	578	1105	802	531	1148	1052	700	1087	632
483	902	911	1066	716	973	835	707	1065	728	676	1093	719	573	1114	805	517	1186	1048	696	1082	638
484	907	891	1064	728	964	847	708	1055	732	663	1091	722	562	1121	804	501	1225	1040	692	1077	645
485	912	869	1058	740	956	856	710	1043	737	651	1091	726	555	1129	808	483	1262	1027	689	1072	653
486	918	843	1047	757	948	855	711	1031	740	640	1091	732	544	1137	809	460	1292	1007	685	1068	663
487	924	815	1030	775	937	856	713	1018	744	629	1092	738	532	1146	808	435	1316	983	682	1063	675
488	929	784	1007	782	917	852	716	1005	748	618	1096	744	519	1154	806	408	1334	954	680	1059	688
489	935	750	979	789	897	846	717	990	752	608	1100	748	506	1161	802	378	1345	921	677	1055	701
490	939	715	945	798	875	836	720	976	753	597	1103	751	493	1166	795	349	1351	884	671	1047	709
491	941	680	907	806	854	822	721	962	753	587	1106	751	479	1170	785	319	1351	846	666	1039	716
492	940	646	866	811	833	803	720	949	753	575	1106	749	465	1170	774	290	1345	805	660	1032	724
493	933	614	822	810	813	787	718	937	753	563	1102	749	450	1167	761	263	1334	763	654	1024	732
494	922	586	777	803	796	769	714	924	751	550	1097	748	435	1159	746	239	1318	721	648	1017	741
495	903	563	730	794	778	751	709	912	750	538	1090	747	421	1148	732	218	1297	680	641	1008	750
496	876	546	684	780	763	734	702	901	749	527	1082	745	408	1134	718	202	1271	639	634	1001	760
497	841	533	639	763	750	718	693	890	749	517	1074	744	397	1117	706	191	1238	599	627	994	770
498	799	527	597	743	739	703	684	881	750	507	1065	742	387	1097	694	188	1195	558	619	986	781

Table A.9: CB T15 C3 445-615

Frame	Primary_P			Wrist_P			Elbow_P			Elbow_S			Wrist_S			Primary_S			Spine_F		
	X	Y	Z	X	Y	Z	X	Y	Z	X	Y	Z	X	Y	Z	X	Y	Z	X	Y	Z
499	755	529	562	719	730	691	676	874	752	500	1056	742	380	1074	685	190	1148	527	611	979	791
500	708	539	534	692	725	684	669	868	756	494	1047	745	376	1049	680	199	1095	500	603	972	801
501	660	556	514	666	723	685	662	864	760	490	1038	749	376	1021	680	216	1040	481	594	965	810
502	611	577	504	641	721	693	656	860	766	487	1030	754	376	994	686	239	983	473	585	958	820
503	562	598	508	617	721	708	650	856	774	485	1022	760	378	970	702	262	927	479	576	950	828
504	516	614	525	595	722	728	645	852	783	483	1015	767	377	950	724	280	875	501	566	942	835
505	480	626	550	575	722	752	641	848	794	480	1009	777	377	937	749	290	833	534	555	934	842
506	454	635	576	557	722	778	635	844	808	478	1004	789	376	926	776	295	803	568	544	925	847
507	439	641	600	543	721	806	627	840	825	474	999	806	375	917	805	296	787	597	533	916	852
508	434	644	621	532	718	833	618	836	845	470	993	826	373	908	834	293	786	619	522	906	855
509	442	647	638	523	713	860	605	835	865	466	982	846	371	899	864	290	796	636	512	896	858
510	461	645	655	514	709	887	586	834	884	463	965	868	370	890	893	287	817	652	500	885	860
511	491	643	678	504	709	915	565	834	900	461	943	888	373	878	919	285	847	672	493	876	862
512	532	638	708	492	716	942	540	834	912	459	919	905	376	856	937	281	887	700	497	875	865
513	580	636	751	474	726	966	515	834	920	459	892	919	376	830	954	277	934	741	508	878	868
514	628	639	812	447	735	982	490	831	922	455	865	927	369	801	966	275	983	801	518	879	872
515	665	648	894	417	733	985	469	826	924	449	838	929	354	774	967	282	1021	881	520	875	875
516	677	668	987	394	713	978	452	818	927	441	814	928	335	759	960	297	1031	974	511	865	878
517	663	690	1078	390	686	975	440	808	930	431	794	928	311	759	957	312	1014	1065	504	856	882
518	623	702	1155	399	658	978	432	796	933	420	781	929	313	749	949	317	975	1141	496	848	886
519	574	699	1214	415	633	983	427	782	936	408	771	931	323	739	941	305	927	1193	487	839	889
520	534	686	1253	431	613	990	425	767	939	395	766	933	321	740	942	285	886	1227	475	830	891
521	508	665	1275	447	597	996	424	752	942	382	764	936	322	741	944	260	858	1246	461	819	893
522	494	638	1281	462	586	1002	426	736	944	368	765	939	305	756	953	230	841	1251	447	808	894
523	490	605	1273	475	578	1006	429	720	945	353	767	941	273	782	966	197	832	1244	431	796	895
524	493	568	1253	488	572	1009	433	705	946	339	772	943	238	807	977	161	831	1226	415	785	897
525	502	527	1222	498	566	1009	437	690	945	324	777	943	211	823	980	123	834	1199	399	773	898

Table A.9: CB T15 C3 445-615

Frame	Primary_P			Wrist_P			Elbow_P			Elbow_S			Wrist_S			Primary_S			Spine_F		
	X	Y	Z	X	Y	Z	X	Y	Z	X	Y	Z	X	Y	Z	X	Y	Z	X	Y	Z
526	516	485	1184	507	559	1006	441	677	943	310	782	942	198	824	973	85	842	1164	384	760	900
527	532	441	1139	515	550	1000	444	665	939	297	786	940	182	826	965	46	851	1124	369	748	902
528	548	398	1089	520	539	990	441	650	934	282	787	933	165	828	953	8	860	1078	356	737	905
529	563	357	1037	523	524	974	435	633	931	269	784	923	148	825	939	-28	868	1030	344	725	909
530	575	318	984	525	507	953	428	617	926	257	774	919	132	816	926	-62	873	979	334	714	914
531	582	283	932	519	488	933	421	602	923	242	762	917	117	803	913	-92	873	929	326	704	920
532	583	253	883	503	465	915	412	588	918	227	749	915	102	786	901	-118	867	880	318	694	927
533	574	229	838	485	443	897	402	576	913	212	736	914	86	766	889	-139	852	833	309	683	933
534	555	213	801	462	423	879	392	562	910	198	723	912	72	743	878	-154	827	791	299	671	940
535	524	203	769	435	405	863	380	550	907	184	711	911	59	718	869	-162	790	755	289	660	948
536	485	200	734	405	392	848	367	538	907	173	698	910	50	691	864	-162	742	725	279	649	955
537	437	202	701	372	383	837	356	529	907	162	685	911	44	665	864	-154	689	699	269	639	962
538	379	209	674	339	380	834	345	519	909	154	673	913	41	640	869	-137	633	680	259	627	969
539	313	223	658	309	377	839	333	513	910	147	662	918	42	616	879	-113	577	671	247	615	976
540	248	241	657	284	373	848	323	508	913	142	650	925	44	593	891	-85	526	674	237	602	983
541	187	261	671	264	368	863	315	501	920	136	640	934	47	569	905	-58	480	689	226	588	990
542	139	278	696	246	362	881	308	495	930	131	629	945	45	554	926	-40	443	714	215	573	995
543	105	290	723	231	356	903	301	489	943	126	619	959	41	544	952	-30	418	742	202	557	1000
544	84	299	746	218	350	927	293	482	957	121	609	976	37	533	979	-30	405	766	192	541	1007
545	75	304	762	207	343	952	283	476	974	118	598	996	35	522	1006	-35	407	783	180	525	1011
546	79	306	772	196	338	979	270	471	992	114	587	1018	34	507	1031	-41	421	795	168	509	1014
547	95	309	777	185	332	1005	253	466	1011	112	574	1038	34	490	1054	-48	446	810	157	494	1017
548	123	310	785	173	328	1030	231	461	1029	111	551	1053	35	471	1075	-54	477	830	146	479	1020
549	162	312	800	159	324	1054	210	453	1045	110	527	1066	36	451	1095	-61	516	861	135	465	1022
550	207	314	825	144	322	1076	190	445	1059	108	503	1077	34	421	1111	-67	558	906	124	452	1025
551	255	315	868	129	321	1098	172	435	1070	105	477	1084	30	391	1115	-66	591	964	113	440	1027
552	294	316	925	116	317	1117	155	424	1080	99	450	1088	21	363	1115	-64	609	1033	103	428	1029

Table A.9: CB T15 C3 445-615

Frame	Primary_P			Wrist_P			Elbow_P			Elbow_S			Wrist_S			Primary_S			Spine_F		
	X	Y	Z	X	Y	Z	X	Y	Z	X	Y	Z	X	Y	Z	X	Y	Z	X	Y	Z
553	317	314	991	104	308	1133	140	413	1088	92	426	1091	7	345	1110	-61	612	1104	92	416	1032
554	325	308	1059	93	297	1146	126	400	1094	83	406	1094	-9	331	1108	-61	600	1167	82	406	1034
555	321	297	1121	84	282	1155	113	387	1098	72	389	1095	-25	320	1111	-63	577	1224	71	395	1036
556	308	282	1173	76	265	1162	101	373	1101	60	376	1096	-41	312	1116	-68	550	1271	61	385	1038
557	292	266	1219	70	246	1166	91	358	1103	47	365	1097	-58	307	1124	-78	521	1309	51	375	1040
558	274	248	1259	66	225	1168	81	343	1104	33	356	1098	-73	304	1133	-91	494	1338	41	365	1043
559	262	224	1287	63	204	1167	72	327	1104	18	350	1098	-88	305	1142	-109	475	1357	31	356	1045
560	258	193	1304	62	183	1165	64	311	1102	2	345	1099	-103	308	1150	-132	463	1369	21	346	1047
561	258	157	1309	62	162	1161	57	295	1100	-14	341	1100	-119	315	1157	-159	456	1373	11	336	1049
562	262	118	1306	64	142	1155	50	279	1098	-31	337	1102	-137	322	1164	-189	454	1371	1	326	1051
563	267	76	1293	68	124	1148	43	263	1095	-48	334	1104	-157	326	1166	-221	456	1363	-8	316	1054
564	272	34	1273	74	107	1140	37	246	1091	-64	331	1107	-177	325	1165	-256	460	1350	-18	306	1056
565	275	-7	1246	81	93	1131	31	230	1087	-81	327	1111	-197	324	1161	-292	465	1333	-27	295	1058
566	274	-45	1213	90	82	1121	25	214	1084	-97	322	1115	-217	323	1157	-329	470	1313	-37	284	1061
567	269	-81	1176	98	70	1109	19	198	1080	-113	318	1117	-237	321	1152	-366	474	1289	-46	272	1063
568	260	-113	1137	96	58	1098	13	183	1076	-129	313	1116	-257	318	1145	-402	476	1264	-55	260	1066
569	248	-142	1097	93	45	1087	6	168	1073	-145	307	1112	-274	313	1138	-437	475	1237	-64	248	1068
570	233	-168	1058	88	31	1074	0	154	1070	-161	300	1108	-289	304	1132	-470	469	1210	-72	237	1071
571	215	-189	1021	80	17	1062	-8	141	1068	-176	288	1109	-306	293	1126	-501	458	1183	-80	225	1074
572	195	-206	989	66	2	1051	-15	128	1066	-190	276	1109	-323	281	1120	-529	439	1157	-89	213	1077
573	172	-219	960	51	-12	1041	-24	117	1063	-205	263	1107	-338	267	1114	-554	416	1134	-99	201	1080
574	146	-231	935	35	-26	1033	-33	107	1062	-220	250	1106	-353	251	1108	-577	388	1116	-109	189	1084
575	116	-241	912	16	-41	1026	-42	97	1060	-234	237	1106	-366	234	1104	-597	358	1103	-120	178	1089
576	84	-248	891	-4	-54	1023	-52	87	1060	-248	224	1106	-378	215	1103	-614	329	1093	-131	166	1093
577	49	-253	873	-24	-67	1022	-63	77	1060	-259	212	1108	-388	196	1104	-626	302	1083	-142	154	1097
578	13	-257	861	-46	-79	1024	-72	68	1061	-269	200	1111	-398	176	1108	-635	279	1072	-155	143	1100
579	-24	-260	855	-67	-90	1029	-82	59	1064	-278	187	1115	-406	156	1114	-641	260	1062	-168	131	1104

Table A.9: CB T15 C3 445-615

Frame	Primary_P			Wrist_P			Elbow_P			Elbow_S			Wrist_S			Primary_S			Spine_F		
	X	Y	Z	X	Y	Z	X	Y	Z	X	Y	Z	X	Y	Z	X	Y	Z	X	Y	Z
580	-60	-263	854	-89	-99	1036	-92	50	1068	-287	175	1119	-413	135	1123	-643	243	1055	-180	117	1106
581	-92	-264	857	-111	-108	1046	-101	42	1073	-295	162	1124	-419	115	1134	-643	228	1054	-191	103	1108
582	-119	-263	862	-129	-116	1059	-111	34	1079	-303	149	1130	-422	96	1145	-642	214	1056	-204	89	1111
583	-141	-262	869	-145	-124	1074	-121	26	1087	-310	134	1138	-426	77	1156	-641	201	1063	-215	75	1114
584	-157	-260	877	-160	-131	1089	-132	18	1095	-318	120	1144	-429	58	1166	-639	191	1072	-227	61	1115
585	-167	-257	886	-174	-137	1106	-147	10	1103	-323	104	1153	-432	40	1175	-636	183	1083	-240	47	1116
586	-172	-254	897	-189	-142	1121	-161	1	1111	-330	89	1159	-433	23	1184	-631	175	1096	-252	32	1117
587	-172	-250	909	-206	-145	1136	-175	-8	1120	-335	72	1165	-435	5	1191	-626	170	1110	-264	18	1118
588	-164	-246	923	-222	-149	1151	-192	-16	1128	-339	55	1171	-437	-12	1198	-620	166	1127	-276	4	1118
589	-154	-241	941	-237	-153	1165	-209	-25	1135	-344	37	1175	-440	-29	1203	-611	163	1145	-287	-10	1119
590	-140	-235	962	-254	-156	1179	-226	-34	1142	-348	19	1177	-443	-47	1208	-601	161	1164	-299	-24	1119
591	-125	-227	987	-270	-159	1192	-243	-45	1148	-353	1	1179	-447	-64	1211	-590	158	1184	-311	-39	1120
592	-110	-217	1017	-291	-163	1202	-258	-57	1153	-357	-17	1180	-453	-81	1213	-577	153	1205	-322	-53	1120
593	-98	-206	1050	-313	-170	1209	-273	-69	1157	-362	-35	1180	-460	-97	1214	-565	148	1226	-334	-68	1121
594	-89	-196	1087	-333	-182	1213	-286	-83	1159	-368	-52	1180	-468	-112	1214	-552	141	1246	-345	-82	1121
595	-84	-187	1127	-349	-197	1215	-299	-97	1161	-374	-70	1178	-477	-126	1213	-539	132	1265	-357	-97	1121
596	-87	-181	1170	-361	-216	1217	-311	-112	1162	-382	-86	1176	-488	-138	1212	-528	122	1282	-368	-111	1121
597	-90	-181	1207	-371	-237	1216	-323	-128	1162	-391	-101	1174	-499	-148	1212	-520	110	1294	-379	-125	1120
598	-94	-188	1235	-378	-259	1215	-334	-144	1162	-401	-114	1172	-511	-156	1212	-517	98	1304	-389	-139	1119
599	-97	-201	1256	-383	-283	1213	-344	-161	1160	-413	-126	1169	-524	-163	1213	-518	88	1308	-399	-153	1118
600	-100	-220	1271	-386	-307	1211	-353	-178	1158	-425	-137	1166	-537	-169	1214	-525	80	1307	-409	-166	1117
601	-104	-244	1279	-387	-331	1209	-362	-195	1156	-438	-146	1163	-549	-175	1216	-536	74	1302	-419	-179	1115
602	-109	-273	1284	-388	-354	1206	-370	-212	1153	-452	-155	1160	-561	-180	1218	-548	69	1291	-428	-191	1114
603	-114	-305	1284	-387	-376	1204	-378	-230	1149	-466	-162	1157	-573	-185	1218	-566	65	1281	-437	-203	1111
604	-120	-341	1281	-387	-395	1202	-385	-247	1145	-480	-169	1154	-585	-189	1217	-584	63	1269	-445	-215	1108
605	-127	-381	1276	-387	-412	1201	-392	-264	1140	-495	-176	1151	-597	-194	1215	-616	54	1253	-453	-226	1105
606	-136	-422	1269	-387	-425	1201	-399	-281	1135	-509	-182	1147	-609	-199	1211	-645	51	1239	-460	-237	1102

Table A.9: CB T15 C3 445-615

Frame	Primary_P			Wrist_P			Elbow_P			Elbow_S			Wrist_S			Primary_S			Spine_F		
	X	Y	Z	X	Y	Z	X	Y	Z	X	Y	Z	X	Y	Z	X	Y	Z	X	Y	Z
607	-146	-466	1262	-388	-436	1202	-405	-297	1130	-523	-188	1144	-621	-205	1206	-684	42	1225	-468	-249	1099
608	-157	-510	1255	-392	-448	1202	-411	-313	1124	-536	-194	1140	-635	-210	1200	-723	33	1212	-476	-261	1097
609	-170	-555	1248	-394	-455	1201	-417	-329	1119	-550	-199	1136	-653	-215	1194	-766	19	1201	-483	-273	1095
610	-185	-598	1240	-401	-466	1196	-427	-347	1115	-565	-205	1131	-676	-222	1188	-808	4	1191	-491	-285	1093
611	-200	-638	1232	-406	-478	1187	-436	-365	1111	-585	-214	1124	-698	-228	1181	-848	-14	1180	-499	-296	1091
612	-216	-675	1222	-410	-490	1177	-445	-380	1108	-605	-225	1115	-721	-235	1171	-887	-35	1170	-507	-307	1089
613	-234	-707	1211	-411	-503	1167	-453	-395	1105	-623	-236	1108	-742	-244	1160	-925	-60	1160	-513	-315	1089
614	-257	-739	1198	-414	-518	1157	-460	-408	1101	-639	-249	1102	-762	-254	1148	-962	-89	1151	-525	-328	1090
615	-284	-769	1185	-415	-533	1148	-469	-421	1099	-653	-261	1098	-779	-265	1139	-995	-122	1141	-531	-335	1088

Appendix B

Avian Motion Capture Plots

The following appendix contains the companion plots to that of figure 3.9. The motion captured points are plot from the tables in appendix A. Markers representing the port side of the avian are presented in red while that of the starboard in blue. These plots represent the data as rotated about the z-axis using the methodology detailed in the main text and as such the body is aligned with the x-z plane. The interval spacing for each frame of motion presented in these plots is not constant. Instead an interval was selected visually for each trial to best present the motion; each frame interval is included in each capture/plot caption.

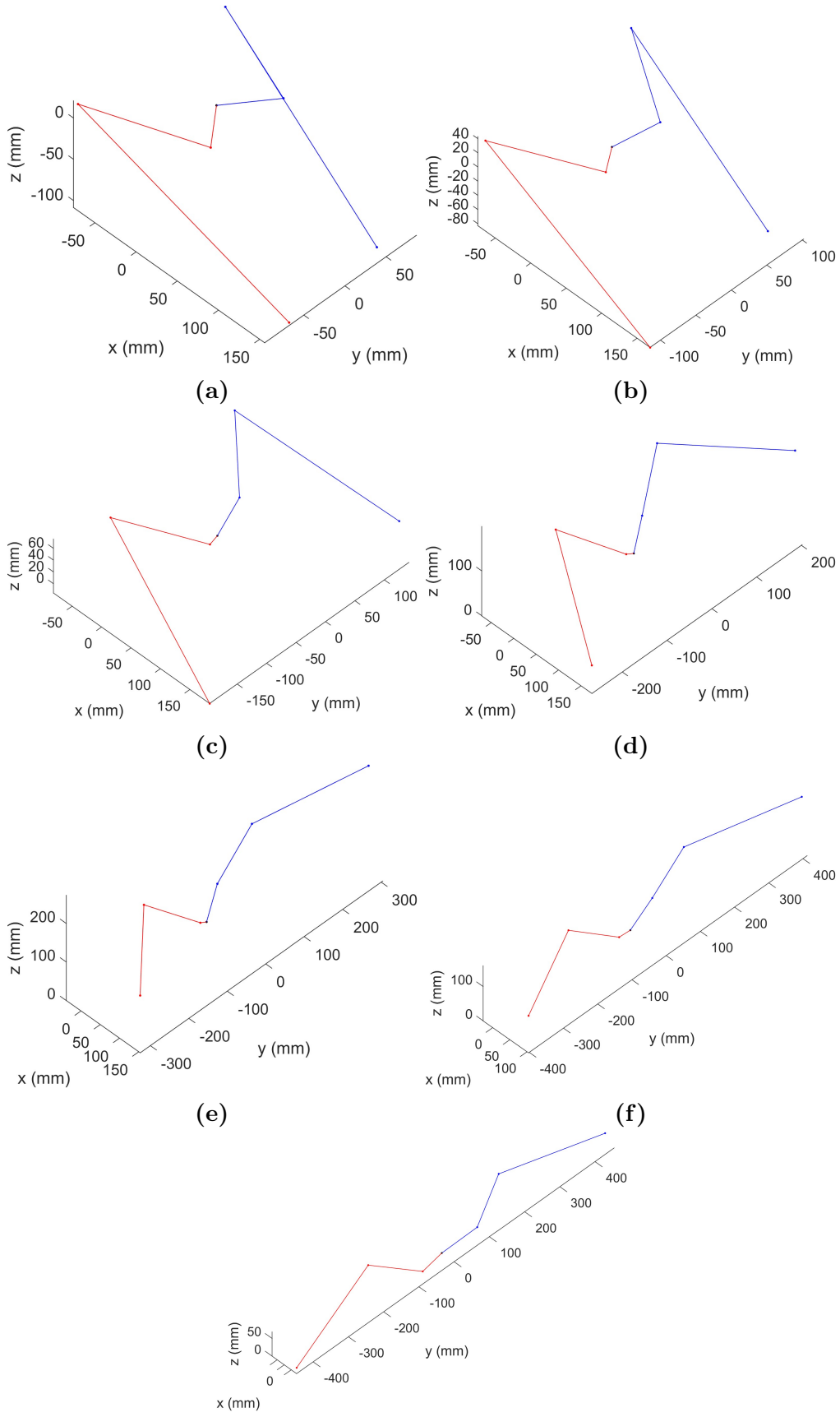


Figure B.1: Common Buzzard - specimen: CB, Trial 4, Capture session 3, Frame interval 0.05 seconds

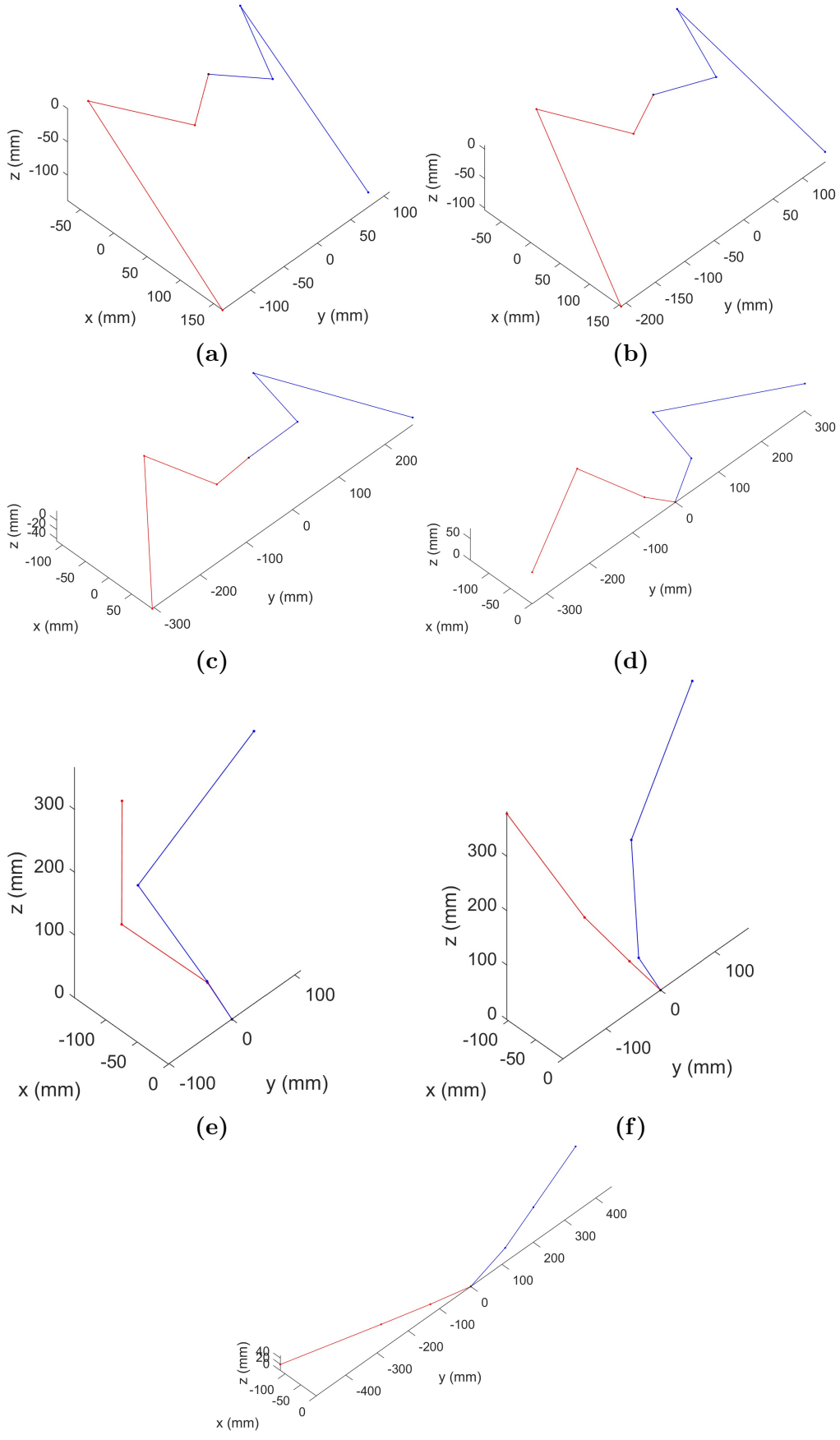


Figure B.2: Common Buzzard - specimen: CB, Trial 7, Capture session 3, Frame interval 0.05 seconds

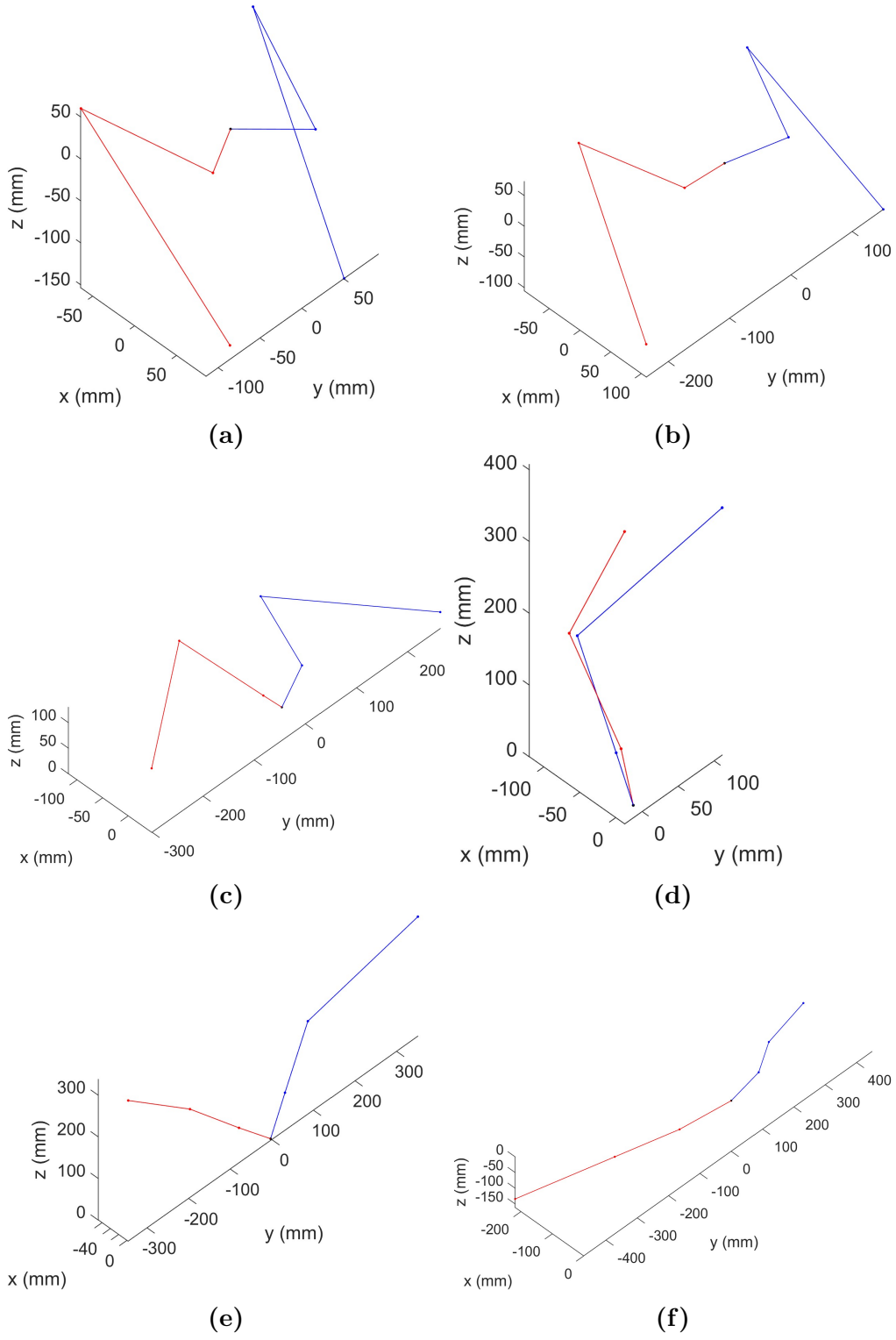


Figure B.3: Common Buzzard - specimen: CB, Trial 8, Capture session 3, Frame interval 0.05 seconds

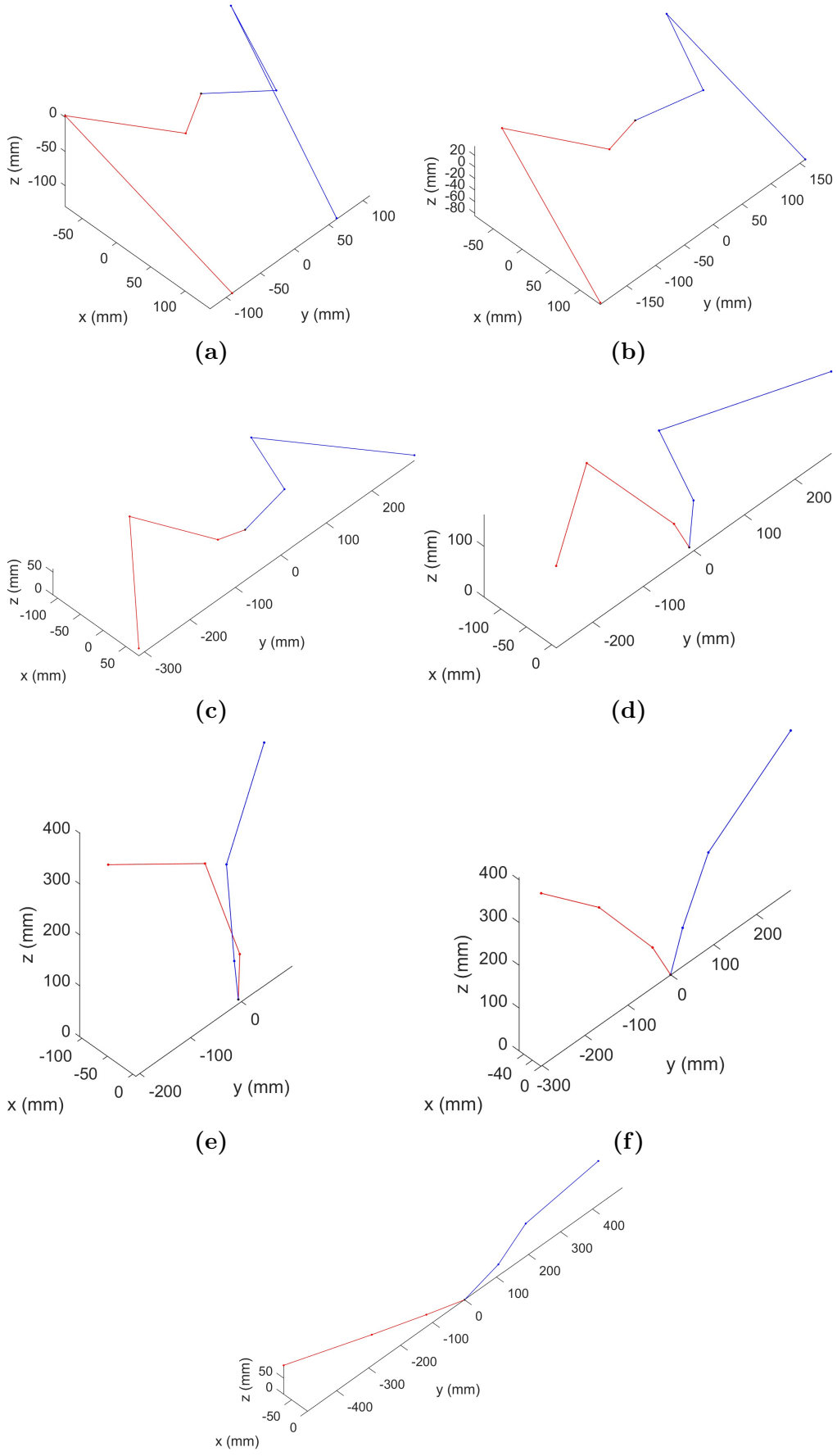


Figure B.4: Common Buzzard - specimen: CB, Trial 15, Capture session 3, Frame interval 0.04 seconds

Bibliography

[1] G. Cervantes, J. Kudva, J. Lilly, W. Buckle, D. Hartl, J. Perry, and D. J. Inman, "Development of a software framework for rapid, optimized design of morphing small uavs," in *AIAA SciTech Forum and Exposition, 2024*. American Institute of Aeronautics and Astronautics Inc, AIAA, 2024.

[2] J. Lilly, W. Buckle, A. Davis, J. Dean, T. White, D. Hartl, and G. Cervantes, "High-throughput analysis and morphing design space decomposition for mission-adaptive air vehicles," in *AIAA SciTech Forum and Exposition, 2024*. American Institute of Aeronautics and Astronautics Inc, AIAA, 2024.

[3] S. Barbarino, O. Bilgen, R. M. Ajaj, M. I. Friswell, and D. J. Inman, "A review of morphing aircraft," *Journal of Intelligent Material Systems and Structures*, vol. 22, no. 9, pp. 823–877, 2011.

[4] J. M. Benyus, "How will we make things?" in *Biomimicry : innovation inspired by nature*. HarperCollins e-books, 2009, ch. 4l, pp. 95–146.

[5] S. Barbarino, O. Bilgen, R. M. Ajaj, M. I. Friswell, and D. J. Inman, "A review of morphing aircraft," *Journal of Intelligent Material Systems and Structures*, vol. 22, no. 9, pp. 823–877, 2011.

[6] J. Sun, Q. Guan, Y. Liu, and J. Leng, "Morphing aircraft based on smart materials and structures: A state-of-the-art review," *Journal of Intelligent Material Systems and Structures*, vol. 27, no. 17, pp. 2289–2312, 2016.

[7] B. K. Woods, M. F. Gentry, C. S. Kothera, and N. M. Wereley, "Fatigue life testing of swaged pneumatic artificial muscles as actuators for aerospace applications," *Journal of Intelligent Material Systems and Structures*, vol. 23, no. 3, pp. 327–343, 2012.

[8] P. K. Panda, *Piezoceramic Materials and Devices for Aerospace Applications*, 2017, pp. 501–518.

[9] R. Vos, R. D. Breuker, R. M. Barrett, and P. Tiso, "Morphing Wing Flight Control Via Postbuckled Precompressed Piezoelectric Actuators," *Journal of Aircraft*, vol. 44, no. 4, pp. 1060–1068, jul 2007.

[10] S. Vijaya, *Piezoelectric Materials and Devices: Applications in Engineering and Medical Sciences*. Taylor Francis, 2012, vol. 1.

[11] P. Santos, J. Sousa, and P. Gamboa, "Variable-span wing development for improved flight performance," *Journal of Intelligent Material Systems and Structures*, vol. 28, no. 8, pp. 961–978, 2017.

[12] R. Ajaj, E. Saavedra Flores, M. Friswell, G. Allegri, B. Woods, A. Isikveren, and W. Dettmer, "The Zigzag wingbox for a span morphing wing," *Aerospace Science and Technology*, vol. 28, no. 1, pp. 364–375, jul 2013.

[13] J. Blondeau, J. Richeson, and D. J. Pines, "Design, development and testing of a morphing aspect ratio wing using an inflatable telescopic spar," in *Structures, Structural Dynamics, and Materials*. Norfolk, Virginia: AIAA, 2003.

[14] M. S. Parancheerivilakkathil, Z. Haider, R. M. Ajaj, and M. Amoozgar, "A polymorphing wing capable of span extension and variable pitch," *Aerospace 2022, Vol. 9, Page 205*, vol. 9, p. 205, 4 2022.

[15] P. L. Bishay, A. Rini, M. Brambila, P. Niednagel, J. Eghdamzamiri, H. Yousefi, J. Herrera, Y. Saad, E. Bertuch, C. Black, D. Hanna, and I. Rodriguez, "Cgull: A non-flapping bioinspired composite morphing drone," *Biomimetics*, vol. 9, p. 527, 9 2024.

[16] B. F. Song, X. Y. Lang, D. Xue, W. Q. Yang, H. Bao, D. Liu, T. Wu, K. Liu, W. P. Song, and Y. Wang, "A review of the research status and progress on the aerodynamic mechanism of bird wings," *Zhongguo Kexue Jishu Kexue/Scientia Sinica Technologica*, vol. 52, pp. 893–910, 2022.

[17] S. Kurumaya, H. Nabae, G. Endo, and K. Suzumori, "Design of thin McKibben muscle and multifilament structure," *Sensors and Actuators, A: Physical*, vol. 261, pp. 66–74, jul 2017.

[18] D. Yang, M. Verma, J.-H. So, B. Mosadegh, C. Keplinger, B. Lee, F. Khashai, E. Lossner, Z. Suo, and G. M. Whitesides, "Buckling Pneumatic Linear Actuators Inspired by Muscle," *Advanced Materials Technologies*, vol. 1, 2016.

[19] A. Concilio, I. Dimino, L. Lecce, and R. Pecora, *Morphing Wing Technologies*. Butterworth-Heinemann, 2017.

[20] A. Y. Sofla, S. A. Meguid, K. T. Tan, and W. K. Yeo, "Shape morphing of aircraft wing: Status and challenges," *Materials and Design*, vol. 31, no. 3, pp. 1284–1292, 2010.

[21] I. Hunter and S. Lafontaine, "A comparison of muscle with artificial actuators," in *Technical Digest IEEE Solid-State Sensor and Actuator Workshop*. IEEE, 1992, pp. 178–185.

[22] R. J. Vazquez, "The automating skeletal and muscular mechanisms of the avian wing (Aves)," *Zoomorphology*, vol. 114, no. 1, pp. 59–71, 1994.

[23] S. Kurumaya, K. Suzumori, H. Nabae, and S. Wakimoto, "Musculoskeletal lower-limb robot driven by multifilament muscles," *Robomech Journal*, vol. 3, no. 1, 2016.

[24] A. A. Biewener, "Muscle function in avian flight: achieving power and control," *Philosophical Transactions of the Royal Society of London B: Biological Sciences*, vol. 366, no. 1570, pp. 1496–1506, 2011.

[25] B. W. Tobalske, "Biomechanics of bird flight," *Journal of Experimental Biology*, vol. 210, no. 18, pp. 3135–3146, 2007.

[26] C. J. Pennycuick, "Mechanics of flight," in *Avian Biology, Vol. 5*, D.S.Farner and J.R.King, Eds. United Kingdom: Academic Press, 1975, vol. Vol 5, Cha, pp. 1–75.

[27] J. B. Wells, "COMPARISON OF MECHANICAL PROPERTIES BETWEEN SLOW AND FAST MAMMALIAN MUSCLES," vol. 178, pp. 252–269, 1965.

[28] A. Huxley, *Reflections on muscle*. Liverpool University Press, 1980.

[29] A. A. Biewener, K. P. Dial, and G. E. Goslow, "PECTORALIS MUSCLE FORCE AND POWER OUTPUT DURING FLIGHT IN THE STARLING," *J. exp. Biol*, vol. 164, pp. 1–18, 1992.

[30] K. P. Dial and A. A. Biewener, "PECTORALIS MUSCLE FORCE AND POWER OUTPUT DURING DIFFERENT MODES OF FLIGHT IN PIGEONS (COLUMBA LIVIA)," *J. exp. Biol*, vol. 176, pp. 31–54, 1993.

[31] C. J. Pennycuick and M. A. Rezende, "The specific power output of aerobic muscle, related to the power density of mitochondria," *exp. Biol*, vol. 108, pp. 377–392, 1984.

[32] C. J. Pennycuick and G. A. Parker, "STRUCTURAL LIMITATIONS ON THE POWER OUTPUT OF THE PIGEON'S FLIGHT MUSCLES," *J. Exp. Biol*, vol. 45, pp. 489–498, 1966.

[33] J. H. Marden, "MAXIMUM LIFT PRODUCTION DURING TAKEOFF IN FLYING ANIMALS," *J. exp. Biol*, vol. 130, p. 5, 1987.

[34] C. P. Ellington, "LIMITATIONS ON ANIMAL FLIGHT PERFORMANCE," *exp. Biol*, vol. 160, pp. 71–91, 1991.

[35] D. R. Wilkie, "The relation between force and velocity in human muscle," *The Journal of Physiology*, vol. 110, no. 3-4, pp. 249–280, dec 1949.

[36] D. R. WILKIE, "THE MECHANICAL PROPERTIES OF MUSCLE," *British Medical Bulletin*, vol. 12, no. 3, pp. 177–182, 1956.

[37] A. A. Amis, D. Dowson, and V. Wright, "Muscle strengths and musculoskeletal geometry of the upper limb," *Engineering in Medicine*, vol. 8, no. 1, pp. 41–48, jan 1979.

[38] G. Klute, J. Czerniecki, and B. Hannaford, "McKibben artificial muscles: pneumatic actuators with biomechanical\nintelligence," *1999 IEEE/ASME International Conference on Advanced Intelligent Mechatronics (Cat. No.99TH8399)*, pp. 1–6, 1999.

[39] Y. Chen, W. Yin, Y. Liu, and J. Leng, "Structural design and analysis of morphing skin embedded with pneumatic muscle fibers," *Smart Materials and Structures*, vol. 20, no. 8, 2011.

[40] N. Feng, L. Liu, Y. Liu, and J. Leng, "A bio-inspired, active morphing skin for camber morphing structures," *Smart Materials and Structures*, vol. 24, no. 3, 2015.

[41] V. S. Chillara, L. M. Headings, and M. J. Dapino, "Multifunctional composites with intrinsic pressure actuation and prestress for morphing structures," *Composite Structures*, vol. 157, pp. 265–274, 2016.

[42] N. M. Wereley, C. S. Kothera, E. A. Bubert, M. Gentry, and R. Vocke, "Pneumatic Artificial Muscles for Aerospace Applications," in *50th AIAA/ASME/ASCE/AHS/ASC structures, Structural Dynamics, and Materials Conference*, no. May. Reston, Virigina: American Institute of Aeronautics and Astronautics, may 2009, pp. 1–11.

[43] "A Survey on applications of Pneumatic Artificial Muscles," in *2011 19th Mediterranean Conference on Control and Automation, MED 2011.* IEEE, jun 2011, pp. 1439–1446.

[44] F. Daerden, D. Lefeber, F. Daerden, and D. Lefeber, "Pneumatic artificial muscles: actuators for robotics and automation," *European Journal of Mechanical and Environmental Engineering*, vol. 47, no. 1, pp. 11–21, 2002.

[45] R. D. Vocke, C. S. Kothera, A. Chaudhuri, B. K. Woods, and N. M. Wereley, "Design and testing of a high-specific work actuator using miniature pneumatic artificial muscles," *Journal of Intelligent Material Systems and Structures*, vol. 23, no. 3, pp. 365–378, 2012.

[46] B. K. Woods, C. S. Kothera, J. Sirohi, and N. M. Wereley, "Pneumatic artificial muscles for trailing edge flap actuation: A feasibility study," *Smart Materials and Structures*, vol. 20, no. 10, 2011.

[47] M. A. Meller, M. Bryant, and E. Garcia, "Reconsidering the McKibben muscle: Energetics, operating fluid, and bladder material," *Journal of Intelligent Material Systems and Structures*, vol. 25, no. 18, pp. 2276–2293, 2014.

[48] R. Tiwari, M. A. Meller, K. B. Wajcs, C. Moses, I. Reveles, and E. Garcia, "Hydraulic artificial muscles," *Journal of Intelligent Material Systems and Structures*, vol. 23, no. 3, pp. 301–312, 2012.

[49] Ning, Feng, Chang, Yingli, and Wang, Jingze, "Variable stiffness structures utilizing pneumatic artificial muscles," *MATEC Web Conf.*, vol. 256, p. 01005, 2019.

[50] Z. Zhang and M. Philen, "Pressurized artificial muscles," *Journal of Intelligent Material Systems and Structures*, vol. 23, no. 3, pp. 255–268, 2012.

[51] G. Immega, *ROMAC muscle powered robots.* Dearborn Mich.: Society of Manufacturing Engineers, 1986.

[52] F. Daerden and D. Lefeber, "The concept and design of pleated pneumatic artificial muscles," *International Journal of Fluid Power*, vol. 2, no. 3, pp. 41–50, 2001.

[53] J. Yarlott, "Fluid Actuator US Patent No 3 645 173," 1972.

[54] Ching-Ping Chou and B. Hannaford, "Measurement and modeling of McKibben pneumatic artificial muscles," *IEEE Transactions on Robotics and Automation*, vol. 12, no. 1, pp. 90–102, 1996.

[55] C. S. Kothera, M. Jangid, J. Sirohi, and N. M. Wereley, "Experimental Characterization and Static Modeling of McKibben Actuators," *Journal of Mechanical Design*, vol. 131, no. 9, p. 091010, sep 2009.

[56] B. K. S. Woods, C. S. Kothera, and N. M. Wereley, "Wind Tunnel Testing of a Helicopter Rotor Trailing Edge Flap Actuated via Pneumatic Artificial Muscles," *Journal of Intelligent Material Systems and Structures*, vol. 22, no. 13, pp. 1513–1528, 2011.

[57] T. A. McMahon, *Muscles, reflexes, and locomotion.* Princeton University Press, 1984.

[58] R. Brunell, *Hydraulic & pneumatic cylinders.* Morden: Trade & Technical Press, 1979.

[59] G. Klute and B. Hannaford, "Fatigue characteristics of McKibben artificial muscle actuators," in *Proceedings. 1998 IEEE/RSJ International Conference on Intelligent Robots and Systems. Innovations in Theory, Practice and Applications (Cat. No.98CH36190)*, vol. 3. IEEE, 1998, pp. 1776–1781.

[60] D. Kingsley and R. Quinn, "Fatigue life and frequency response of braided pneumatic actuators," in *Proceedings 2002 IEEE International Conference on Robotics and Automation (Cat. No.02CH37292)*, vol. 3. IEEE, 2002, pp. 2830–2835.

[61] B. K. S. Woods, C. S. Kothera, and N. M. Wereley, "FLUIDIC ARTIFICIAL MUSCLE ACTUATOR AND SWAGING PROCESS THEREFOR," pp. 0–2, nov 2009.

[62] D. Yang, B. Mosadegh, A. Ainla, B. Lee, F. Khashai, Z. Suo, K. Bertoldi, and G. M. Whitesides, "Buckling of Elastomeric Beams Enables Actuation of Soft Machines," *Advanced Materials*, vol. 27, no. 41, pp. 6323–6327, 2015.

[63] B. Mosadegh, P. Polygerinos, C. Keplinger, S. Wennstedt, R. F. Shepherd, U. Gupta, J. Shim, K. Bertoldi, C. J. Walsh, and G. M. Whitesides, "Pneumatic networks for soft robotics that actuate rapidly," *Advanced Functional Materials*, vol. 24, no. 15, pp. 2163–2170, 2014.

[64] T. Zarrin-Ghalami and A. Fatemi, "Multiaxial fatigue and life prediction of elastomeric components," *International Journal of Fatigue*, vol. 55, pp. 92–101, 2013.

[65] R. Pecora and I. Dimino, " SMA for Aeronautics," in *Shape Memory Alloy Engineering: For Aerospace, Structural and Biomedical Applications*, A. Concilio and L. Lecce, Eds. Butterworth Heinemann, Sep 2015, ch. 10, pp. 275–303.

[66] K. Melton, "General applications of SMA's and smart materials," in *Shape Memory Materials*, 1st ed., K. Otsuka and C. M. Wayman, Eds. Cambridge University Press, 1999, ch. 10, pp. 220–240.

[67] V. Antonucci and A. Martone, " Phenomenology of Shape Memory Alloys," in *Shape Memory Alloy Engineering: For Aerospace, Structural and Biomedical Applications*, A. Concilio and L. Lecce, Eds. Butterworth Heinemann, Sep 2015, ch. 2, pp. 33–53.

[68] W. J. Buehler, J. V. Gilfrich, and R. C. Wiley, "Effect of Low-Temperature Phase Changes on the Mechanical Properties of Alloys near Composition TiNi," *Journal of Applied Physics*, vol. 34, no. 5, pp. 1475–1477, may 1963.

[69] S. H. Ko, J. S. Bae, and J. H. Rho, "Development of a morphing flap using shape memory alloy actuators: The aerodynamic characteristics of a morphing flap," *Smart Materials and Structures*, vol. 23, no. 7, 2014.

[70] D. J. Hartl and D. C. Lagoudas, "Aerospace applications of shape memory alloys," *Proceedings of the Institution of Mechanical Engineers, Part G: Journal of Aerospace Engineering*, vol. 221, no. 4, pp. 535–552, 2007.

[71] C. Xiang, J. Guo, Y. Chen, L. Hao, and S. Davis, "Development of a SMA-Fishing-Line-McKibben Bending Actuator," *IEEE Access*, vol. 6, pp. 27 183–27 189, 2018.

[72] D. Hwang and T. Higuchi, "A rotary actuator using shape memory alloy (SMA) wires," *IEEE/ASME Transactions on Mechatronics*, vol. 19, no. 5, pp. 1625–1635, oct 2014.

[73] S. Barbarino, R. Pecora, L. Lecce, A. Concilio, S. Ameduri, and L. De Rosa, "Airfoil structural morphing based on S.M.A. actuator series: Numerical and experimental studies," *Journal of Intelligent Material Systems and Structures*, vol. 22, no. 10, pp. 987–1004, 2011.

[74] N. B. Morgan, "Medical shape memory alloy applications - The market and its products," *Materials Science and Engineering A*, vol. 378, no. 1-2 SPEC. ISS., pp. 16–23, 2004.

[75] J. Mohd Jani, M. Leary, A. Subic, and M. A. Gibson, "A review of shape memory alloy research, applications and opportunities," *Materials and Design*, vol. 56, pp. 1078–1113, apr 2014.

[76] C. Pfeiffer, K. DeLaurentis, and C. Mavroidis, "Shape memory alloy actuated robot prostheses: initial experiments," *Proceedings 1999 IEEE International Conference on Robotics and Automation (Cat. No.99CH36288C)*, vol. 3, pp. 2385–2391, 1999.

[77] E. Kaplanoglu, "Design of shape memory alloy-based and tendon-driven actuated fingers towards a hybrid anthropomorphic prosthetic hand," *International Journal of Advanced Robotic Systems*, vol. 9, 2012.

[78] S. Jung, J. Bae, and I. Moon, "Lightweight prosthetic hand with five fingers using SMA actuator," *Control, Automation and Systems (ICCAS), 2011 11th International Conference on*, pp. 1797–1800, 2011.

[79] A. Atasoy, E. Toptas, S. Kuchimov, E. Kaplanoglu, S. Takka, M. Ozkan, and Enstit, "SMA Actuated Prosthetic Finger Desgin," pp. 3–5, 2016.

[80] H. I. Kim, M. W. Han, S. H. Song, and S. H. Ahn, "Soft morphing hand driven by SMA tendon wire," *Composites Part B: Engineering*, vol. 105, pp. 138–148, 2016.

[81] I. Ohkata and Y. Suzuki, "General applications of SMA's and smart materials," in *Shape Memory Materials*, 1st ed., K. Otsuka and C. M. Wayman, Eds. Cambridge University Press, 1999, ch. 11, pp. 240–267.

[82] S. M. An, J. Ryu, M. Cho, and K. J. Cho, "Engineering design framework for a shape memory alloy coil spring actuator using a static two-state model," *Smart Materials and Structures*, vol. 21, no. 5, 2012.

[83] D. Grant and V. Hayward, "Variable structure control of shape memory alloy actuators," *Control Systems, IEEE*, vol. 17, no. 3, pp. 80–88, jun 1997.

[84] H. Kim and K. Kang, "Ultralight shape memory actuator from wire-woven Kagome truss," *International Journal of Mechanical Sciences*, vol. 134, pp. 511–524, dec 2017.

[85] A. Hadi, A. Yousefi-Koma, M. M. Moghaddam, M. Elahinia, and A. Ghazavi, "Developing a novel SMA-actuated robotic module," *Sensors and Actuators, A: Physical*, vol. 162, no. 1, pp. 72–81, 2010.

[86] H. Taniguchi, "Flexible Artificial Muscle Actuator Using Coiled Shape Memory Alloy Wires," *APCBEE Procedia*, vol. 7, pp. 54–59, 2013.

[87] C. Xiang, H. Yang, Z. Sun, B. Xue, L. Hao, M. D. Rahoman, and S. Davis, "The design, hysteresis modeling and control of a novel SMA-fishing-line actuator," *Smart Materials and Structures*, vol. 26, no. 3, 2017.

[88] K. Takashima, J. Rossiter, and T. Mukai, "McKibben artificial muscle using shape-memory polymer," *Sensors and Actuators, A: Physical*, vol. 164, no. 1-2, pp. 116–124, 2010.

[89] H. Yuan, J.-C. Fauroux, F. Chapelle, and X. Balandraud, "A review of rotary actuators based on shape memory alloys," *Journal of Intelligent Material Systems and Structures*, vol. 28, no. 14, pp. 1863–1885, 2017.

[90] L. Manfredi, Y. Huan, and A. Cuschieri, "Low power consumption mini rotary actuator with SMA wires," *Smart Materials and Structures*, vol. 26, no. 11, 2017.

[91] G. Scire'mammano, S. Scire'mammano, and E. Dragoni, "Modeling of Wire-on-Drum Shape Memory Actuators for Linear and Rotary Motion**," *Journal of Intelligent Material Systems and Structures*, pp. 1129–1140, 2011.

[92] S. Viscuso and S. Pittaccio, "Design and implementation of a portable amagnetic shape memory rotary actuator," *Journal of Intelligent Material Systems and Structures*, vol. 24, no. 4, pp. 454–472, 2013.

[93] J. Huber, N. Fleck, and M. Ashby, "The selection of mechanical actuators based on performance indices," in *Proc. R. Soc. A*, vol. 453, no. 1965, 1997, pp. 2185–2205.

[94] B. K. S. Woods and M. I. Friswell, "Preliminary Investigaion of a Fishbone Active Camber Concept," in *ASME Conference on Smart Materials, Adaptive Structures and Intelligent Systems*, 2012, pp. 1–9.

[95] S. Ameduri, G. Amendola, and A. Concilio, "Conceptual Models of SMA Actuators for Blade Twist," in *ACTUATOR 2018: 16th International Conference on New Actuators*, no. June, Bremen, 2018, pp. 25–27.

[96] A. Jardine, J. Bartley-Cho, and J. Flanagan, "Improved design and performance of the SMA torque tube for the DARPA Smart Wing Program," in *Proceedings of SPIE*, J. H. Jacobs, Ed., vol. 3674, no. July 1999, jul 1999, pp. 260–269.

[97] J. N. Kudva, "Overview of the DARPA smart wing project," *Journal of Intelligent Material Systems and Structures*, vol. 15, no. 4, pp. 261–267, 2004.

[98] D. J. Hartl, D. C. Lagoudas, F. T. Calkins, and J. H. Mabe, "Use of a Ni60Ti shape memory alloy for active jet engine chevron application: I. thermomechanical characterization," *Smart Materials and Structures*, vol. 19, no. 1, 2010.

[99] D. Hartl, J. Mooney, D. Lagoudas, F. Calkins, and J. Mabe, "Use of a \chem{Ni_{60}Ti} shape memory alloy for active jet engine chevron application: {II}. Experimentally validated numerical analysis, volume = 19, year = 2010," *Smart Materials and Structures*, p. 15021.

[100] S. Barbarino, E. L. Saavedra Flores, R. M. Ajaj, I. Dayyani, and M. I. Friswell, "A review on shape memory alloys with applications to morphing aircraft," *Smart Materials and Structures*, vol. 23, no. 6, p. 63001, 2014.

[101] S. Barbarino, R. Pecora, L. Lecce, A. Concilio, S. Ameduri, and E. Calvi, "A novel SMA-based concept for airfoil structural morphing," *Journal of Materials Engineering and Performance*, vol. 18, no. 5-6, pp. 696–705, aug 2009.

[102] S. Barbarino, S. Ameduri, L. Lecce, and A. Concilio, "Wing shape control through an SMA-based device," *Journal of Intelligent Material Systems and Structures*, vol. 20, no. 3, pp. 283–296, 2009.

[103] R. Featherstone and Y. H. Teh, "Improving the speed of shape memory alloy actuators by faster electrical heating," *Springer Tracts in Advanced Robotics*, vol. 21, pp. 67–76, 2006.

[104] C. S. Loh, H. Yokoi, and T. Arai, "Improving heat sinking in ambient environment for the shape memory alloy (SMA)," in *2005 IEEE/RSJ International*

Conference on Intelligent Robots and Systems, IROS. IEEE, 2005, pp. 2277–2282.

[105] P. Motzki, T. Gorges, M. Kappel, M. Schmidt, G. Rizzello, and S. Seelecke, "High-speed and high-efficiency shape memory alloy actuation," *Smart Materials and Structures*, vol. 27, no. 7, 2018.

[106] Y. Tadesse, N. Thayer, and S. Priya, "Tailoring the response time of shape memory alloy wires through active cooling and pre-stress," *Journal of Intelligent Material Systems and Structures*, vol. 21, no. 1, pp. 19–40, 2010.

[107] R. Russell and R. Gorbet, "Improving the response of SMA actuators," in *Proceedings of 1995 IEEE International Conference on Robotics and Automation*, vol. 3. IEEE, 1995, pp. 2299–2304.

[108] O. Bilgen and M. I. Friswell, "Piezoceramic composite actuators for a solid-state variable-camber wing," *Journal of Intelligent Material Systems and Structures*, vol. 25, no. 7, pp. 806–817, 2014.

[109] R. Paradies and P. Ciresa, "Active wing design with integrated flight control using piezoelectric macro fiber composites," *Smart Materials and Structures*, vol. 18, no. 3, 2009.

[110] O. Bilgen, K. B. Kochersberger, and D. J. Inman, "Macro-Fiber Composite actuators for a swept wing unmanned aircraft," *Aeronautical Journal*, vol. 113, no. 1144, pp. 385–395, 2009.

[111] R. Barrett, R. McMurtry, R. Vos, P. Tiso, and R. D. Breuker, "Post-buckled precompressed piezoelectric flight control actuator design, development and demonstration," *Smart Materials and Structures*, vol. 15, pp. 1323 – 1331, 2006.

[112] M. S. Vijaya, "Piezoelectric Characteristics," in *Piezoelectric Materials and Devices: Applications in Engineering and Medical Sciences*, 1st ed. CRC Press, 2017, ch. 2, pp. 15–39.

[113] C. Thill, J. Etches, I. Bond, K. Potter, and P. Weaver, "Morphing Skins," *The Aeronautical Journal*, no. 7, 2008.

[114] D. P. Wang, J. D. Bartley-Cho, C. A. Martin, and B. J. Hallam, "Development of high-rate large-deflection hingeless trailing-edge control surface for the Smart Wing wind tunnel model," A.-M. R. McGowan, Ed., vol. 4332. International Society for Optics and Photonics, jun 2001, pp. 407–418.

[115] O. Bilgen, K. B. Kochersberger, D. J. Inman, and O. J. Ohanian, "Macro-Fiber Composite actuated simply supported thin airfoils," *Smart Materials and Structures*, vol. 19, no. 5, 2010.

[116] ——, "Novel, Bidirectional, Variable-Camber Airfoil via Macro-Fiber Composite Actuators," *Journal of Aircraft*, vol. 47, no. 1, pp. 303–314, jan 2010.

[117] R. Vos, R. Barrett, R. D. Breuker, and P. Tiso, "Post-buckled precompressed elements: A new class of control actuators for morphing wing UAVs," *Smart Materials and Structures*, vol. 16, no. 3, pp. 919–926, 2007.

[118] V. Giurgiutiu, "Recent advances in smart-material rotor control actuation," in *Proc. 41st AIAA/ASME/ASCE/AHS/ASC Structures, Structural Dynamics, and Materials Conference and Exhibit*, 2000, pp. 237–247.

[119] F. K. Straub, D. K. Kennedy, D. B. Domzalski, A. A. Hassan, H. Ngo, V. Anand, and T. Birchette, "Smart Material-actuated Rotor Technolnnogy - SMART," *Journal of Intelligent Material Systems and Structures*, vol. 15, no. 4, pp. 249–260, 2004.

[120] F. K. Straub, M. A. Ealey, and L. M. Schetky, "Application of smart materials to helicopter rotor active control," in *Smart Structures and Materials 1997: Industrial and Commercial Applications of Smart Structures Technologies*, J. M. Sater, Ed., vol. 3044, no. 1. International Society for Optics and Photonics, may 1997, pp. 99–113.

[121] M. S. Vijaya, "Engineering Applications of Piezoelectric Materials," in *Piezoelectric Materials and Devices: Applications in Engineering and Medical Sciences*, 1st ed. CRC Press, 2017, ch. 4, pp. 57–109.

[122] M. Goldfarb and N. Celanovic, "Modeling Piezoelectric Stack Actuators for Control of Micromanipulation," *IEEE Control Systems*, no. June, pp. 69–79, 1997.

[123] M. S. Vijaya, "Piezoelectric Materials," in *Piezoelectric Materials and Devices: Applications in Engineering and Medical Sciences*, 1st ed. CRC Press, 2017, ch. 3, pp. 39–57.

[124] N. Murayama and H. Obara, "Piezoelectric polymers and their applications." *Japanese journal od Applied Physics*, vol. 22, pp. 3–6, 1983.

[125] M. F. Ashby, *Materials selection in mechanical design*. Butterworth-Heinemann, 1999.

[126] E. L. Corvidae, R. O. Bierregaard, and S. E. Peters, "Comparison of wing morphology in three birds of prey: Correlations with differences in flight behavior," *J. Morphol*, vol. 267, pp. 612–622, 2006.

[127] V. A. Tucker, "Gliding Birds: The Effect of Variable Wing Span," *J. exp. Biol*, vol. 133, no. 1, pp. 33–58, 1987.

[128] C. Pennycuick, *Modelling the flying bird*, 1st ed. Academic, 7 2008, vol. 5.

[129] E. L. Simons, "Forelimb skeletal morphology and flight mode evolution in pelecaniform birds," *Zoology*, vol. 113, pp. 39–46, 1 2010.

[130] E. L. Simons, T. L. Hieronymus, and P. M. O'connor, "Cross sectional geometry of the forelimb skeleton and flight mode in pelecaniform birds," *Journal of Morphology*, vol. 272, pp. 958–971, 8 2011.

[131] T. N. Sullivan, T. T. Hung, A. Velasco-Hogan, and M. A. Meyers, "Bioinspired avian feather designs," *Materials Science and Engineering C*, vol. 105, dec 2019.

[132] C. Otto, "Comparative morphological studies on detached bones [translated]," 1981. [Online]. Available: \url{http://www.palaeo.vetmed.uni-muenchen.de/download/dissertationen/otto_1981_accipitridae.pdf}

[133] R. L. Nudds, "Wing-bone length allometry in birds," *Journal of Avian Biology*, vol. 38, pp. 515–519, 2007.

[134] J. Mitchell, L. J. Legendre, C. Lefèvre, and J. Cubo, "Bone histological correlates of soaring and high-frequency flapping flight in the furculae of birds," *Zoology*, vol. 122, pp. 90–99, 6 2017.

[135] G. Viscor and J. F. Fuster, "Relationships between morphological parameters in birds with different flying habits," *Comparative Biochemistry and Physiology Part A: Physiology*, vol. 87, pp. 231–249, 1 1987.

[136] H. Beaufrere, "A review of biomechanic and aerodynamic considerations of the avian thoracic limb," *Journal of Avian Medicine and Surgery*, vol. 23, pp. 173–186, 9 2009.

[137] A. C. Carruthers, S. M. Walker, A. L. R. Thomas, and G. K. Taylor, "Aerodynamics of aerofoil sections measured on a free-flying bird," *Journal of Aerospace Engineering*, vol. 224, no. 8, pp. 855–864, 2010.

[138] T. Liu, K. Kuykendoll, R. Rhew, and S. Jones, "Avian wing geometry and kinematics," *AIAA Journal*, vol. 44, no. 5, pp. 954–963, may 2006.

[139] J. McKittrick, P. Y. Chen, S. G. Bodde, W. Yang, E. E. Novitskaya, and M. A. Meyers, "The structure, functions, and mechanical properties of keratin," *JOM*, vol. 64, no. 4, pp. 449–468, apr 2012.

[140] T. L. Hieronymus, "Flight feather attachment in rock pigeons (Columba livia): covert feathers and smooth muscle coordinate a morphing wing," *Journal of Anatomy*, vol. 229, no. 5, pp. 631–656, 2016.

[141] N. E. Durston, Y. Mahadik, and S. P. Windsor, "Quantifying avian inertial properties using calibrated computed tomography," *J Exp Biol*, 1 2022.

[142] C. J. Pennycuick, "Power requirements for horizontal flight in the pigeon columba livia," vol. 49, pp. 527–555, 1968.

[143] G. Taylor, M. Bacic, R. Bomphrey, A. Carruthers, J. Gillies, S. Walker, and A. Thomas, "New experimental approaches to the biology of flight control systems," *The Journal of Experimental Biology*, vol. 211, pp. 258–266, 2008.

[144] S. Shepherd and J. Valasek, "Modeling and analysis of eagle flight mechanics from experimental flight data," 2012.

[145] J. K. Boye, H. Thomsen, T. Pfau, and E. Olsen, "Accuracy and precision of gait events derived from motion capture in horses during walk and trot," *Journal of Biomechanics*, vol. 47, pp. 1220–1224, 2014.

[146] M. S. Fischer and R. Blickhan, "The tri-segmented limbs of therian mammals: kinematics, dynamics, and self-stabilization—a review," *Journal of Experimental Zoology Part A: Comparative Experimental Biology*, vol. 305A, pp. 935–952, 11 2006.

[147] Z. da Silva, S. Shield, P. E. Hudson, A. M. Wilson, F. Nicolls, and A. Patel, "Markerless 3d kinematics and force estimation in cheetahs," *Scientific Reports 2024 14:1*, vol. 14, pp. 1–13, 5 2024.

[148] GlueDots Adhesive products, "TDS Low Tack Adhesive," Tech. Rep., 2011. [Online]. Available: https://gluedotseurope.com/wp-content/uploads/2019/07/TDS{_}LOW{_}TACK.pdf

[149] ——, "TDS High Tack Adhesive," Tech. Rep., 2011. [Online]. Available: https://gluedotseurope.com/wp-content/uploads/2019/07/TDS{_}HIGH{_}TACK.pdf

[150] ——, "TDS Super High Tack Adhesive," p. 1, 2011. [Online]. Available: https://gluedotseurope.com/wp-content/uploads/2019/07/TDS{_}SUPER{_}HIGH{_}TACK.pdf

[151] ——, "MSDS Removable," Tech. Rep., 2012. [Online]. Available: https://gluedotseurope.com/wp-content/uploads/2019/07/MSDS{_}Removable.pdf

[152] ——, "MSDS Permanent," Tech. Rep., 2012. [Online]. Available: https://gluedotseurope.com/wp-content/uploads/2019/07/MSDS{_}Permanent.pdf

[153] "Wind Tunnel Testing of a Helicopter Rotor Trailing Edge Flap Actuated via Pneumatic Artificial Muscles," *Journal of Intelligent Material Systems and Structures*, vol. 22, no. 13, pp. 1513–1528, 2011.

[154] A. Hay and M. Visonneau, "Local Mesh Adaptation and Remeshing Technique Applied to a Multiple Element Airfoil," in *17th AIAA Computational Fluid Dynamics Conference*. Reston, Virigina: American Institute of Aeronautics and Astronautics, jun 2005.

[155] H. K. Versteeg and W. Malalasekera, *An Introduction to Computational Fluid Dynamics Second Edition*, 2nd ed. Pearson Education, 2007.

[156] C. A. Lyon, P. Broeren, Andy P, A. Gopalarathnam, and M. S. Selig, "Summary of Low-Speed Airfoil Data," Tech. Rep., 1998.

[157] R. S. Hartenberg and J. Denavit, "A kinematic notation for lower-pair mechanisms based on metrics," *Transactions of the ASME. Journal of Applied Mechanics*, vol. 22, pp. 215–221, 1 1955.

[158] P. Srisuk, A. Sento, and Y. Kitjaidure, "Inverse kinematics solution using neural networks from forward kinematics equations," in *2017 9th International Conference on Knowledge and Smart Technology (KST)*. IEEE, 2 2017, pp. 61–65.

[159] B. Tondu, "Modelling of the mckibben artificial muscle: A review," *Journal of Intelligent Material Systems and Structures*, vol. 23, pp. 225–253, 2 2012.

[160] B. K. Woods, C. S. Kothera, G. Wang, and N. M. Wereley, "Dynamics of a pneumatic artificial muscle actuation system driving a trailing edge flap," *Smart Materials and Structures*, vol. 23, 2014.

[161] W. Scaff, O. Horikawa, and M. de Sales Guerra Tsuzuki, "Pneumatic artificial muscle optimal control with simulated annealing," *IFAC-PapersOnLine*, vol. 51, pp. 333–338, 1 2018.

[162] Festo, "Mpye-5-...-b proportional directional control valve," pp. 1–10, 2024. [Online]. Available: https://www.festo.com/gb/en/p/proportional-directional-control-valve-id_MPYE_1/?categoryCode=pim369&q=%7E%3AsortByCoreRangeAndNewProduct&tab=SUPPORT_PORTAL&documentTypeGroup=USER_DOCUMENTATION&documentTypes=

[163] E. Richer and Y. Hurmuzlu, "A high performance pneumatic force actuator system: Part i—nonlinear mathematical model," *Journal of Dynamic Systems, Measurement and Control, Transactions of the ASME*, vol. 122, pp. 416–425, 2000.

[164] R. H. Gaylord and R. H. Gaylord, "Fluid actuated motor system and stroking device," 1 1958.

[165] H. F. J. Schulte, *The Characteristics of the McKibben artificial muscle.* National Academy of Sciences-National Research Council, 1961.

[166] B. Tondu and P. Lopez, "Modeling and control of mckibben artificial muscle robot actuators," *IEEE Control Systems*, vol. 20, pp. 15–38, 2000.

[167] B. S. Kang, C. S. Kothera, B. K. Woods, and N. M. Wereley, "Dynamic modeling of mckibben pneumatic artificial muscles for antagonistic actuation," in *Proceedings - IEEE International Conference on Robotics and Automation*, 2009, pp. 182–187.

[168] A. A. Ozdemir and S. Gumussoy, "Transfer function estimation in system identification toolbox via vector fitting," *IFAC-PapersOnLine*, vol. 50, pp. 6232–6237, 7 2017.

[169] D. H. Lee and T. A. Weisshaar, "Aeroelastic on a folding wing configuration," *Collection of Technical Papers - AIAA/ASME/ASCE/AHS/ASC Structures, Structural Dynamics and Materials Conference*, vol. 4, pp. 2452 – 2464, 1 2005.

[170] S. Zhao, D. Li, J. Zhou, and E. Sha, "Numerical and experimental study of a flexible trailing edge driving by pneumatic muscle actuators," *Actuators 2021, Vol. 10, Page 142*, vol. 10, p. 142, 6 2021.

[171] L. Straka, "Operational reliability of mechatronic equipment based on pneumatic artificial muscle," *Applied Mechanics and Materials*, vol. 460, pp. 41 – 48, 1 2014.

[172] P. Li, Y. Liu, and J. Leng, "A new deformation monitoring method for a flexible variable camber wing based on fiber bragg grating sensors," *Journal of Intelligent Material Systems and Structures*, vol. 25, pp. 1644 – 1653, 9 2014.

[173] X. Changchuan, C. Zhiying, and A. Chao, "Aeroelastic response of a z-shaped folding wing during the morphing process," *AIAA Journal*, vol. 60, pp. 3166 – 3179, 1 2022.

[174] B. J. Stacey and P. R. Thomas, "A biomimetically derived method for control of span-wise morphing wings," *AIAA Science and Technology Forum and Exposition, AIAA SciTech Forum 2022*, 2022.

[175] D. Ahmad, R. M. Ajaj, and M. Amoozgar, "Elastomer-based skins for morphing aircraft applications: Effect of biaxial strain rates and prestretch," *Polymer Testing*, vol. 113, p. 107655, 9 2022.

[176] K. E. Evans and A. Alderson, "Auxetic materials: Functional materials and structures from lateral thinking!" *Advanced Materials*, vol. 12, pp. 617–628, 2000.

[177] B. Xu, H. Fang, Y. He, S. Jiang, and L. Lan, "Design of a morphing surface using auxetic lattice skin for space-reconfigurable reflectors," *Lecture Notes in Computer Science (including subseries Lecture Notes in Artificial Intelligence and Lecture Notes in Bioinformatics)*, vol. 12634 LNCS, pp. 55–67, 2021.

[178] J. B. Barlow, W. H. Rae, and A. Pope, *Low-speed wind tunnel testing*. Wiley, 1999.

[179] S. N. Skinner and H. Zare-Behtash, "Semi-span wind tunnel testing without conventional peniche," vol. 58, p. 163, 2017.

[180] S. Eder, K. Hufnagel, and C. Tropea, "Semi-span testing in wind tunnels," vol. 2, pp. 1293–1301, 01 2006.